PLASMONIC FIELD EFFECTS ON THE SPECTROSCOPIC AND PHOTOBIOLOGICAL FUNCTION OF THE PHOTOSYNTHETIC SYSTEM OF BACTERIORHODOPSIN

A Thesis
Presented to
The Academic Faculty

by

Arianna Biesso

In Partial Fulfillment
of the Requirements for the Degree
Doctor of Phylosophy in Chemistry in the
School of Chemistry and Biochemistry

Georgia Institute of Technology
May / 2009

PLASMONIC FIELD EFFECTS ON THE SPECTROSCOPIC AND PHOTOBIOLOGICAL FUNCTION OF THE PHOTOSYNTHETIC SYSTEM OF BACTERIORHODOPSIN

Approved by:

Dr. Mostafa A. El-Sayed Advisor
School of Chemistry and Biochemistry
Georgia Institute of Technology

Dr. Adegboyega K. Oyelere
School of Chemistry and Biochemistry
Georgia Institute of Technology

Dr. Joseph W. Perry
School of Chemistry and Biochemistry
Georgia Institute of Technology

Dr. Mark R. Prausnitz
School of Chemical and Biomolecular Engineering
Georgia Institute of Technology

Dr. Bridgette Barry
School of Chemistry and Biochemistry
Georgia Institute of Technology

Date Approved: [February 26, 2009]

To my parents

ACKNOWLEDGEMENTS

The completion of my thesis has been a journey, and the people that I have met along such journey are those who really made it possible. The people who really made it possible are my parents that have always been so supportive and loving though this time.

I want to thank Prof. Mostafa and Prof. Perry for their support and for teaching me about science, allowing me to become a better scientist. The groups I have worked in: Perry's group and El-Sayed's group for providing me with helpful discussions and assistance. I want to thank Mariacristina Rumi for her help in the lab, but mostly for being extremely supportive both inside and outside the working environment.

The list of people that made my staying in Atlanta so great and enjoyable is very long, more than I can remember. Some of them are very special and among all Bob Letiecq has been constantly there for me, through the happy and not so happy times of this journey. I am very grateful to him and to all my dear friends: Mehmet Kutukcu, Matija Crne, Vivek Sharma, Richard Bedell, Sarah Chi, Federico Polo and Giuseppe Brunello, .

TABLE OF CONTENTS

LIST OF TABLES

LIST OF FIGURES

LIST OF SYMBOLS AND ABBREVIATIONS

bR	Bacteriorhodopsin
WT	Wild type
hR	Halorhodopsin
sRI	Sensory rhodopsin I
sRII	Sensory rhodopsin II
PM	Purple Membrane
kDa	Kilodalton
ATP	Adenosine-5$^{'}$-Triphosphate
PSB	Protonated Schiff Base
LA	light adapted
DA	dark adapted
RR	Resonance Raman
EC	Extracellular half channel
CP	Cytoplasmic half channel
LSPs	Localized Surface Plasmons
NPs	Nanoparticles
NRs	Nanorods
PH	Plasmon Hybridization
CTAB	hexadecyltrimethylammonium bromide
BDAC	benzyldimethylammoni-umchloride hydrate
fs	femtosecond
ps	picosecond
e-p	electron-phonon

p-p	phonon-phonon
ITO	indium-tin-oxide
WF	water filter
bO	Bacterioopsin
R	aspect ratio
TPA	two-photon absorption
RSA	reverse saturable absorption
NIR	Near Infrared
NLO	nonlinear optics
Vis-NIR	Visible Near Infrared
D-A-D	Donor-Acceptor-Donor
SOS	Sum-over-states
Γ	damping factor
BLA	bond length alternation
HOMO	highest occupied molecular orbital
LUMO	lowest unoccupied molecular orbital
ESA	excited state absorption
DFWM	Degenerate Four Wave Mixing
LIG	laser-induced grating

SUMMARY

The first part of this thesis (chapter I through VI) has been developed to study the interactions of bacteriorhodopsin (bR) with the local plasmon field generated by noble metal nanoparticles. The main question that this section poses is whether the proximity of the strong plasmonic field to the protein of bR can affect its functionality. The rationale behind this hypothesis can be retraced to the ability of the oscillating field from gold and silver nanoparticles to enhance the optical response, and induce SERS on nearby molecules; it is than foreseeable that this field could affect the bR photocycle.
The rise and decay lifetime of key intermediates in the bR photocycle are measured in presence of gold nanoparticles via femtosecond pump-probe spectroscopy, and nanosecond flash photolysis.

The first light-induced event in bR photocycle involves the isomerization of the Retinal Base Schiff (RBS). An electron is promoted from the ground state S_0 to the first excited state S_1 to form the short lived (500 fs) intermediate I_{460}; a transition involving a large change in the dipole moment (about 12 Debye). The decay of I_{460} was found to be affected by the presence of gold nanoparticles in the bR sample, when excited by the femtosecond laser along with RSB. The increase in I_{460} lifetime was found to be dependent both on the concentration and particle size. It was concluded that S_1 electronic state was perturbed by the presence of the nanoparticles plasmonic field affecting the decay lifetime of intermediate I_{460}. The concentration and size dependence can be directly related to the intensity of the plasmonic field; both larger size and concentration induce larger plasmonic field intensity, amplifying the effect.

The other intermediate of interest is M_{412}. During its formation and decay the RBS get deprotonated and protonated respectively. This is the most studied among all intermediates, where the transport functions of bR are exploited. In chapter IV a nanosecond flash photolysis experiment was set-up and the M_{412} rise and decay dynamics monitored.

The rise and decay of M_{412} are measured in presence of gold nanorods, M_{412} decay lifetime experiences a decrease. The nanorods longitudinal plasmon is continuously excited by an independent CW source at 808 nm and the decay rate shown to be dependent both on the concentration of nanorods as well as the intensity of the CW exciting source while the rise time was not affected by it. The reason why only the decay dynamic gets affected by the nanorods plasmonic field is believed to be related to the longer distance travelled by the proton during such process compared to the much faster proton transfer taking place during the deprotonation stage.

The other physical effect could be due to temperature. However, both theoretical prediction and experimental observation do not support this mechanism

On chapter V the vicinity of the bR protein to plasmonic structure is used to induce SERS on the protein using NIR excitation wavelength. Various gold and silver nanostructures are added to the bR protein, both in solution or organized on a monolayer. It is observed than when silver nanospheres are used and aggregation is favored, SERS is observed in the low energy region of the Raman spectrum.

In chapter VI the bR photoconversion efficiency is measured in solid films of the protein on a conductive substrate (ITO) while excited by a modulated while light source. The integrated area of the differential current generated by the bR film was found to

experience an increase when silver nanoparticles are embedded in the film. The conversion efficiency is then improved (about 30%) compared to the pure bR (chapter under revision)

The second part of this thesis consists in the study of the third-order nonlinear properties of extended conjugated squaraine dyes in the 1300 to 1500 nm region also known as the telecommunication range. Chapter X provides the microscopic (γ) and macroscopic ($\chi^{(3)}$) nonlinearity of a series of dye having a common squarylium delocalized core, acting as an acceptor group, with increasing conjugated chain length where weak donor groups are added on both sides of the acceptor forming a donor-acceptor-donor type of structure. These are compared to a shorter dye with only two donor groups but a double squarylium core providing twice the delocalized length.

The magnitude of the microscopic nonlinearity normalized by the number of double bond in the main chain was found to be the largest for the shorter dye concluding that in order to increase the third-order nonlinearity in conjugated squaraines in this spectral range, longer delocalization length provides a more efficient way to increase their nonlinearity. The macroscopic nonlinearity $\chi^{(3)}$ was measured in thin films of the neat dyes and large two photon absorption cross sections were measured in an area where the film are still transparent, with very low linear losses. Properties that make these dye good candidates for high performance optical limiter.

CHAPTER I

INTRODUCTION

1.1 Structure of bR in the purple membrane of H. Salinarum

The wild type (WT) *Halobacterium Salinarium* is found in high-temperature saturated salt marshes that have exposure to bright sunlight[1]. From the sunlight they extract both information and precious energy to fuel themselves in anaerobic conditions. *H. Salinarum* WT posses 3 retinal related proteins, Bacteriorhodopsin (bR), halorhodopsin (hR) and two sensory rhodopsins (sRI and sRII).

The role of hR is to maintain iso-osmolarity in the cell cytoplasm during its growth, accomplished through the transport of chloride ions [2-4] into the cell. Sensory rhodopsin I and II have photosignaling roles, they gather information from the surrounding environment keeping the cell from harmful blue rays (phototaxis), while determining the most favorable conditions for the photosynthesis[5] (chemotaxis). These signals are relayed to the flagellae, that can propel the cell in different directions as a response to different environmental stimuli[6, 7], while gas vacuoles[8] are believed to mediate cell buoyancy and ultimately control its depth in water. *H. Salinarum* is a rod-shaped bacterial cell (fig. 1.1), about 10 μm in size, with flagellae on both sides.

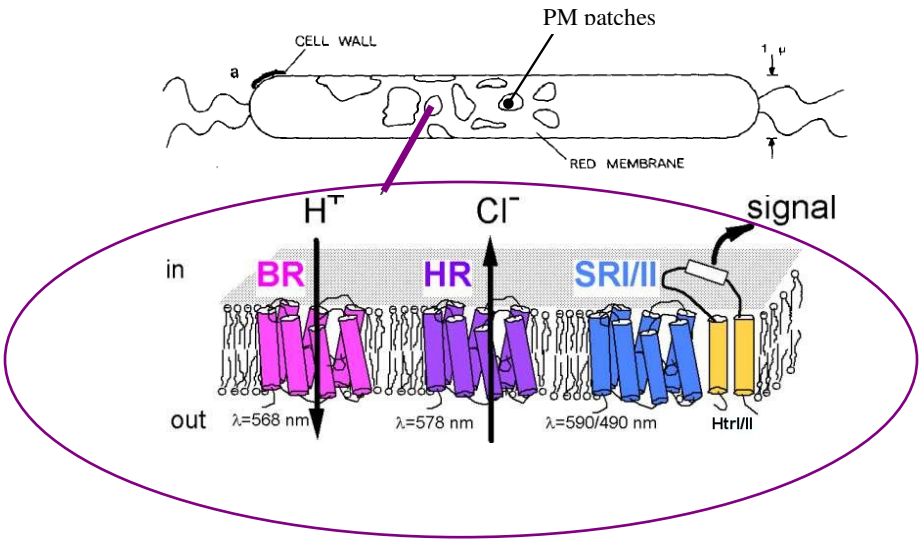

Fig. 1.1: *H. Salinarum* cell (top) with an enlarged structure illustrating one of the purple membrane (PM) patches. From the website http://www.mpg.de

Of all the retinal proteins in nature, only one is capable of forming organized 2D patches with crystal structure[9], the purple membrane (PM) of *H. Salinarium*. PM contains trimers of bR protein organized in a hexagonal close 2-dimensional crystal held together by lipids that account for 20% of the membrane weight. For each bR protein, an average of 10 lipids are present[10]. An illustration of a bR trimer is shown on fig. 1.2. Such organized structures led to believe that rapid energy transfer (the antenna effect) among the photoexcited and the unexcited retinal molecules were the underlying reason for this. As it turned out, there is no antenna effect[11], and until now, the reason for such arrangement is still unknown.

bR protein is constituted of 248 amino acids, organized in 7α-helices (named A to G) connected by short interconnecting loops. The protein is about 4.7 nm long, and it spans across the whole length of the membrane. The other two directions are about 2.5 nm and 3.5 nm, excluding lipids[12]. Surrounded by the α-helices, in a tight protein pocket, lies the retinal Protonated Schiff Base (PSB), covalently attached to the protein through the residue Lys-216 on helix G. The Schiff Base is transversal to the helices, and is located roughly midway through the membrane thickness, at an angle of about 20 degrees respect

to the membrane plane[13, 14] (see fig. 1.2). The retinal divides the protein cavity in two 'half channels', the extracellular channel, which contains polar residues, forming hydrogen bonds with the nearby, orderly situated water molecules providing an overall polar environment, while the cytoplasmic one is mostly hydrophobic.

The knowledge collected over the last 30 years came from different spectroscopic techniques and molecular biology.

Molecular biology had a large impact in determining the amino acid sequence together with the electron density map of the structure[15, 16]. The electron density map allowed making predictions on the structure of the polypeptide along with position of the amino acid side chains. A great help in understanding the photocycle was represented by studies done on site-specific mutants, where replacement of residues directly involved in the protein functionality gave great insights to their roles[17, 18].

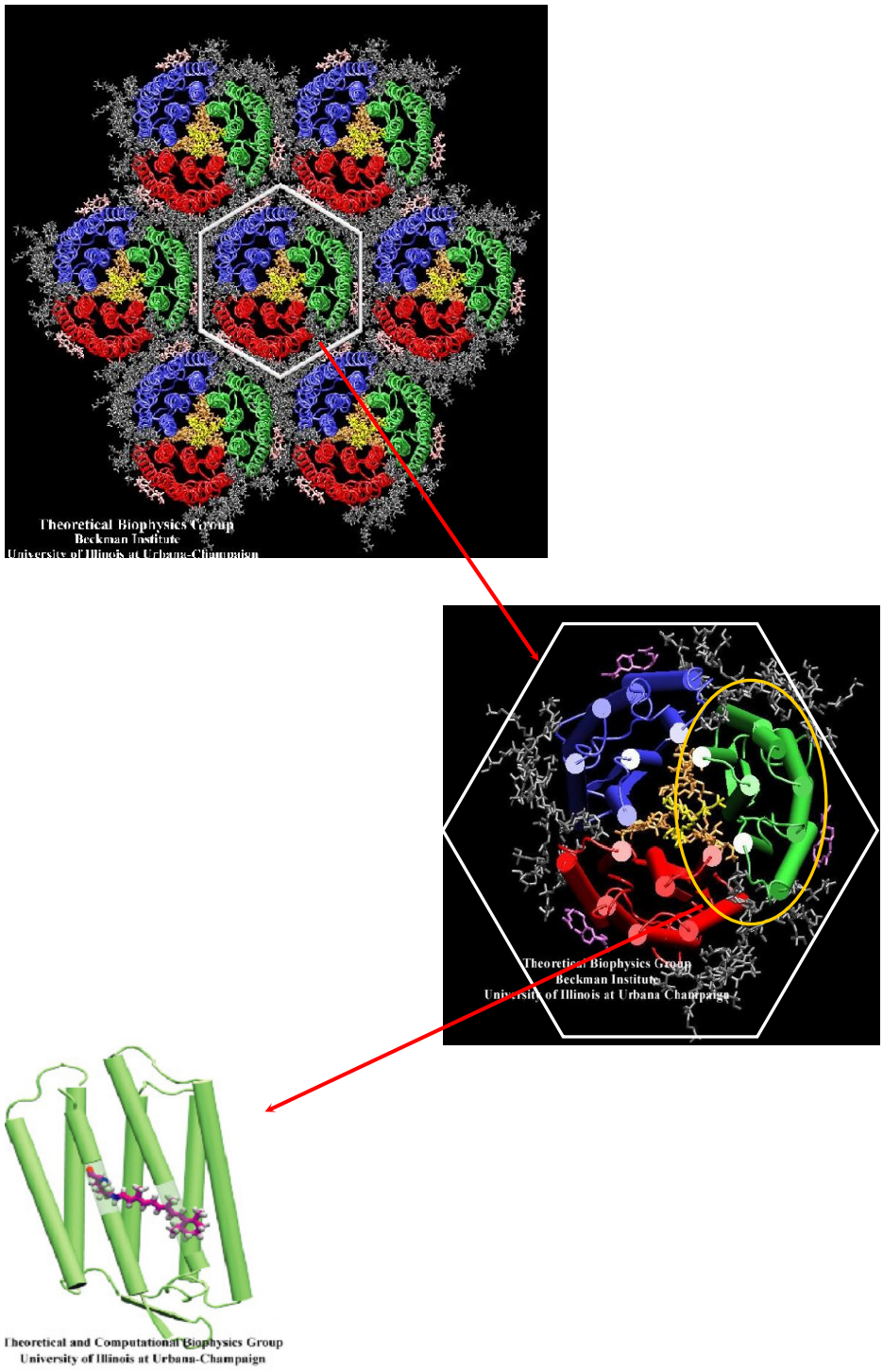

Fig. 1.2: Structure of bR patches. From the top, trimers of bR protein forming a 2D crystalline structure kept together by lipids. Each trimer is composed of 3 bR units

Vital structural information of bR, as observed by X-ray data, has gone through improvements over the years. The first cryo-electron microscopy of bR was performed in 1975 by Henderson and Unwin[9] and had a resolution of 7 Å. Since then, huge improvements on X-ray crystallography and overcoming the difficulties related to the crystallization of proteins, drastically improved the resolution; in particular the use of three-dimensional crystal growth with the cubic lipid phase mothod[19] allowed to better defined the protein structure, reaching resolution as high as 1.43 Å[20].

1.1.1 BR linear absorption spectrum and the "opsin" shift

The absorption spectrum of a chromophore is sensitive to its electronic state, to the conformation and on its environment. In bR, the chromophore RBS is surrounded by the protein, which acts as a very selective solvent and is fundamental in determining the RBS kinetics following photon absorption. The absorption spectrum of bR in water is reported in fig 1.3. The broad peak near 568 nm is the RBS in its light adapted (LA) form, composed of 90% *all-trans* retinal. When an unprotonated retinal base Schiff is dissolved in methanol, its absorption maximum is at 360 nm, and after protonation, it shifts to 450 nm. The red shift experienced by the RBS in the protein pocket is commonly known as the "opsin" shift, and is believed to have a very well defined purpose in optimization of the photosynthesis process. In fact, the RBS band is now centered around the peak of the solar irradiance, which happens to be around 500 nm. Another interesting comment about the spectra absorption of bR is that if compared to that of chlorophyll, the two appear to be somehow complementary. Whether this has evolutionary reasons, is still to be determined, but certainly helps in providing a niche for purple membrane bacteria[21].

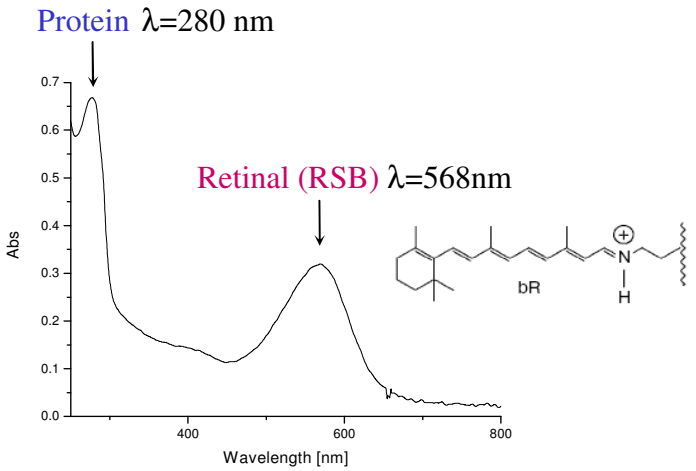

Fig 1.3: Linear absorption spectrum of bR in water after being light adapted (LA).

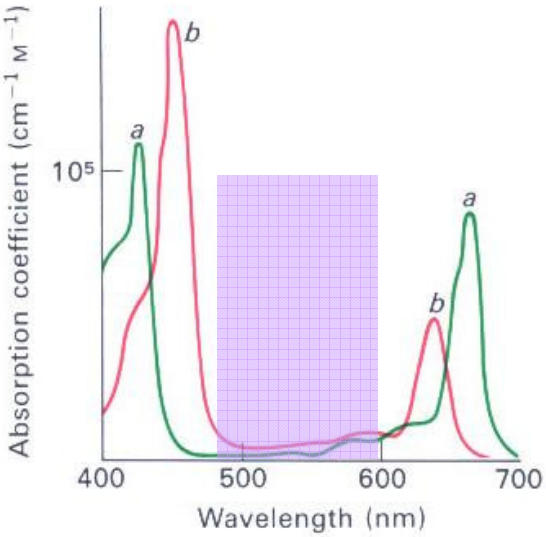

Fig 1.4: Absorption spectra of photoreceptor chlorophylls a and b, located in chloroplast of green plants. The purple rectangle indicates the region of absorption of purple membrane bacteria. From the website http://sel18.hut.fi/304/Valomylly/bio.htm

The photocycle of bR is triggered by a first and only photoinduced event consisting of isomerization around a double bond. The choice of a conjugated polyene as the center of

reaction might, in theory, compromise the selectivity of the process; in fact, RBS has 5 double bonds that could undergo isomerization. For a PSB in methanol solution, the isomerization takes place on 3 sites forming 9-*cis*, 11-*cis* and 13-*cis* with efficiencies of 2, 14 and 2% respectively[22]. When in the protein pocket, the RSB isomerization goes from *all-trans* to 13-*cis* only, with an efficiency of 64%. It is obvious that the environment created by the protein is responsible for such large efficiency and selectivity, but how? Different theories are present in the literature, some suggest a catalytic role of the protein[23], where specific steric and electronic interactions are accounted for[24], some authors discriminate between selectivity and efficiency, arguing that the rate of isomerization does not need to be fast in order to be efficient[25], while others claim the opposite[26]. This mechanism involving highly selective isomerization is extremely important and is the foundation of many processes in nature commonly found in retinal proteins, which are the basis of mammalian vision[27]. More details on the isomerization process are reported on paragraph 1.2.1

After bR is kept from in darkness for some time, the retinal reaches an equilibrium of two isomers: *all-trans* and 13-*ci*s, with a ratio of about 50:50[28], known as dark adapted state (DA). The opsin shift turns out to be different for the DA form compared to the LA, where the ratio between the two isomers is instead 95:5[29]. The absorption maximum for the LA state is in fact 568 nm versus 560 nm for the DA. The blue shift for the DA form comes with a decreasing in absorption molar absorptivity as shown in fig 1.5. It is important to clarify which of the two forms bR is in when measurements are taken. The LA form will be the one chosen, unless otherwise stated. The LA form is achieved upon light exposure for 1 hr before all measurements.

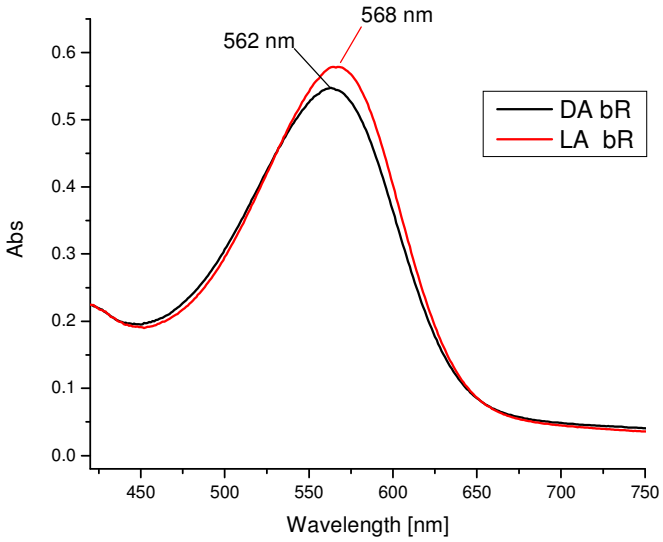

Fig. 1.5: Linear absorption spectra of LA and DA bR in buffer pH 7

1.2 Bacteriorhodopsing photocycle

Upon bR light absorption, structural transformations take place finalized to the transport of a proton from the cytoplasmic to the extracellular side of the membrane. Changes at the chromophore site can be identified through shifts occurring over time to its absorption band. Several intermediates have been identified with lifetime spanning from picosecond to microsecond time-scales. The intermediates are labeled according to theSchiff base absorption maximum as described in (1.1):

$$\rightarrow bR_{568} \xrightarrow{h\nu} I_{480} \xrightarrow{0.5\ ps} J_{625} \xrightarrow{2\ ps} K_{610} \xrightarrow{2\ \mu s} L_{550} \xrightarrow{80\ \mu s} M_{412} \xrightarrow{10\ ms} N_{550} \xrightarrow{ms} O_{640} \rightarrow \quad (1.1)$$

Besides the species indicated above in 1.1, there are others that are related to structural arrangements at the protein level[30], considering that the chromophore is very much a

small part of a more intricate system. Nonetheless, the PSB has been the focus of many studies due to easier access to the visible spectroscopic range.

Great improvements have been made towards understanding the role played by proteins, thanks to X-ray diffraction data of the intermediates, which allows us to finally see and assign changes of the protein structure, as well as the PSB, during the photocycle. Together, with time-resolved spectroscopy like Resonance Raman[31] differential FTIR[32],[33], NMR[34] and ESR measurements of covalently linked spin labels, a more complete understanding of the proton transport properties of bR has been achieved. The importance of such efforts is to unravel the mechanism of G proteins in general, of which bR is recognized as a model protein for this category.

The ultimate tool to understand the link between proteins structure and their functionality is probably X-ray time-resolved crystallography, already available with both nanosecond[35] and picosecond resolution. For Bacteriorhodopsin, many of the intermediate structures are now available, and this chapter describes what has been learnt, in particular, the isomerization and proton pump mechanism together with other spectroscopic evidence.

1.2.1 The first light-induced event in Bacteriorhodopsin: from bR to K

The ground state (bR) λ_{max}=568nm

This is the best-described state among all. The light-adapted form contains all-*trans* retinal in a tight protein pocket, in contact with surrounding protein residue that helps stabilize the positive charge[36]. Important residues involved in the stabilization include Asp85, Asp212, Arg82, Tyr185, and hydrogen bonds, water 402.

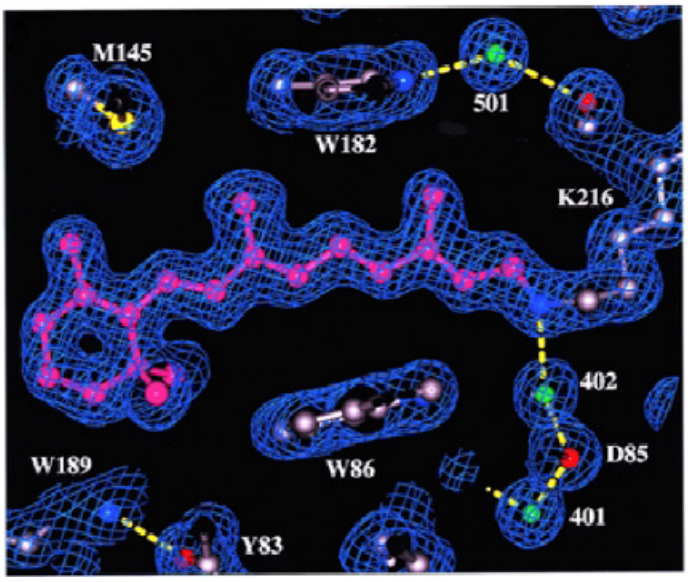

Fig. 1.6: Electron density map of the all-trans Schiff base at 1.55 Å. Water 402 forms a bridge between the PSB and Asp-85. From ref. [37].

From the PSB, an extended 3-dimentional hydrogen-bonded network is formed among the side chain and 4 molecules of water reaching throughout the extracellular surface, such structure is believe to stabilize the PSB inhibiting the proton transfer to Asp-85[38]. In contrast, the cytoplasmic side is hydrophobic, with no polar residue or organized water between the Schiff base and Asp-96.

The pK_a of the PSB at this stage is extremely high, a value of 13 were found[39, 40] by Druckmann and coworkers. Many scientists consider this an unusually high pK_a, again, related to specific stabilizing interactions from the nearby residues and water[41]. The pK_a of the Asp-85 is about 2.5 while that of Asp-96 is above 11[42].

Absorption of light in the 500-600nm region promote the PSB from the S_0 electronic state to the S_1 excited state. Immediately after excitation, while still in the Frank Condon region, the system is referred as bR^*; but quickly evolves to the short lived intermediate I_{480}, which thermally evolves to J_{625} and then to K_{610} as shown below:

What is known from vibrational spectroscopy studies using ultrashort pulses[43-45] on intermediates bR^* and $I_{460,}$ is that the chromophore has an *all-trans* conformation. Widely accepted is the chromophere conformation of the ground state intermediate K_{610} with an already converted 13-*cis* PSB. The molecular processes between bR^* and K_{610} have been controversial and a complete molecular description for the first light-induced event in bR is a matter of current interest.

The aim of this paragraph is to present what is currently known and what are the questions that still need answers.

There are 2 main models that are widely reported and utilize to support experimental data; the first model is called *two-state model,* published independently in 1988 by Mathies[46] and Dobler[47]. A schematic of the model illustrating the energy levels of the PSB are shown below (fig 1.7).

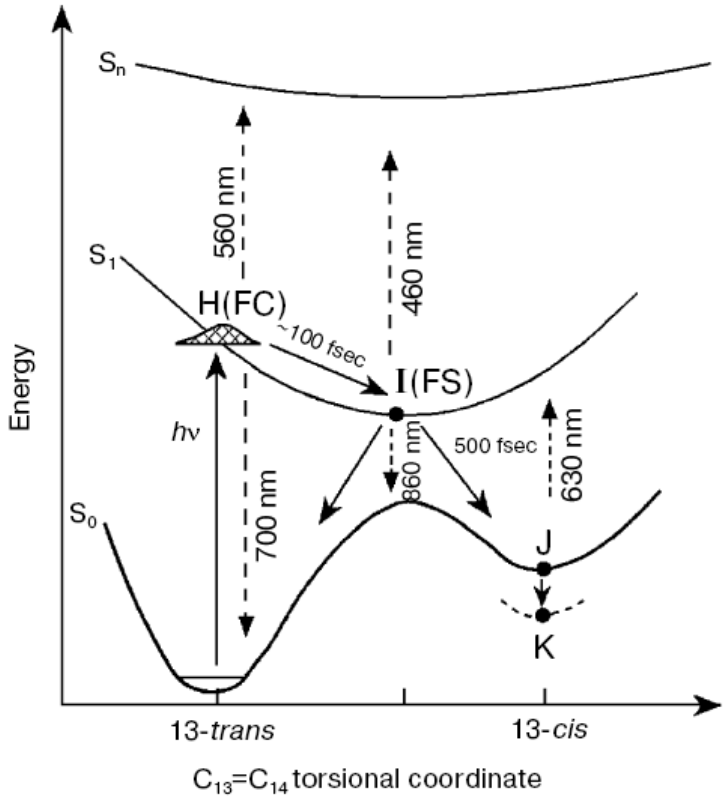

Fig 1.7: Energy levels in the *two-state model* as hypothesized by Mathies and Dobler

The *two-state model* was the first attempt in trying to describe the ultrafast photoisomerization of the retinal chromophore in the protein cavity. The idea is that upon vertical excitation to the Franck-Condon region, the non-zero slope (repulsive energy) of the S_1 state reaction coordinate favors the double bond torsional mode, accelerating the isomerization process. The double bond isomerization for the retinal "confined" inside the protein is in fact, faster than the free molecule in solution[48]. In the same paper published by Mathies in 1988, he reported a study where 6 fs pulses are used to temporally resolve the excitation and the subsequent photoisomerization of bR. Mathies interpretation of what is known as the exit from the FC region to form $I_{460,}$ was instead a partial "90°" twisting of the double bond. It is known, instead, that at this stage, no real twisting takes place as later studies on locked C_{13}=C_{14} pigments showed[49]. The S_1 surface potential invoked by this model has some implications that are not fully supported by the experimental data. For instance, as the S_1 state moves from the FC region towards the energy minimum, changes in the stimulated emission of the excited state would be expected, but it was not detected[50, 51]. Dexheimer and coworkers[52] first and Anfinrud later[51], found that the S_1 spectrum develops in about 30 fs and remains stable beyond 1 ps, a behavior that is in agreement with the spectroscopy of retinal in solution, where the FC region lies at an extremum, in a region with zero slope. Also, temperature dependence data on the fluorescence of bR, indicate the presence of an activation energy along the potential surface of the excited state[53] that could not be explained with the *two-state model*.

These results led some scientists to propose a different model for the bR photoinduced isomerization: a *three-state model* where the S_1 potential surface in the FC region is relatively flat, not repulsive[54]. This model involves three electronic states, the ground, the first and a doubly excited state. The formulation of the *three-state model* is inspired by a polyene type of system, where the two-photon state lays just above the one photon allowed state. A two-photon state was in fact found at about 480 nm for bR retinal

chromophore, with symmetry $^1A_g^{*-}$ [55, 56], while the one photon allowed state has symmetry $^1B_u^{*+}$. The excited state (S_1), on the *three-state model,* is the result of mixing the one and two-photon allowed states.

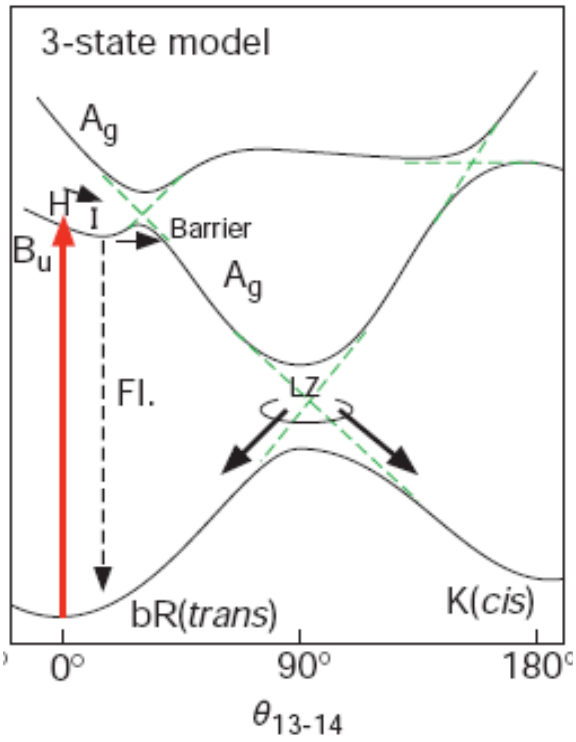

Fig. 1.8: Energy states for the *three-state model* according to Weiss and Warshel

The sequence of events, according to the *three-state model,* is that upon excitation to the S_1 state, the small barrier forces the population to stay localized for a few hundred femtoseconds in the region of zero rotation, at this stage, the intermediate I_{460} is formed. After crossing the barrier, the reaction begins, leading to a red shift in the stimulated emission[50]. At the second crossing, the intermediate J_{625} is formed. I_{460} decays after overcoming the barrier, but this does not correspond to the twisting of the double bond; which instead takes place at the second crossing, as the system goes from J to K.

This model partially solves the inconsistency of the Two-state Model, but it is still not completely accurate in describing the isomerization event. For instance, the chromophore conformation in J_{625} is still a matter of debate, this has been described in the literature both as *all-trans* and 13-*cis*.

Recent experiments and *ab initio* calculations[57] favor the three state model, asserting that early intermediates I and J only involve structure rearrangements before the actual isomerization process[58-60].

One of the most complete descriptions of the dynamic evolution of the system up to now is probably provided by Kobayashi et al.[61], where a 5fs pump probe experiment was used. The measured ΔT/T is modulated in time by Raman active vibrational modes capable of providing information on the chromophore structure[62]. By Fourier transformation of ΔT/T for a specific delay time is possible to obtain amplitude and frequencies of such vibrational modes. By studying the evolution of the Raman modes of PSB, they were able to establish the sequence of four events characterizing the retinal isomerization. In the first 50-100 fs, the wave-packet reaches a flat potential. The second event, takes place in the 100-200 fs timeframe, featuring torsional motion happening at the RBS, and contrary to the Two-state model view, there was no evidence of the product K_{610} formation to be found. The third event, occuring in the 200-600 fs time-region, is the formation of an intermediate named the "tumbling state", where the isomerization has not completely occurred yet (fig. 1.9).

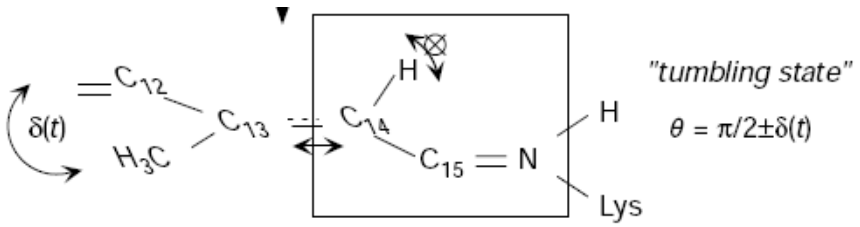

Fig. 1.9: Suggested structure by Kobayashi for the tumbling state.

The fourth stage occurs 700 fs later, when the planarity of the system is partially recovered and the isomerization has been completed, forming K_{610}.
Kobayashi's study supports the Three-state model, and "firmly discounts the initially suggested Two-State Model" to use his own words. The data shows the presence of a new intermediate "tumbling state", where C_{13}=C_{14} double bonds are partially twisted.
It has to be mentioned that in 2007, Kahan et al.[63] challenged the work of Kobayashi, claiming that some of the assumptions made from the data were not correctly interpretated.

No direct femtosecond pump-probe data have given any irrefutable answers thus far. Sectroscopic techniques like FTIR and CARS, even though extremely useful on later stages of the photocycle, are not applicable in such short time-scale. So far, even though there is no unanimous agreement on a model for the isomerization, the Three-level system seems to be more accurate in describing what has been observed experimentally. Still, many questions remain on the actual role of the protein and what makes the PSB isomerization so efficient and fast.
Still of much interest, but elusive, is the mechanism to which the free energy accumulated during the isomerization is ultimately transferred to the protein to drive the photocycle.

I state λ_{max}=460 nm

The absorption of a photon induces dramatic spectral changes in bR with the appearance of a NIR stimulated emission band at about 850 nm and a strong absorption band centered at 460 nm. The stimulated emission kinetics have been compared to the transient absorption kinetics at 480 nm, and found to be closely correlated with a lifetime of 500 fs. This strongly suggests that the 460 nm absorption and the stimulated emission at 850 nm have a common origin, the excited state I_{460}, often denoted in the literature as

the fluorescent state (FS) due to its spontaneous fluorescence at 730 nm. The discrepancy between the stimulated emission spectrum and the fluorescence can be accounted for in terms of additional absorption bands around 720 nm, that partially cancel the stimulated emission[64].

The experimental proof that I_{460} is in fact a state that comes from Ruhman and coworkers[65], with the use of a three-pulse ultrafast pump-probe. The induced stimulated emission at 1070 nm is delay dependent in agreement with the formation of the I_{460} state.

Early in the study of bR, I_{460} was not individuated as an intermediate but rather thought to be the first stage of the bond twisting. A very elegant way to resolved this misconception was offered by Zhong in 1996[49] by using an artificial bR pigment in which the C_{13}=C_{14} is locked by a 5-membered ring (indicated as bR 5.12 in fig 1.10)

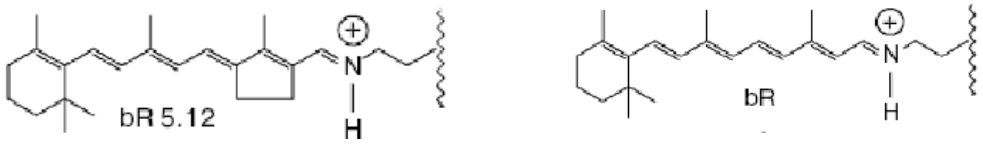

Fig: 1.10: Structure of the synthetic chromophore having a locked C_{13}=C_{14} on the left. On the right the structure of the PSB

The pump-probe experiment on the two species proved that: (a) the locked bR exhibits a 460 nm intermediate analogous to the I_{460}, generated in about 30 fs from the excitation, (b) the stimulated fluorescence at 850-900 nm is present as well[66]. The locked pigment decays with a lifetime of 18 ps regenerating the original state, none of the other double bonds undergoes isomerization and the photocycle is stopped, stressing the strong selectivity of the bR photocycle.

The similarity between the behavior of the native and locked pigment in their earliest stages of the I_{460} formation, strongly suggests that the process $S_1 \xrightarrow{FC} I_{460}$ does not

involve substantial torsion of the C_{13}=C_{14} bond, a result that is confirmed by theoretical calculation[67] along with time-resolved Raman study[58].

The nature of the decay of I_{460} has been described both as a mono-exponential and in some other cases with a bi-exponential[51, 68, 69]. In the latter case, a fast component of about 100-130 fs is found and a slow component of about 1 picosecond follows. The fast component is assigned to the "direct" isomerization[25, 66], while the slower is tight to the regeneration of the initial state (the all-*trans* configuration).

Below is a schematic of the isomerization dynamics in native bR and in locked bR pigment.

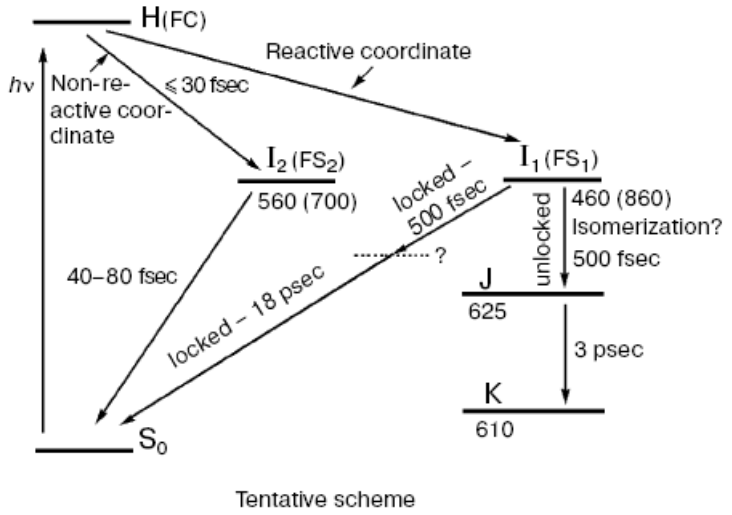

Fig. 1.11: Tentative scheme describing the early events after bR photoexcitation

The structures of these intermediates are another important point. K_{610} is the first "real" intermediate that can be isolated at low temperature; its structure has been assigned to a C_{13}-*cis*.

Not much is known of I_{460} structural details, both *ab initio* calculations[57, 70] and experiments[58] seems to agree on rearrangement in the molecular structure preceding the *trans-cis* isomerization. Useful dynamic information on geometrical changes that

accompany I_{460} formation could be provided by vibrational spectra from short IR pulses for instance, which are not available at the moment.

J state λ_{max}=625 nm

According to the two-state model, the J_{624} state is a thermally excited intermediate of the S_0 ground state (see fig.1.7). Resonance Raman anti-Stokes measurement[71, 72] of ethylenic stretch intensity in the chromophore, reveals a decay time of 2.5 ps. This result led to consider J as a vibrationally hot K intermediate. The difficulty in distinguishing the excited state from other vibrationally excited photoproduct weakens the argument. Lately, two independent measurements revealed that the stimulated emission spectrum does not change between 50fs to 1 ps after excitation forced to review the two-state model as described previously, and according to this later version, the crossing takes place between S_1 and S_0, as the system goes from J_{625} to $K_{610.}$ In support of such theory are several time resolve Raman studies from Atkinson, who claims the intermediate J_{625} has a chromophore that is structurally closer to bR ground state rather than in a 13-*cis* conformation[43, 73]. Again, the current understanding of the primary events in bacteriorhodopsin are not completely disproved nor proved, thus requiring more experimental work.

K state λ_{max}=610 nm

The K intermediate contains the 13-cis isomer of the PSB, the C_{13}=C_{14} bond has rotated, forcing the polyene chain to assume a sharply bent shape. The conformation of the RSB in K_{610} was identified using vibrational spectroscopy technique like Resonance Raman (RR) and infrared spectroscopy (FT-IR). Raman lines at 1516, 1294, 1194, 957 and 811 cm^{-1} were considered by Mathies and Brainman as a signature of the 13-cis configuration[74]. The Schiff base N-H bond goes from pointing towards the extracellular side, in particular, towards the anionic Asp-85 and Asp-212, to the apolar

environment offered by the cytoplasmic side[20]. The intermediate K_{610} has been described as a highly strained (twisted) 13-*cis,* 15-*anti* retinal[20] still containing excess enthalpy (about 50KJ/ mol), enough to drive the photocycle through the rest of the non-radiative steps. Changes in the Schiff base C=N stretching modes to 1609 cm^{-1} for the K intermediate, have led to the conclusion of a change in the environment, probably related to a displacement from a counterion that stabilized the charge on the ground state[75].

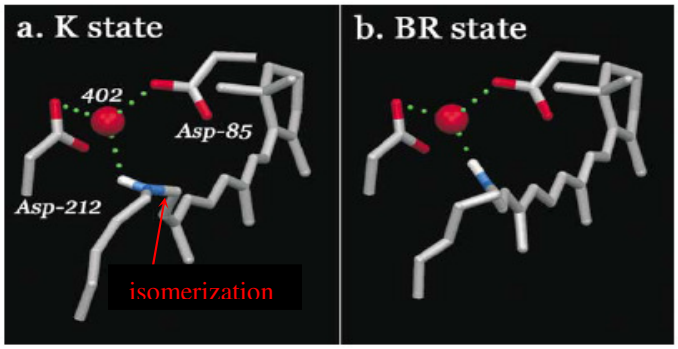

Fig. 1.12: Structural changes in the K intermediate from water 402 point of view. In the K intermediate, the N-H··O hydrogen bond angle is unfavorable. From ref [20]

At the protein level, the FT-IR spectrum shows that the C=O residue of Val49 upon K_{610} formation, weakens its hydrogen bond with Asp96 via Thr46 [32, 76-78].

The X-Ray diffraction spectra of the K intermediate shown in fig. 1.12 was obtained with resolution of 1.43 Å on 3D crystals[20]. Upon isomerization, the hydrogen bond network between the N-H of the Schiff base, water 402, Asp85 and Asp212 is not as favorable as in the bR ground state, which might account for the deprotonation process later on.

K evolves to L in about 1 μs, as determined by time-resolved absorption measurements[79]. Investigations on the K to L transition indicate the formation of

multiple K intermediates with kinetics that are solvent and temperature dependent. Changes in the ethelynic stretching frequency between 200ps and 20 ns have been attributed to the formation of a KL intermediate[80].

1.2.2 Photocycle intermediates driven by excess free energy.

L state λ_{max}=550 nm

The strained retinal has partially relaxed away from the immediate region of the $C_{14}C_{15}$=N- segment. At this stage, rearrangements at the protein and PBS level take place[81]. The system is getting ready for the main event, which is the deprotonation of the Schiff Base to Asp-85.

Crystallographic structure of L were determined first by Royant and Edman[30] in 2000 and later by Lanyi in 2003[82] at 170 K with 1.62 Å resolution. This investigation revealed that the previous conclusion, stating an approach between the retinal and the C=O of the Asp-85 due to the mutual electrostatic interaction in the L structure, were not accurate.

It is interesting to consider the change in the pK_as of the main players. Due to the change in geometries and environment, the pK_a of the RSB decreases to about 8; while that of Asp-85 increases to 9[83]. The angle increase in the hydrogen bond to 132° provides a more efficient pathway for the deprotonation via water 402 than in the K state. This might be the reason why the proton transfer takes place in L rather than in K[84, 85]. The pK_a of Asp-96 remains unchanged at this stage. Lately, Lanyi and coworkers[86] have proposed the existence of two kinetically distinct L intermediates, named L_1 and L_2, that sequentially form during the photocycle.

M state λ_{max}=412 nm

The L to M transition is accompanied by a relatively large blue shift, due to the Base Schiff deprotonation. The negatively charged residue Asp85 acquires the released proton. The assignment of Asp85 as the proton acceptor was first made in 1988, when a site-specific mutant of Asp85 with Asn (D85N) caused the proton pump to cease[87]. Successive site-specific mutations were usefull in clarifying the role of other residues, like Asp212 and Arg82 in the proton release process beyond that of Asp85[88]. Confirming the role of Asp85 as a counterion of the Schiff base came later by other techniques: FT-IR[89], NMR[90] and finally the X-ray diffraction of the M intermediate[78, 91]

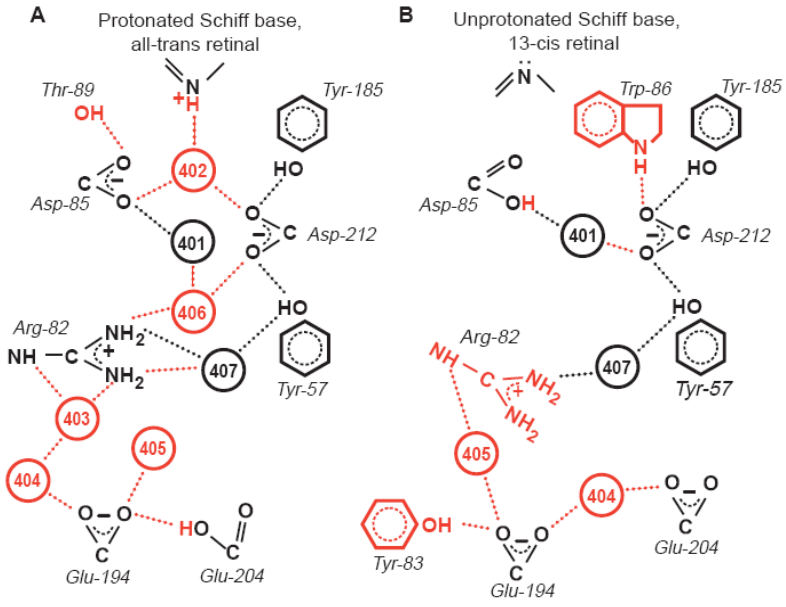

Fig 1.13: Schematic representation of the hydrogen bond rearrangement upon M formation in the extracellular region. A) bR state B) M state. Both Arg82 and Asp 212 undergo major hydrogen bond rearrangements, following Asp85 protonation. Ref [91]

Proton release: the rise of M_1

The time-course formation of M_{412} fits a multiexponential kinetics, which sparked different theories on the origin of such phenomenon. One hypothesis supports the idea that it could be due to back reactions due to the establishment of equilibrium between the proton acceptor, Asp-85. It is also believed that these different M substates are just different forms of the Base Schiff coming to sequential proton equilibrium with Asp-85[83, 92]. In the M_1 structure, water 402 has moved away from the Base Schiff, but is still hydrogen bonded with Asp-85[93]. It is found that M_1 evolves in about 100 μs to form another substate, $M_{2[94]}$. During the rise of M_1, a proton is released to the extracellular surface[95-97], but such proton does not come from the Schiff Base or Asp-85, instead, the release site is probably a residue close to the extracellular surface. The release site for the proton is not certain yet, and many theories on the identity of the releasing group have been published in the literature. At first, Glu-204 was proposed[98], and later, a complex involving both Glu-204 and Glu-194[99]. Lany argued that the releasing site could be an $H_5O_2^+$ cluster[100] present in the protein cavity. What is certain, is the coupling existing between the Asp-85 and the release group HX, demonstrated by the anomalous titration behavior of Asp-85[101]. According to the rules of coupling[101, 102], after the proton is released by the HX group, the pK_a of Asp-85 will raise, shifting the equilibrium toward a more complete deprotonation of the Schiff Base in the M_2 to M_2' reaction step. In the M_1 to M_2 transition, an equilibrium is establish for the proton transfer[103, 104], while in the M_2 to M_2', the reverse process of the protonation is prevented, bringing the deprotonation to completion.

The decay of M_2'

The decay of M is also complex, suggesting again, an equilibrium between the M_2' and N, which forms in few ms. During the decay of M_2', the Schiff base is reprotonated by

Asp-96, and it is likely that an equilibrium could occur between the newly reprotonated Base Schiff and the Asp-96 itself.

Proton transfer between Asp-96 and retinal Schiff base requires the pK_a of Asp-96 to be lowered from 11 to about 8 (the pK_a value for retinal base Schiff at this stage), along with the creation of a hydrogen bond network to displace the proton along a distance of about 10 Å. Even though there is no direct evidence of such process, both theoretical[105-107] and experimental data[108-110] suggest that water is allowed in from the cytoplasmic side to accomplish both requirements. Supporting experimental data include the dependence of the M→N from the hydrostatic pressure[110] and the osmotic pressure[109].

What has been observed, is that when M_2 is formed, a cluster of hydrogen-bonded water appears near Asp-96[111]. The direct effects are the lowering of the unusually high pK_a of Asp-96 and the formation of a water network before formation of the N intermediate. The closest water cluster is still, at this stage 7.4 Å away from the Schiff base. There are no current crystallographic information about the cytoplasmic region for $M_{2,}$' and it is believed that the water network is not in place before N starts to form. What has been detected, are large conformational changes on helices F and G via X-ray[112, 113] and neutron diffraction[114] around the cytoplasmic region, suggesting that such distortions are ultimately responsible in allowing water to enter this region.

N state λ_{max}=560 nm

In the M_2'→N step, the Schiff base is reprotonated by Asp96 [115]. The X-ray diffraction of the N intermediate shows changes in the F and G helices area[112]. Such movements could be the reason for the higher hydration level in the cytoplasmic side as mentioned. The other advantage for widening of the proton channel would be to increased access to the cytoplasmic surface, and allow the capture of the proton necessary for the Asp-96 reprotonation[116] while the Schiff Base is still facing the cytoplasmic

side[117]. N must include two substates, since during its lifetime, Asp96 first gets deprotonated, then reprotonated from the CP; the existence of two N intermediates (N_1 and N_2) as theoretically predicted, and was indeed uncovered by Borucki[118] and coworkers in 2004.

O state λ_{max}=660 nm

The reprotonation of Asp-96[119, 120] and the thermal reisomerization of the PSB happens simultaneously in the N→O transition, suggesting that the two events are coupled.

Proof that such coupling exists came from the behavior observed in D85N/F42C mutant[121].

Little is known about the X-ray structure of the O state, the only one comes from a D85S[122] mutant, where the all-*trans* retinal is in a mixture with 13-*cis*, 15-*anti*.

Another attempt to prolong O lifetime led to an intense study of another mutant L93A where 13-cis was found long after the deprotonation and reprotonation of the chromophore took place[123] (decrease in the reisomerization rate of 250-fold), highlighting the importance of the residue Leu93 situated in the close proximity of the 13-*cis* chromophore in the reisomerization process.

Recovery O→bR

In the O state, Raman bands indicate that the formed all-trans retinal is twisted[124] compared to the DA form. The complete relaxation occurs after the deprotonation of Asp-85, restoring the original charge density in the EC and the protein returns to its initial state. The Asp85 deprotonation must be driven by an increase of its pK_a to the original value. The mechanism of such deprotonation seems to have multiple stages as FT-IR suggests, pointing out Asp212 as the residue involved in the process[125].

For pH's<6, this is the time when the proton is released to the extracellular surface.

A good approximation to the intermediates created during the bR photocycle involves 9 spectroscopically different states. Most of these intermediates are identified by their absorption maxima in the visible and unique Raman and FTIR bands from the chromophore and protein.

A more accurate scheme for the photocycle of bR might be the one shown in fig 1.14 below

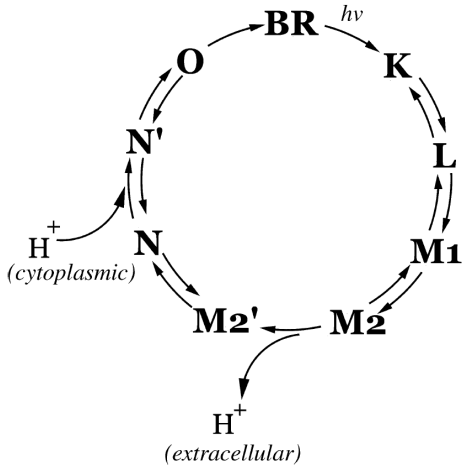

Fig. 1.14: The main intermediates formed during bR photocycle.

The proton pump mechanism and different forms of M: M_1, M_2 and M_2'

The proton pump intermediates and their dynamics has been studied more than any other intermediates or processes in the photocycle, being the crucial step in defining the properties of proton transport for protein.

The existence of substates of M are supported by a large variety of experimental evidence[126-129], including time-resolved absorption studies where it has long been recognized that M rises and decays with more than one time constant. Varo and Lanyi

introduced a linear model: $K \leftrightarrow L \leftrightarrow M_1 \rightarrow M_2 \leftrightarrow N \leftrightarrow O \leftrightarrow bR$, where an irreversible step between M_1 and M_2 was proposed to model the data[127, 130]. Results that were later confirmed by resonance Raman study[131, 132].

In the literature, it is possible to find at least five competitive theories attempting to explain the presence of multiple M substates, they are briefly summarized below.

i) The heterogeneity theory, which states the presence of at least two different unphotolyzed ground state for bR[133-135]. Each one of these two bR structure goes through it own photocycle, with the same intermediates but with different kinetics.

ii) The cooperativity theory[136] claims that one population is present, but that there is a cooperative effect of the light that could hit the target (bR) multiple times. bR systems that are hit by a single photon would give rise to the slow decaying form of M (M_S) while the multi-photons hit to the fast decaying M (M_F).

iii) A third possibility was suggested by Stockburger, where in his theory, the K intermediate, upon formation, would be susceptible to a direct transition to $M_{S[137]}$.

iv) The IST model[138, 139] where three different events occur, isomerization (I) where disruption of the PSB and Asp85 connection takes place. Switch event (S), involving reorientation of the chromophore from the EC to the CP channel. And lastly, the proton transfer (T), involving protein movement to allow water in the CP channel and allowing Asp96 to deprotonate. All this stages are considered independent, with stage S and T being in "kinetic competition". In this model the protein conformational changes along with bending of the chromophore are believed to be the basis for the switch function.

v) The equilibration theory (or local access theory) was presented by Varo and Lanyi in 1991[127], and states the presence of the two forms, M_1 and M_2, being in equilibrium with the L precursor and N product respectively ($L \leftrightarrow M_1 \rightarrow M_2 \leftrightarrow N$).

In the past, some authors hypothesized that since the different M substates were not distinguishable spectroscopically, structural differences must have been at the protein level only. But recently refined crystal structure of the deprotonated Base Schiff have shown that M substates are instead subject to reorganization at the chromophore level as well[78, 82, 140].

The conformational changes going from M_1 to M_2 were assigned to two different proton accessibility configurations of the Schiff base[126].

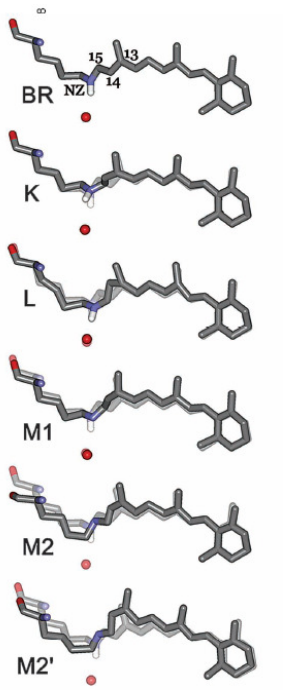

Fig 1.15: Evolution of the Retinal Schiff Base respect to water 402 during the first half of the photocycle. Structure for M substates showing modification at the chromophore site. Ref[82]

This overview of the proton pump process gives an idea of the rather complex dynamics involved in the proton pump process. One of the most complete description of the rearrangements taking place during this key step of the photocycle is provided by Lany and Schibert, where X ray diffraction with a relatively high resolution of 1.43 Å of the

early intermediate M_1 was obtained along with the other later intermediates[82, 140]. The main event in going from K_{610} to M_1 is the displacement of water 402 away from the unprotonated Schiff base, followed by what the authors the irreversible $M_1 \rightarrow M_2$ step where the C_{15}=N goes from facing the extracellular side to the cytoplasmic side. At the same time Arg-82 moves toward Glu-194 and Glu-204. In the $M_2 \rightarrow M_2'$ transition the retinal acquires a fully relaxed structure, indicating the completion of the deprotonation process.

1.3 The Plasmon band in noble metal nanoparticles: theory and properties.

The optical properties of noble nanoparticles have attracted interest since Faraday, in 1857. The reported synthesis of Au nanoparticles having vibrant colors ranging from ruby to amethyst[141]. Besides their obvious optical properties, the interest of nanoparticles range from biological applications, which is the focus of this thesis, to catalysis and sensor applications.

This section is aimed to describe the physical origin of the localized surface plasmons (LSPs) in nanoparticles and what of the properties derived from it could affect biological function.

We are witnessing the use of surface plasmon in the biology and mediacal more and more. Surface plasmon based instruments are now commercially available for protein sensoring[1] and they find application as labels for detection and even deseeses treatment. The use of plasmonic based properties for biological applications is being investigated largely in the literature, what is under analysis in this thesis is whether the presence of a

[1] Biacore Surface Plasmon Resonance monitors real-time changes in the local index change. Index-change are then associated to changes in the substrate due to association or dissociation reaction.

plasmonic field in the vicinity of a biological system could affect its functionality and what are requisites for that to happen

1.3.1 Physical properties

Noble metals like Au, Ag and Cu at the nanoscale size, exhibit very different optical properties than in bulk, with the presence of a strong absorption band in the UV-Vis region for the metals listed (other metals shows the same phenomenon but at higher energies) named surface plasmon band. The band is sometime addressed as the Mie band, named from one of the most prominent contributors to the understanding of its origin: Gustav Mie. The plasmon band originates from a coherent oscillation of the conduction-band electron interaction with an electromagnetic field[142-144]. Its position and intensity is sensitive to the particles size and shape, as well as the surrounding medium. When a metal nanoparticles is irradiated with electromagnetic waves (light), for a certain range of frequency, the nanoparticles interact with the lights electric field, causing the conducting electrons to oscillate coherently. An illustration of the phenomenon is represented in fig. 1.16.

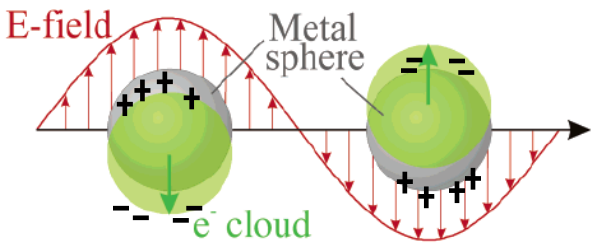

Fig 1.16: Representation of the free electron oscillation upon interaction of a metal nanoparticle with an oscillating electric field. Ref. [145]

The oscillation displaces the free conducting electrons away from the much heavier nuclei, and the net charge generated acts as a restoring force. The effect is similar to that of a spring, with the surface electrons oscillating against the much havier metal core. The frequency of this oscillation is determined by the electron density, the effective electron mass and the geometry and size of the electron distribution.

The solution of Maxwell equations for an electromagnetic wave interacting with a small sphere was offered by Mie in 1908[146]. In his approach, Mie used the same frequency-dependent dielectric function as for the bulk metal[145], and was able to solve each of the 2 contributions of the extinction spectra: the scattering and the absorption cross sections, with the following relationship: $\sigma_{ext}(\omega)=\sigma_{sca}(\omega)+\sigma_{abs}(\omega)$. The solution for nanoparticles that are much smaller than the wavelengths of light, where only the dipole contributes significantly to the extinction cross section, has the expression in equation 1.3:

$$\sigma_{\mathrm{ext}}(\omega) = 9\frac{\omega}{c}\varepsilon_{\mathrm{m}}^{3/2} V\frac{\varepsilon_2(\omega)}{[\varepsilon_1(\omega)+2\varepsilon_{\mathrm{m}}]^2+\varepsilon_2(\omega)^2}, \qquad 1.3$$

Where V is the particle volume, c is the speed of light, ω is the angular frequency of the exciting radiation, ε_{m} and $\varepsilon(\omega) = \varepsilon_1(\omega) + i\varepsilon_2(\omega)$ are the dielectric functions for the surrounding medium and the nanoparticles respectively. The dielectric function of the medium is considered constant, while that of the nanoparticles is clearly wavelength dependent.

The resonance condition is obtained when $\varepsilon_1 = -2\varepsilon_m$ when ε_2 is small or weakly dependent on ω[142].

Equation 1.3 described from a qualitative and quantitative standpoint the plasmon band for metal nanoparticles when no appreciable quadrupole contribution is present; for Au

nanoparticles it can be used for particles with diameter less than 20 nm. For larger nanoparticles the full Mie equation is required, where scattering and higher order modes are taken into account. For very small size nanoparticles, below 2 nm, Mie description does not comply anymore, since they are better treated as molecular clusters having discrete electronic states[147].

A more complete description of Mie's work is offered in refences[142, 148] while Schatz and coworkers recently proposed a method to solve Maxwell equations , for nanoparticles optical properties of any arbitrary shape[145].

As we move away from the high symmetry of spherically shaped nanoparticles, the surface plasmon becomes unevenly distributed and shape dependent LSPR are observed[149, 150]. Gans[151] expanded Mie theories for non spherical shaped nanoparticles to cylindrical and needle-like geometries[152]. Lastly Mie theory is able to describe the behavior of isolated nanoparticles, while it does not contain information on near-field coupling or far-field dipole interaction among nanoparticles arrays, both responsible for the red shift in the plasmon band.

1.3.2 Shape dependent plasmonic band

The plasmon absorption properties of nanoparticles are strongly dependent on their shape and sizes. As the shape of the nanoparticles goes from resembling that of a sphere to a rod, the plasmon properties change dramatically[153-155]. Nanorod (NRs) shaped particles have two surface resonant plasmon peaks, a strong long wavelength one in the NIR region assign to longitudinal electrons mode, and one at higher energies assigned to the transverse surface electron oscillations center around 520 nm.

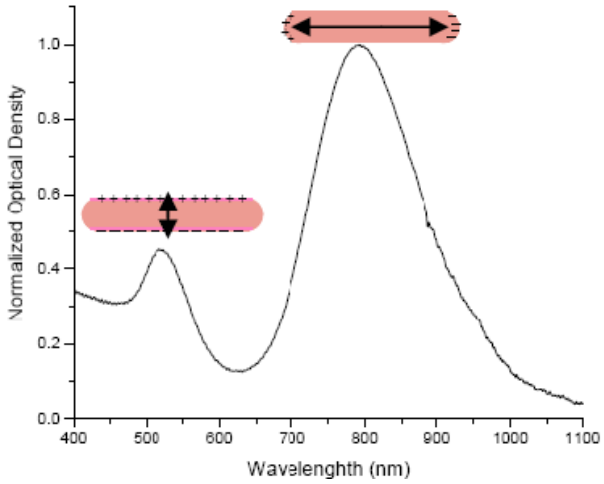

Fig 1.17: Linear absorption of Au Nanorods in water solution. Two plasmon bands are present, one related to the electron oscillation along the axis perpendicular to the major axis (high energy) and one at lower energies related to the electron oscillation along the major axis

The tuning of the nanoarods plasmonic field is achieved by changing their aspect ratio *R*; defined as the ratio between its long dimension divided by the small one. Higher aspect ratios, *R,* have a longitudinal plasmon band further in the NIR as shown by theoretical calculations[156]. A linear dependence between R and the transversal plasmon wavelength maximum is shown in fig 1.18[157].

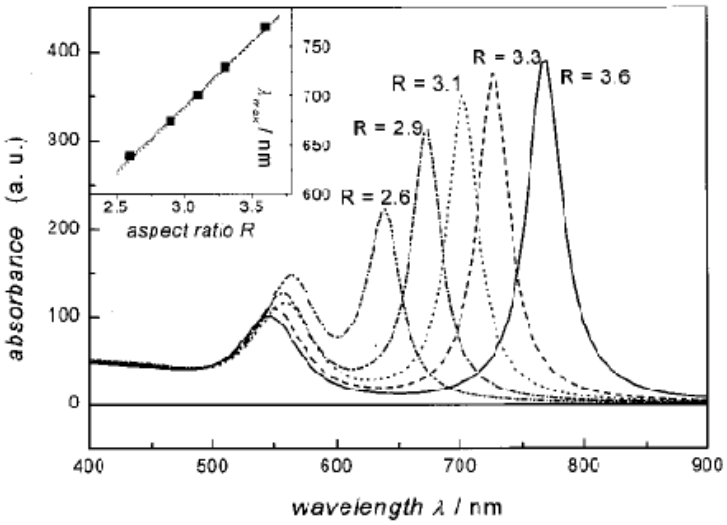

Fig. 1.18: Linear relationship of the aspect ratio *R* versus the longitudinal plasmon band wavelength maximum. Ref [149]

Nanorods will be used in this study because of their ample tunebility range, compared to individual nanospheres and for the larger field enhancement that is conferred by their shape as described later on in this chapter.

Nanorods have very large absorption cross section, and the energy absorbed is ultimately dissipated as heat through electron-phonon and phonon-phonon relaxation processes[152]. The efficient heat release is desirable for applications like cancer theraphy[158], but it would have to be considered when dynamics of other systems are determined in presence of NRs, due to the possibility of thermal effects.

Improvements on the synthesis of colloidal nanostructures have allowed scientists to create new shapes, like disks[159], cubes[160], triangles[161], stars[162], etc. in order to study the impact of the shape on the surface plasmon band.

1.3.3 Nanoshell plasmon band.

Nanoshell consist of a nanoparticle dielectric core surrounded by a thin metal layer. It is found that such hollow metallic nanosphere produces plasmon resonance band that is sensitive both to the inner and outer shell diameter[163, 164].

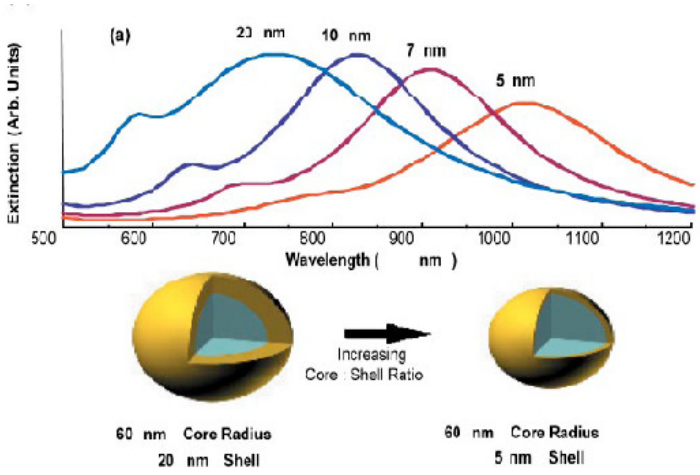

Fig. 1.19: It is possible to tune the resonant plasmon band across the visible and the NIR range by changing the relative size of the core and/ or the shell. Ref [165]

The plasmon band for these structures can be explained using Mie theory, although a new approach, called Plasmon Hybridization (PH) theory has been found to be more appropriate, not only capable of predicting the plasmon resonance but the relative charge distribution in complex nanostructures as well[163, 166]. PH describes the plasmon in nanoshell structures as interaction (hybridization) between a metal nanosphere and a spherical cavity. Fig 1.20 illustrates the concept.

The plasmon tunability of hybrid nanostructures have found several biomedical applications[165, 167], as well as molecular tags for diagnostic purposes[168].

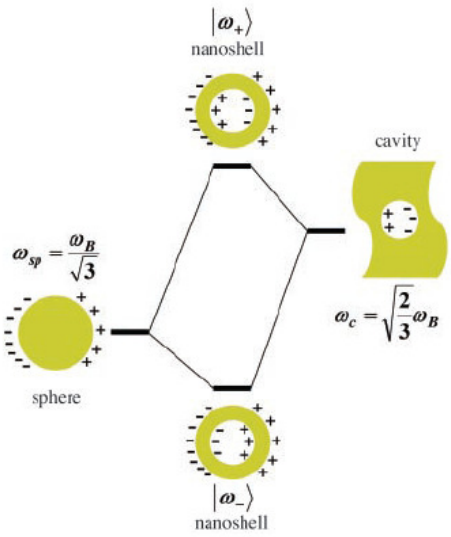

Fig. 1.20: Illustration of the PH theory. The nanoshell structure is decomposed in a nanosphere and a cavity. Their interaction produces two plasmon modes; one that is antisymmetrically coupled (ω_+) and a symmetrically coupled (ω_-). Ref [163]

1.3.3 Plasmonic field from metal nanoparticles

One of the main features, which will be widely used in this thesis, is the ability of the resonance plasmon in nanoparticles to generate a plasmonic field. The nature of this field and its applications will be discussed in this paragraph.

As mentioned previously, when downsized at the nanometer scale, noble metals have very brilliant colors associate with LSP absorptions[169].

The LSP oscillates coherently with the exciting waves, generating radiations that are characteristic of the oscillating dipole. The spatial distribution of the nanoparticle field magnitude comes from focusing of the surrounding light on portions of its surface[170] causing local depletion of the incident waves (see Fig 1.19A). As a consequence the spatial distribution of the generated electric field results inhomogeneous, as shown in Fig 1.21B

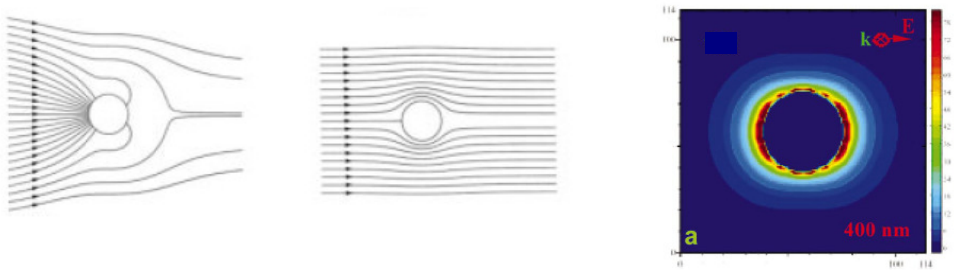

A B

Fig.1.21: A) Field lines of the Poynting vector for an aluminum nanosphere irradiated with 2 different wavelengths (not including scattering). In the left image, the light causes plasmon resonance (8.8 eV), on the right one no resonance takes place (5 eV). Ref [144] B) Plasmonic field distribution and its magnitude on the nanosphere surface of Silver at the plasmon peak. Ref [171]

The strength of the local field and its spatial distribution is highly dependent on the nature of the metal and on the nanoparticles size and morphology[172, 173]. A common way to quantify the strength of the local field is through a parameter called enhancement (indicated as G), which is the ratio between the plasmon field generated and the incoming or exciting field. Two parameters are important to consider when enhancement factors are considered: the average of $|E^2|$ over the whole particle surface (relevant to conventional SERS measurements) and peak value of $|E^2|$ (relevant for single molecule application). The strong local electric field, created upon plasmon excitation has been proven to affect the Raman signal of molecular systems adsorbed or simply present in the vicinity of the nanoparticles surface. In particular Surface Enhanced Raman Scattering (SERS) is a known phenomenon, recently discovered in 1974 by Fleischmann and coworkers while working with pyridine adsorbed on silver electrodes, where they observed unusually large Raman signal from the adsorbed pyridine[174].
Silver nanoparticles, have SERS enhancement factors[173-175] around 10^6 (G is proportional $\propto |E^4|$ [170]), which are among the largest known. Peak enhancement factors can reach values[176] up to 10^{12} or higher. In the case of gold, the enhancement

factors are slightly smaller, the reason is believe to be related to the rapid increase in the imaginary part of its dielectric constant above 2 eV (about 630 nm), due to interband transitions[175] . They are found to be within a factor of 2 comparable with those of silver[175]. Local field enhancement is highly desired for other type of applications like nonlinear-optics, where the nonlinear response of molecular systems close to the surface plasmon of noble metal nanoparticles is larger for processes like Second Harmonic Generation (SHG)[177], Two-photon absorption[178], $\chi^{(3)}$[147] and so on. It is important then, to understand how the shape and other factors can affect the field enhancement; this is why a large number of papers are published every year on the topic. The surface shape has been shown to have large effects on the enhancement factor as mentioned[171]. In the table below values of the average enhancement factor, calculated using DDA, for silver nanoparticles of different shapes are reported. The same shape dependent behavior is observed with gold nanoparticles.

Table 1.1: Enhancement factors for the generated plasmonic electric field in silver nanoparticles of different shapes at the peak resonance wavelength. The theoretical values were obtained by DDA calculation from Ref. [173].

Particle shape	Enhancement factor at the peak resonant wavelength
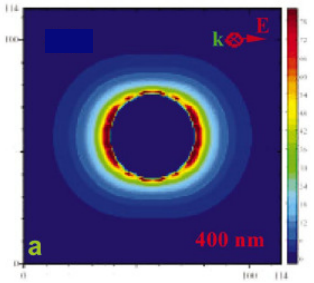 Ag nanosphere 40nm diameter	**180** **(36) for Au**
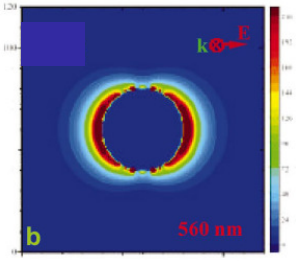 Ag nanodisk 40 nm diameter 9 nm thick	**550**
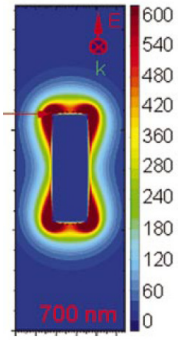 Ag nanorod	**4500**

To have an idea of the electric field generated, if we assume an incoming field of 1 V/m, in the vicinity of a silver nanorod, the plasmon field generated will be of few μV /nm at peak resonant wavelength.

The strongly enhanced surface plasmon of noble metal nanoparticles not only has superior absorption and scattering properties, which finds applications in optics and photonics[179-181]; but lately the attention has moved on biological applications like sensing and cellular imaging. The use of localized plasmon absorption for sensing is typically associated to a red shift and broadening of the plasmon due to inter-particle coupling, and it can occur along a distance up to two and a half times the diameter of the nanoparticle[182, 183]. Nanoparticles proximity sensors have been created for pH[184], DNA[185], metal ions[186], antibody[187] and many more. Such ability of nanoparticles to dipole-couple over relatively long distances has also increased the fluorescence resonance energy transfer (FRET) limit compared to traditional organic fluorescence dye[188].

This thesis focuses on the study of the interaction of the plasmonic field generated by LPS from gold and silver nanoparticles in the vicinity of bR, a well known G-protein functioning as proton pump.

1.3.5 Dimers of nanoparticles and "hot spots".

Early calculations[189] revealed the possibility of having extremely large enhancement factor (G) due to hot spots, present between or at the junction of two or more nanoparticles[176, 190].

Recent theoretical calculations[173] support such possibility, proving that as nanoparticles get closer, the field between spheres, for examples, gets increased by a factor of 10^2 compared to that of isolated sphere. In the case of nanoparticles with sharp

curvatures like nanoprisms or nanorods, the enhancement (for the dipole) is 35,000 along the inter-particle distance for the "tip to tip" configuration[173]. Experimental data support these findings as well[191, 192], undoubtedly proving an increase in the field enhancement when aggregates of nanoparticles are present. A direct consequence is that when nanoparticles aggregate, the resulting plasmonic field is much larger than the simple vector sum of each particle field.

1.3.6 .Plasmonic field and bR proton pump dynamics.

A complete treatment of the plasmon dynamic was done in chapter 3; here a summary of the key points is made.

The local field effect is a direct consequence of the coherent oscillation of the free electron in the conduction band in colloidal structure as mention previously. An important aspect to consider is the dynamic of this plasmon and its evolution in time. Upon excitation, the free electrons start oscillating in phase. The width of the plasmon band gave indications that the dephasing time for such system is few femtoseconds, suggesting that the main relaxation path is electron-electron collision[193].

The relaxation of the plasmonic field generated upon excitation has been measured and it was found to have indeed a very short lifetime, <20 fs[194]. The processes that we are considering in bR are the isomerization (intermediate I_{460}) , and both the deprotonation and reprotonation of the Retinal Schiff Base (intermediate M_{412}). It is important to realize that while the isomerization takes place on a 500 fs time-scale, deprotonation and protonation occur on a much longer time-scale. With the reprotonation being a relatively long process, on the order on 10^{-3} s, the disparity between the two processes is of 10^{12} order of magnitudes. Any effect generated in such ultra short time-scale compare to the duration of the whole process cannot be detected. For this reason the plasmon field will

have to be kept on while M_{412} dynamics are taking place, in order to see its effect on the proton pump dynamic as discussed on chapter 4.

1.4 The plasmonic field and its penetration depth: can it work for bR?

Surface plasmon depends strongly on the nature of the surface and its size, as mentioned above. Another important aspect to analyze when considering the interaction of such plasmonic field with other systems, is its propagation dependence in space. The plasmonic field generated upon excitation has an intensity that is function not only of the local surface geometry, but of the distance from such surface, as it is shown on table 1.1. In other words, how fast does the plasmonic field intensity drop as we move away from the particle surface? Does it reach far enough to potentially affect protein systems present in the vicinity of the nanostructure surface? And for that matter, how close do they need to be to be included by the plasmonic field?

The answer to the first question can be found on results from theoretical calculations published by Schatz and collaborators. The dependence of the plasmonic field intensity from the surface distance was simulated for a silver nanosphere of 20 nm in diameter

It was found that the plasmonic field intensity (E*E) drops exponentially as the distance from the surface increases as shown in fig. 1.22

The bR protein system needs to be contained within such area, to have exposure to the plasmonic field.

Dark field picture of bR solution with nanoparticles, or nanorods, show that the bR patches are coated by nanoparticles absorbed to their surface. The nature of their interaction is believed to be electrostatic.

The thickness of the purple membrane is about 5 nm, and the patches are few microns in size[195]. A possible picture for the system bR/NPs could be that of fig. 1.23, where for

convenience only one nanoparticles is shown. In reality each single patch would have nanoparticles adsorbed on both sides.

For nanoparticles with a diameter larger or equal to 10 nm, their plasmonic field will be able to penetrate through bR thickness. How such field is able to affect the protein functionality will be the topic of the next chapters.

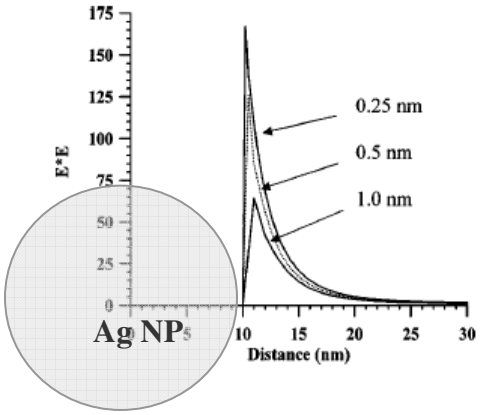

Fig. 1.22: Profile of the plasmonic field intensity as we move away from the surface of a silver nanoparticle

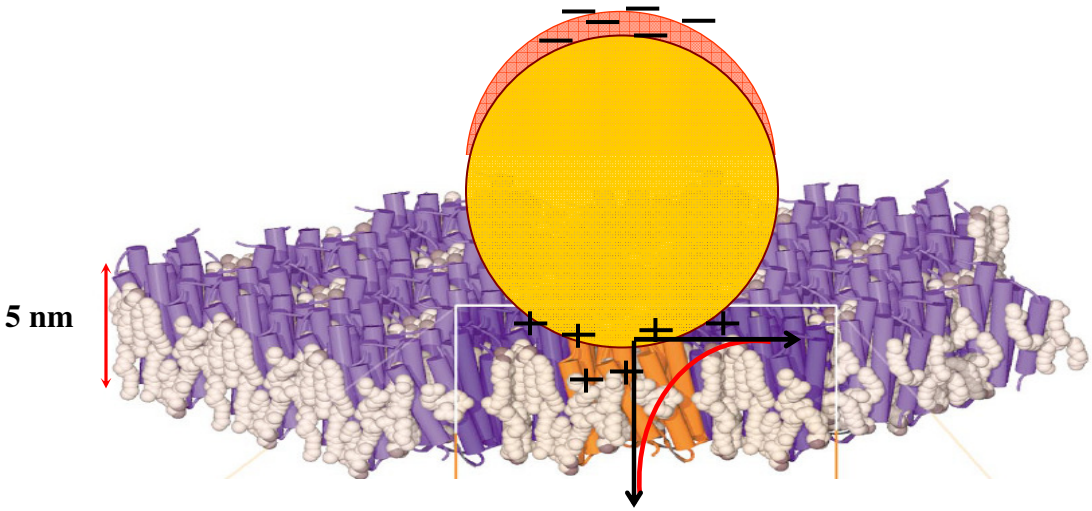

Fig. 1.23: Illustration of a gold nanoparticles adsorbed on bR patches and the decay of the plasmon field magnitude with particles surface distance.

REFERENCES:

[1] Stoeckenius, W., Rowen, R., J. Cell Biol. 38, 337 (1968)

[2] Oesterhelt, D., Isr. J. Chem., 35, 475 (1995)

[3] Muneyuki, E., Shibazaki, C., Wada, Y., Yakushizin, M., Ohtani, H., Biophys. J. 83, 1749 (2002)

[4] Kolbe, M., Besir, H., Essen, L.-O., Oesterhelt, D., Science. 288, 1390 (2000)

[5] Hoff, W. D., Jung, K. H., Spudich, J. L., Ann. Rev. Biophys. Biomol. Struct. **26**, 223 (1997)

[6] Spudich, J. L., Yang, C. S., Jung, K. H., Spudich, E. N., Ann. Rev. Cell Dev. Biol. **16**, 365 (2000)

[7] Meltina, A. L., Biochemistry. 69, 1203 (2004)

[8] Stoeckenius, W., Rowen, R., J. Cell Biol. 34, 365 (1967)

[9] Henderson, R., Unwin, P. N., Nature. 257, 28 (1975)

[10] Drackev, A. L., Bose, S., Hendler, R. W., FEBS Lett. **382**, 209 (1996)

[11] El-Sayed, M. A., Acc. Chem. Res. 25, 279 (1996)

[12] Korenbrot, J.I., Ann. Rev. Physiol. 39, 19 (1977)

[13] Mathies, R. A., Lin, S. W., Ames, J. B., Pollard, W. T., Ann. Rev. Biophys. Chem. **20**, 491 (1991)

[14] Lin, S.W., Mathies, R. A., Biophys. J. 56, 653 (1989)

[15] Baldwin, J.M., Curr. Opin. Cell. Biol. 6, 180 (1994)

[16] Henderson, R., Baldwin, J. M., Ceska, T. A., Zemlin, F., Beckmann, E., Downing, K. H., 18, 844 (1990)

[17] Lanyi, K. J., J. Struct. Biol. 124, 164 (1998)

[18] Kataoka, M., Kamikubo, H., Tokunaga, F., Brown, L. S., Yamazaki, Y., Maeda, A., Shenes, M., Needleman, R., Lanyi, J. K., J. Mol. Biol. 243, 620 (1994)

[19] Rummel, G., Hardmeyer, A., Widmer, C., Chiu, M. L., Noller, P., Locker, K.P., Pedruzzi, I., Landau, E.M., Rosenbush, J.P., J. Struct. Biol. 121, 82 (1998)

[20] Schobert, B., Cupp-Vickery, J., Hornak, V., Smith, S., Lanyi, J., J. Mol. Biol. 321, 715 (2002)

[21] Stoeckenius, W., Lozier, R. H., Bogomolni, R., Biochim. Biophys. Acta. 505, 215 (1978)

[22] Koyama, Y., Kubo, K., Komori, M., Yasuda, H., Mukai, Y., Photochem. PhotoBiol. 54, 433 (1991)

[23] El-Sayed, M.A., Lougonov, S., Pure Appl. Chem. 69, 749 (1997)

[24] Milder, S.J., Biophys. J. 60, 440 (1991)

[25] Gai , F., Hasson, K. C., McDonald, J. C., Anfinrud, P. A., Science. 279, 1186 (1998)

[26] Kochendoerfer, G., Mathies, R., Isr. J. Chem. 35, 211 (1996)

[27] Sakmar, T. P., Menon, S. T., Marin, E. P., Awad, E. S., Ann. Rev. Biophys. Biomol. Struct. 31, 443 (2002)

[28] Smith, O.S., Pardoen, A. J., Lugtenburg, J., Mathies, R., J. Phys. Chem. 91, 804 (1987)

[29] Smith, O.S., Braiman, M. S., Myers, A. B., Pardoen, A. J., Courtin, J. M., Winkel, C., Lugtenburg, J., Mathies, R., J. Am. Chem. Soc. 109, 3108 (1987)

[30] Royant, A., Edman, K., Ursby, T., Pebay-Peyroula, E., Landau, M. E., Neutze, R., Nature. 406, 645 (2000)

[31] Althaus, T., Eisfeld, W., Lohrmann, R., Stockburger, M., Isr. J. Chem. 35, 227 (1995)

[32] Rothschild, K.J., J. Bioenerg. Biomembr. 24, 147 (1992)

[33] Maeda, A., Isr. J. Chem. 35, 387 (1995)

[34] Herzfeld, J., Lansing, J. C., Ann. Rev. Biophys. Biomol. Struct. 31**,**. 73 (2002)

[35] Srajer, V., Teng, T., Ursby, T., Pradervand, C., Ren, Z., Adachi, S., Scildkamp, W., Bourgeois, D., Wulff, M., Moffat, K., Science. 274, 1726 (1996)

[36] Luecke, M., Biochimica et Biophysica Acta, 2000. **1460**: p. 133-156.

[37] Luecke, H., Schobert, B., Richter, T. H., Richter, H-T., Cartailler, J-P., Lanyi. K. J., J. Mol. Biol. 291, 899 (1999)

[38] Belrhali, H., Nollert, P., Royant, a., Menzel, C., Rosenbusch, P. J., Landau, M. E., Pebay-Peyroula, E., Structure. 7, 909 (1999)

[39] Druckmann, S., Ottolenghi, M., Pande, A., Callender, H. R., Biochemistry. 21, 4953 (1982)

[40] Sheves, M., Albeck, A., Friedman, N., Ottolenghi, M., Proc. Nat. Acad. Sci. USA. 83, 3262 (1986)

[41] Baasov, T., Sheves, M., Biochemistry. 25, 5249 (1986)

[42] Szaraz, S., Oesterhelt, D., Ormos, P., Biophys. J. 67, 1706 (1994)

[43] Atkinson, G.H., Ujj, L., Zhou, Y., J. Phys. Chem. A. 104, 4130 (2000)

[44] van der Berg, R., Jang, D. J., Bitting, H. C., El-Sayed, M. A., Biophys. J. 58, 135 (1990)

[45] Diller, R., Maiti, S., Walker, G. C., Cowen, B. R., Pippenger, R., Bogomolni, R. A., Hochstrasser, R. M., Chem. Phys. Lett. 241, 109 (1995)

[46] Mathies, R.A., Brito Cruz, C. H., Pollard, W. T., Shank, C. V., Science. 240, 777 (1988)

[47] Dobler, J., Zinth, W., Kaiser, W., Chem. Phys. Lett. 144, 215 (1988)

[48] Sension, R. J., Repinec, S. T., Szarka, A. Z., Hochstrasser, R. M., J. Chem. Phys. 98, 6291 (1993)

[49] Zhong, Q., Ruhman, S., Ottolenghi, M., J. Am. Chem. Soc. 118, (1996)

[50] Haran, G., Wynne, K., Xie,A., He, Q., Chance, M., Hochstrasser, R. M., Chem. Phys. Lett. 261, 389 (1996)

[51] Hasson, K.C., Gau, F., Anfinrud, P. A., Proc. Nat. Acad. Sci. USA. 93, 15124 (1996)

[52] Dexheimer, S. L., Wang, Q., Peteanu, L.A., Pollard, W.T., Mathies, R.A., Shank, C. V., Chem. Phys. Lett. 188, 61 (1992)

[53] Shapiro, S. L., Campillo, A. J., Lewis, A., Perreault, G. J., Spoonhover, J. P., Clayton, R. K., Stoeckenius, W., Biophys. J. 23, 383 (1978)

[54] Weiss, R. M., Warshel, A., J. Am. Chem. Soc. 101, 6131 (1979)

[55] Birge, R. R., Zhang, C.-F., J. Chem. Phys. 92, 7178 (1990)\

[56] Stuart, J. A., Vought, B. W., Zhang, C.-F., Birge, R., R., Biospectroscopy. 1, 9 (1995)

[57] Vreven, T., Bernardi, F., Garavelli, M., Olivucci, M., Robb, M. A., Schlegel, H. B., J. Am. Chem. Soc. 119, 12687 (1997)

[58] Song, L., El-Sayed, A. M., J. Am. Chem. Soc. 120, 8889 (1998)

[59] Ye, T., Friedman, N., Gat, Y., Atkinson, H. G., Sheves, M., Ottolenghi, M., Ruhman, S., J. Phys. Chem. B. 103, 5122 (1999)

[60] Zhong, Q., Ruhman, S., Ottolenghi, M., J. Am. Chem. Soc. 118, 12828 (1996)

[61] Kobayashi, T., Saito, T., Ohtani, H., Nature. 414, 531 (2001)

[62] Pollard, W. T., Dexheimer, S. L., Wang, Q., Peteanu, L. A., Shank, C. V., Mathies, R. A., J. Phys. Chem. 96, 6147 (1992)

[63] Kahan, A., Nahmias, O., Friedman, N., Sheves, M., Ruhman, S., J. Am. Chem. Soc. 129,. 537 (2007)

[64] Ahroni, A., Hou, B., Friedman, N., Ottolenghi, M., Rousso, I., Ruhman, S., Sheves, M., Ye, T., Zhong, Q., Biochemistry. 66, 1210 (2001)

[65] Ruhman, S., Hou, B., Friedman, N., Ottolenghi, M., Sheves, M., J. Am. Chem. Soc. 124, 8854 (2002)

[66] Du, M., Fleming, G. R., Biophys. Chem. 48, 101 (1993)

[67] Akiyama, R., Yoshimori, A., Kakitani, T. et al., J. Phys. Chem. 101, 412 (1997)

[68] Ye, T., Friedman, N., Gat, Y., Atkinson, G. H., Sheves, M., Ottolenghi, M., Ruhman, S., J. Phys. Chem. 103, 5122 (1999)

[69] Logunov, S.L., Masciangioli, T. M., Kamalov, V. F., El-Sayed, M. A., J. Phys. Chem. 102, 2303 (1998)

[70] Garavelli, M., Negri, F., Olivucci, M., J. Am. Chem. Soc. 121, 1023 (1998.)

[71] Doig, S.J., Reid, P. J., Mathies, R. A., J. Phys. Chem. 95, 6372 (1991)

[72] Brack. T. L., Atkinson, G. H., J. Phys. Chem. 95, 2351 (1991)

[73] Delaney, J. K., Brack , T. L., At.kinson, G. H., Ottolenghi, M., Steinberg, G., Sheves, M., Proc. Nat. Acad. Sci. USA. 92,. 2101 (1995)

[74] Braiman, M., Mathies, R., Proc. Nat. Acad. Sci. USA. 79, 403 (1982)

[75] Rothschild, K. J., Roepe, P., Lugtenburg, J., Pardoen, J. A., Biochemistry. 23, 6103 (1984)

[76] Kandori, H., Kinoshita, N., Shichida, Y., Maeda, A., J. Phys. Chem. B. 102, 7899 (1998)

[77] Kandori, H., Kinoshita, N., Yamazaki, Y., Maeda, A., Shichida, Y., Needleman, R., Lanyi, J., Bizounok, M., Herzfeld, J., Raap, J., Lugtenburg, J., Proc. Nat. Acad. Sci. USA. 97, 4643 (2000)

[78] Schobert, B., Brown, S. L., Lanyi, J. K., J. Mol. Biol. 330, 553 (2003)

[79] Milder, S. J., Kliger, D., Biophys. J., 53, 465 (1988)

[80] Stern, D., Mathies, R., *In time Resolved Vibrational Spectroscopy*. Springer 1985, New York: New York Inc.

[81] Maeda, A., Kandori, H., Yamazaki, Y., Nishimura, S., Hatanaka, M., Chon, Y. S., Sasaki, J., Needleman, R., Lanyi, K. J., J. Biochem. 121, 399 (1997)

[82] Lanyi, K. J., Schobert, B., J. Mol. Biol. 328, 439 (2003)

[83] Zimanay, L., Varo, G., Chang, M., Ni, B., Needleman, R., Lanyi, K. J., Biochemistry. 31, 8535 (1992)

[84] Lanyi, K. J., Ann. Rev. Physiol. 66, 665 (2004)

[85] Zimanay, L., Lanyi, K. J., Photochem. PhotoBiol. 56, 1049 (1992)

[86] Zimanay, L., Saltiel, J., Brown, L. S., Lanyi, K. J., J. Phys. Chem. A. 110, 2318 (2006)

[87] Mogi, T., Stern, L. J., Marti, T., Chao, B. H., Khorana, H. G., Proc. Nat. Acad. Sci. USA. 85, 4148 (1988)

[88] Otto, H., Marti, T., Holz, M., Mogi, T., Stern, L. J., Engel, F., Khorana, H. G., Heyn, M. P., Proc. Nat. Acad. Sci. USA. 87, 1018 (1990)

[89] Brainman, M. S., Mogi, T., Marti, T., Stern, L. J., Khorana, H. G., Rothschild, K. J., Biochemistry. 27, 8516 (1988)

[90] Metz, G., Siebert, F., Engelhard, M., FEBS Lett. 303, 237 (1992)

[91] Luecke, H., Schobert, B., Richter, T. H., Cartailler, J-P., Lanyi. K. J., Science. 286, 255 (1999)

[92] Althaus, T., Stockburger, M., Biochemistry. 37**,** 2807 (1998)

[93] Lanyi, K. J., Mol. Membr. Biol., 21**,** 143 (2004)

[94] Varo, G., Lanyi, K. J., Biochemistry. 30, 7165 (1991)

[95] Drackev, A. L., Kaulen, D. A., Skulachev, P. V., FEBS Lett. 178, 331 (1984)

[96] Grzesiek, S., Dencher, A. N., FEBS Lett. 208, 337 (1986)

[97] Heberle, J., Dencher, A. N., Proc. Nat. Acad. Sci. USA. 89, 5996 (1992)

[98] Brown, S. L., Sasaki, J., Kandori, H., Maeda, A., Needleman, R., Lanyi, K. J., J. Biol. Chem. 270, 27122 (1995)

[99] Balashov, P. S., Imasheva, E., Ebrey G. T., Menick, R. D., Crouch, K. R., Biochemistry. 37, 5001 (1997)

[100] Spassov, Z. V., Luecke, H., Gerwert, K., Bashford, D., J. Mol. Biol. 312, 203-219 (2001)

[101] Balashov, P. S., Imasheva, E., Govindjee, R., Ebrey G. T., Biophys. J. 70, 473 (1996)

[102] Richter, T. H., Brown, S. L., Needleman, R., Lanyi, K. J. 35,4054 (1996)

[103] Brown, S. L., Dioumaev, K. A., Needleman, R., Lanyi, K. J. Biophys. J. 75, 1455 (1998)

[104] Brown, S. L., Dioumaev, K. A., Needleman, R., Lanyi, K. J., Biochemistry. 37, 3982 (1998)

[105] Zhou, F., Windemuth, A., Schulten, K., Biochemistry. 32, 2291 (1993)

[106] Humphrey, W. L., I.; Schulen, K.; Sheves, M., Biochemistry. 33, 3668 (1994)

[107] Roux, B., Nina, M., Pomes, R. Smith, C. J., Biophys. J. 71, 670 (1996)

[108] Varo, G., Lanyi, K. J., Biophys. J. 59, 313 (1991)

[109] Cao, Y., Vàrò, G., Chang, M., Ni, B., Needleman, R., Lanyi, J.K., Biochemistry. 30, 10972 (1991)

[110] Varo, G., Lanyi, K. J., *Effects of hydrostatic pressure on the kinetics reveal a valume increase during bacteriorhodopsin photocycle.* Biochemistry. 34, 12161 (1995)

[111] Luecke, H., Schobert, B., Richter, T. H., Cartailler, J-P., Rosengarth, A., Needleman, R., Lanyi. K. J., J. Mol. Biol. 300, 1237 (2000)

[112] Kamikubo, H. K., M.; Varo, G.; Oka, T.; Tokunaga, F., Proc. Nat. Acad. Sci. USA. 93, 1386 (1996)

[113] Oka, T., Yagi, N., Tokunaga, F., Kataoka, M., Biophys. J. 82, 2610 (2000)

[114] Drencher, A. N., Dresselhaus, D., Zaccai, G., Bueldt, G., Proc. Nat. Acad. Sci. USA. 86, 7876 (1989)

[115] Gerwert, K., Hess, B., Soppa J., Oesterhelt, D., Proc. Nat. Acad. Sci. USA. 89, 4943 (1989)

[116] Brown, S. L., Varo, G., Needleman, R., Lanyi, K. J. Biophys. J. 69, 2103 (1995)

[117] Dioumaev, K. A., Richter, H. T., Brown, S. L., Michikazu, S. T., Hazime, Y. K., Needleman, R., Lanyi, K. J., Biochemistry. 37, 2496 (1998)

[118] Borucki, B., Otto, H., Heyn, M. P., J. Phys. Chem. B. 108, 2076 (2004)

[119] Bousche, O., Braiman, M., He, Y, W., Marti, T., Khorana, H. G., Rothschild, K. J., J. Biol. Chem. 266, 11063 (1991)

[120] Cao, Y., Brown, S. L., Needleman, R., Lanyi, J., Biochemistry. 32, 10239 (1993)

[121] Dioumaev, K.A., Brown, S. L., Needleman, R., Lanyi, K. J., Biochemistry. 37, 9889 (1998)

[122] Rouhani, S., Cartailler, P. J., Facciotti, T. M., Walian, P., Needleman, R., J. Mol. Biol. 313, 615 (2001)

[123] Delaney, J. K., Schweiger, U., Subramaniam, S., Proc. Nat. Acad. Sci. USA. 92, 11120 (1995)

[124] Smith, O. S., Pardoen, A. J., Mulder, J. P.P., Curry, B., Lugtenburg, J., Mathies, R., Biochemistry. 22, 6141 (1983)

[125] Dioumaev, A. K., Brown, L. S., Needleman, R., Lanyi, J. K., Biochemistry. 38, 10070 (1999)

[126] Hessling, B. H., J.; Rammelsberg, R.; Gerwert, K., Biophys. J. 73, 2071 (1997)

[127] Varo, G., Lanyi, K. J., Biochemistry. 30, 5008 (1991)

[128] Druckmann, S., Friedman, N., Lanyi, J. K., Needleman, R., Ottolenghi, M., Sheves, M., Photochem. Photobiol. 56, 1041 (1992)

[129] Nagel, B. G., Kelety, B.; Mockel, G.; Bamberg, E., Biophys. J. 74, 403 (1998)

[130] Varo, G., Lanyi, K. J., Biochemistry. 30, 7165 (1991)

[131] Ames, J. B., Mathies, R. A., Biochemistry. 29, 7181 (1990)

[132] Nagle, J. F., Photochem. PhotoBiol. 54, 897 (1991)

[133] Diller, R., Stockburger, M., Biochemistry. 27, 7641 (1988)

[134] Hendler, W.R., Dancshazy, Z.; Bose, S.; Shrager, I. R.; Tokaji, Z., Biochemistry. 33, 4604 (1994)

[135] Hanamoto, H. J., Dupuis, P., El-Sayed, A. M., Proc. Nat. Acad. Sci. USA. **81**: p. 7083 (1984)

[136] Kouyama, T., Nasudakouyama,-K., A.; Ikegami, A.;Mathew, K. M., Stoeckenius, W., Biochemistry. 27, 5855 (1988)

[137] Eisfeld, W., Pusch, C., Diller, R., Lohrmann, R., Stockburger, M., Biochemistry. 32, 7196 (1993)

[138] Hauptus, U., Tittor, J., Bamberg, E., Oesterhelt, D., Biochemistry. 36, 2 (1997)

[139] Subramaniam. S., Lindahl, I., Bullough, P., Faruqi, A. R., Tittor, J., Oesterhelt, D., Brown, L., Lanyi, J., Henderson, R., J. Mol. Biol., 287, 145 (1999)

[140] Lanyi, K. J., Schobert, B., J. Mol. Biol. 321, 727 (2002)

141. Faraday, M., Philos. Trans. R. Soc. London. 147, 145 (1857)

[142] Kreibig, U., Vollmer, M., *Optical properties of metal clusters*, ed. Springer. 1995, Berlin.

[143] Kerker, M., *The scattering of light and other electromagnetic radiation*, ed. Academic. 1969, New York.

[144] Bohren, C. F., Huffman, D. R., *Absorption and scattering of light by small particles*, ed. Wiley. 1983, New York.

[145] Kelly, K.L., Coronado, E., Zhao, L. L., Schatz, G. C., J. Phys. Chem. B. 107, 668 (2003)

[146] Mie, G., Ann. Phys. 25, 377 (1908)

[147] Yong, Y., Masayuky, N., Jianlin, S., Hangrong, C., Guohong, M., Singhai, T., J. Phys. Chem. B. 109**,** 4865 (2005)

[148] Kerger, M., *The scattering of light and other electromagnetic radiation*. 1969, Academic Press: New York.

[149] Link, S., Mohamed, M. B., El-Sayed, M. A., J. Phys. Chem. B. 103, 3073 (1999)

[150] Link, S., El-Sayed A. M., Int. Rev. Phys. Chem. 19, 409 (2000)

[151] Gans, R., Ann. Phys. 47, 270 (1915)

[152] Link, S., El-Sayed, A. M., Ann. Rev. Phys. Chem. 54, 331 (2003)

[153] Yu, Y.Y., Chang, S. S., Lee, C. L., Wang, C. R. C., J. Phys. Chem. B. 101, 6661 (1997)

[154] van der Zande, B. M. I., Bohmer, M. R., Fokking, L. G. J., Schonenberger, C., J. Phys. Chem. B. 101, 852 (1997)

[155] Nikoobakht, B., El-sayed, A. M., Chem. Mater. 15, 1957 (2003)

[156] Lebedeva, V. N., Distler, G. I.,Opt. Spektrosk. 23, 968 (1967)

[157] Link, S., Mohamed, M. B., El-Sayed, A. M., J. Phys. Chem. B. 103, 3073 (1999)

[158] Huang, X., Jain, P. K., El-Sayed, I. H., El-Sayed, M. A., Nanomedicine. 2, 681 (2007)

[159] Maillard, M., Giorgio, S., Pileni, M. P., J. Phys. Chem. 107, 2466 (2003)

[160] Yu, D., Yam, V. W. W., J. Am. Chem. Soc. 126, 13200 (2004)

[161] Sau, T. K., Murphy, C. J., J. Am. Chem. Soc. 126, 8648 (2004)

[162] Nehl, C. L., Liao, H., Hafner, J., Nano Lett. 6, 683 (2006)

[163] Prodan, E., Radloff, C., Halas, N. J., Nordlander, P., Science. 302, 419 (2003)

[164] Lal, S., Grady. N. K., Kundu, J., Levin, C. S., Lassiter, J. B., Halas, N. J., Chem. Soc. Rev. 37, 898 (2008)

[165] West, J. L., Halas, N., Ann. Rev. Biomed. Eng. 5, 285 (2003)

[166] Prodan, E., Nordlander, P., J. Chem. Phys. 120, 5444 (2004)

[167] O'Neal, D. P., Hirsch, L. R., Halas, N. J., Payne, J. D., West, J. L., Canc. Lett. 209, 171 (2004)

[168] Loo, C., Hirsch, L., Lee, M. H.; Chang, E., West, J., Halas, N., Drezek, R., Opt. Lett. 30, 1012 (2005)

[169] Liz-Marzan, M. L., Mater. Today. 7, 26 (2004)

[170] Moskovits, M., J. Raman Spectrosc. 36, 485 (2005)

[171] Hao, E., Schatz, C. G., Hupp, T. J., J. Fluorescence. 14, 331 (2004)

[172] Zeman, J.Z., Schatz, C. G., Jerusalem Symposia on Quantum Chemistry and Biochemistry. **17**, 412 (1984)

[173] Hao, E., Schatz, C. G., J. Chem. Phys. 120, 357 (2004)

[174] Fleishmann, M., Hendra, P.J., McQuillan, A. J., Chem. Phys. Lett. 26, (1974)

[175] Schatz, C. G., Acc. Chem. Res. 17, 370 (1984)

[176] Nie, S., Emory, Steven R., Science. 275**,** 1102 (1997)

[177] Quail, J. C., Rako, J. C., Simon, H. J., Deck, R. T., Phys. Rev. Lett. 50, 1987 (1993)

[178] Weseleers, W., Stellacci, F., Meyer-Friedrichsen, T., Mangel, T., Bauer, A. C., Pond, J. K. S., Marder, R. S., Perry, W. J., J. Phys. Chem. B. 106, 6853 (2002)

[179] Maier, A. S., Brongersma, M. L., Kilk, P.G., Meltzer, S., Requicha, A. A.G. Adv. Mater. 13, 1501 (2001)

[180] Barnes, L. W., Dereux, A., Ebbsen, W. T., Nature. 412, 824 (2003)

[181] Andersen, C. P., Rowlen, L. K., Appl. Spectros. 56, 120A (2002)

[182] Su, K.-H., Wei, Q.-H., Zhang, X., Mock, J. J., Smith, D. R., Schultz, S., Nano Lett. 3, 1087 (2003)

[183] Aslan, K., Lakowicz, R. J., Geddes, D. C., Anal. Chem. 77, 2008 (2005)

[184] Mayya, S. K., Patil, V., Sastry, M., Langmuir. 13, 3944 (1997)

[185] Mirkin, A. C., Letsinger, L. R., Mucic, C. R., Storhoff, J. J., Nature. 382, 607 (1996)

[186] Kim, Y. J., C. R.; Hupp, J. T., Nano Lett. 1, 165 (2001)

[187] Thanh, T. N., Rosenzweig, Z., Anal. Chem. 74, 1624 (2002)

[188] Aslan, K., Lakowicz, R. J., Geddes, D. C., Curr. Opin. Chem. Biology. 9, 538 (2005)

[189] Metiu, H., Prog. Surf. Sci. 17, 153 (1984)

190. Michels, M. A., Nirmal, M., Brus, E. L., J. Am. Chem. Soc. 121, 9932 (1999)

[191] Jiang, J., Bosnick, K., Maillard, M., Brus, L., J. Phys. Chem. B. 107, 9964 (2003)

[192] Xu, H., Aizpura, J., Kall, M., Apell, P., Phys. Rev. E. 62, 4318 (2000)

[193] Link, S., El-Sayed, A. M., J. Phys. Chem. B. 103, 4212 (1999)

[194] Puech, K., Henari, Z. F., Blau, W. J., Duff, D., Schmid, G., Chem. Phys. Lett. 247, 13 (1995)

[195] Wang, Z., Hartmann, T., Baumeister, W., Guckenberger, R., Proc. Nat. Acad. Sci. USA. 87, 9343 (1990)

CHAPTER II

SYNTHESIS AND INCORPORATION OF GOLD NANOPARTICLES IN BACTERIORHODOPSIN MEMBRANE PATCHES

Abstract:

This chapter deals with the procedures used to prepare and synthesize the bR protein and the colloidal systems used in the studies described on the following chapters.

The description of various attempts aimed at growing NPs on the bacteria and in bR patches are described.

2.1 Growth and purification of bR

A standard procedure for growing bR was published in 1974 by Oesterhelt and Stoeckenius[1]. Our procedure has been adapted to a volume of 21 liters instead that the original 3 liters described in the literature. The advantages of using the Stain S9-P versus the WT are greater yield[2] and the absence of carotenoids; which allows to skip the sucrose gradient treatment.

The full protocol for the purification procedure is reported in ref [3].

After purification, spectra are taken to establish whether the protein is spectroscopically pure.

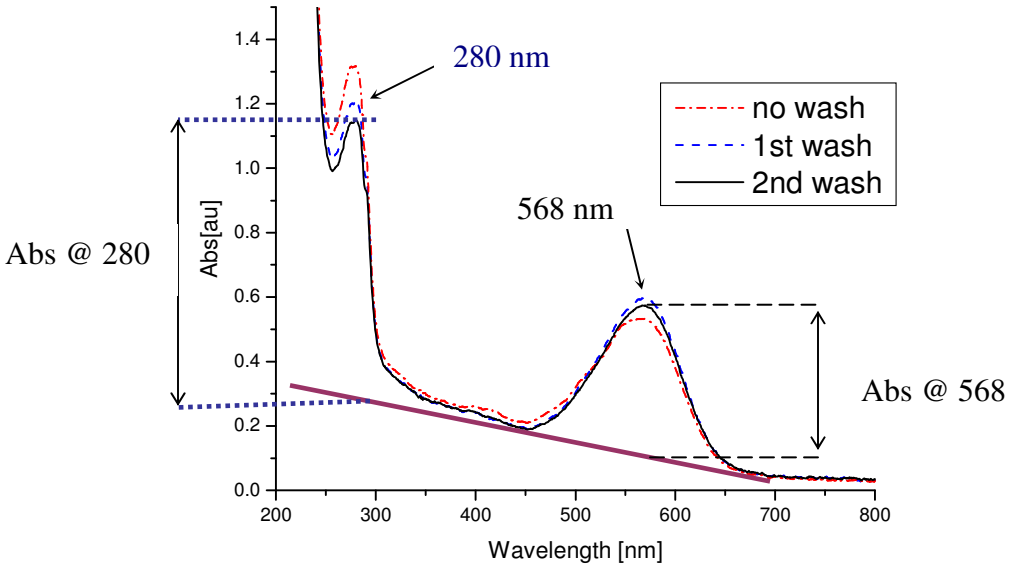

Fig. 2.1: Linear absorption spectra of bR after two consecutive washes with deionized water following by centrifugation.

The purity is determined as shown in fig. 2.1, and the intensity of the absorption at 280 nm is divided by that at 568 nm. The value should be smaller than 1.8 to ensure that no other proteins or impurities are present in the sample.

2.2 Imaging bR patches using bright and dark field microscopy

A schematic of the basic arrangement for bright and dark field imaging is illustrated in fig. 2.2. While a regular bright field microscope collects the light transmitted trough the sample, the dark field arrangements allow only the light that is scattered by the sample to be collected, while blocking the transmitted light. Dark field has found several applications in the biomedical field, since it is complementary to the bright field in revealing very fine details in cells and in tissue specimens. In our study, dark field imaging was able to provide a better understanding of the nanoparticles arrangement on the surface of bR patches, a task that would not be possible by regular bright field

imaging. In our lab, the two arrangements are obtained using the same microscope: an Inverted Olympus IX70 Microscope.

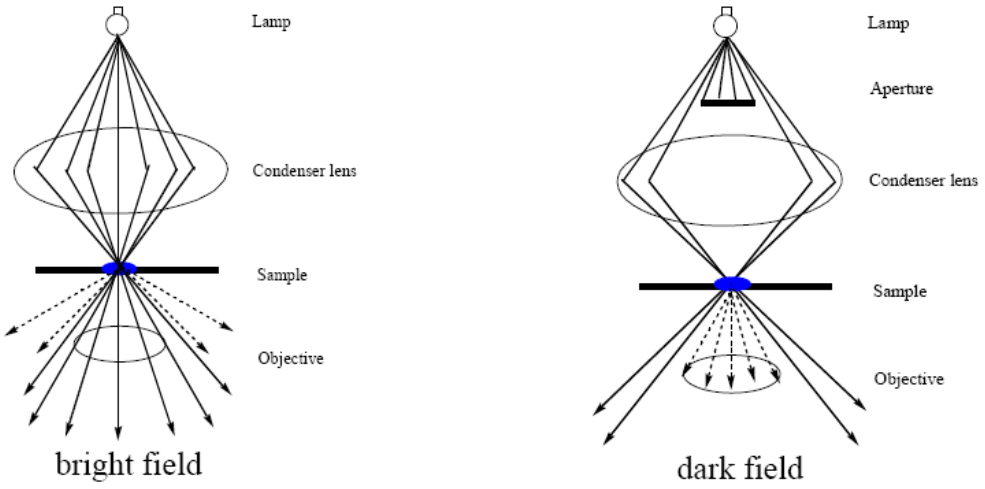

Fig. 2.2: Bright and Dark field schemes. From ref [4]

Bright field images are taken when there is enough contrast in the subject matter, in this case, the tungsten lamp is focused by a bright field condenser onto the sample, the transmitted light from the sample is then focused into a camera (Olympus) through an objective. For dark field imagining, a different condenser is used, one with a higher numerical aperture than the objective.

In our lab, dark field pictures of bR were taken using a U-DCW dark field condenser with a large numerical aperture (0.9-1.2). A 100x / 1.35 oil Iris objective (UPLANAPO) collects the light scatted from the sample.

Below are pictures of bR patches in water under bright and dark field microscope.

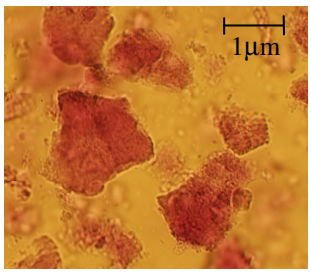

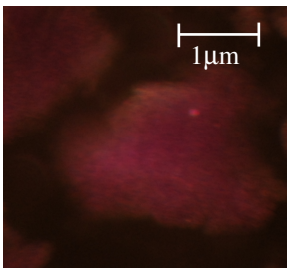

Fig. 2.3: Bright (left) and dark (right) field images of bR patches in water solution, under magnification 100X

2.3 Gold nanoparticles and nanoshells preparation:

Materials

All the glassware used for the nanoparticles preparation is cleaned by aqua regia (3 /1 V/V HCl and HNO_3 conc.) rinsed with deionized water (18 MΩ resistance) and dried in oven at 100° C.

All the reagents are used as purchased by Sigma Aldrich.

2.3.1 Gold nanosphere

Gold nanospheres citrate capped are synthesized by reduction of a Gold (III) salt ($HAuCl_4$) by sodium citrate. The citrate; according to Turkevich[5] acts both as a reducing agent and capping material as the nanoparticles are forming in solution. Different nanosphere sizes are obtained using Frens method[6]; simply by changing the ratio between the Gold (III) versus the reducing agent concentration, in this case citrate. Table (2.1) reports the relative concentration of the reagents use in the synthesis and the size obtained.

Table 2.1: Reagents used for the preparation of Au NPs of various sizes and relative surface plasmon band absorption maxima.

Gold (III) salt Vol/ conc.	**Sodium citrate solution Vol/ conc.**	**Nanosphere size/nm**	**λ_{max} abs./ nm**
50mL / 0.25 mM	350 μL / 1% w/v	30	525
50ml / 0.25mM	330 μL / 1% w/v	40	530
50ml / 0.25mM	230 μL / 1% w/v	60	540
50ml / 0.25mM	210 μL / 1% w/v	80	545

The Gold (III) salt solution is heated up until reaching boiling; a reflux column is placed on the flask, as shown in fig. 2.4. After reaching boiling point, the solution is vigorously stirred before adding the citrate solution. Immediately after adding citrate, the solution goes from yellow to colorless. After about one minute, a grayish colors appears, changing to blue and finally to a brilliant red within a period of few minutes.

The absorption spectra for the different sizes obtained are taken by Ocean Optic diode array. The plasmon band experiences a red shift as the nanoparticles size increases

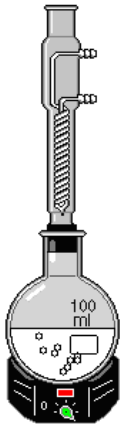

Fig. 2.4: Apparatus for the synthesis of Au NPs

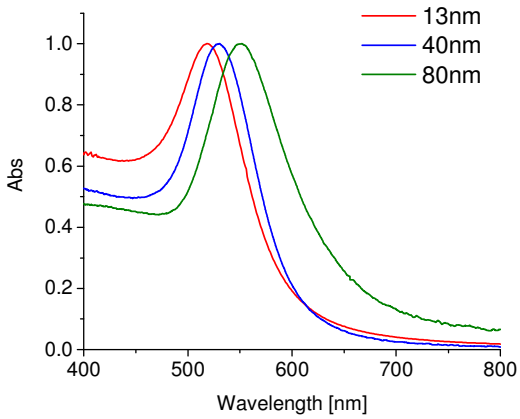

Fig. 2.5: Extinction spectra of Au nanospheres of different sizes in water.

The TEM images for the nanoparticles extinction spectra are reported below:

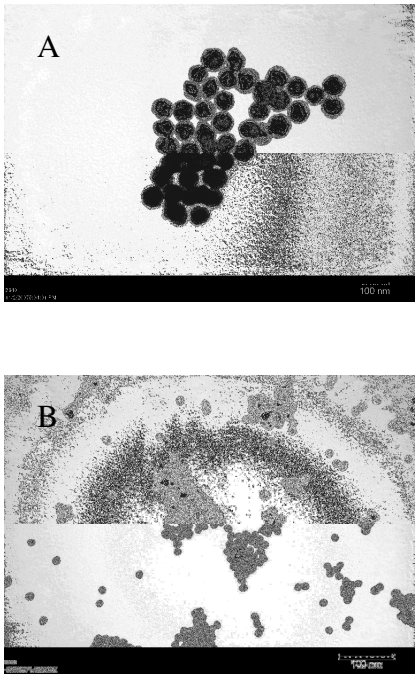

Fig 2.6: TEM image of (A) 80 nm Au nanosphere sample (B) 13 nm Au nanosphere sample

2.3.2 Synthesis of Gold Nanorods (Au NRs) by seed-mediated growth method.

Gold NRs have the intrinsic advantage of having a highly tunable surface plasmon band. The synthesis of gold nanorods (NRs) with different aspect ratios is done by following the procedure published by Murphy[7] and Nikoobakht[8]. The synthesis consists of 2 steps: the first, involving "seed" preparation, and a second, where the seeds are grown in solution containing rod-like micellar templates and gold salt. Very important is the presence of additive like $AgNO_3$ that are critical to the rod formation. The Nanorod aspect ratio is controlled simply by changing the ratio of the seed to gold salt[7] or the amount of Ag^+ present[8].

A complete description of the procedure is reported in ref. [4].

The NRs synthesized by this procedure are stabilized by a bilayer of cationic surfactant molecule[9], which is extremely stable and difficult to remove[10]. The structure of the surfactant molecules, hexadecyltrimethylammoniumbromide (CTAB) and benzyldimethylammoniumchloride hydrate (BDAC) used are reported below:

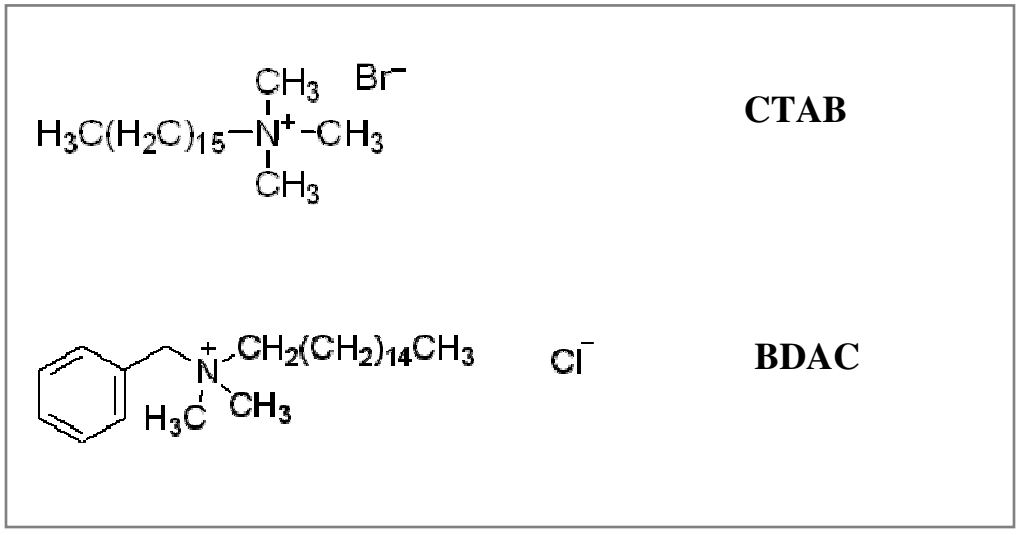

Fig 2.7: Chemical structures of CTAB and BDAC surfactants used in the Au NRs synthesis

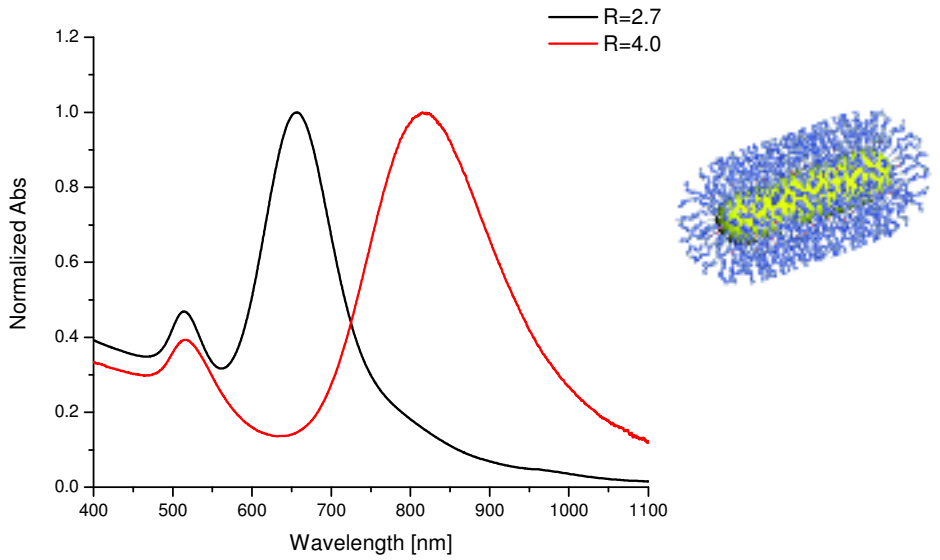

Fig. 2.8: Linear absorption spectrum of Au NRs in water with different aspect ratios *R* obtained by varying the amount of Ag^{+}. On the right, an illustration of NRs capped by cationic surfactants.

The presence of high concentrations of surfactant in the NRs solution represents a problem. When the NRs solution is added to the bR, the free CTAB and BDAC in the solution cause the protein to denature[11, 12]. It is important to remove the excess of surfactant by centrifugation. The NRs sample is centrifuged at 13,000 rpm for 10 minutes, the supernatant is carefully removed and deionized water is added afterwards. The solution is then spun again for 10 minutes and the supernatant removed one more time. A concentrated solution of Au NRs is obtained at the end, which only contains traces of free surfactants, besides those bound to the NRs surface.

The procedure should not be repeated more than twice, since the NRs will aggregate.

2.3.3 Synthesis of Gold Nanocages via galvanic replacement reaction.

The other approach used to tune the surface resonance plasmon of colloidal particles is to empty their core to form hallow structure[13]. Such particles are known as nanoshells (or coreshells) and they consist of concentric spheres with a dielectric material (silica or gold sulfide typically) surrounded by a thin layer of gold. The dimensions of the core along with thickness of the Au layer determine the surface plasmon position. Nanoshell are not easily synthesized and because of this, a different approach is used. One option is represented by Au nanocages, where the empty core is achieved by galvanic substitution from Ag nanocubes used as templates[14]. The first step involves the synthesis of PVP capped silver nanocubes (other shapes are possible as well) and in presence of $HAuCl_4$, the more reactive silver is replaced with gold according to the redox reaction below.

$$3Ag(s) + AuCl_4^-(aq) \rightarrow Au(s) + 3Ag^+(aq) + 4Cl^-(aq)$$

As gold is added to the solution, the replacement of silver goes through stages. After the surface of the cages has been completely covered by an alloy of Ag-Au (nanobox), the replacement continues (simply by adding more Au^{3+}), the silver is selectively reduced, leaving porous walls, until the silver template is completely oxidized. The remaining structure, after all the silver is gone, is gold porous structure called nanocages. The stages leading to the formation of nanocages are shown in fig. 2.9.

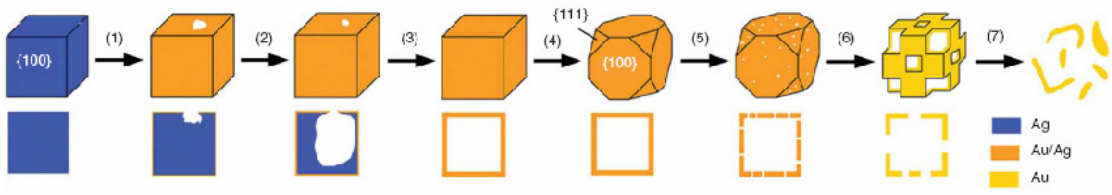

Fig. 2.9: Schematic evolution of Ag nanocubes after addition of increasing volumes of $HAuCl_4$. The de-alloying process starts on stage 4 and it continues until Au nanocages are formed Ref.[15].

As the de-alloying process takes place, a red shift on the SPR peak takes place all the way to the NIR[16].

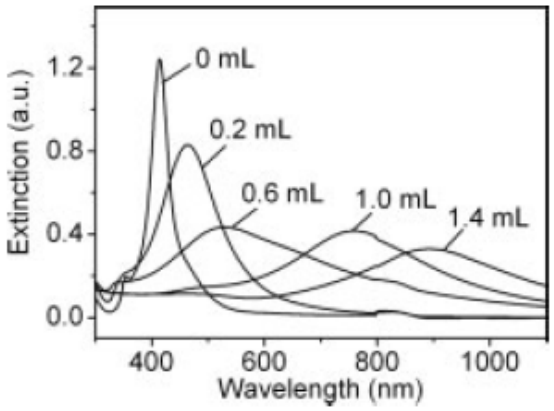

Fig 2.10: Extinction spectra for solution of Ag nanocubes after addition of different volume of $HAuCl_4$. A red shift of the surface plasmon takes place all the way to the NIR. Ref.[14]

The synthesis of such nanocages is found to be relatively easy and reproducible. As it has been reported, these empty structures are quite delicate, they melt and damage easily upon absorption of light[14]. The capping material represents the other disadvantage, in this case, represented by a bulky polymer. The ideal case would be having small charged molecules to facilitate the adsorption, and allowing at the same time, the nanostructures to get as close as possible to the bR.

Below is a spectrum of nanocages with different plasmon band absorption. Nanoshell type structures with sharp corners, like in the case of nanocages, are expected to have large plasmon field enhancements, on the same order of magnitude as Au NRs , although no calculation have been published to the best of our knowledge.

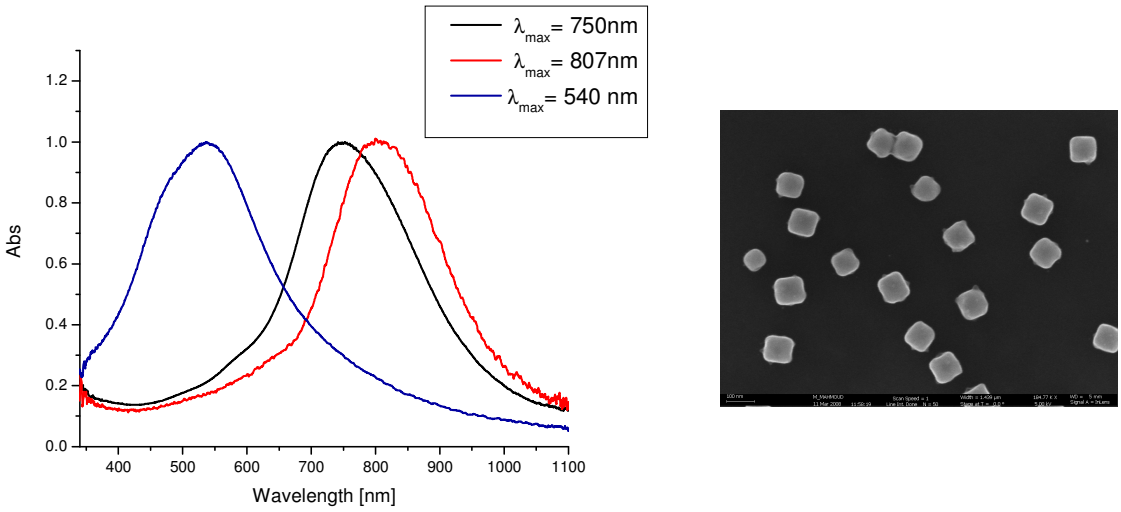

Fig 2.11: Linear absorption spectra of Au nanocages obtained by adding different volume of $HAuCl_4$ to silver nanocubes about 80 nm in size. A SEM picture of the starting Ag nanocubes PVP capped is shown on the right.

2.4 Introduction of Au NPs on the surface of bacteria cells.

Nanoparticles need to be place in close proximity of the purple membrane. In order to do so, different approaches were attempted: the nanoparticles were added at different stages of the cell growth and after the purple membrane purification.

2.4.1 Biosynthesis of nanoparticles by bacteria cell.

It has been reported in literature that several microorganisms like fungi[17], bacteria[18] and even human cells[19] are able to synthesized nanoparticles when placed in contact with the salt of a noble metal (Au or Ag for instance).

An attempt was made to grow the bacteria in presence of $HAuCl_4$ salt, but the presence of sodium citrate in the growth medium produces nanoparticles that aggregate almost immediately, due to the high sodium chloride concentration.

Bacteria were then grown under regular conditions and centrifuged at 8,000 rpm for 15 minutes. After removing the supernatant, a solution 4 M of NaCl is added to the bacteria to avoid bursting of the cells. The procedure is repeated several times to remove and eliminate chemicals present in the growth medium that might contribute to reduce the gold salt. $HAuCl_4$ is then added to the bacteria to a concentration of about 10^{-3} M. The bacteria are left in presence of Au^{3+} for 24 hrs in a dark environment at room temperature. Absorption spectra taken before and after addition of the gold salt indicate the presence of nanoparticles (fig. 2.12).

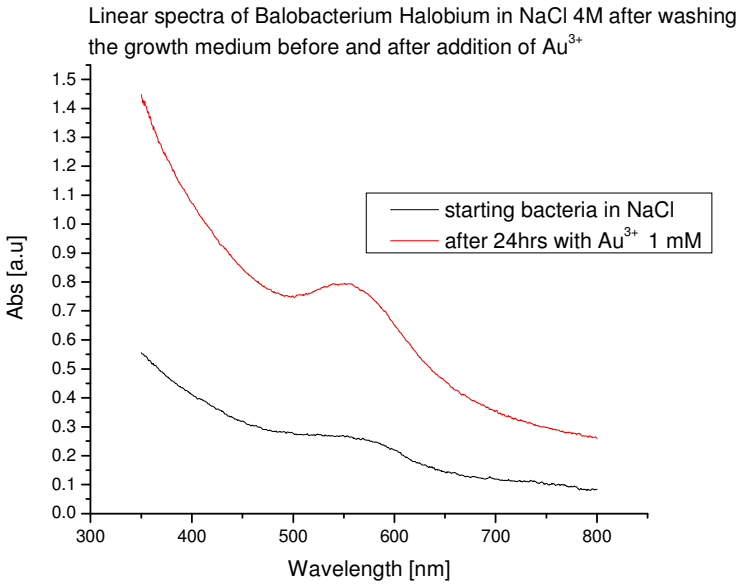

Fig. 2.12: Absorption spectra of the washed bacteria solution in NaCl 4 M before and after addition of HAuCl4 in concentration 1 mM. Increase in the absorption band around 540 nm indicated the presence of Au colloids

TEM images of the bacteria are taken afterwards, showing various size nanoparticles along with the bacteria, made visible because of gold salt staining.

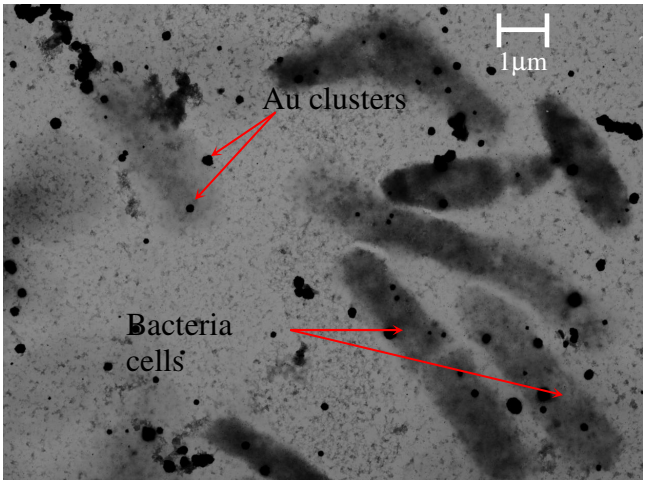

Fig. 2.13: TEM image of the bacteria cells (S9-P strain) after 24 hrs exposure to $HAuCl_4$

The images obtained by TEM revealed Au clusters present in the sample, it was not possible to establish whether any of them were inside the bacteria or only on the outside. The bacteria and the nanoparticles went through the standard purification process to extract the purple membrane from the cells, but after such process, there was no spectroscopic trace of nanoparticles remaining anymore.

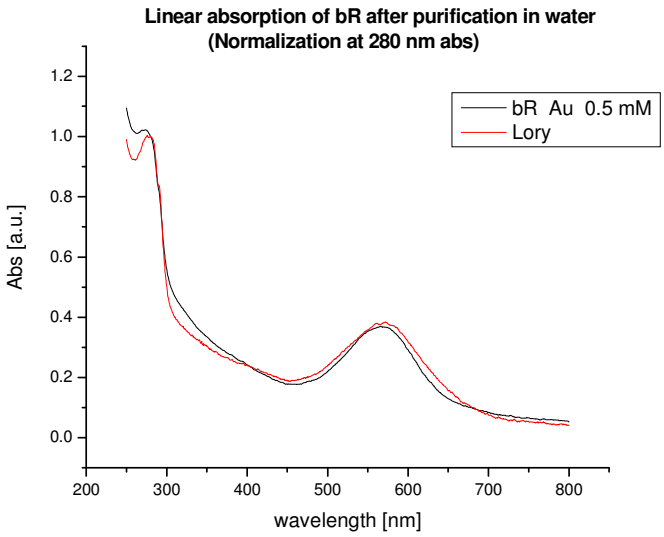

Fig. 2.14: Absorption spectra of the bR obtained after exposure to $HAuCl_4$ compared to regular bR.

The absorption spectrum does not show the presence of nanoparticles; the spectra of a bR sample already present in our lab, overlaps with the gold exposed sample. As a confirmation, dark field microscope of the obtained bR patches did no show any scattering from nanoparticles. No TEM images were taken.

2.4.2 Biosynthesis of nanoparticles by the purple membrane

The purification process involves dialysis, followed by centrifugations and washes with deionized water, in order to isolate the purple membrane from the rest of the bacteria cell.

It is very then difficult for the nanoparticles to "survive" through such a procedure, and remain attached to the bacteria surface.

From this came the idea to expose the already purified PM to the gold salt and allow for nanoparticles to form. Solutions of bR in deionized water were prepared in glass vials and various concentration of $HAuCl_4$ was added. A picture showing the samples 1 hour after from pouring the gold salt is presented below and the evolution of their absorption spectra is shown in fig. 2.12. Auric acid causes the RSB to detach from the protein. The absorption band of the RSB slowly decreases as time goes on, and after about 1.5 hrs, a new band at 415 nm appears, likely due to the free retinal produced. The bleaching of the PM is accompanied by precipitation of the protein as shown in fig.2.15 on sample #4. Dark field images of the PM treated with $HauCl_4$ revealed the presence of a large population of nanoparticles and TEM images showed Au nanoparticles with very different sizes.

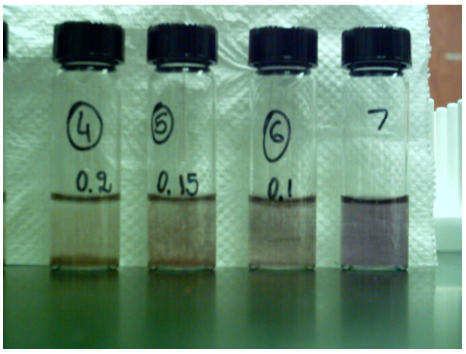

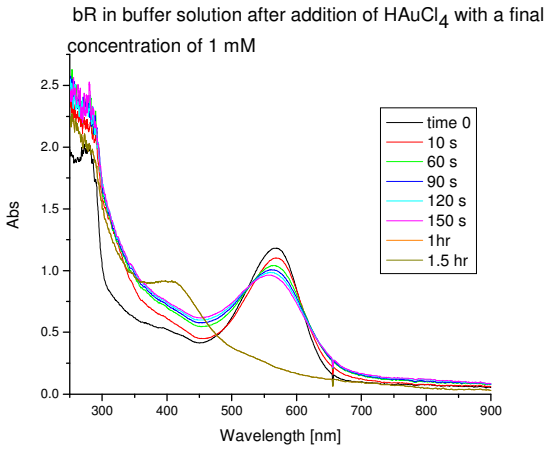

Fig 2.15: From left to right. BR sample in deionized water after addition of $HAuCl_4$ in concentration 0.2, 0.15 and 0.1 mM. Sample number 7 shows the color of a bR solution in water.

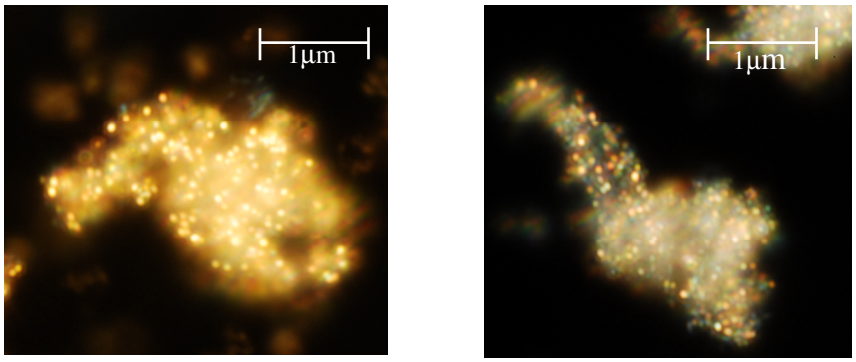

Fig 2.16: Dark field microscope images showing the scattering of nanoparticles on bR patches after adding $HAuCl_4$ 1 mM.

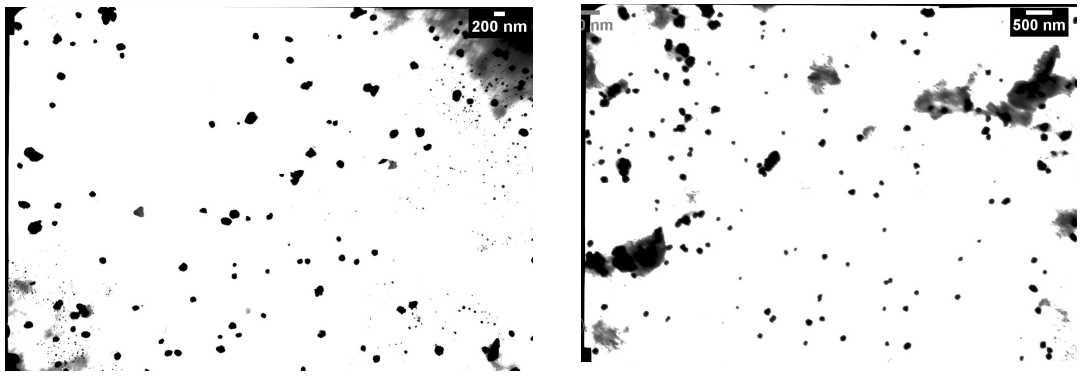

A B

Fig. 2.17: TEM images of bR after treatment with $HAuCl_4$ A) 1 mM B) 2 mM for 24 hrs.

UV-Vis spectrum does not provide detailed information on the protein part of bR, the spectrum on fig. 2.15 in fact, does not show clearly what happens at the protein level after addition of the gold salt. FT-IR spectra of regular bR patches compared to those of the bR exposed to $HAuCl_4$ tell us that no major changes at the protein level take place. The amide I and amide II peaks at 1543 cm^{-1} and 1650 cm^{-1} are not affected, nor are the other bands.

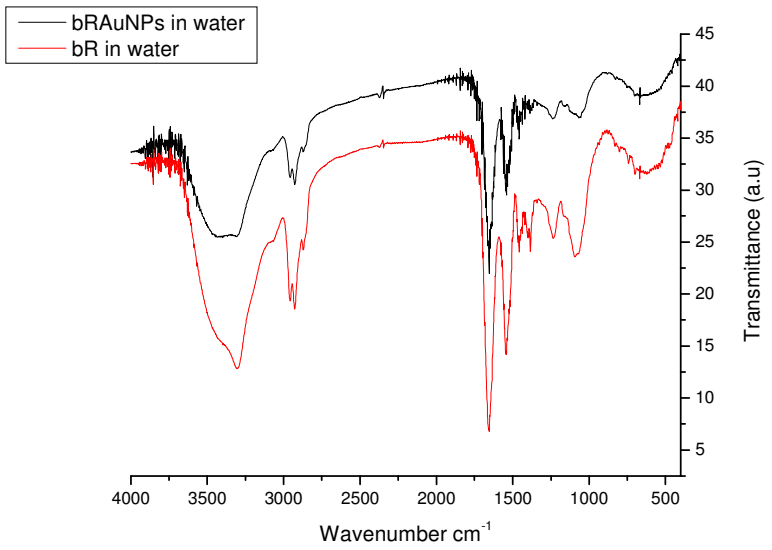

Fig. 2.18: FT-IR spectra of bR patches (red) and bR patched after NPs formation (black).

Even though nanoparticles were successfully formed on the surface of bR patches, partial to complete loss of the chromophore takes place depending upon the concentration of the $HAuCl_4$ added, makes this approach not applicable.

2.5 Direct addition of previously synthesized Au nanoparticles to the bR

Another option is constituted by addition of previously synthesized nanoparticles to the purified bR patches. Citrate capped, 13 nm in size Au nanospheres were used first. Few drops of a concentrate solution of the nanosphere are added to a bR solution in a phosphate buffer at pH=7 100 mM. After mixing the solution for few seconds dark field images were taken; and surprisingly the nanoparticles spontaneously adsorbed on the surface of the patches.

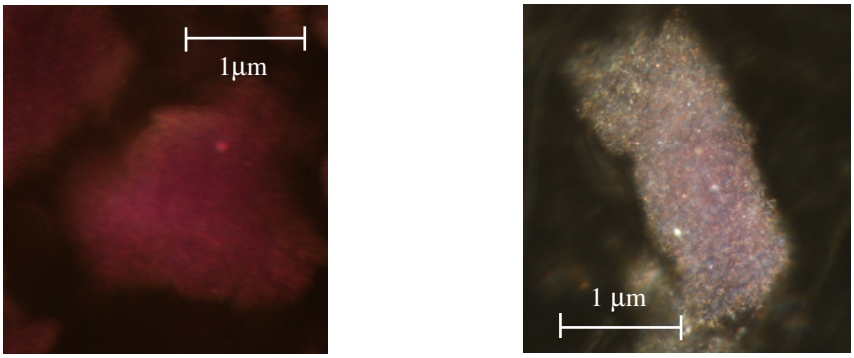

Fig. 2.19: Dark field microscope pictures of bR patch (left) and bR patch with 13 nm Au NPs (100X magnification).

As fig. 2.17B shows, the surrounding areas around the bR patch does not contain nanoparticles that are instead concentrated on the surface of the patch. It is still possible to see the purple color underneath the bright light scatter from the nanoparticles.

The nature of the adsorption is believed to be electrostatic. The protein is known to have a negative charge[20, 21] around pH 7 on both the cytolasmic and to extracellular side. The negative charges attract protons from the solution causing the pH to be lower in the vicinity of the surface membrane than in the bulk, it also attracts positively charged ions that might be present as well. The Au NPS are instead capped with citrate ions that are negatively charged. It is possible that the positive charges attract by the bR surface attract the negatively charged citrate ions, drawing the nanoparticles close to the surface. Fig. 2.20 is a tentative to illustrate what described above.

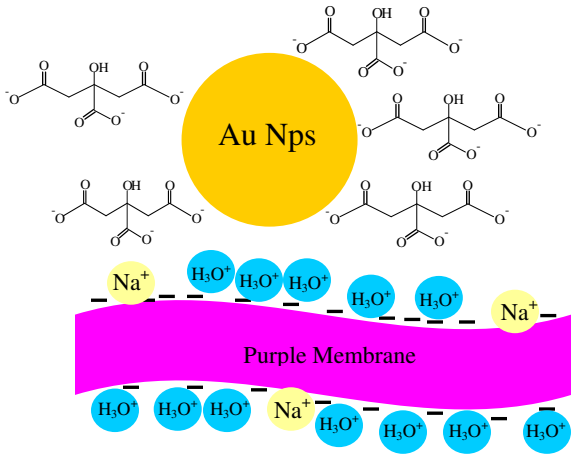

Fig: 2.20: Schematic of the charge distribution on the purple membrane surface and the possible interaction between the positive charges and the nanoparticles capping material (not in scale).

Discussion:

Various attempts were made to physically put nanoparticles in close vicinity the surface of bR. Initially $HAuCl_4$ was added to the bacteria, NPs were formed, but they were completely removed after purification of the cells. The second attempt was the addition of gold salt directly to the purified bR patches, where again, NPs formed, but at the same time the retinal chromophore was bleached by the presence of Au^{3+}.

The most successful attempt was the addition of previously synthesized Au NPs to bR patches. Interactions of electrostatic nature are believed to be at the origin of the NPs adsorption on bR patches.

Fig. 2.21 provides a comparison for bR patches after undergoing the different treatments.

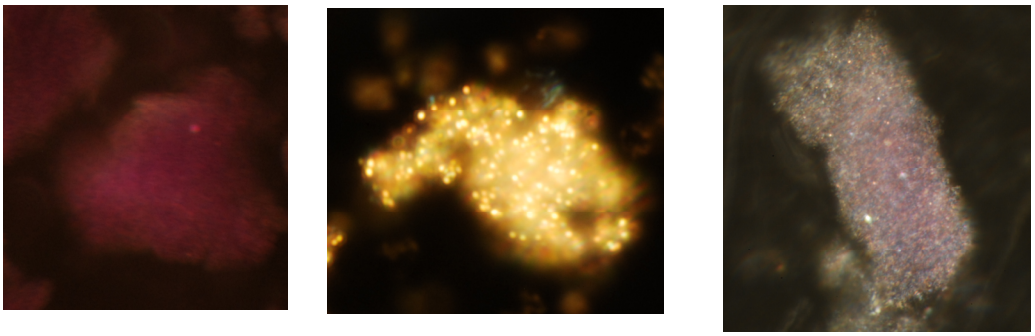

Fig. 2.21: Dark field images of bR pure bR patches (left), after treatment with $HAuCl_4$ (center) and after mixing with 13nm Au NPs citrate capped (right)

REFERENCES:

[1] Oesterhelt, D., Stoeckenius, W., Methods Enzymol. 31, 667 (1974)

[2] Lorber, B., DeLucas, L. J. 261, 14 (1990)

[3] Heyes, D.C., *Effect of pH, cations and lipids on the structure, stability and function of bacteriorhodopsin*. 2002, Georgia Institute of technology: Atlanta.

[4] Xiaohua, H., *Gold Nanoparticles used in cancer cell diagnostics, selective photothermal therapy and catalysis of NADH oxidation reaction*, in *Chemistry and Biochemistry*. 2006, Georgia Institute of Technology: Atlanta.

[5] Turkevich, J., Stevenson, C. P., Hiller, J.,. Discus. Faraday. Soc. 11, 55 (1951)

[6] Frens, G., Nature. 241, 20 (1973)

7. Jana, R.N.G., L.; Murphy, J. C., J. Phys.Chem. B. 105, 4065 (2001)

[8] Nikoobakht, B., El-sayed, A. M., Chem. Mater. 15, 1957 (2003)

[9] Nikoobakht, B., El-sayed, A. M., Langmuir. 17, 6368 (2001)

[10] Liao, H., Hafner, J. H., Chem. Mater. 17, 4636 (2005)

[11] Oesterhelt, D., Stoeckenius, W., Nature. 233, 149 (1971)

[12] Tan, E., Birge, R. R., Biophys. J. 70, 2385 (1996)

[13] West, J.L., Halas, N., Ann. Rev. Biomed. Eng. 5, 285 (2003)

[14] Chen, J., Wiley, B., Li, Z.-Y., Campbell, D., Saeki, F., Cang, H., Au, L., Lee, J., Li, X., Xia, Y., Adv. Mater. 17, 2255 (2005)

[15] Skrabalak, S.E., Au, L., Li, X., Xia, Y., Nature Protocols. 2,. 2182 (2007)

[16] Sun, Y., Xia, Y., Nano Lett. 3, 1569 (2003)

[17] Mukherjee, P., Senapati, S., Mandal, D., Ahmad, A., Khan, M. I., Kumar, R., Sastry, M., Chem. Bio. Chem. 5, 461 (2002)

[18] Gericke, M., Pinches, A., Hydromet. 83, 132 (2006)

[19] Anshup, J., Venkataraman, J., S., Subramaniam, C., Kumar, R. R., Priya, S., Kumar, T. R. S., Omkumar, R. V., John, A., Pradeep, T., Langmuir. 21, 11562 (2005)

[20] Alexiev, U., Marti, T., Heyn, M., Khorana, H. G., Sherrer, P., Biochemisty. **33**, 298 (1994)

[21] Jonas, R., Koutalos, Y., Ebrey, T. G., Photochem. PhotoBiol. 52, 1163 (1990)

CHAPTER III

EFFECT OF THE PLASMONIC FIELD FROM GOLD NANOPARTICLES ON BACTERIORHODOPSIN FIRST LIGHT-INDUCED EVENT.

Abstract:

The decay rate of intermediates I_{460} and J_{625} formed upon excitation of the retinal chromophore by visible light are measured in presence of Au Nanoparticles by fs pump-probe spectroscopy.

Lifetimes are measured for different nanoparticle concentrations. It was found that the decay lifetime of intermediate I_{460} increases with the concentration of nanoparticles, while the formation of the intermediate J_{625} is not affected.

Introduction

Bacteriorhodopsin is the representative of a series of retinal proteins including visual pigments having in common the ability to undergo isomerization along one of the double bonds. The process is extremely fast; takeing place in the picosecond time scale, which many scientists believe to be the key to high efficiency of these systems[1].

For bR the energy stored in the isomerization is used to transport protons across the bacteria membrane that ultimately stimulates the formation of ATP.

The first light-induced event in bR involves the photoexcitation of Retinal Schiff Base followed by isomerization from all- *trans* to 13- *cis*. The isomerization is highly selective in the protein environment, taking place on only one of the 5 possible retinal

double bonds[2]. Such selectivity and high quantum yield that is common to all retinal-based G-protein coupled receptors have fascinated scientists since their discovery, and until now there is no agreement on its molecular nature. The first intermediate that can be isolated at low temperature, indicated on (3.1) as K_{610}, has a 13-*cis* retinal configuration determined via Raman spectroscopy[3].

Although it is known that the protein undergoes structural rearrangements within 500 fs from its photoexcitation[4, 5], mainly involving conformational changes [6], its role has not been fully understood yet, but it is widely accepted as fundamental in determining the chromophore dynamics upon excitation[7-9]. The sequence of events following the RSB photo-excitation is illustrated in 3.1, where the chromophore evolves from being in the Frank-Condon region, indicated as bR^*, to form intermediate I_{460}, then J_{625} and ultimately K_{610}.

$$\underset{\textit{all-trans}}{bR} \xrightarrow{h\nu} \underset{\textit{all-trans}}{bR^*} \longrightarrow \underset{\textit{all-trans}}{I_{460}} \xrightarrow{500fs} \underset{?}{J_{625}} \xrightarrow{3ps} \underset{\textit{13-cis}}{K_{610}} \qquad (3.1)$$

Both I_{460} and J_{625} are short lived and their structures are more difficult to determine. The structure of the RBS in I_{460} is not completely known yet[10], even though it has been determined that no isomerization has taken place up to this point, implying that the retinal is still in the *all-trans* configuration[11, 12].

At what stage the isomerization takes place is still a matter of debate. Each of the two models proposed in the literature (*two-state* and the *three-state* models discussed on chapter I) place the isomerization at different stages. The two possibilities are either, the system goes from I_{460} to J_{625} (*two-state* model) or from J_{625} to K_{610} (*three-state* model).

The excitation of the RSB to a higher electronic energy level is accompanied by a large charge redistribution; where the positive charge over the nitrogen atom, migrates toward the β ionone ring[13].

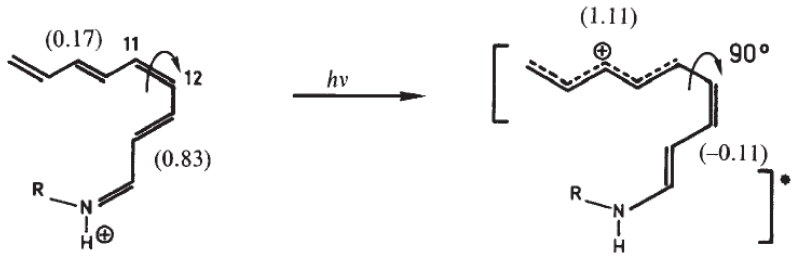

Fig. 3.1: Model molecule for a protonated retinal base Schiff illustrating the charge migration upon photo-excitation according to theoretical calculation. Ref [13]

The dipole change ($\Delta\mu$), upon excitation, has been measured for a free protonated Schiff base, and was found to be about 12 Debye[14]. For bR, the dipole change was found to be very similar, 11 Debye[15, 16]. Such a large $\Delta\mu$ is believed to generate a short lived electrical signal that would be responsible for the protein reaction, not only in bR but in other retinal based protein systems, in particular in visual pigments like Rhodopsin[7]. Proof that the actual dipole change $\Delta\mu$, rather than the retinal conformational change triggers the protein response, comes from a series of studies where artificial chromophores having a locked C_{13}=C_{14} double bond were used and no isomerization could take place. For thse system protein response was registered via atomic force sensing[6, 17]. Moreover when the RSB is replaced with synthetic chromophores having a dipole change substantially reduced, the photocycle is interrupted[9].
The J_{625} to K_{610} transition as already discussed in chapter I is interpreted either as a simple vibronic relaxation from a hot *13-cis* retinal[18], or the step at which the isomerization takes place[19, 20], and no common agreement has been reach at this time.

In this chapter we report the use of nanoparticle, in particular Au nanospheres with two different sizes, to observe the impact of the plasmonic field on the bR first light induced event. In particular the decay lifetime of I_{460} and J_{625} is measured via femtosecond (fs) pump-probe spectroscopy for pure bR and bR in presence of 40 and 13 nm Au NPs.

Materials and methods:

Bacteriorhodopsin was grown and purified according to the procedure taken from ref ([21]). The concentrated solution of bR is dissolved in a phosphate buffer solution at pH 7.2 and 100 mM in concentration, to an optical density of about 0.5 at 568 nm in a 0.2 cm quartz cell. All the solutions spectra were taken using an Ocean Optics HR4000-UV-NI both before and after pump probe measurements. To these solutions different volumes of nanoparticles prepared following Frens[22] method (see chapter II) having OD of 1 at the plasmon peak in a 1 cm quartz cell were added as shown in table 3.1. The buffer is used to insure constant pH as the nanoparticles are added to the bR solution.

Tab 3.1: Relative volumes of bR and nanoparticles solution used in preparing the samples for the pump-probe measurements.

NPs diameter	**NPs solution volume/ μL**	**BR solution volume/ μL**	**Sample Code**
40 nm	50	450	**A**
	100	400	**B**
	150	350	**C**
13 nm	50	450	**D**

Pump-Probe set-up description:

For a more complete description of the set-up ref ([23]) can be consulted. Here we give a short description of it.

In the pump-probe experiment a frequency-doubled Nd: vanadate laser (Coherent Verdi) is used to pump a Ti: sapphire oscillator (80 MHz), that provides the seed, that is then amplified by a Clark MXR CPA 1000. This generates laser pulses of about 100 fs in duration (FWHM) with energy of 1 mJ/pulse at 800 nm at 1 KHz repetition rate. The 800

nm beam is sent to an Ultrafast Optical Parameter Amplifier (Light Conversion TOPAS) where the wavelength can be tuned throughout the visible range. The output represents the pump beam, tuned to 560 nm, and is mechanically chopped down to 500 Hz. The diameter of the laser focus spot at the sample was 300 μm, and the laser energy used in our experiment was reduced to about 50 nJ by using neutral density filters. A white-light continuum probe was generated by focusing a small portion of the beam at 800 nm (about 4%) to a 1 mm sapphire plate. The differential transmission signal $S(t)$ was recorded with a pair of silicon photodiodes (Thorlab) and a lock-in amplifier (Stanford Research Systems). The recorded signal $S(t)$ is obtained by the following:

$$S(t) = \Delta A = A_{\lambda,t} - A_{\lambda,0}$$

where ΔA represent the change in the absorbance of the probe light. $A_{\lambda,t}$ is proportional to the intensity of the probe light, after a time delay (t) from the pump pulse, which is considered t=0. $A_{\lambda,0}$ is the absorbance of the probe light at the same wavelength of the probe light without the pump.

Positive value for $S(t)$ implies formation of species that absorb at the specific wavelength selected for the probe. By following the absorbance at different delay times t, it is possible to monitor the evolution of such specie in time, in this specific case, its lifetime.

Results:

Pump probe experiment were conducted to measure the decay lifetime of intermediate I_{490} in pure bR and bR samples containing nanoparticles. The pump beam is set at 560 nm, while the probe beam at 490 nm. The intermediate I_{460} maximum absorption is at

460 nm, such value was not chosen since the probe beam is very weak in such region of the spectrum. The samples are placed on a round shaped quartz cuvette and spun at about 4 Hz to continuously allowing fresh solution to be probed since the repetition rate of the laser (500 Hz) does not allow completion of the photocycle, which takes about 10ms. For each solution a series of 15 data sets were taken and then averaged.

3.1 Effect of Au NPs on I_{460} decay lifetime

The decay lifetime of I_{460} is measured in pure bR and for samples A, B and C. The results are shown below:

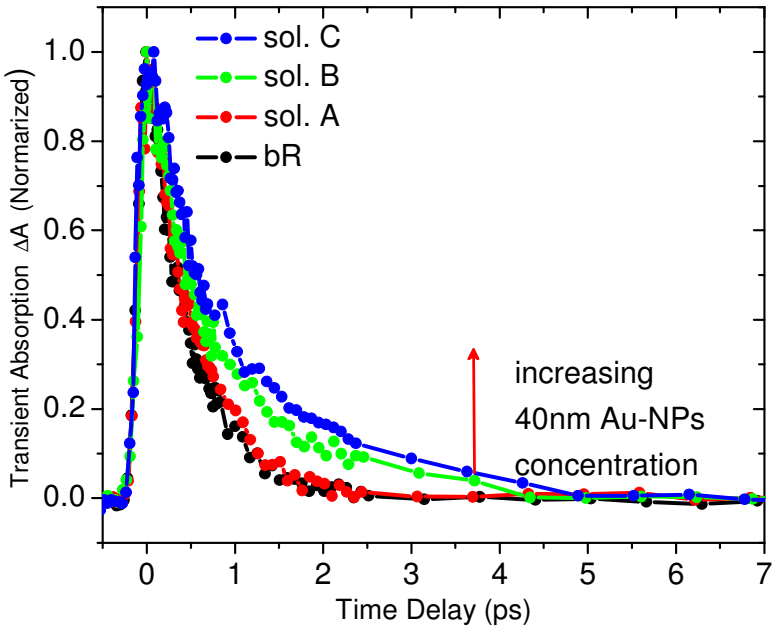

Fig 3.2: Decay lifetime dynamics for I_{460} as increasing concentration of 40 nm NPs are added.

A table containing the values for the lifetime of I_{460} is shown below

Table 3.2: Decay lifetime for intermediate I_{460} in pure bR and bR with different concentrations of Au NPs 40 nm in diameter

Sample	Au-NPs conc./10^{-11} Mol	NPs size/nm	Decay lifetime / fs
Pure bR	-	-	470± 25
A	1.3	40	515± 25
B	2.5	40	720± 35
C	3.8	40	800± 40

For pure bR a decay lifetime of 470 fs is found, in agreement with values reported in the literature [24-29].

Solutions with different size nanoparticles, but similar concentration, are compared. What was found is that smaller size nanoparticles have a smaller overall effect on the lifetime of I_{460} compared to larger nanoparticles.

Table 3.3: Solutions having similar Au NPs concentration but smaller sizes show smaller overall effect on I_{460} decay lifetime

Sample	Au-NPs conc./10^{-11} Mol	NPs size/nm	Decay lifetime / fs
BR	-	-	470± 25
Solution C	3.8	40	800± 40
Solution D	3.7	13	530± 25

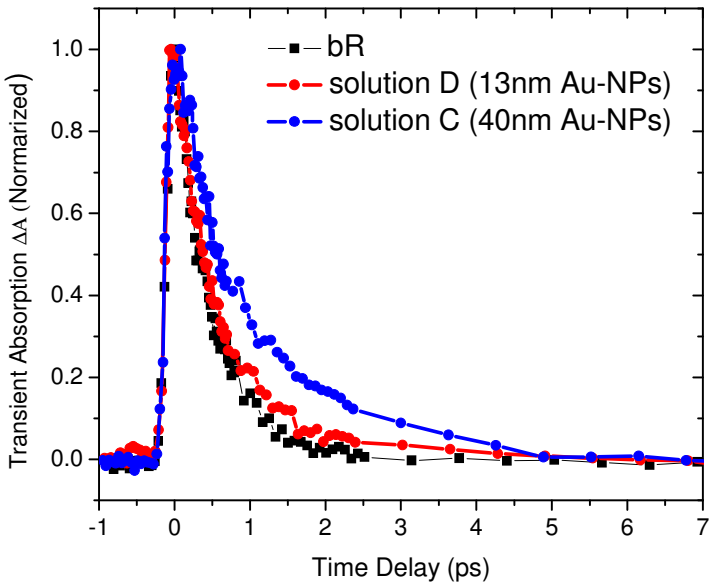

Fig. 3.3: Data showing the NPs size effect on the lifetime of I_{460}.

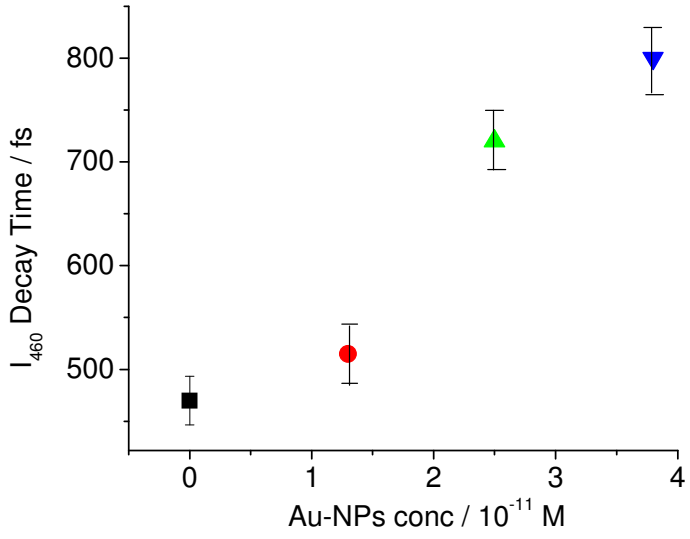

Fig. 3.4: Decay lifetime of I_{460} versus 40 nm Au NPs concentration

The Gold nanoparticles used absorb at 560 nm. It is important to establish whether any of the signal registered at 490 nm is due to nanoparticles dynamics[30]. The pump-probe experiment is then run with a solution of pure nanoparticles having the same

concentration as solution C, with the highest concentration of 40 nm Au nanospheres. For such solution, the signal amplitude at 490 nm was less than 2% than the amplitude of solution C with bR on it. This experiment proved that the signal observed is actually due to the intermediate I_{460} and not the nanoparticles.

Electron dynamics in Gold Nanoparticles and electron-phonon coupling

The temporal and spatial evolution of electrons heated by ultrafast laser pulses are mapped by the two-temperature model[31] (TTM). The model describes the temporal profile coupling between the hot surface metal electrons of nanoparticles upon excitation and its lattice.

Excitation of the plasmon electrons in metal nanoparticles, where the electron density is high, causes strong electron-electron interactions Such interactions are strong enough to heat up the surface metal electrons increasing their temperature. The bulk electron do not get affected when ultrashort laser pulses are used, while the surface electrons heat up very quickly (in less than a picosecond) to thousands of degree in temperature due to their very small heat capacity[32]. The heat is ultimately transferred to the bulk after going though electron-phonon (e-p) coupling, involving the hot surface metal electrons and the metal lattice, followed by phonon-phonon (p-p) interactions between the metal lattice and the bulk lattice.

The timeframe for all such process to occur is illustrated in fig. 3.4, where the electron-phonon coupling takes place few picosecond (ps) after the pulse excitation, while the phonon-phonon coupling is a relatively longer process on the order of 100 ps.

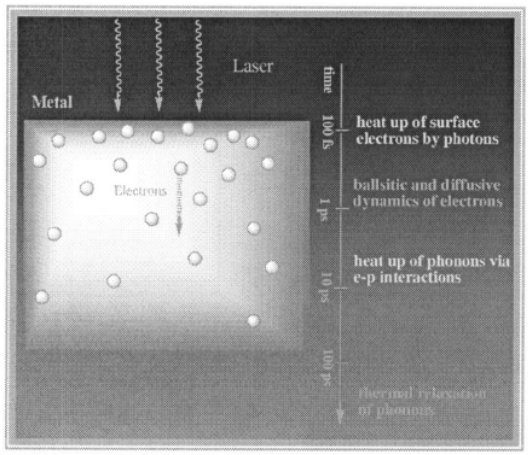

Fig. 3.5: Schematic illustrating the time frame for the e-p, and p-p coupling dynamic for surface metal electrons upon ultrafast pulse absorption. Ref [32]

The electron-phonon coupling can be followed using ultrafast pulses for metal nanoparticles and it is found that the electron-phonon coupling time is a function of the energy used to excite the electrons. It is found in fact that as the pump energy increases and the electrons reach higher temperatures, the electron-phonon coupling lifetimes goes up.

The electron-phonon coupling is followed through pump-probe spectroscopy for 40 nm Au NPs using the same experimental conditions (energies etc.) as the samples.

The data is shown in fig. 3.6. In this case, the bleach recovery of the excited electrons is probed at different delay times. A recovery time of 1.8 ps was found for the pump energy used.

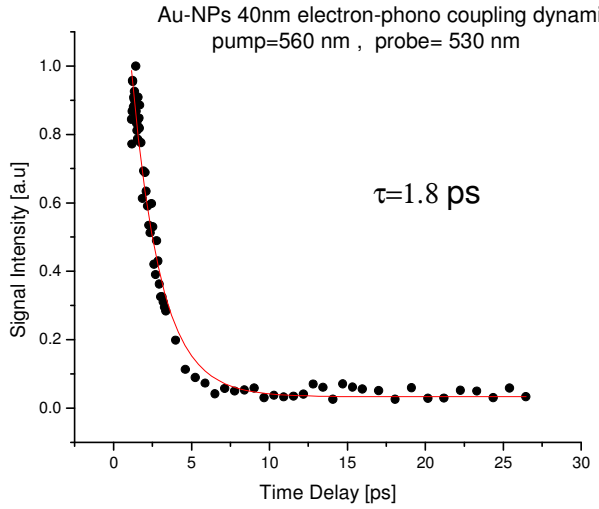

Fig. 3.6: Electron phonon coupling dynamics in 40 nm Au NPs via pump-probe spectroscopy. Pump wavelength at 560 nm (0.1 μJ), probe was at 530 nm. A bleach recovery time of 1.8 ps was measured.

Comparing the dynamics of I_{460} intermediate and that of electron-phonon coupling is shown in fig. 3.7.

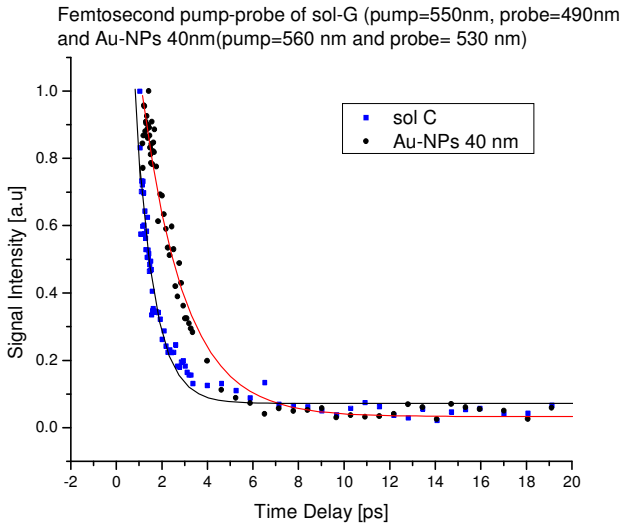

Fig. 3.7: Comparison of e-p coupling dynamics for a concentrated solution of 40 nm Au NPs after pumping at 560 nm and probing at 490 nm (red) with I_{460} decay lifetime in sample C (black).

The e-p coupling happens on a longer timescale than the I_{460} decay lifetime for sample C (the one with the longest lifetime), concluding that the changes taking place at the I_{460} level are not induced by thermal effects. In fact, during I_{460} intermediate lifetime, the e-p process did not have the time to fully take place, and there could not have been heat release at the bulk level. This was an important point that needed to be clarified, and indeed thermal processes are not the cause for the changes observed in bR intermediate under analysis.

3.2 Effect of NPs on J_{625} decay lifetime.

The intermediate formed upon I_{460} decay is J_{625}. This intermediate structure and dynamics has been reported in the literature by several groups[4, 18-20, 27, 33], but disagreement still remains. The conformation of J_{625} is described both as an *all-trans* as well as a *13-cis*[18]. We studied the decay lifetime of J_{625} in pure bR and for the sample C. The pump probe revealed there were no changes in lifetime for this range of NPs concentrations as shown in fig. 3.8:

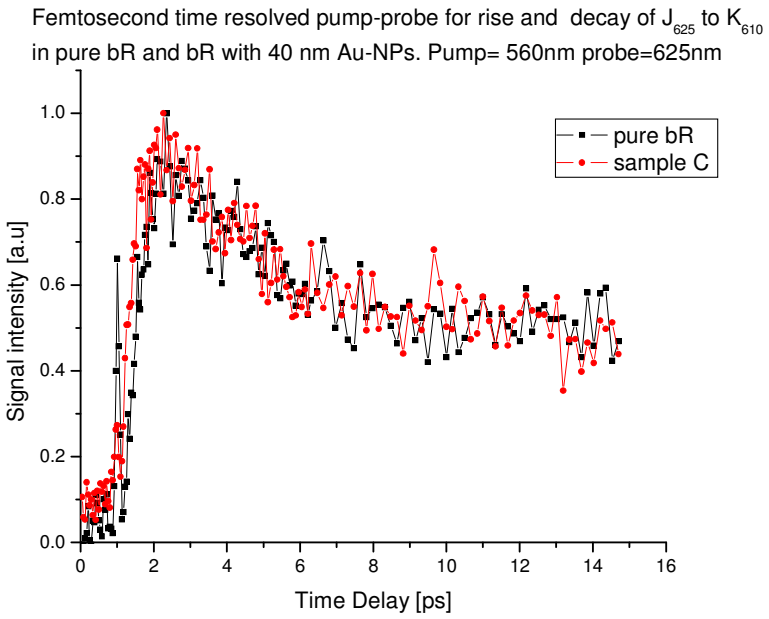

Fig 3.8: Signal decay for intermediate J_{625} measured via pump-probe spectroscopy. For pure bR (black data points) and bR with 40 nm Au NPs (sample C red data points). The pump wavelength was set at 560 nm and the probe at 625 nm. The signal does not go to zero due to the next specie forming, K_{610}, which absorbs at this wavelength as well and has a long lifetime.

The two values obtained are reported below:

Table 3.4: Decay lifetime for intermediate J_{625} in pure bR and sample C

Sample	Au-NPs conc./10^{-11} Mol	NPs size/nm	Decay lifetime / ps
Pure bR	-	-	3.1± 0.2
Solution C	3.8	40	3.4± 0.2

The decay lifetime for J_{625} was found to be 3.1 ps, which is in agreement with value reported in literature[4, 34].

Upon addition of nanoparticles, no significant change in the decay lifetime of the intermediate is observed for the Au NPs concentration used.

Discussion:

The decay dynamic of the intermediate I_{460}, formed upon absorption of green light by bR; was monitored by measuring the transient absorption at 490 nm at different delay times after the pump pulse. When Au NPs are present, the lifetime of I_{460} increases as reported in table 3.2 with a dependence on the Au NPs concentration as shown in Fig. 3.1. The rationale behind this phenomenon can be found analyzing the surface plasmon dynamic during the pump-probe experiment. The nanoparticles surface plasmonic field is formed by the pump pulse at 560 nm and decays in a few femtoseconds, but is then turned on again when the probe irradiates through the sample, providing a plasmonic field at different delay times after excitation. When gold nanoparticles are present, the decay of the intermediate I_{460} is then determined in presence of the plasmon field induced by the monitoring light. Furthermore, as the NPs concentration increases, so is their effect on I_{460} lifetime. The effect is size dependent as well, solution D has similar Au NPs concentration as solution C, but of smaller size (and thus smaller plasmonic field) and clearly shows a smaller effect on the decay lifetime as shown in fig. 3.3. The contribution to the total signal decay from the pure NPs was estimated to be less than 2% for the highest concentration, eliminating the possibility of overlap with the bleach signal from the NPs. The other possibility would be that the change in lifetime is due to photothermal effects from gold nanoparticles; but the phonon-phonon relaxation time in gold nanospheres is on the order of hundreds of picoseconds[35]. This, and the fact that the repetition rate of the laser system at 500 Hz, eliminates the possibility that the observed change in dynamic is a result of thermal effects resulting from the phonon-phonon relaxation of the gold nanoparticles. This suggests that the field generated upon the plasmon excitation is the only cause contributing to the observed changes in excited state I_{460} intermediate lifetime.

In order to understand the origin of the observed effect of the plasmon field on the I_{460} decay time, the dynamic evolution of the excited state of the protonated Schiff base of bR within the protein cavity has to be considered. An aspect where theoretical calculation and experiment agree upon is the large charge redistribution in and around PSB, following the retinal absorption of light in bR[36, 37]. In fact, theoretical prediction for a Schiff base immediately after excitation consists of a system having a neutral amino group and a positively charged polyene chain[38], a result that is supported by other indirect measurements[39, 40]. This charge-unbalanced system should induce large polarization on the protein cavity around the retinal electronic system. In the presence of a plasmonic electric field, present because of the pump and probe light, the retinal electronic system is going to have a slightly perturbed potential energy surface than in the unperturbed system. This undoubtedly could affect the rate of its dynamic within the protein pocket.

As more and more NPs accumulate on bR surface, favoring plasmon coupling with the strong enhancement of the associated electric field, the effect is amplified. The environment created by the protein is known to ensure selectivity of the photoproducts[41] and to ultimately acquire from the PSB the energy necessary for bR proton pump functions. Electronic theory[42, 43] on protein response upon retinal excitation suggests that the early spectroscopic events are effected by the protein environment leaving no doubt for an active role of the protein itself. Experimental data on protein conformational changes though atomic force sensing (AFS) measurements seems to connect the large polarization change occurring at the chromophore site to protein structural changes[44]. It is more accurate to think of the system as PSB-protein rather than as individual components. The plasmonic field thus affects both the protein and the retinal system as a whole.

The plasmonic field can propagate over distances comparable to the nanoparticle size. Thus the nanoparticles do not have to bind to the retinal to affect the rate of its excited

state decay. Furthermore, the observed field effect could result from aggregated nanoparticles, which is known to have much stronger plasmonic field. This might also explain the concentration effect. The size effect can be explained by the dependence of the plasmonic field on the nanoparticle size. Furthermore, different sizes could occupy different site on the protein, causing an overall different effect.

The lifetime of J_{625} is found not to be affected by the presence of NPs and it remains at 3 ps. It should be mentioned, however, the decay of J_{625} to form K_{610} does not involve a charge rearrangement and according to the explanation given for the changes observed in I_{460} it would not be expected for this transformation to be perturbed by the plasmonic field as observed.

REFERENCES:

[1] Kochendoerfer, G., Mathies, R., Isr. J. Chem. 35, 211 (1996).

[2] Gai , F., Hasson, K. C., McDonald, J. C., Anfinrud, P. A., Science. 279, 1186 (1998).

[3] Braiman, M., Mathies, R., Proc Natl. Acad. Sci. USA. 79, 403 (1982).

[4] Diller, R., Maiti, S., Walker, G. C., Cowen, B. R., Pippenger, R., Bogomolni, R. A., Hochstrasser, R. M., Chem. Phys. Lett. 241, 109 (1995)

[5] Schenkl, S., Mourik, F., Zwan. G., Haacke, S., Chergui, M., Science. 309, 917 (2005.)

[6] Rousso, I., Khachatryan, E., Gat, Y., Brodsky, I., Ottolenghi, M., Sheves, M., Lewis, A., Proc. Nat. Acad. Sci. USA. 94, 7937 (1997)

[7] Lewis, A., Proc. Nat. Acad. Sci. USA. 75, 549 (1978)

[8] Ahroni, A. Ottolenghi, M., Sheves, M., Biochemistry. 40, 13310 (2001)

[9] Zadok, U., Khatchatouriants, A., Lewis, A., Ottolenghi, M., Sheves, M., J. Am. Chem. Soc. 124, 11844 (2002)

[10] Song, L., El-Sayed, A. M., J. Am. Chem. Soc. 120, 8889 (1998)

[11] Zhong, Q., Ruhman, S., Ottolenghi, M., J. Am. Chem. Soc. 118, 12828 (1996)

[12] Haacke, S., Vinzani, S., Schenkl, S., Chegui, M., Chem. Phys. Chem. 2, 310 (2001)

[13] Salem, L., Bruckmann, P., Nature, 258**,** 526 (1975)

[14] Mathies, R.A., Stryer, L., Proc. Nat. Acad. Sci. USA. 73, 2169 (1976)

[15] Colonna, A., Groma, Geza, I., Martin, J.-L., Joffre, M.,Vos, M. H. J., Phys. Chem. B. 111, 2707 (2007)

[16] Chen, Z., Sheves, M., Lewis, A., Bouevitch, O., Biophys. J. 67, 1155 (1994)

[17] Losi, A., Michler, I., Gartner, W., Braslavsky, S. E., Photochem. PhotoBiol. 72, 590 (2000)

[18] Doig, S.J., Reid, P. J., Mathies, R. A., J. Phys. Chem. 95, 6372 (1991)

[19] Hasson, K.C., Gau, F., Anfinrud, P. A., Proc. Nat. Acad. Sci. USA. 93, 15124 (1996.)

[20] Kobayashi, T., Saito, T., Ohtani, H., Nature. 414, 531 (2001)

[21] Heyes, D.C., *Effect of pH, cations and lipids on the structure, stability and function of bacteriorhodopsin*. 2002, Georgia Institute of technology: Atlanta.

[22] Frens, G., Nature. 241, 20 (1973)

[23] Logunov, S.L., Volkov, V. V., Braun, M., El-Sayed, M. A., Proc. Nat. Acad. Sci. USA. 98, 8475 (2001)

[24] Nuss, M.C., Zinth, W., Kaiser, W., Koelling, E., Oesterhelt, D., Chem. Phys. Lett. 117, 1 (1985)

[25] Ippen, E.P., Shank, C. V., Lewis, A., Marcus, M. A., Science. 200, 1279 (1978)

[26] Sharkov, A.V., Pakulev, A. V., Chekalin, S. V., Matveets, Yu. A., Biochim. Biophys. Acta. 808, 94 (1985)

[27] Mathies, R.A., Brito Cruz, C. H., Pollard, W. T., Shank, C. V., Science. 240, 777 (1988)

[28] Petrich, J.W., Breton, J., Martin, J. L., Antonetti, A., Chem. Phys. Lett. 137, 369 (1987)

[29] Dexheimer, S.L., Wang, Q., Peteanu, L.A., Pollard, W.T., Mathies, R.A., Shank, C. V., Chem. Phys. Lett. 188, 61 (1992)

[30] Link, S., El-Sayed, A. M., Int. Rev. Phys. Chem. 19, 409 (2000)

[31] Anisomov, L., Kapeliovich, B. L., Perel'man, T. L., Soviet. Phys. JETP. 39, 375 (1975)

[32] Tang, J., J. Chem. Phys. 128, 164702-1 (2008)

[33] Atkinson, G.H., Ujj, L., Zhou, Y., J., Phys. Chem. A. 104, 4130 (2000)

[34] van der Berg, R., Jang, D. J., Bitting, H. C., El-Sayed, M. A., Biophys. J. 58, 135 (1990)

[35] Link, S., El-Sayed A. M., Int. Rev. Phys. Chem. 19, 409 (2000)

[36] Huang, Y.J., Chen, Z., Lewis, A., J. Phys. Chem. 93, 3314 (1989)

[37] Mathies, A.R., Stryer, L., Proc. Natl. Acad. Sci. USA. 73, 2169 (1976)

[38] Salem, L., Bruckmann, P., Nature. 258, 526 (1975)

[39] Schenkl, S., van Mourik, F., van der Zwan, G., Haache, S., Chergui, M., Science. 309, 917 (2005)

[40] Schenkl, S., van Mourik, F., Friedman, N., Sheves, M., Schlesinger, R., Haache, S., Chergui, M., Proc. Natl. Acad. Sci. USA. 103, 4101 (2006)

[41] Song, L., El-Sayed, A. M., Lanyi, J. K., Science. 261(5123), 891 (1993)

[42] Lewis, A., Proc. Natl. Acad. Sci. USA. 75, 549 (1978)

[43] Xu, D., Martin, C., Schulten, K., Biophys. J. 70, 453 (1996)

[44] Rousso, I., Khachatryan, E., Gat, Y., Brodsky, I., Ottolenghi, M., Sheves, M. Lewis, A., Proc. Natl. Acad. Sci. USA. **94**, 7937 (1997)

CHAPTER IV

EFFECT ON THE BACTERIORHODOPSIN PROTON PUMP KINETICS INDUCED BY DIFFERENT SHAPES OF GOLD COLLOIDAL NANOSTRUCTURES PLASMONIC FIELDS

Abstract

The bR proton pump involves the transport of a proton from the cytoplasmic half channel to the extracellular half channel, a process involving large charge movement and structural rearrangement at the protein level. The proton pump can be monitored spectroscopically by following the formation and the decay lifetime of intermediate M_{412}. The effect of a plasmonic field from Au nanostructure of different shapes, placed in the vicinity of bR, was studied as the bR proton pump was activated. While Au nanospheres plasmonic field, does not affect proton pump, intermediate M_{412} decay lifetime decreased in presence of the plasmonic field generated from gold NRs and NCs. The plasmonic field intensity generated by nanostructures is known to be highly shape-dependent, with Au NRs and NCs expected to deliver higher field intensities than Au nanospheres, a theory that is in agreement with our findings. The possibility of thermal effects in the sample was considered and the results discussed.

Introduction

Bacteriorhodopsin (bR) is the only protein found on the purple membrane of *Halobacterium Salinarium*, an halophilic organism. bR is a transmembrane G protein that regulates the energy production (ATP) of the cell[1,2].

The purple color is due to a retinal chromophore covalently attached to the protein structure through an Schiff base to Lys-216 that has broad absorption spectra centered around 570 nm. The chromophore light absorption triggers an *all-trans* to *13-cis* isomerization, that initiate a photocycle, whose function is to transport protons across the membrane. The proton gradient created drives the ATP synthesis, required for its metabolism in low oxygen conditions.

The simplicity of the bR system associated with its chemical stability, has made it a model for biological ion-pump studies[3]. The ability of bR to produce intermediates with distinct absorption spectra has found applications in optical devices, as well as biomolecular electronics[4, 5].

Proton transport and in general, ion transport, is of fundamental importance for cell functions. In biological systems, in fact, the production of ATP is coupled to the electrochemical gradient generated by charges moved across the membrane.

Charge transport across membranes is achieved trough channels and pumps. The main difference between the two is that for pumps the pathway is not completely connected between the cytoplasmic and extracellular side of the membrane, unlike in the case of channels. The switching type of mechanism is implemented in pumps to ensure the vectoriality of the pumping process. Proton pumps can, in fact, transfer protons even against concentration gradients.

Proton pump proteins like bR are membrane proteins which are generally hydrophobic, and the presence of water molecules in such protein is believed to assists the charge

transportation process[6], providing stabilization trough a higher dielectric constant. The extended network of water molecules present in the protein cavity is actively involved in the functionality of the system as a whole[7], their positions are well defined such that they can be identified by X-ray crystallography[8, 9].

The step-by-step mechanism of the proton transport is now understood and it can be roughly summarized by the following sequence of events for pHs>6:

1- Absorption of a photon by the PSB and isomerization from *all-trans* to 13-*cis*
2- Protonation of Asp-85 by the 13-*cis* Schiff Base
3- Proton release to the extracellular side either by Glu-204 or Glu-194 (the releasing group not known at this time)
4- Reprotonation of the Schiff Base by Asp-95
5- Reprotonation of Asp-95 from the cytoplasmic side
6- Proton transfer from the Asp-85 to the proton release group.

For pH< 6, in the wild type bR, proton release to the EC surface occurs, but only at the end of the photocycle[10-12] when Asp-85 regains its low pK_a.

As shown in fig 4.1, the result is the vectorial transport of a proton from the cytoplasmic side to the extracellular side, and in order to transport a single proton from one side to the other, two cycles are necessary.

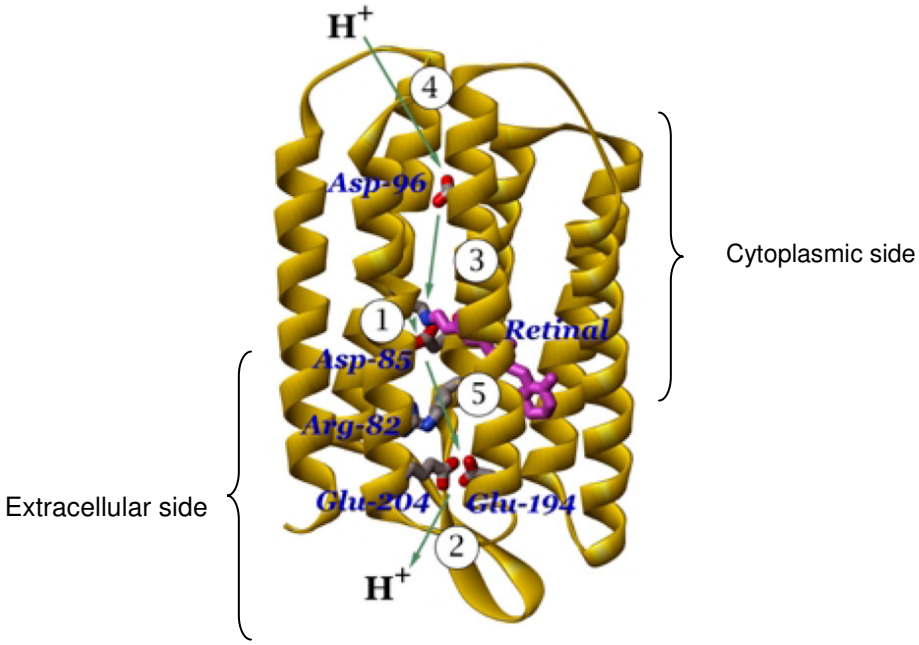

Fig 4.1: Sequence of events concerning the proton pump function of bacteriorhodopsin. Ref [13].

The possibility of modulating the proton pump mechanism in bR has been investigated using the plasmonic field generated by gold nanostructures. Gold rather than silver is used for two reasons: it is biocompatible and its plasmon absorption band position does not interfere with the spectrum of the specie under investigation, the intermediate M_{412}. This blueshifted intermediate forms after the photoinduced isomerization causes a rearrangement of the surrounding water molecule, inducing a decrease in the pK_a of the PBS, which loses a proton to Asp85 located in the extracellular half channel. The deprotonated retinal Base Schiff absorption peak is distinctively blue shifted compared to all the others intermediates making it easy to detect. The following event consists on the reprotonation of the Base Schiff by another residue; Asp96, located in the cytoplasmic half channel, after the pK_a of the cis- Retinal Base Schiff is again increased. This change in accessibility on the retinal Schiff Base is ultimately the driving

force for the proton pump mechanism of bR and is known in literature as the proton switch. The change in local accessibility is caused either by structural arrangements at the chromophore, or protein sites (or both). Besides the proton making its journey across the protein, charged protein residues play major roles in the proton transport, and their behavior could, in principle, be affected by the presence an external field as well. Groma[14] first in 1984 and Nagel[15] later in 1988 have observed, using an external static field, changes in the relative amplitude of M_1 and M_2 without an effect on the overall decay lifetime of M_{412}. They could not quite explain their results considering that 80% of the total charge transported is translocated during the M_{412} reprotonation (M decay)[16-18] The present study poses the question on whether the plasmonic field from colloidal gold nanostructures is able to affect the proton pump dynamic of the protein.

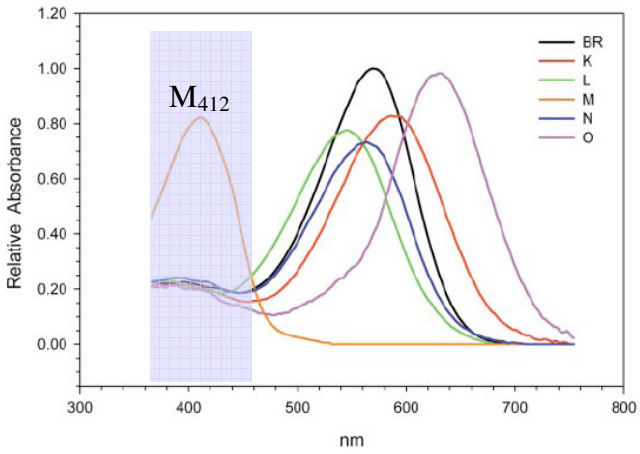

Fig 4.2: Different spectroscopic signatures of bR photocyle intermediates. Highlighted is the absorption spectra of intermediate M_{412} visibly blueshifted compared to all the others [19].

The protonation and deprotonation rate of the Retinal Schiff Base was then investigated in presence of Au nanostructure of different shapes: nanospheres, nanorods and nanocages were studied.

Materials

Bacteriorhodopsin is grown and purified as described in Chapter II. A bR solution is prepared in a phosphate buffer 100 mM at pH=7 unless indicated differently.
Solution of Au nanosphere citrate capped, was synthesized as described in Chapter II and added to the bR solution. The 13 nm nanosphere were synthesized in our lab, while 80 nm nanospheres were purchased from Ted Pella Inc. The resulting solutions are mixed for few seconds to homogenize them.
A solution of bR in phosphate buffer 100 mM is prepared with an OD of about 1.3 in 1 cm path length cuvette. The buffer is chosen to maintain a constant pH upon addition of nanoparticles to the bR solution. The pH and the ionic strength of the solutions need to be under control since the decay dynamic are affected by them.
A fixed volume of 1 ml of bR solution is used and variable volume of nanoparticle solutions are added. The nanoparticles solutions have an OD at the absorption peak equal to 1. Volumes of 100, 200, 300 and 400 μL are used for each nanoparticle size.
Linear absorption spectra of the solutions are taken using 5mm quartz cuvette before and after laser exposure using an Ocean Optic HR4000CG-UV-NIR to control eventual bleaching of the sample.

4.1 Experimental set-up for measuring M_{412} rise and decay dynamics

Flash Photolysis studies were performed using a Nd:YAG laser (1064 nm Spectra-Physic GCR-250) frequency doubled to 532nm with a 10 Hz repetition rate. A mercury-xenon arc lamp (200W) is used in combination with a power supply (PTI model) for continuous probing. Filters are used to limit the probing wavelength range of the lamp to minimize heating effects at the sample, only wavelengths in the range between 380nm

and 450 nm are transmitted. The pump laser and the probing lamp are arranged at a 90-degree angle. The formation (rise) and the disappearing of the M intermediate (decay), are characterized by monitoring the transient absorption maximum at 412 nm, selected by a monochromator (Acton research 300i). The detection system consists of a PMT (Hamamatsu R1477-06), which collects the light intensity after the monochromator and is connected to a 500 MHz oscilloscope (LeCroy 9350A), where the response is digitalized. A voltage of 700 V was applied to the PMT for all measurements. The PMT time response at 412 nm is 25 ns, allowing real-time monitoring of the intermediate created upon excitation at 532 nm. For each measure, an average over 3000 laser shots is taken to improve the signal to noise ratio. The slit width of the monochromator was adjusted so that DC offset for the PMT was 2 Volts with 1 MΩDC coupled impedance. A filter to block scattered light from the pump laser is placed in front of the entrance slit.
The change in absorbance were about 3-4 % for a bR solution with an OD of about 1.5 at 568 nm in a 1 cm cuvette. Typical energy for the pump laser would be 1 mJ and for the Hg-Xe lamp the power was set to 60 W.
A schematic of the set-up is shown on fig. 4.3 and 4.4

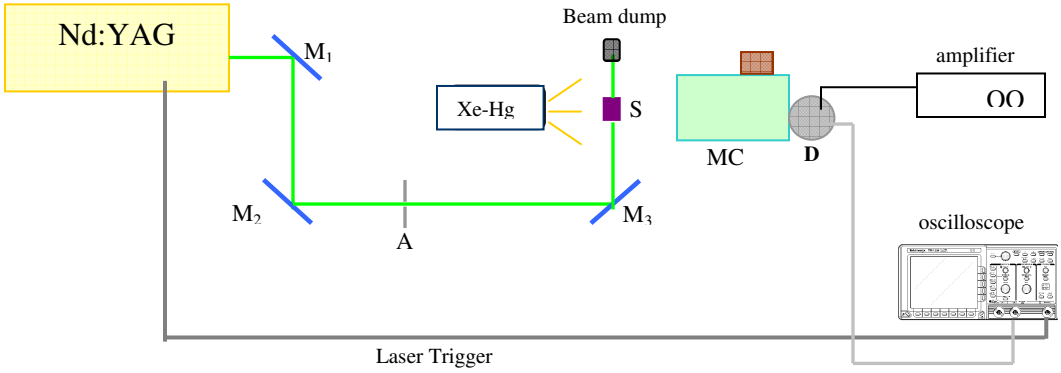

$M_{1,2,3}$= Mirrors A=aperture MC=monochromator D=detector (PMT) S=Sample

Fig. 4.3: Schematic of the set-up used for flash photolysis experiments.

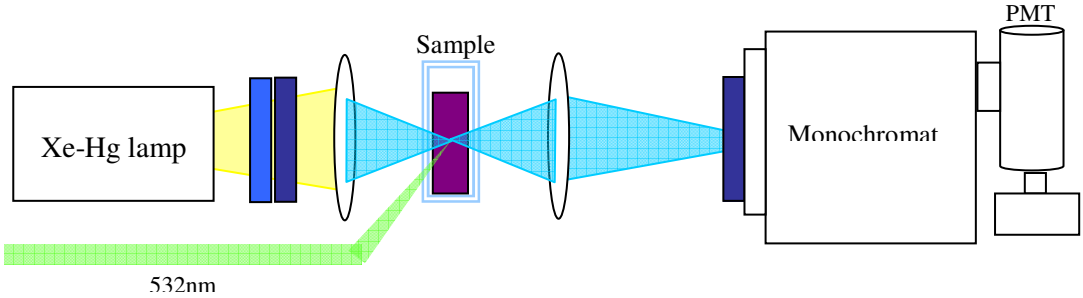

Fig 4.4: Side view of part of the set-up used for bR with gold nanoparticles of different sizes.

4.2 M_{412} rise and decay in pure bR

The M_{412} rise and decay for pure bR solutions in water and in buffer solutions have been measured in our set-up and the values are in agreement with previously measured valued reported by El-Sayed[20, 21] and Dencher[22]. The rise time proved to be less dependent from solvent conditions like pH and ionic strength, for 4<pHs<8[23] it can be described by a single exponential. The decay dynamic on the contrary is more sensitive to the solution ionic strength, solvent, pHs and environmental conditions in general, as already reported in the literature[24, 25].

Values obtained from our set-up for the rise and decay of M_{412} in different conditions is reported below, the pulse energy was 1 mJ, and the arc lamp power 60 mW. The decay lifetimes were obtained using a single exponential function except for pH 9 where a double exponential was required:

Table 4.1: Decay and rise time constants for pure bR at different buffer pHs

Conditions	Decay lifetime/ ms	Rise lifetime / μs
Deionized water pH 7	10.5±1	95±5
Phosphate Buffer pH 7 100mM	4.3±0.5	95±5
Buffer pH 3 100mM	5.5±0.4	Not available
Buffer pH 5 100mM	6.1±0.5	65±5
Buffer pH 9 100mM	2.6±0.3 (Fast) (50%) 28.9±3 (Slow) (50%)	Not available

What is relevant for our purposes is determining what variables, in our set-up, could affect the intermediate lifetime. For instance, it was found that the M_{412} decay lifetime value is function of the probe intensity. As the lamp power is increased, shorter values

for the decay are registered. The results are shown on table 4.2 for the rise and decay dynamics respectively.

As long as the Hg-Xe lamp intensity remains constant, the M_{412} decay dynamic is independent from it. Again, a 1 mJ pulse energy was used for the pump laser and no bleaching was observed on the sample. The change in M_{412} decay dynamics versus the source intensities has been reported by Hendler and coworkers[26]; in their study, they concluded that the source was affecting the ratio between the two different M forms, named M_s and M_f, having different lifetimes.

Table 4.2: Dependence of the decay dynamic of M_{412} to the probe light intensity

Laser @ 532nm	Arc Lamp/W	Decay/ ms	Rise time/μs
1 mJ	45	5.4±0.5	95±5
1 mJ	55	4.0±0.5	95±5
1 mJ	65	4.3±0.5	90±5
1 mJ	75	3.2±0.3	95±5

4.3 M_{412} rise and decay dynamics in presence of gold nanospheres

When gold nanoparticles are added to a bR solution, their plasmon absorption partially overlaps to the retinal absorption band. Below are the absorption spectra of bR in presence of Au nanoparticles with different sizes. Even in presence of a buffer it is interesting to notice that the nanoparticles are kept from aggregating and folling off the solutions. The stabilizing factor is their absorption on the surface of the bR patches.

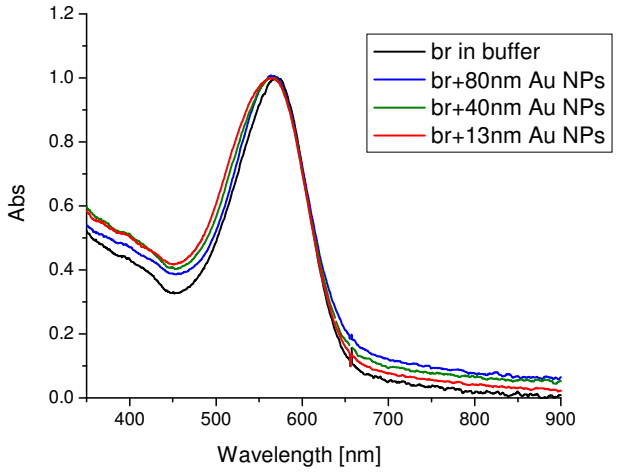

Fig 4.5: Linear absorption spectra of bR solutions with 13, 40 and 80 nm NPs in buffer solution pH=7, 100 mM

The overall scattering goes up, as it is possible to see from the baseline being higher for solutions containing nanoparticles. The high energy side of the band instead shows a blue shift that is more prominent for the 13 nm size gold nanosphere

4.3.1 Rise and decay of M_{412} in presence of Au nanosphere under different probing conditions

The ach lamp used has a very broad emission spectrum (200 to 2300 nm). For the purpose of our experiment, the photons of interest are limited to the 400 nm wavelength range, where the intermediate M_{412} has its absorption maximum (see fig 4.2). Different wavelength ranges of exposure can be chosen for the sample simply by introducing filters on the probe light path. Two different excitation conditions are chosen for the samples containing nanoparticles; set-up#1, where the probing light provides no plasmon excitation. A second, set-up#2, where the arc lamp instead provides continuous plasmon excitation. By placing different filters in front of the sample, as shown in fig. 4.6 and 4.7,

the two set-up conditions are achived, as the wavelength being monitored remains fixed at 412 nm in all cases.

The purpose of changing the probing wavelength range was to determine M_{412} dynamics in absence and in presence of a continuous plasmonic field from the nanoparticles. The nanosecond pulses at 532 nm, about 8 ns in duration, although capable of providing plasmon excitation and consequently the generation of a plasmonic field, its effect is extremely short-lived compared to the intermediate M_{412} lifetime (several orders of magnitude difference).

Two different nanoparticles sizes, 13 and 80 nm are chosen. The reason lies on the two very different scattering and absorption properties[27] related to their size difference, not to mention different plasmonic field intensities associated with them

Set-up #1: no plasmonic excitation:

Two filters are used in front of the sample so that only the wavelengths in the region around 400 to 430 nm are transmitted. This set-up does not allow for continuous plasmon excitation of the sample containing nanoparticles. The plasmon excitation is provided solely by the YAG laser.

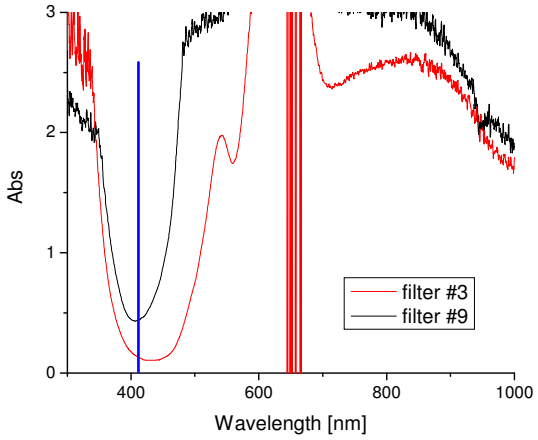

Fig.4.6: Absorption spectra of the filters used in set-up#1 where no excitation for the surface plasmon is provided

Set-up #2: continuos plasmonic excitation

One filter is used in front of the sample to allow surface plasmon excitation and the associated plasmonic field will be turned on. Filter #3 (spectrum reported above) is used after the sample to reduce the light intensity entering the monochromator.

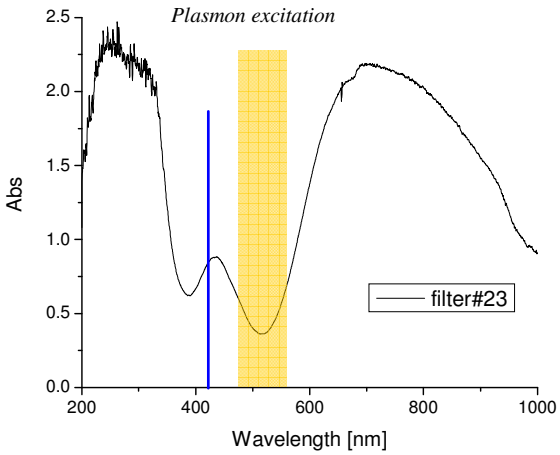

Fig. 4.7: Absorption spectra of filter used in set-up#2 where excitation of the surface plasmon is provided instead.

4.3.2 Rise of M_{412} in presence of Au nanosphere

The rise time of bR occurs in the 100 μs time scales. The addition of nanoparticles to the solution does not change the dynamic of the M_{412} formation as shown in the table below. The rise dynamic is independent from the different excitation provided by set-up#1 or #2.

Table 4.3: Values for the rise lifetime of M_{412} in presence of 13 nm NPs for set-up #1 and #2

SET-UP #	Sample	M_{412} Rise time/ μs
1	Pure bR in buffer	85±5
1	BR buffer + 100 μL 13 nm Au-NPs	80±5
1	BR buffer + 400 μL 13 nm Au-NPs	80±5
2	Pure bR in buffer	75±5
2	BR buffer + 100 μL 13 nm Au-NPs	75±5
2	BR buffer + 400 μL 13 nm Au-NPs	80±5

Table 4.4: Values for the rise lifetime of M_{412} in presence of 80 nm NPs for set-up #1 and #2

SET-UP #	Sample	M_{412} Rise time/ μs
1	Pure bR in buffer	85±5
1	BR buffer + 100 μL 80 nm Au-NPs	75±5
1	BR buffer + 400 μL 80 nm Au-NPs	80±5
2	Pure bR in buffer	75±5
2	BR buffer + 100 μL 80 nm Au-NPs	75±5
2	BR buffer + 150 μL 80 nm Au-NPs	80±5

Decay of M_{412} in presence of 80 Au nm nanoparticles

The decay lifetime of intermediate M_{412} in presence of 80 nm Au nanosphere is measured for solutions containing increasing concentrations of the nanoparticles.

The decay lifetime is obtained by fitting the decay curve with a single exponential function using origin 7.0. The values are reported on table 4.3, both for set-up #1 and #2 respectively. The error bars are obtained by repeated measurements on the same sample. The decay values for pure bR are slightly different for the two set-ups, due to the different excitation conditions as mentioned above.

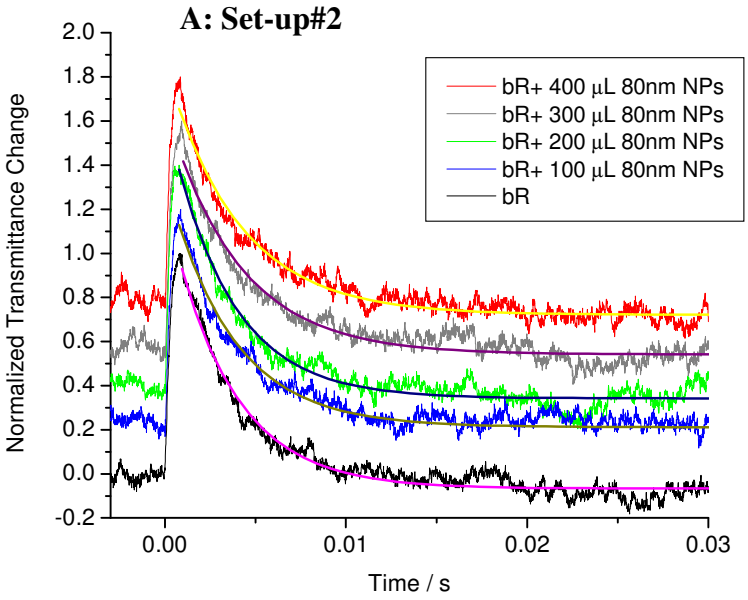

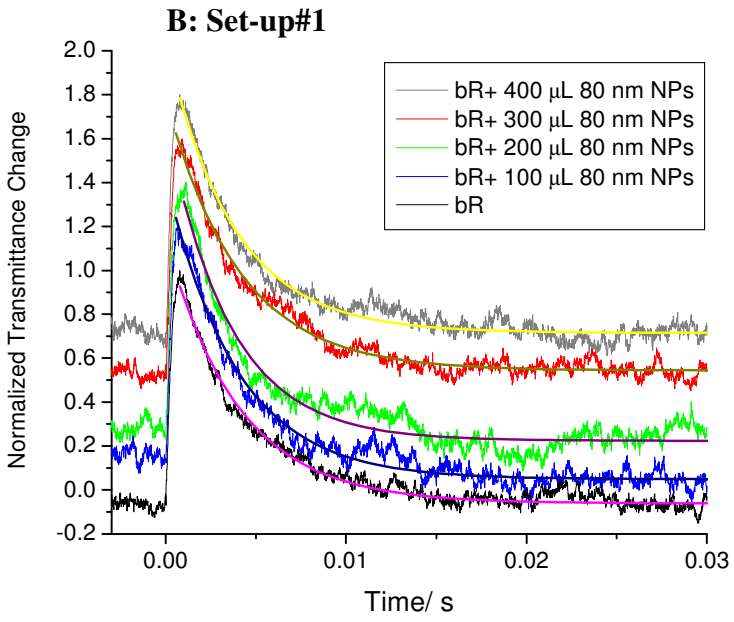

Fig. 4.8: Decay lifetime for M_{412} intermediate in presence of 80 nm Au nanospheres A) in presence of plasmonic field. B) In absence of plasmonic field

Table 4.5: Decay lifetime for intermediate M_{412} in presence of different concentration of 80 nm Au NPs for set-up#1 and #2

80 nm NPs conc. / 10^{-12} M	**Decay Lifetime /ms**	
	Set-up#1	*Set-up#2*
0	3.7	3.4
1.43	3.8	3.6
2.6	3.5	3.4
3.6	4.0	3.85
4.4	3.72	3.9

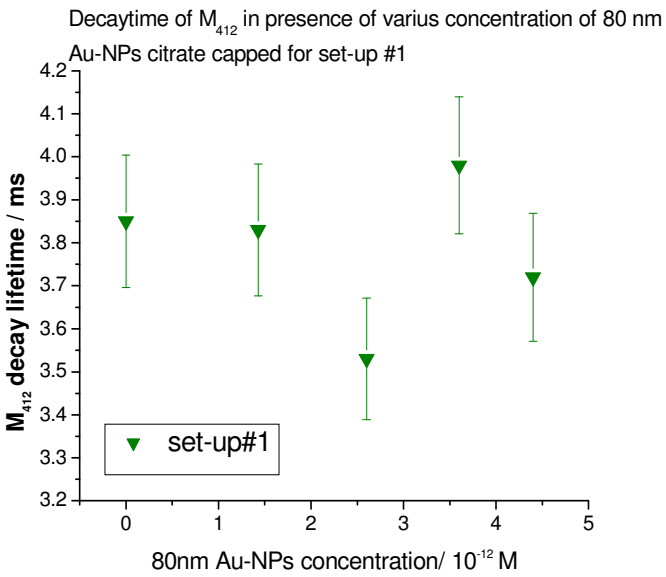

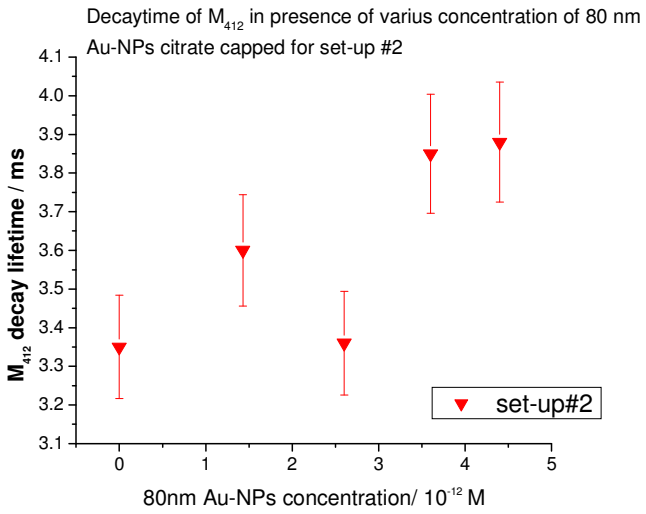

Fig. 4.9: Plots showing the decay lifetime values for bR in presence of increasing concentration of Au NPs 80 nm in diameter for set-up #1 and #2

Decay of M_{412} in presence of 13 nm nanoparticles

A similar behavior is observed when Au nanoparticles of smaller size are added to the sample. When 13 nm nanosphere are used, again no significant differences in the M_{412} decay dynamic are observed for the two set-ups. The data are reported below.

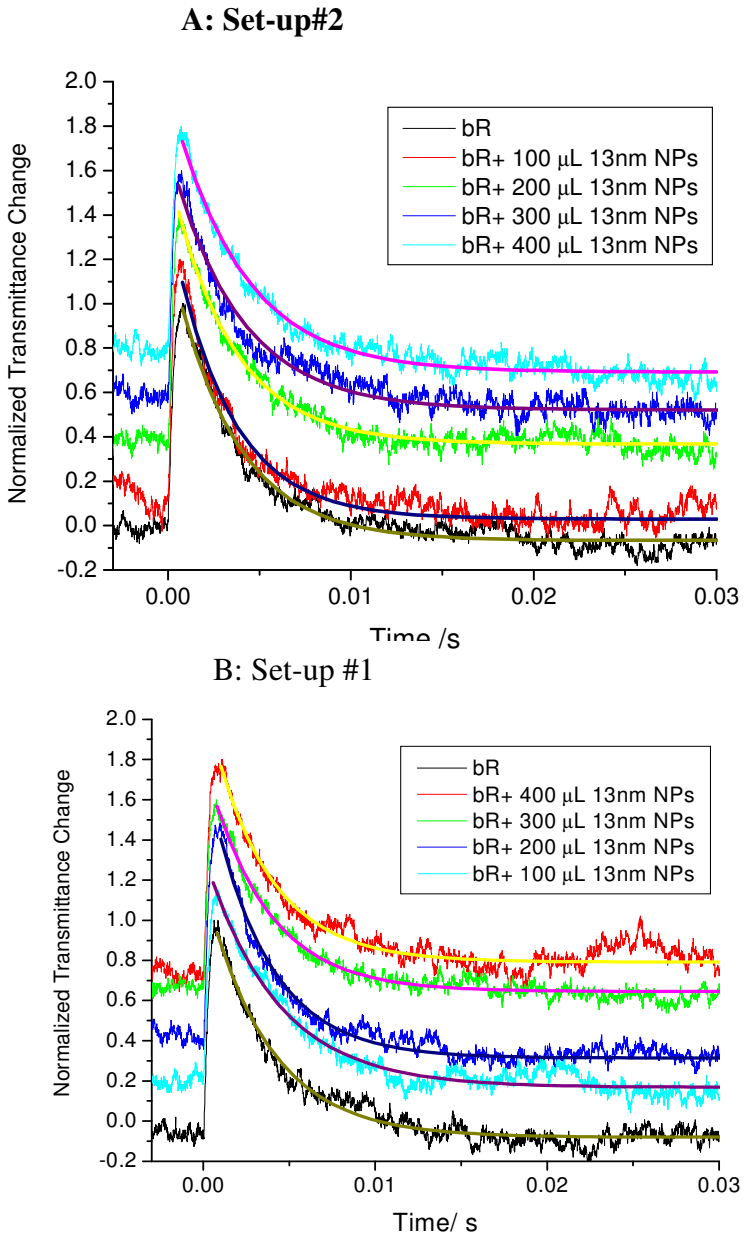

Fig. 4.10: Decay lifetime for M_{412} intermediate in presence of 13 nm Au nanospheres A) in presence of plasmonic field. B) In absence of plasmonic field

Table 4.6: Decay lifetime for intermediate M_{412} in presence of different concentration of 13 nm Au NPs for set-up#1 and #2

13 nm NPs conc. / 10^{-9} M	**Decay Lifetime /ms**	
	Set-up#1	*Set-up#2*
0	3.7	3.35
0.33	4.1	3.15
0.61	3.1	3.4
0.85	3.5	3.8
1.03	3.35	3.85

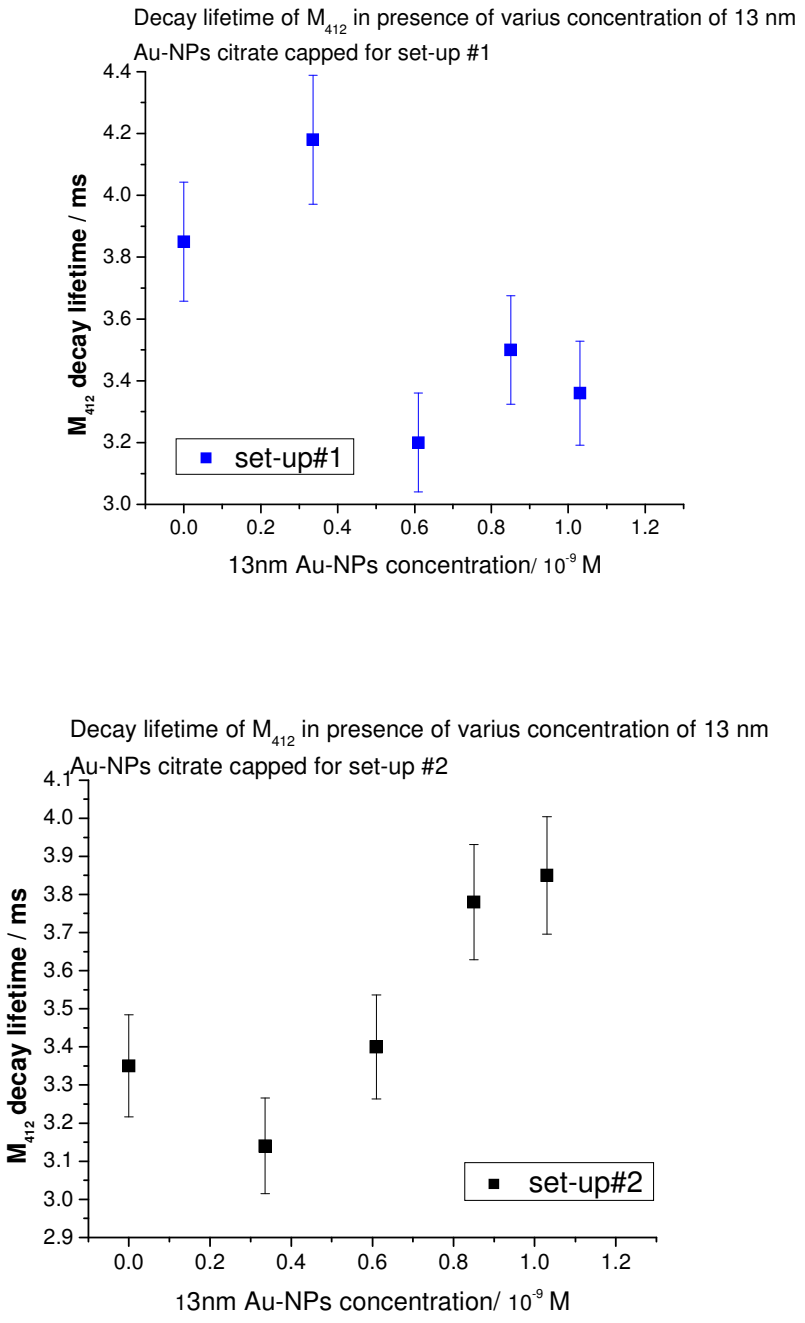

Fig. 4.11: Plots showing the decay lifetime values for bR in presence of increasing concentration of Au NPs 13 nm in diameter upon different sample illumination conditions

Discussion:

The rise and decay dynamics for intermediate M_{412} have been measured for bR solution in presence of Au NPs having diameter of 13 and 80 nm under different probing conditions: one where the probe light would not provide any plasmon excitation (set-up#1) and one with continuous plasmon excitation (set-up#2).

The use of nanoparticles with different sizes, and different scattering properties were aimed at disclosing possible size (and consequently plasmonic field magnitude) dependence on the M_{412} dynamics.

We believe that the data obtained do not provide solid proof of an existing effect on the bR proton pump from the plasmonic field generated by the Au nanospheres. Many samples were prepared and measured, but and after taking into consideration the large error associated with each measurement (in particular for the decay dynamics), no clear trend emerged from them. No size dependence is observed either.

4.4 Rise and decay dynamics of M_{412} in the presence of Au nanorods (Au NRs) and Au nanocages (Au NCs)

The outcome of the experiments involving bR and Au nanospheres led us to utilize other Au colloidals capable of delivering larger plasmonic fields intensities; like gold nanorods and nanocages. The other advantage of using such systems lies on the possibility of tuning their plasmon absorption peak away from the absorption peak of the RBS, allowing continuous and controlled excitation of the surface plasmon without initiating the photocycle.

Materials and methods

Strain S9P of bR was purified according to the standard procedure.

bR solutions are prepared either in deionized water (18 MΩ) or phosphate buffer at pH 7, 100 mM. The solutions OD at 570 nm varies between 1.0 and 1.8 in a 5 mm path length cuvette.

Gold nanorods are prepared with different aspect ratios by following the procedure reported in ref [28]. The NRs are threated before adding them to the bR solution, and the procedure is reported below. Solutions of light adapted bR with different nanorod aspect ratios are obtained by adding the nanorod solution in deionized water prepared as described above to the bR solution. Linear spectrum of each solution is taken using an Ocean Optic spectrometer HR4000GC-UV-NIR before and after laser exposure and no more than 5-6% bleaching is observed.

4.4.1 The effect of the capping material

Nanorods with different aspect ratios are synthesized as described in Chapter II. As previously describe, their synthesis via wet methods involves the use of relatively high concentration (0.2 M) of cationic surfactant like hexadecyltrimethylammoniumbromide (CTAB) and benzyldimethilammoniumchloride (BDAS). The presence of free surfactant causes the bR protein to denature[29, 30], changing the protein absorption spectrum (see fig. 4.12) and the proton pump dynamics are observed as well. We observed an increase in the decay lifetime of M_{412} upon addition of free CTAB, for concentration as low as $3*10^{-5}$ M. The presence of CTAB always causes the decay lifetime of M_{412} to increase, this is in agreement with the claim of Birge[30] and coworkers that surfactant hydrophobic tails

penetrate inside the cytoplasmic part of protein interfering with the proton path. A typical decay for M_{412} in presence of CTAB is shown in fig.4.13

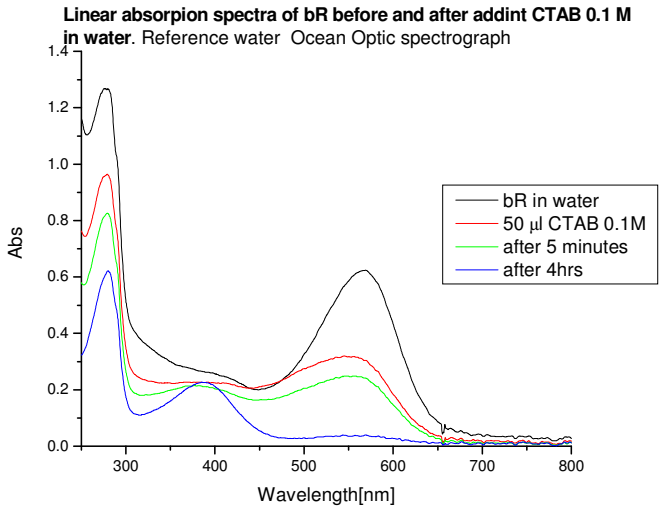

Fig. 4.12: Absorption spectra of bR in water (black) and after adding a small volume of CTAB 0.1 M in water. The RBS absorption band gets broadened and blue shifted, after few hours the RBS band has disappeared leaving instead a band at about 380 nm.

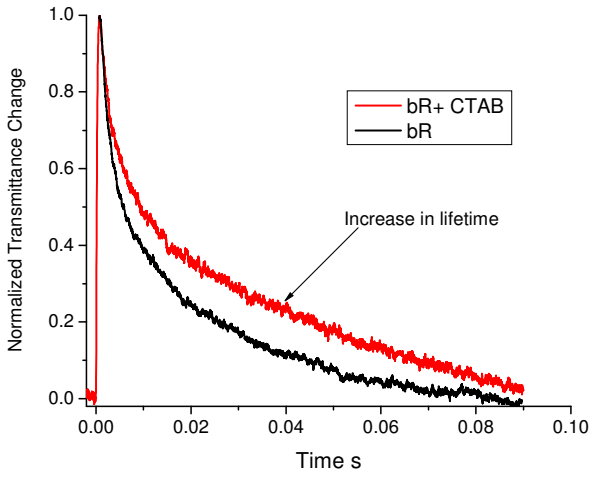

Fig. 4.13: Effect of CTAB on the deprotonation dynamic of bR in buffer at pH 9 right after additions to the bR solution. A visible increase in M_{412} decay lifetimed is observed.

A crucial step on the sample preparation involves centrifugation of the synthesized nanorods solutions. The solution is centrifuged at 13,000 rpm for about 7 minutes, the nanorods collect at the bottom of the centrifuge tube and the supernatant is removed carefully. The centrifuge tube is then filled up with deionized water and the process repeated. In our experience, centrifuging the nanorods more than twice will cause them to aggregate.

At the end, we are left with a very concentrated nanorods solution, and only traces of free CTAB. Centrifuging of the nanorods twice and careful removal of the supernatant has proven to efficiently remove the excess of free CTAB and BDAS, so that no effect from the capping material is observed during the Schiff base reprotonation. What we have noticed instead, was that preparation of nanorods solution as described from day to day would generate different results. From a qualitative standpoint the effect was consistent, meaning that a reduction in M_{412} decay lifetime was always observed all the times, but the lifetime value obtained was not always reproducible for equal concentration of nanorods added to the bR solution. This problem has to do with the reproducibility of the sample as a whole. In fact, without any specidic bonding, the nanorods are not uniformly distribuited on the bR patches, their interaction rely simply on electrostatic intereactions. Whenever a systematic study is presented in this chapter (for instance, concentration dependence study) the data was obtained by adding nanorods to the same original solution.

Nanorods are prepared with aspect ratio (*R*) of 2.8, 4.2 and 5.6 giving longitudinal plasmon absorption at 660, 820 and 1100 nm respectively (fig. 4.14).

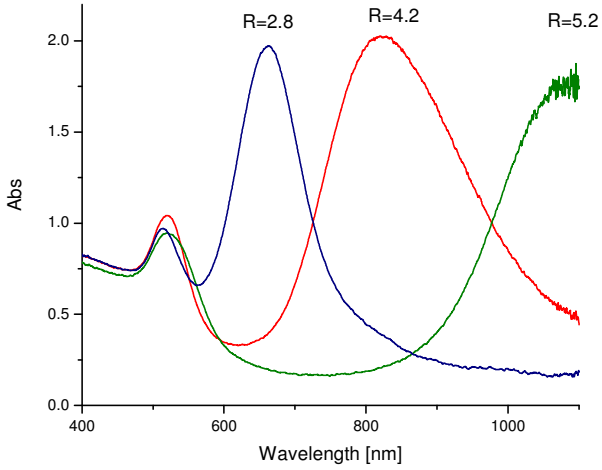

Fig. 4.14: Absorption spectra of Au nanorods solutions of different aspect ratios. The longitudinal band for the highest aspect ratio goes beyond the spectra range of the spectrometer.

Experimental set-up

When Au nanorods and nanocages are used the set-up is slightly modified from that in fig. 4.4. In this case, a cw laser source at 808 nm (Power Technology Inc., 1000 mW) is introduced. The additional source is added to provide continue excitation to the NRs or NCs absorbing in the 800 nm range while the intermediate M_{412} forms and decays. The cw laser beam is not focused and at the sample and is about 1 cm in diameter, the laser power is controlled with neutral density filters.

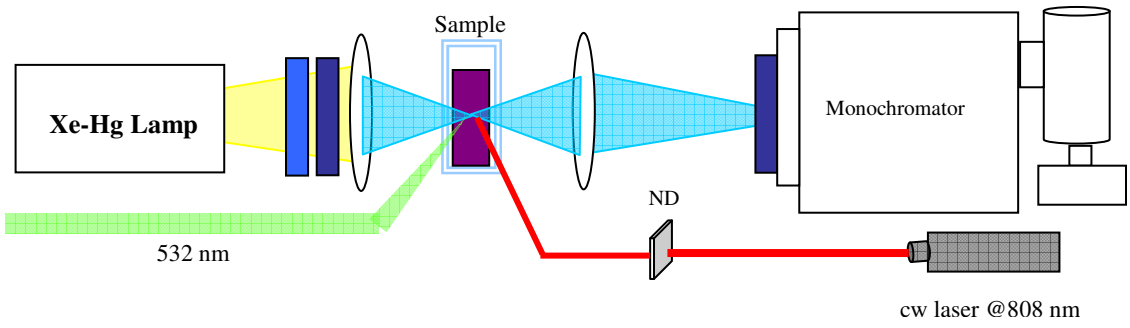

Fig 4.15: Set-up used for bR with gold nanorods and nanocages of different sizes.

4.4.2 Results

M rise:

The rise dynamic of intermediate M_{412} for pure bR solutions and solutions containing gold nanorods having different longitudinal band at 660, 820 and 1100 nm were obtained with and without cw laser at 808nm on. No effects from the presence of a nearby plasmonic field from NRs with aspect ratio 4.2 (longitudinal band at 820nm) were observed on the dynamic of retinal deprotonation, no effects were registered in the case of the other NRs aspect ratios. Figure 4.16 shows the experimental data obtained for pure bR and bR with NRs aspect ratio 4.2 when the cw laser at 808 nm is on.

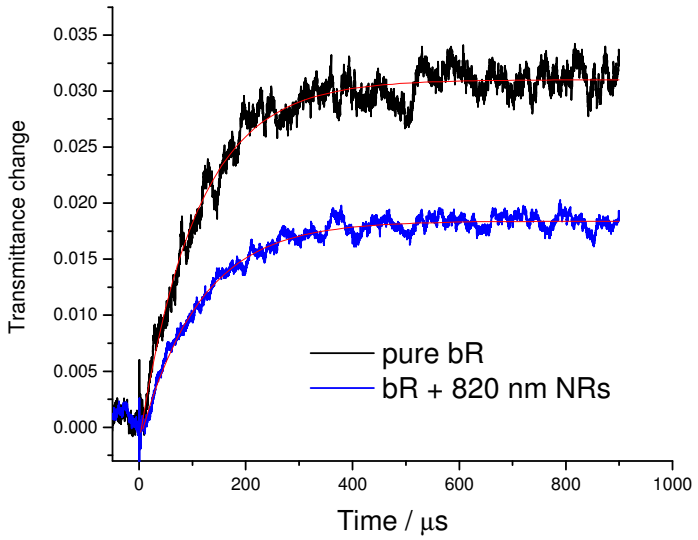

Fig. 4.16**:** Rise dynamic of pure bR (black τ= 112 μs) and bR with 820 nm NRs in presence of cw excitation at 808 nm (blue τ=117 μs)

M decay:

The effect of Au NRs with different aspect ratios on the RBS reprotonation dynamic is shown in fig. 4.18. When gold nanorods having a longitudinal band in resonance with the cw laser (808 nm) are added to the bR solution, (in this case 820 nm), a decrease in the decay lifetime of the intermediate M_{412} is observed. NRs with aspect ratios that are only weakly excited by the cw laser do not produce any effect on the M_{412} decay dynamics.

The cw laser power was 0.128 W/ cm^2 for all samples.

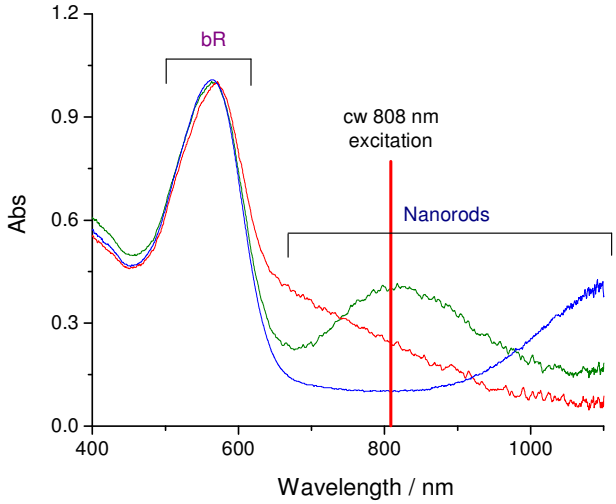

Fig.4.17: Absorption spectra of bR solutions with different NRs aspect ratio. A red line indicates the excitation wavelength at 808 nm

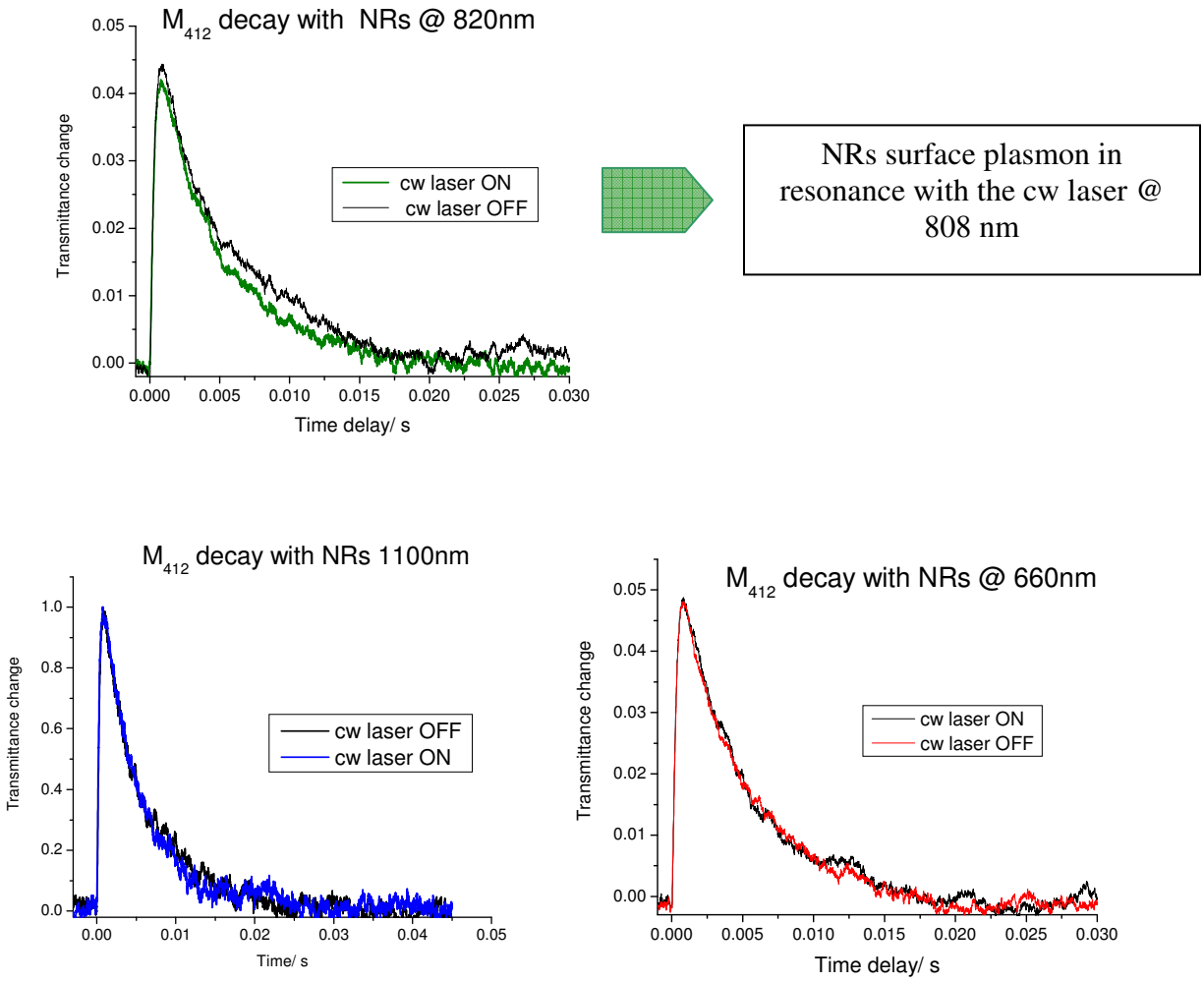

Fig. 4.18: Corresponding dynamics for M_{412} decay lifetime when cw laser at 808 nm is ON and OFF. Only the nanorods with plasmon band at 820 nm causes a shorter M_{412} decay lifetime when the laser is ON. The linear absorption spectra of bR in presence of Au nanorods with different aspect ratios; 2.8 nm (red), 4.2 nm (black) and 5.2 nm (blue) having similar OD is shown if fig. 4.17

For the NRs with *R*= 4.2, the effect on both the concentration and the intensity of the exciting source have been determined as shown in fig. 4.19 and 4.20 respectively. For the same cw laser excitation energy, as the concentration of the nanorods is increased, a larger effect on M_{412} is observed. The rate of M_{412} decay lifetime is found having a nonlinear dependence from the NRs concentration as cleary show in fig. 4.18. When the NRs concentration is kept constant, while the cw laser intensity is increased, a similar behaviour is observed, M_{412} decay lifetime decreases in a nonlinear fashion with tha laser intensity as well. It is interesting to note that the nanorods concentrations are in the nanomolar range and the cw laser energy density are as low as 80 mW/cm^2.

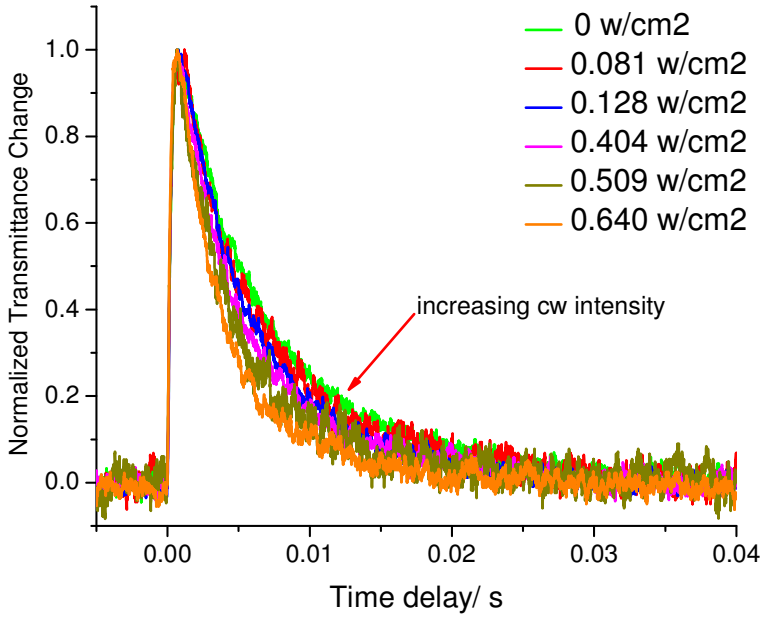

Fig. 4.19a. Decay dynamics of M_{412} intermediate with different cw laser power in presence of gold nanorods with *R*= 4.2. The NRs concentration was 0.07 nM

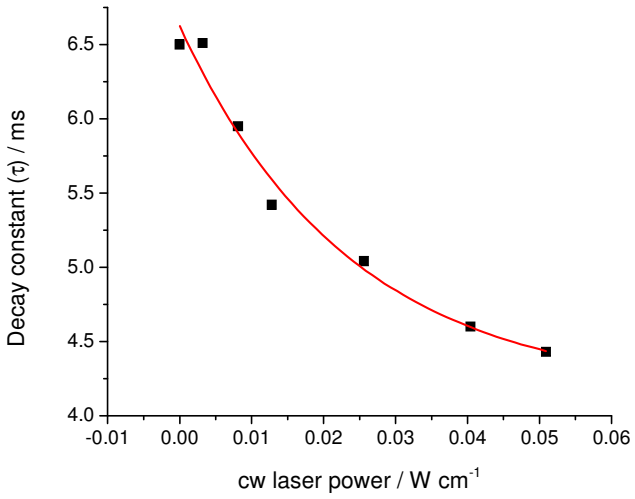

Fig. 4.19b: Decay constant for M_{412} intermediate with different cw laser power in presence of gold nanorods with *R*= 4.2. The NRs concentration was 0.07 nM

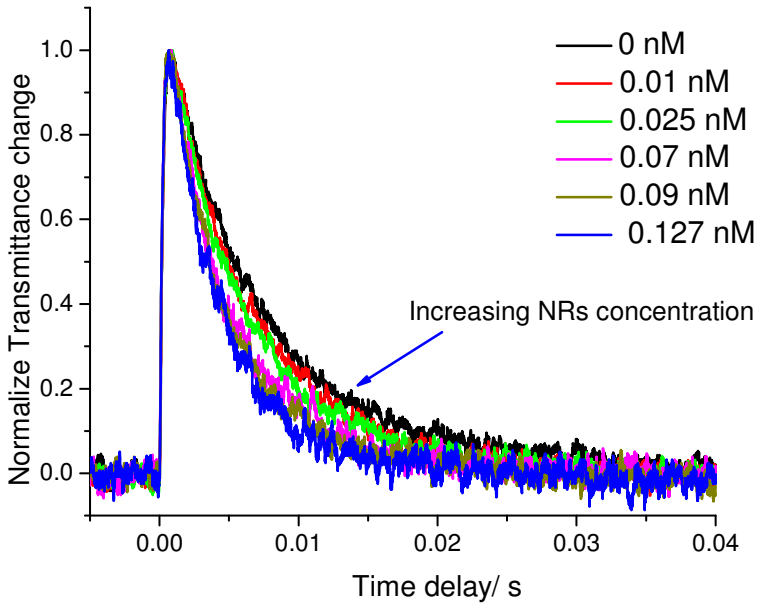

Fig. 4.20a: Decay dynamics of intermediate M_{412} in presence of different Au nanorods concentrations having *R*=4.2 at cw laser power of 0.404 W/cm^2.

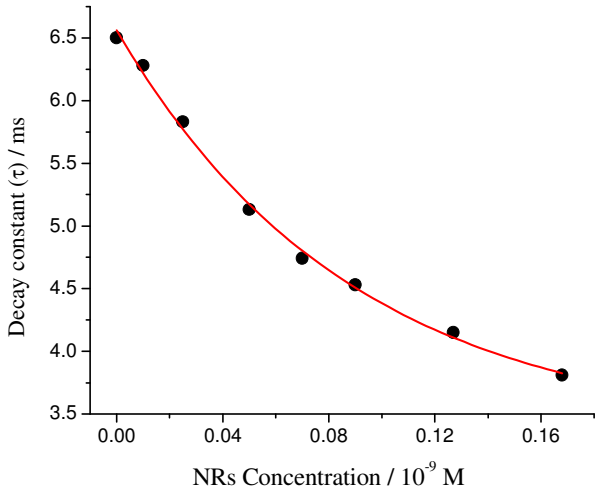

Fig. 4.20b**:** Decay constant for M_{412} intermediate in presence of different Au nanorods concentrations having *R*=4.2 at cw laser power of 0.404 W/cm^2.

4.4.3 Decrease in M_{412} decay lifetime: could it be a thermal effect?

The reason for the rate increase in the decay of the intermediate M_{412} could be appointed to thermal effect from the presence of absorbing nanorods, which are known to have efficient electron-phonon coupling[31, 32]. To verify such hypothesis the temperature of samples with increasing concentration of nanorods having *R*= 4.2 are prepared, both in deionized water and in buffer, and their temperature is monitored by thermocouple after the cw laser is turned on. Figure 4.21 reports the temperature increase over time in the samples at various nanorods concentrations.

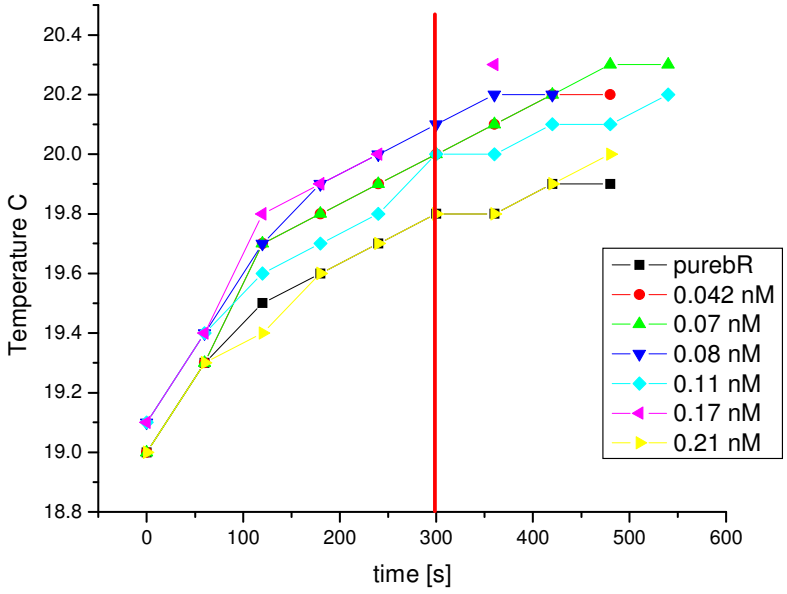

Fig. 4.21: Temperature as function of time for bR samples containing different concentrations of NRs with aspect ratio 4.2 with a cw laser power of 0.404 W/cm^2.

The sample temperature is plotted in function of the concentration for an exposure time of 300 seconds (average tine for data taking), the trend shown in fig. 4.22 is obtained

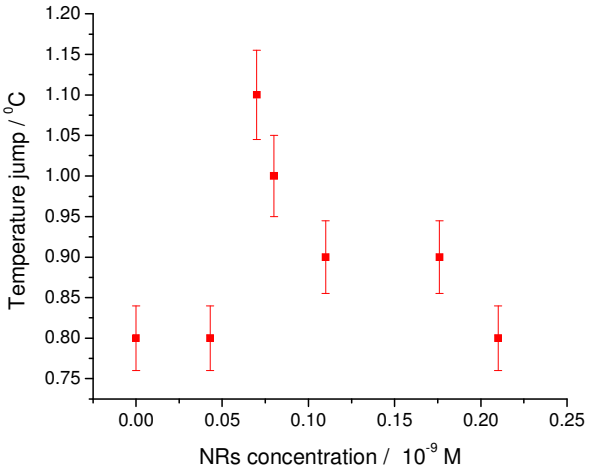

Fig. 4.22**.** Temperature change in the sample containing increasing concentration of NRs after exposure to the cw laser for 300 seconds, the time required for measurements

4.4.4 Effect of particle aggregation on M_{412} decay

Decay lifetime of M_{412} intermediate is measured in presence of the similar concentration of gold nanorods having longitudinal peak at 820 nm in two different solvents: deionized water and phosphate buffer solution 100 mM at pH 7. Absorption spectra of the two solutions are reported in fig. 4.23. The buffer solutions show an overall lower OD at 808 nm as the spectra in fig. 4.23 is showing.

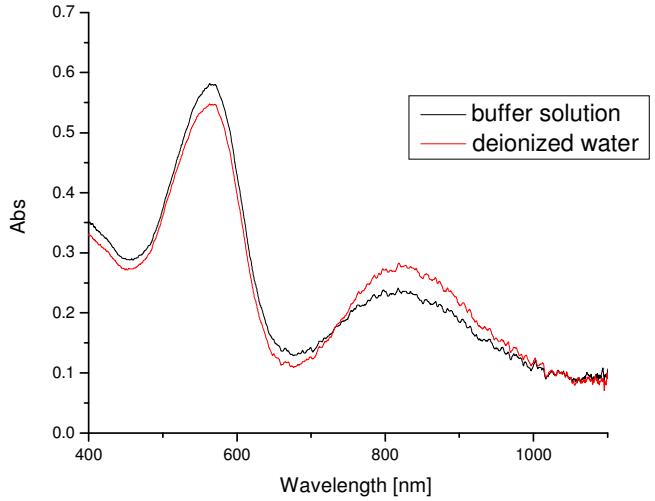

Fig. 4.23**:** Absorption spectra of bR in buffer (black) and in deionized water (red) after adding gold nanorods.

After preparing the solutions the decay lifetime was measured and the following decay dynamics shown in fig. 4.24 were obtained for the water and buffer respectively. A cw laser power of 0.12 W/cm^2 at 808 nm was applied for both samples. From the spectra in fig. 4.23, the deionized water solution has a slightly larger OD at 808 nm than the buffer.

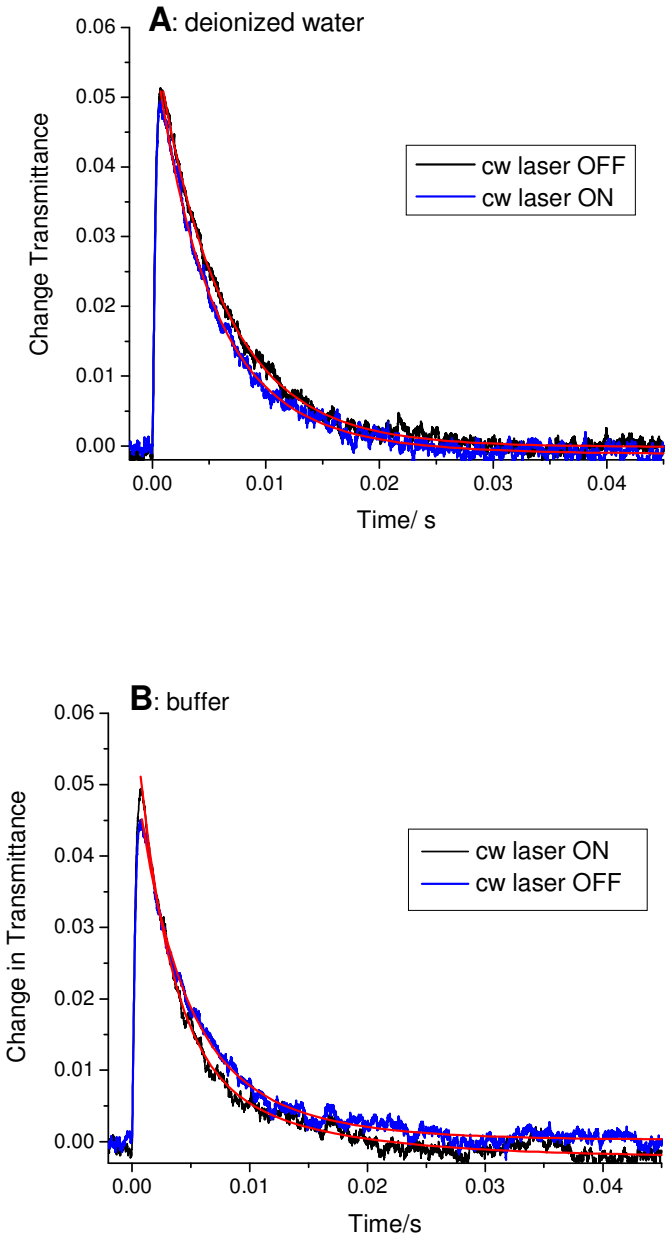

Fig.4.24. M_{412} decay dynamics in deionized water (A) black line no cw at 808 nm, blue line cw laser on 0.12 W/cm^2. In phosphate buffer (B) black line no cw at 808 nm, blue line cw laser on 0.12 W/cm^2

The fitting parameters for the decay dynamics are reported on table 4.7. A single exponential function is used to plot the data. Compare to the pure bR, the relative change

in lifetime is larger for the buffer solution rather than the water (about 30%). Higher degree of aggregation induced by the buffer among The NRs is believe to be at the origin of this behavior.

Table 4.7**:** A larger change in the M_{412} decay lifetime is observed when buffer is used. This proves that aggregation, even partial, increases the field effect, as it would be expected for a plasmon field induced type of effect.

Solvent	**τ/ ms**	**Δτ(cw OFF-cw ON)/ ms**
Deionized water pH 7	5.9 (cw laser OFF)	0.5
	5.4 (cw laser ON)	
Buffer pH 7	5.0 (cw laser OFF)	0.7
	4.3 (cw laser ON)	

Discussion:

We have observed that upon addition of NRs (where the excess of surfact is carefully removed) to bR solutions, decrease of the intermediate M_{412} lifetime is observed when the NRs surface plasmon is continuosly excited. The change in kinetics has been proven not to be due to the presence of NRs, rather to the presence of a plasomic field. In fact, bR solutions containing NRs whose surface plasmon is only partially or not excited at all, because detuned from the frequency of the CW exciting laser, did not cause any change in the dynamic. The effect on the lifetime was shown to be dependent both on the concentration of the NRs, in particular larger concentration, increase the effect on the intermediate lifetime causing it to get shorter and shorter, as well as dependent on the CW excitation power, as larger plasmonic fields were created.

The argument of thermal effects taking place in the sample was raised, and the temperature trend at increasing nanorods OD (fig 4.22) is compared with the equivalent

concentration dependence on the decay lifetime of the M intermediate (fig 4.20), but no correlation was found between the two. In the case of a thermally driven process, it would be expected to have a larger increase in temperature at larger OD, to explain the concentration dependence observed in fig. 4.20. Although there is an increase in temperature for all the samples, there is no direct correlation between the decay dynamics observed in presence of nanorods and the temperature increase; leading to the conclusion that the rate increase cannot be purely a thermal effect. Another argument can be made simply considering the kinetics of the rise and decay of M; the activation energies for the Retinal Base Schiff deprotonation and reprotonation have been measured and according to Varo and Lanyi[33] values of 70±2 kJ (rise) and 68±3 kJ (decay), were obtained for the two transition respectively. With activation energies so close, it is hard to explain why one transition would get thermally affected while the other not at all.

Further experimental evidence in favor of the plasmonic field theory comes from the larger effect observed in buffer solution compared to deionized water, in this case aggregation induced by the saline buffer solution would create hot spots with very large plasmonic field intensities, which would lead to an overall larger effect. . Going back to a basic knowledge of the two processes, the differences are clearly defined; one involves the Retinal loosing its proton to the Asp-85 residue laying less than 4 Å[34, 35] away (M rise) in the extracellular half channel rich in charges and hydrophilic, a second process involving the reprotonation of the Schiff base (M decay), with a proton coming from Asp-96, about 12 Å away and located in the hydrophobic and apolar cytoplasmic half channel. Two main differences are clearly stated. First, the distance covered by the proton in the M_{412} decay process is more than three times longer, compared to the distance traveled by the proton during the M_{412} rise dynamic. Second, the different environments where the two protons are moving, one rich in charges where the presence of an external field could be more easily screened (Faraday cage effect) versus an

environment with almost no charges, where the plasmonic field might have a larger impact. These factors could help explain why the retina Base Schiff reprotonation (M decay) gets affected unlike the deprotonation. In support to the findings are results from current measurements on bR done by Keszthelyi and coworkers[16]. They found that the charge-displacement taking place during the M decay is at least 6 times larger than during M rise. These results were later confirmed by other studies, making the reprotonation process altogether more susceptible to the presence of a nearby plasmonic field.

4.4.5 Intermediate M_{412} rise and decay in presence of Au Nanocages

The same set-up used for the nanorod study is applied for Au nanocages. Nanocages are capped with ethylene glycol (reducing agent) and PVP (55000 MW). The two capping material, contrary to CTAB and BDAS have no effect on the M intermediate dynamics for the concentrations used, so the nanocages are used as synthesized, without further treatment.

Nanocages with different surface plasmon resonance are synthesized starting silver nanocubes, 50 nm in size, upon addition of different volumes of $HAuCl_4$. Below is the spectrum of 2 different nanocages, both 50 nm in size, but with different wall thickness (see Chapter II). The nanocages with surface plasmon absorption at 540 nm have a broader absorption band than the one at 782 nm; such band broadening is caused by inhomogeneity in the cages wall thickness.

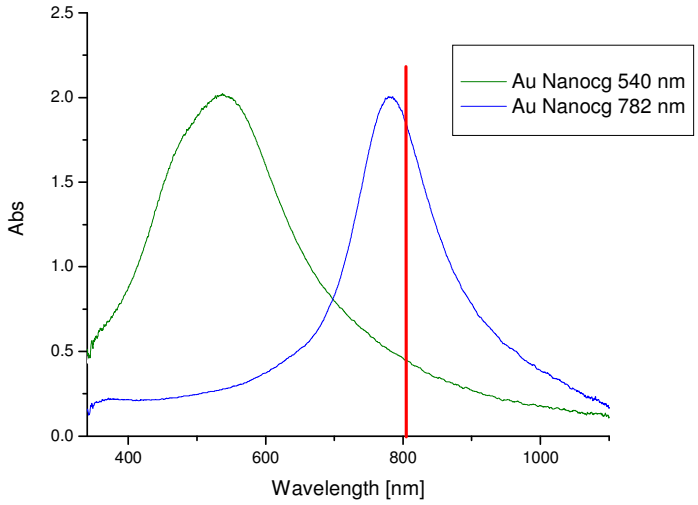

Fig 4.25: Linear absorption of nanocages, 50 nm size, with different wall thickness used in the M_{412} dynamic study.

M rise:

For bR solutions containing gold nanocages with plasmon band at 549 and 782 nm, no change on the dynamic of M_{412} formation are observed. Even when the cw laser at 808nm is turned on and the surface plasmon of the NCs is excited (NCs with λ_{max} at 782 nm), no effect on the rise dynamic is observed.

M decay:

When gold nanocages having a surface plasmon band at 782 nm, in resonance with the cw laser (808 nm) are added to the bR solution, a decrease in the decay lifetime of the intermediate M_{412} is observed. When equal ODs and cw laser intensity are used for nanocages having SPR far away from the 808 nm, and consequently the LSP is only weakly excited, no effect on M_{412} decay dynamic is observed. The decay of M_{412} intermediate in this case remains unchanged respect to that of pure bR.

CW laser intensity dependence on M_{412} decay dynamic:

As the cw laser intensity used to excite the nanocages surface plasmon is increased, a larger effect on the M_{412} decay lifetime is observed. This is consistent with what observed in presence of NRs (see fig. 4.27)

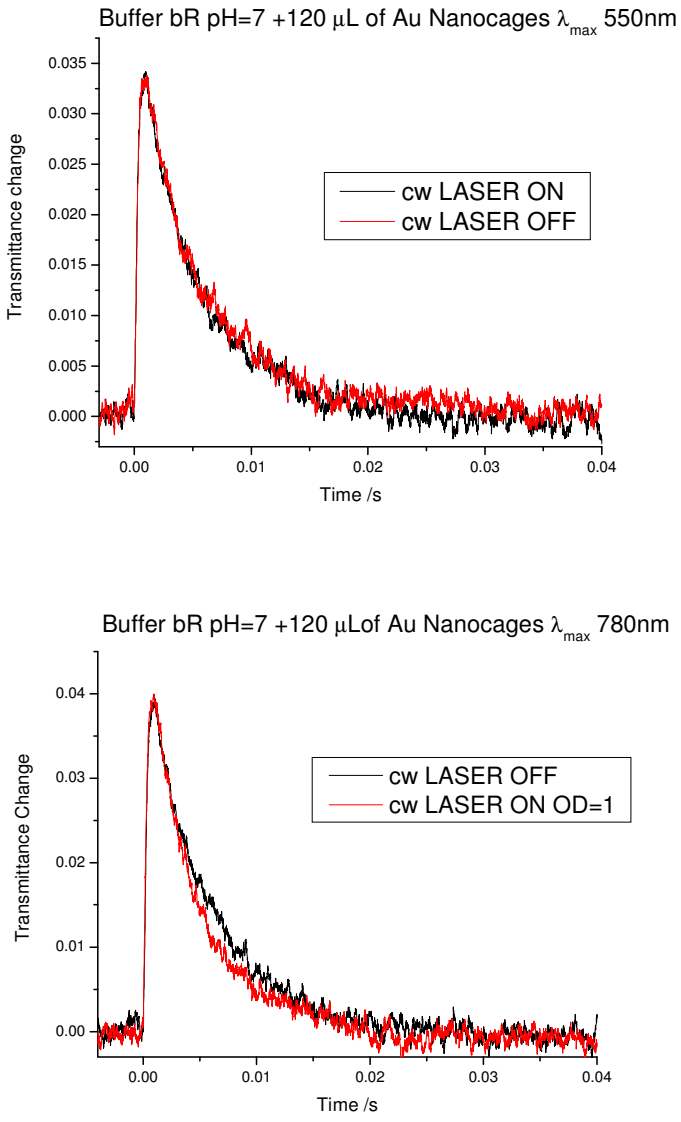

Fig. 4.26: Decay lifetime dynamics for intermediate M_{412} with two different Au NCs. When the plasmonic field is created (sample at the bottom) changes in the intermediate dynamic occur.

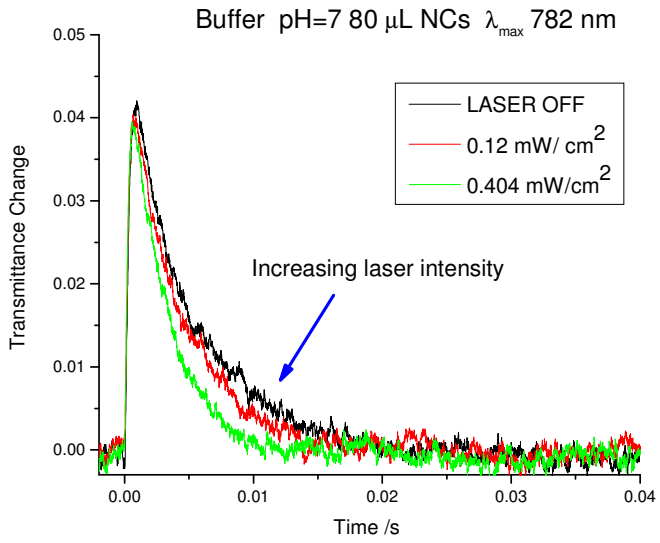

Fig. 4.27: Effect of the exciting laser on the M_{412} in presence of Au NCs

One major problem encountered when working with nanocages is large bleaching followed by light exposure as shown in fig. 4.28. Nanocages are found to be sensitive to light exposure, even for brief times, causing damage to their fragile empty shell structure.

Absorption spectra of the solutions used to measure M_{412} decays were taken before and after exposure and large bleaching is seen. A solution of nanocages with plasmon absorption at 782 nm was exposed for few minutes on the set-up shown in fig. 4.15 and about 15% bleaching is observed.

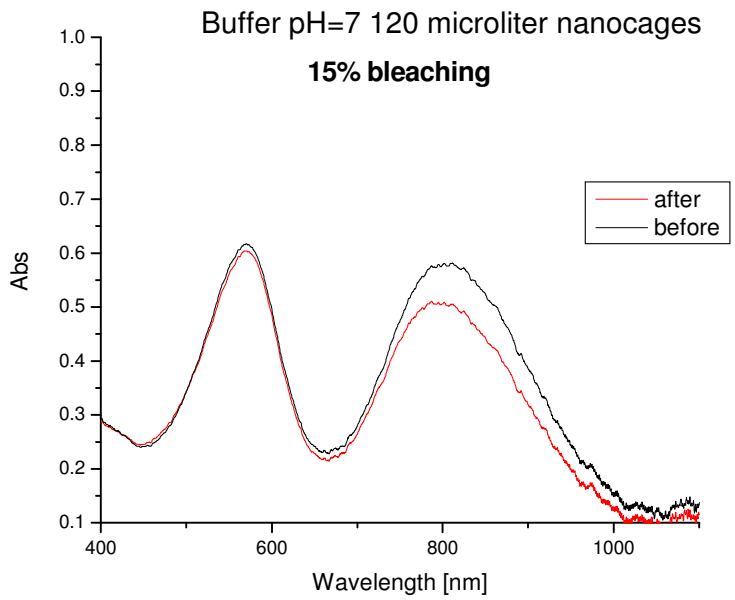

Fig. 4.28: Absorption spectra of bR containing Au NCs before and after flash photolysis measurement

The lack of photostability makes them not ideal for the purpose of this study.

Discussion:

A reduction on the M_{412} decay lifetime is observed when the NCs local surface plasmon is turned on, while the rise lifetime is not affected, in agreement with what was observed for Au NRs. The reduction in lifetime was shown to be proportional to the laser intensity as well. No figures on the field enhancement factor have been published to the best of our knowledge for Au NCs, but the presence of sharp corners on their structure led to believe that they should be close to that of NRs.

Compared to Au NRs, Au NCs need to have larger OD in solution in order to see an affect the dynamic of M_{412}, but the lack of photostability could be a reason for that. Another possible explanation might be the different capping material, bulky PVP polymer surrounds the metal surface, keeping the protein further away from the metal surface.

REFERENCES:

[1] Mitchell, P. J., Bioenerg. Biomembr. 3, 5 (1972)

[2] Danon, A., Stoeckenius, W., Proc. Nat. Acad. Sci. USA. 71, 1234 (1974)

[3] Lanyi, K. J., Nature. 375, 461 (1995)

[4] Birge, R. R., Gillespire, B. N., Izaguirre, W. E., Kusnetzow, A., Lawrence , F. L., Singh, D., Song, Q. W., Schmidt, E., Stuart, A. J., Seetharaman, S., Wise, J. K., J. Phys. Chem. B. 103, 10746 (1999)

[5] Pandey, C. P., Anal. Chim. Acta. 568, 47 (1999)

[6] Kandori, H., Biochim. Biophys. Acta. 1460, 177 (2000)

[7] Maeda, A., Sasaki, J., Yamazaki, Y., Needleman, R., Lanyi, K. J., Biochemistry 33, 1713 (1994)

[8] Lanyi, K. J., Mol. Membr. Biol. 21, 143 (2004)

[9] Luecke, M., Biochim. Biophys. Acta. 1460, 133 (2000)

[10] Zimanay, L., Varo, G., Chang, M., Ni, B., Needleman, R., Lanyi, K. J., Biochemistry. 31, 8535 (1992)

[11] Balashov, P. S., Govindjee, R., Kono, M., Imasheva, E., Lukashev, E., Ebret, G. T., Crouch, K. R., Menick, R. D., Feng, Y., Biochemistry. 32, 10331 (1993)

[12] Cao, Y., Brown, S. L., Sasaki, J., Maeda, A., Needleman, R., Lanyi, J., Biophys. J. 68, 1518 (1995)

[13] Luecke, H., Schobert, B., Richter, H.-T., Cartailler, J. P., Lanyi, J. K., Science 286, 255 (1999)

[14] Groma, G. I., Helgerson, S. L., Wolbert, P. K., Beece, D., Dancshazy, Zs, Keszthelyi, L., Stoeckenius, W., Biophys. J. 45, 985 (1984)

[15] Nagel, B. G., Kelety, B.; Mockel, G.; Bamberg, E., Biophys. J. 74, 403 (1998)

[16] Keszthelyi, L. O., P., FEBS Lett. 109, 189 (1980)

[17] Butt, H. J., Fendler, K., Bamberg, E., Tittor, J., Oesterhelt, D., EMBO J. 8, 1657 (1980)

[18] Drackev, D. A., Kaulen, D. A., Khitrina, L.V., Skulachev, V. P., Eur. J. Biochem 117, 461 (1981)

[19] Cartailler, J.-P., Luecke, H., Ann. Rev. Biophys. Biomol. Struct. 32, 285 (2003)

[20] Jang, D.-J., El-Sayed, A. M., Proc. Nat. Acad. Sci. USA. 85, 5918 (1988)

[21] Heyes, D. C., El-Sayed, M. A., Biophys. J. 85, 426 (2003)

[22] Dencher, A. N., Kohl, K-D., Heyn, M., Biochemistry 22, 1323 (1983)

[23] Eisfeld, W., Pusch, C., Diller, R., Lohrmann, R., Stockburger, M., Biochemistry. 32, 7196 (1993)

[24] Eisenbach, M., Garty, H., Bakker, P. E., Klemperer, G., Biochemistry. 17, 4691 (1978)

[25] Drackev, A. L., Dracheva, V. S., Kaulen, D. A., FEBS Lett. 332, 67 (1993)

[26] Hendler, W. R. D., Z.; Bose, S.; Shrager, I. R.; Tokaji, Z., Biochemistry. 33, 4604 (1994)

[27] Jain, P. K. J., Seok Lee, K., El-Sayed, I.H., El-Sayed, M. A., J. Phys. Chem. B. 110, 7238 (2006)

[28] Nikoobakht, B., El-sayed, A. M., Chem. Mater. 15, 1957 (2003)

[29] Oesterhelt, D., Stoeckenius, W., Nature, New Biology. 233, 149 (1971)

[30] Tan, E., Birge, R. R., Biophys. J. 70, 2385 (1996)

[31] Huang, X. J., K. P.; El-Sayed, I.; El-Sayed A. M., Photochem. Photobiol. 82, 412 (2006)

[32] Link, S., El-Sayed A. M., Int. Rev. Phys. Chem. 19, 409 (2000)

[33] Varo, G., Lanyi, K. J., Biochemistry. 30, 7165 (1991)

[34] Luecke, H., Schobert, B., Richter, T. H., Richter, H-T., Cartailler, J-P., Lanyi. K. J., J. Mol. Biol. 291, 899 (1999)

[35] Hauptus, U., Tittor, J., Oesterhelt, D., Ann. Rev. Biomol. Struct. 28, 367 (1999)

CHAPTER V

RAMAN SCATTERING OF bR IN PRESENCE OF Au AND Ag COLLOIDAL STRUCTURES USING NIR EXCITATION WAVELENGTH.

Abstract

Resonance Raman (RR) spectroscopy is an invaluable tool to obtain structural information of molecules, especially in the visible range, where a large number of lasers and wavelengths are available. RR has been largely used in the biological field to determine vibrational modes of prosthetic groups, while protein amino acid residues require high energies wavelengths, in the UV range, often causing photochemical damage.

Inclusion of plasmonic gold and silver adsorbed on the surface of holoprotein introduces the possibility of studying protein residues at wavelength in the near IR by taking advantage of SERS, with almost no interference from the chromophore. SERS high sensitivity would in principle allow protein residues detection and the use of NPs assure minimal invasion, important to preserves protein structures and their functionality. In this chapter colloidal structure of both Au and Ag are used to obtain SERS from the bR protein using a Raman with excitation wavelength in the NIR (785 nm). Films of bR embedded with Ag and Au nanosphere turned out to be the most promising among all the different nanostructures used. The role of the different capping materials will be discussed.

Introduction

Holoprotein functionality is studied largely at the prosthetic group (chromophore) site[1], due to its easier access in the visible range, when conventional spectroscopic techniques are used. For bR in particular the Retinal Base Schiff (RBS) has been the focus of purple membrane studies[2-9] for more than 30 years. It is common knowledge that the protein plays an essential role in catalyzing[10, 11] the RBS high conversion efficiency and selectivity[12] but still relatively little is known about the protein dynamic during its photocycle[13-16].

FTIR is still the most important tool to determine individual amino acid residues[17] and protein secondary structure[18], differential FTIR spectroscopy instead offers the possibility to follow protein dynamics, like in the case of bR where it was heavily used in concomitance with difference Resonance Raman to follow changes occurring both at the protein and chromophore level[19-21].

Few studies report the use of UV Resonance Raman (UVRR) where the protein is probed directly, and still only aromatic type amino acid residues show[22-24], leaving out many of the residues with major roles in the proton pump function, like Aspartame for instance.

The large effort done towards finding ways to monitor proteins led to the use of alternative spectroscopic techniques, like SERS[25, 26] and SERRS[25, 27].

The advantages of SERS spectroscopy over regular solution Raman scattering are well known; the enhancement factor of the Raman scattering drastically improve its sensitivity decreasing the concentration of biomaterial required, at the same time the presence of a metal surface quenches the fluorescence along with the usual advantage of using Raman in aqueous solutions with virtually no water interference.

Some of the pioneering work in this field was carried out by deposition of the biomaterial on silver electrodes[28, 29]. Such method has proven its versatility from simple amino

acids[30] to large biopolymers, but a problem still remains; after deposition the biopolymer secondary structure is usually not retained compromising the protein functionality[31].

The remarkable advantages of SERS motivated scientists to look for different substrates like metal colloids of different shapes as marker to study living cells[32, 33] and biomaterials by means of both SERS and SERRS. Numerous publications can be found on this topic along with a large variety of biosensor applications[34]. The use of SERS to selectively enhance a protein from its prosthetic group is altogether a new approach with virtually no impact on protein functionality, and no electrodeposition required.

Holoprotein type systems are constituted of a protein structure surrounding a chromophore. As a consequence the protein is left exposed and in direct contact with the surrounding medium. And as the nanostructures are placed in the vicinity of the protein, by using site-specific bindings or just electrostatic attractions, SERS from protein could be detected as their surface plasmon is excited.

The study reported on this chapter deals with the attempts of obtaining SERS from the protein using various colloidal structures. An excitation wavelength in the NIR was chosen to suppress RR signal from the chromophore.

Raman spectra of bR films in presence of Ag NPs, Au NPs with different capping materials, Au NRs with longitudinal surface plasmon in resonance with the laser wavelength were used as well. Raman spectra at 785 nm were attempted for films of bR over monolayers of nanoparticles obtained via Langmuir-Blodgett deposition as well. The results will be discussed

Materials and methods

Halobacterium halobium, strain S9-P, was grown and the purple membrane was purified by the standard technique reported in chapter II. Gold nanoparticles with the 40 and 50

nm were synthesized by citrate reduction[35]. Silver nanoparticles about 50 nm size, citrate capped, were prepared[36] as well. Au NPs capped with sodium dodecyl sulfate (SDS) were obtained by place exchange. After centrifugation and wash with deionized water, FTIR spectra of the Au NPs revealed the characteristic band for SDS, with no citrate bands as shown in fig 5.1.

bR was dissolved in a phosphate buffer solution 50 mM (Sigma Aldrich) at pH 7.0 to this solutions nanoparticles were added. Films of the samples were obtained by evaporating the excess water at 4° C on aluminum foil substrate.

Raman spectra at 785 nm were carried out using a Holoprobe series 5000 microspectrometer (Kaiser Optical Systems, Inc., Amm Arbor, MI) configured in a back scattering geometry with a resolution of 5 cm^{-1}. The output energy of the laser can be adjusted up to 400 mW and the Raman spectra were obtained using 200 mW laser power, correspondent to output energy at the microscope of about 22 mW. The time exposure was set to 5 seconds and for each spectrum 30 accumulations were taken. For all the spectra a 50X objective was used unless differently specified.

Nanoparticles monolayers were obtained using a NIMA 611 D Langmuir Blodgett trough filled up with ultrapure water. The surface pressure was measured using a Wilhelmy plate attached to a D1L-75 model pressure sensor[37].

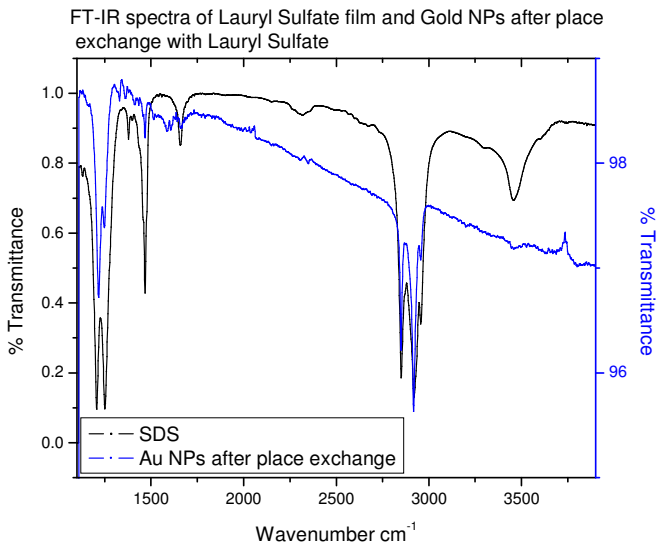

Fig. 5.1: FTIR spectra on CaF_2 substrate of pure SDS and Au NPs after place exchange with SDS.

5.1 Raman spectra of bR films in presence of Au and Ag nanosphere at 785 nm

Raman spectra of pure bR films at 785 nm produce only vibration peaks of the PSB chromophore, and detailed assignment is available in the literature[38].

When Au nanoparticles are present in the film, the Raman spectrum contains extra peaks besides those directly related to the RBS. Raman spectra of the pure nanoparticles under the same conditions were taken. After overruling bands assigned to the RBS and to citrate, unknown peaks indicated in Fig 5.3 with black arrows the are neither retraceable to the citrate nor to the RBS; can only be due to the protein.

The presence of protein bands imply that SERS takes place; an the intensity dependence of its signal the same spot was taken (data in fig. 5.3 are relative to the peak at 390 cm^{-1})

revealing a linear dependence as expected[39]. Not surprisingly the Raman signal changes quite drastically as we move across the sample, because of the intrinsic inhomogeneity of the films, retraceable to different degrees of aggregations among nanoparticles. Consistent with the previous result are the Raman spectra from bO embedded with 40 nm Au NPs, no RBS is present in this case, and still extra peaks (besides the capping material) are present, reinforcing the SERS theory. Spectra of bO film embedded with Au NPs in different spots is reported, showing low reproducibility as mentioned. The degree of aggregation plays an important role in creating so called "hot spots", where two or more particles plasmonic fields couple generating very high intensities and as direct consequence large SERS signals from the nearby molecular systems are registered (see Chapter I)

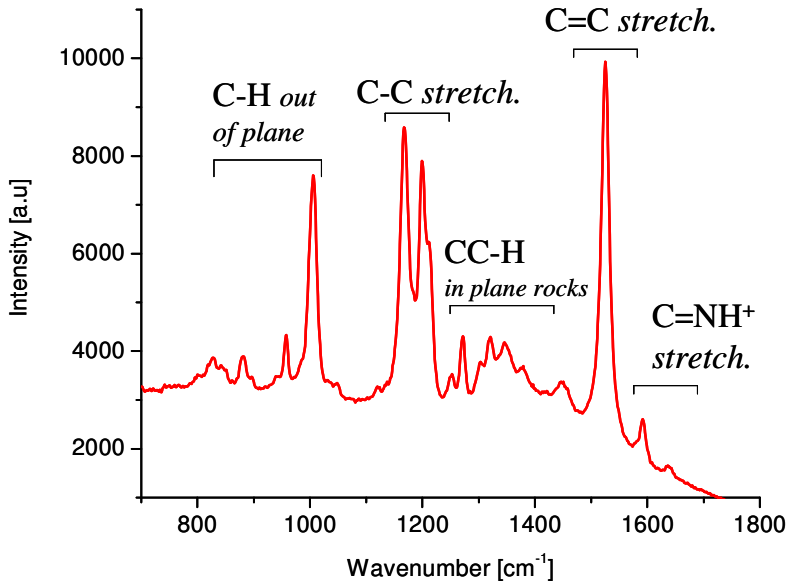

Fig. 5.2: Raman spectra of pure bR film on aluminum foil at 785 nm.

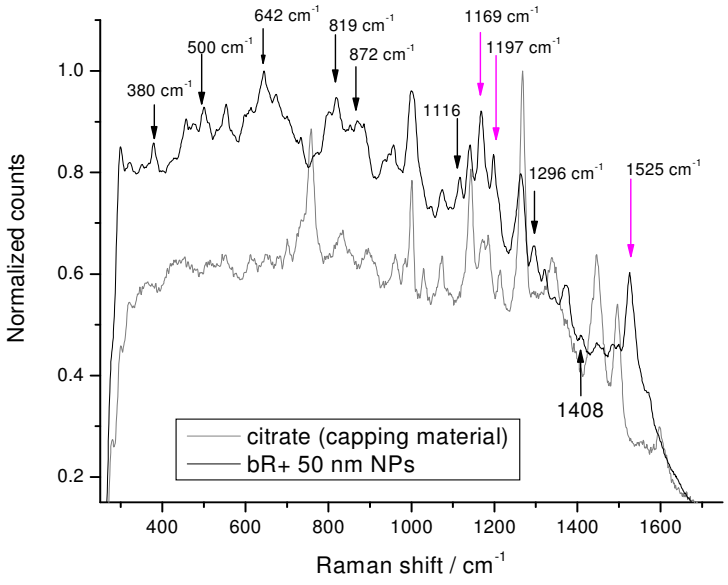

Fig. 5.3: Raman spectrum of bR film embedded with 50nm Au NPs overlapped with Raman spectrum of the capping material (citrate). Pink arrows indicate RBS related vibrations

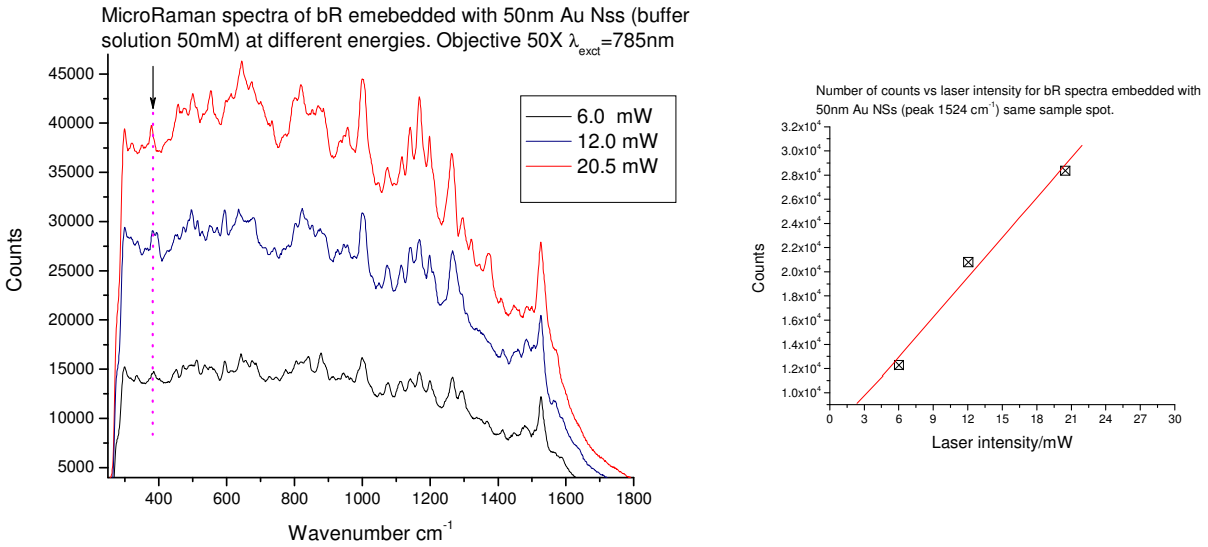

Fig. 5.4: Raman spectra of bR film embedded with 50 nm Au NPs at different laser energies. On the right the intensity of the peak at 380 cm^{-1} is plotted vs the laser incident energy.

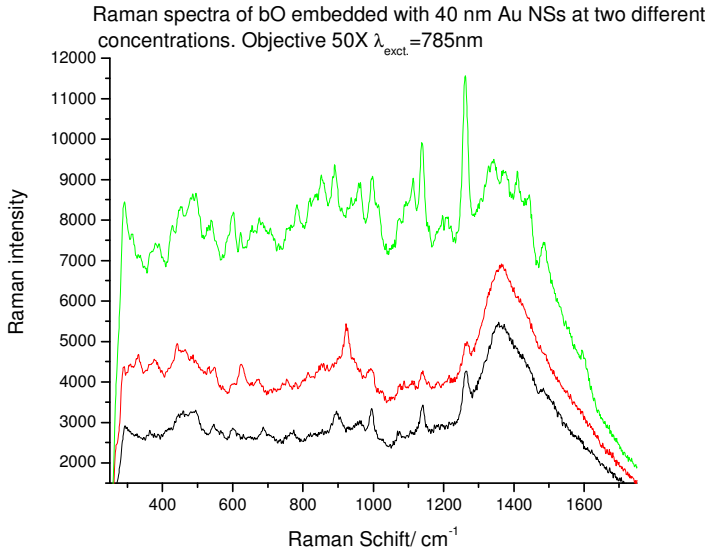

Fig: 5.5: The Raman spectra of bO with 40 nm nanoparticles on different area of the same film.

When the capping material was substituted with SDS and Raman spectra taken for the pure nanoparticles and for the nanoparticles embedded in a bR film, again peaks that can

be attributed to the protein were recorded, in this case only in the low energy part of the spectrum as shown in fig 5.5 (black arrows).

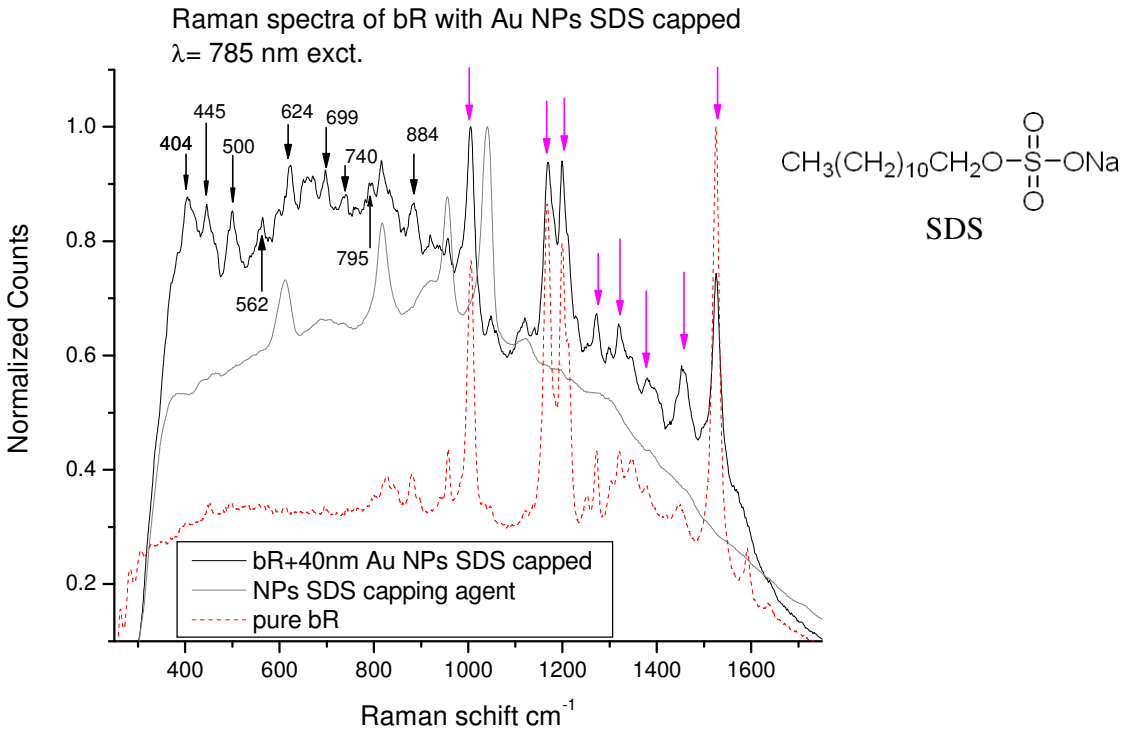

Fig. 5.6: Normalized Raman signal from bR film embedded with Ag NPs, and that of the capping material

Silver nanoparticles are known to have larger SERS enhancement factors, and although their surface plasmon further detuned to the Raman excitation wavelength compared to Au NPs, at 785 nm, bR films containing Ag nanoparticles gave the best SERS signals. When silver nanoparticles are added to bR there is almost no contribution from the chromophore unlike with Au colloids. The signal counts gets larger improving the signal to noise ratio, unfortunately the signal from the capping material is largely enhanced too.

As in the case of Au nanoparticles the Raman spectrum varies significantly as different spots in the sample are analyzed.

An example of SERS from bR embedded in Ag nanoparticles is reported in Fig.5.7, the Raman of the capping material (citrate in this case) is reported as well. Blue arrows indicate peaks that are protein related.

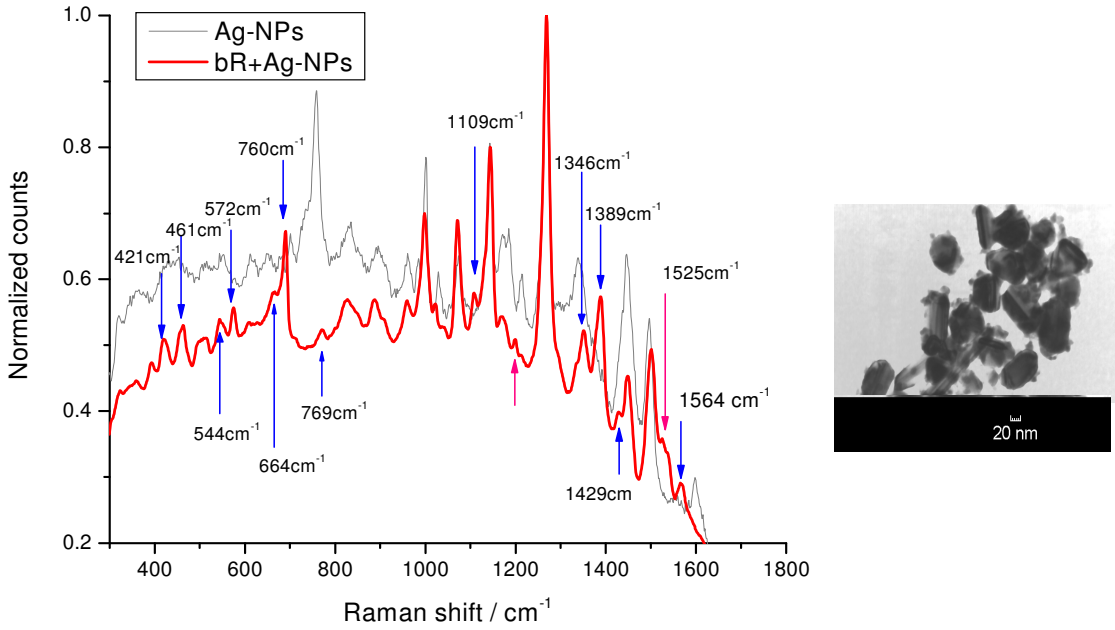

Fig. 5.7: Normalized Raman signal from bR film embedded with Ag NPs, and that of the capping material. On the right TEM image of the Ag NPs used in the sample preparation

In an effort to improve the reproducibility of the samples a different approach was taken. The nanoparticles are first organized on a monolayer over a glass substrate and afterwards a thin film of bR is deposited on top. The monolayer is obtained by Langmuir-Blodgett through.

The physical properties of the capping material is critical for the successful formation of the monolayer, unfortunately citrate does not have the desirable characteristic, and a different system is used instead of the nanospheres, Ag nanocubes PVP capped. Ag nanocubes were previously described on chapter IV as precursor to the synthesis of Au nanocages.

The idea of the different bR films arrangement is illustrated below: the organized manolayer would introduce a higher degree of homogeneity across the sample, the idea is shown below.

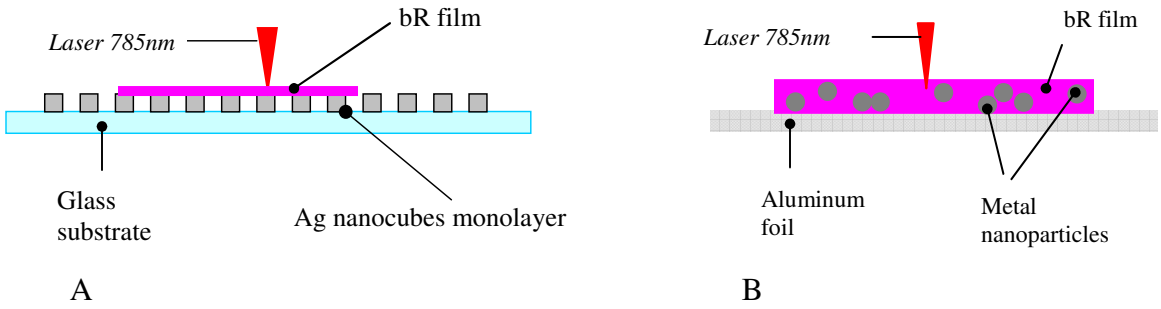

Fig. 5.8: A) bR film over Ag nanocubes monolayer B) bR film obtained by solvent evaporation from a solution containing metal nanoparticles.

Absorption spectra of the Ag nanocubes monolayer revealed the presence of a plasmon bands at 486 nm as shown in fig. 5.9.

Raman spectra of the bR film on Ag nanocubes manolayer were obtained, but no SERS was observed. The Raman spectra at different energies shows the characteristic chromophore vibrations peaks, and one belonging to the capping material (PVP), indicate in fig. 5.10.

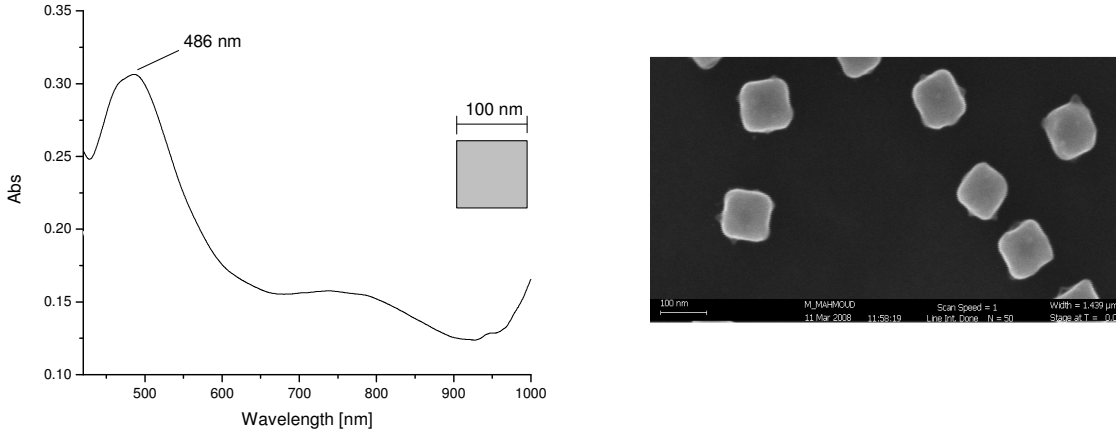

Fig. 5.9: Absorption spectrum of 100 nm in side Ag nanocubes on glass substrate. On the right is a SEM picture of the nanocubes

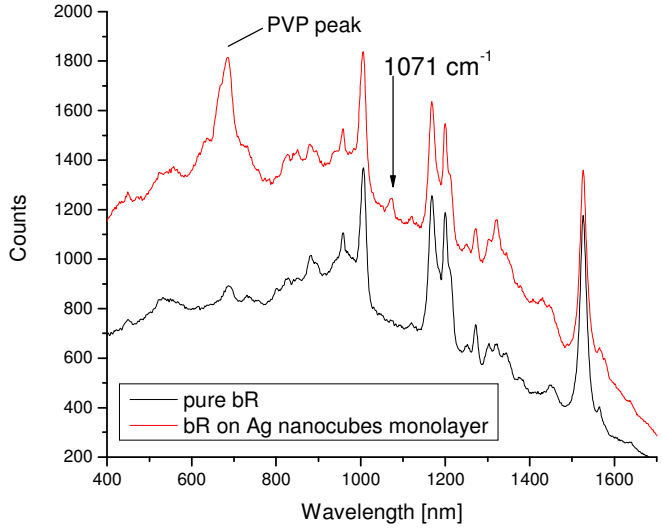

Fig. 5.10: Raman spectra of bR film on silver nanocube PVP capped monolayer.

5.2 Colloidal systems with plasmon resonance at 785 nm: Au nanorods and nanocages.

The colloidal system used so far (Ag NPs, Au NPs, and Ag nanocubes) have surface plasmon band that are relatively detuned from the Raman excitation wavelength. It is well known that enhancement factors are maximized when the excitation wavelength is in resonance with the peak of the plasmon peak. In order to take advantage of the resonance with the surface plasmon, more tunable nanostructures, like Au NRs and NCs are synthesized and added to bR films.

Au NRs with aspect ratio 4 are synthesized and after removal of the excess CTAB (see chapter IV) by centrifugation, are added to the bR solution. The absorption spectra of the films with different concentration of Au NRs are shown in fig. 5.11.
Surprisingly the Raman spectra of bR films embedded with NRs does not show sign of SERS. The vibration in fig. 5.13 can only be assigned either to the RBS chromophore or the capping material (fig. 5.12).

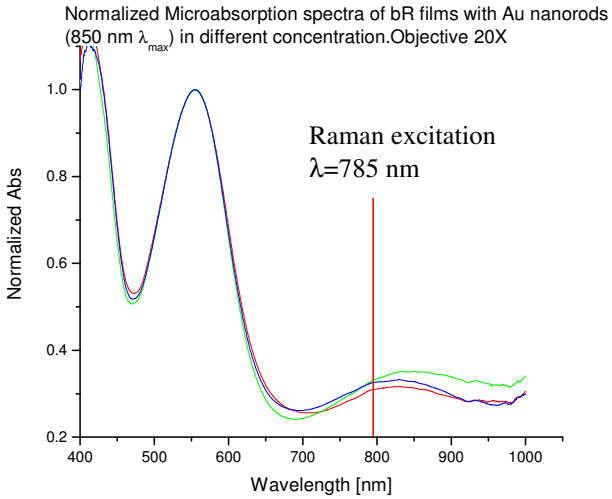

Fig 5.11: Absorption spectra of bR films after adding different amount of Au NRs

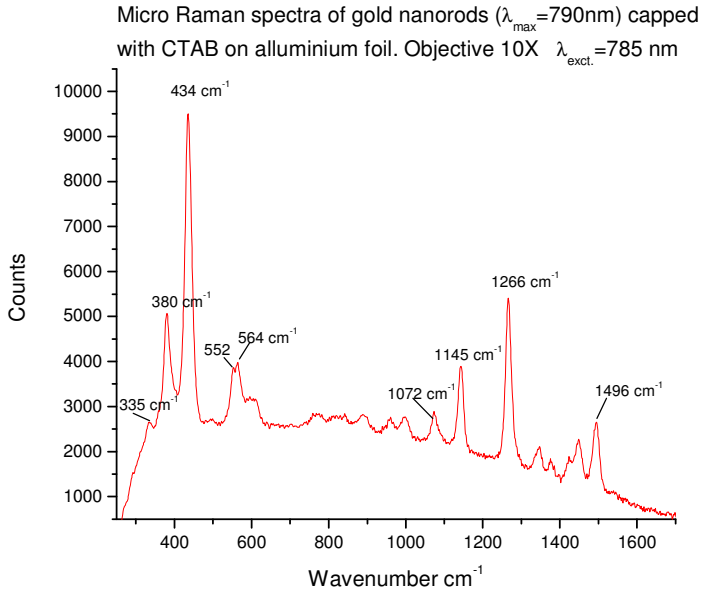

Fig.5.12: Raman spectrum of the NRs capping material, CTAB

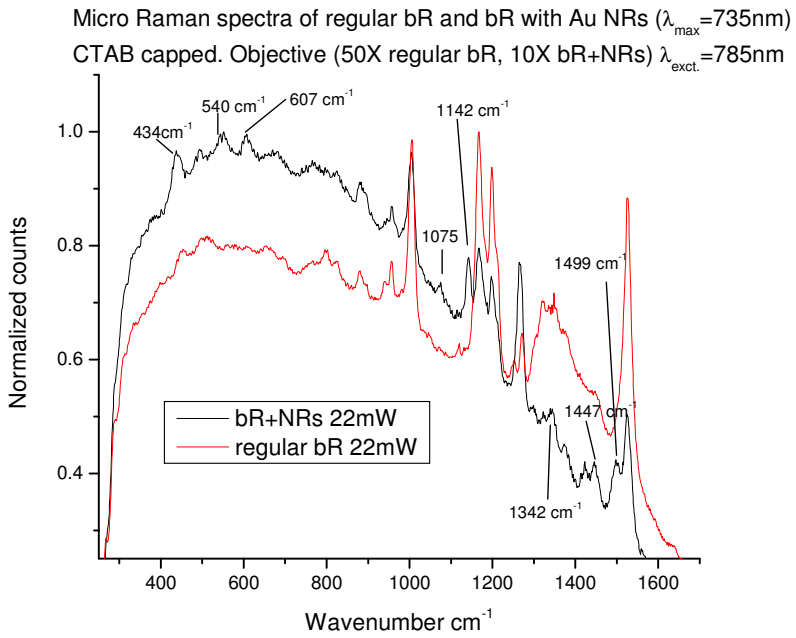

Fig. 5.13: Raman spectra of bR film containing NRs having λ_{max}=740nm

The other highly tunable system chosen was a coreshell type system; Au nanocages (see Chapter II).

Again the Au NCs PVP capped were organized on a monolayer using Langmuir-Blodgett technique on a glass substrate. Linear spectra of the monolayer shows a plasmon peak closely tuned with the Raman excitation wavelength of 785 nm. After deposition of a thin film of bR, Raman spectra for the system are taken and unfortunately only the chromophore RBS signature spectrum was obtained.

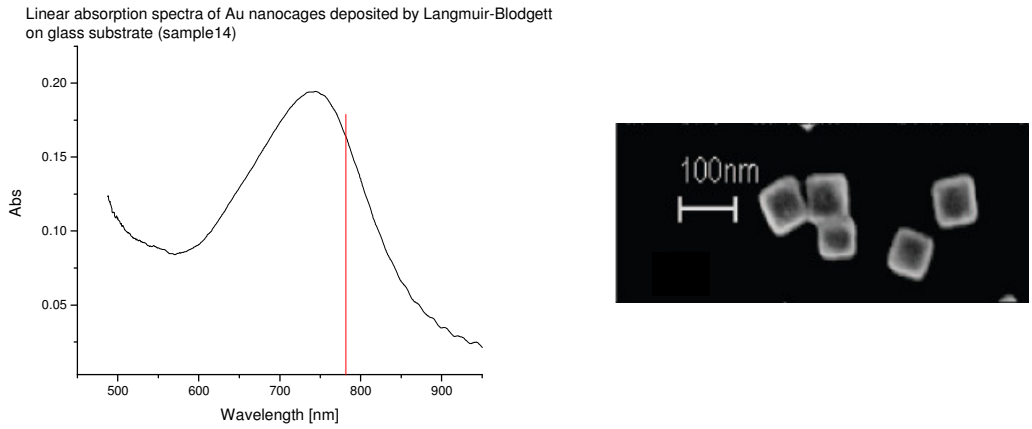

Fig. 5.14: Absorption spectra of Au NCs monolayer PVP capped on glass substrate

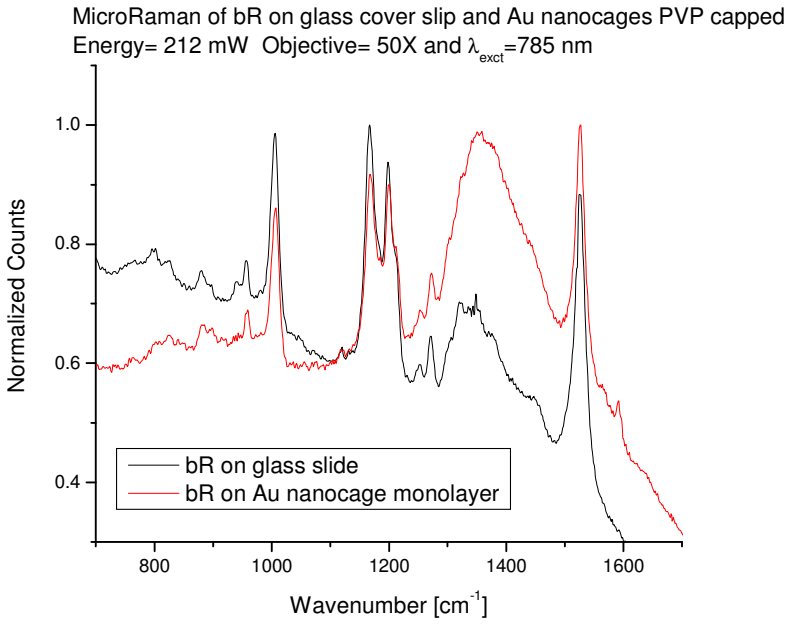

Fig. 5.15: Raman spectra of bR film on Au NCs monolayer (red) and pure bR film on glass substrate

Discussion:

Raman spectra at 785 nm are taken for bR films embedded with Au and Ag nanospheres. Different capping materials were used with Au nanoparticles: citrate and SDS to explore its effect on SERS. SERS was registered when Au and in particular Ag nanosphere were embedded in the bR film. Silver nanoparticles reported the best SERS signal, so that almost no signal from the RSB chromophore was registered. The field enhancement factor, known to be directly related to SERS[39] signal intensity, is calculated to be larger for silver than gold. Gold nanospheres surface plasmon is less detuned from the excitation wavelength than silver, still, silver nanoparticles managed to give larger SERS signals. We believe that the signal is mainly due to "hot spots" in the sample where the aggregation of two or more nanoparticles creates areas with very large field enhancement[40, 41]. Again silver has proved very large enhancement factors for dimers or higher degrees of aggregation among particles, enough to be able to detect single molecule[42]. This could explain why we did not observed SERS from monolayer type of arrangements where aggregation is inhibited. When Ag nanocubes were added to the bR solution like in the case of Au nanospheres, again no SERS was detected, which led us to believe that the capping materials plays a very important role. In the literature SERS is often associated with adsorption of the molecule under analysis to the colloidal surfaces and some instances even chemically bound to the surface (chemical enhancements). Even though direct chemical binding is not required to get SERS, vicinity to the colloidal surface is critical. Very likely bulky capping material like PVP or CTAB bilayer, create a barrier to the colloidal surface, too difficult to penetrate for the protein which cannot get sufficiently close to the metal surface and as a direct consequence strongly reducing the

field effect enhancement. Citrate on the other hand is a very small molecule, which still allows close proximity to the protein. Bulky capping material could limit the degree of aggregations or the proximity of one to the other, reducing the degree of coupling in these aggregates. It is interesting to compare citrate with SDS. SDS unlike CTAB does not form packed bilayer, but it is bulkier than citrate. For the same Au NPs size and excitation conditions, less protein related peaks are obtained, located only on the low energy part of the Raman spectrum. This confirms how important is the capping material size in having SERS from colloidal nanoparticles especially when no specific binding between the nanoparticles and colloidal surface are present.

The lack of reproducibility for films obtained by simply mixing NPs to a bR solution, like in the case of gold and silver nanospheres was overcame by deposition of the nanostructures on a substrate. Langmuir-Blodgett monolayers of Ag nanocubes were obtained in order to create more homogeneous nanoparticles distribution, over which bR solution was let to evaporate to form a thin film. No SERS at 785 nm was registered for such samples. Reasoning being the lack of aggregation, as mentioned above, along with the sample morphology, which allows only the very first bR layers in contact to the nanostructure to benefit from field enhancement, leaving out layers that are further away from it.

REFERENCES:

[1] Anderson, J. L. R., Chapman, K. C., Dalton Trans. 1, 13 (2004)

[2] Brainman, M., Mathies, R., Biochemistry 19, 5421 (1980)

[3] Doig, J. S., Reid, J. P., Mathies A. R., J. Phys. Chem. 95, 6372 (1991)

[4] Gai, F., Hasson, K. C., McDonald, J. C., Anfinrude A. P., Science 279, 1886 (1998)

[5] Haupts, U., Tittor, J., Oesterhelt, D., Ann. Rev. Biophys. Biomol. Struct. 28, 367 (1999)

[6] Kung, M. C., Devault, D., Hess, B. Oesterhelt, D., Biophys. J. 15, 907 (1975)

[7] Lozier, H. R., Bogomolni, A. R., Stoeckenius, W., Biophys. J., 15, 955 (1975)

[8] Smith, O. S., Pardoen, A. J., Lugterburg, J., Mathies, A. R., J. Phys. Chem. 91, 804 (1987)

[9] Smith, O. S., Brainman, S. M., Myers, B. A., Pardoen, A. J., Courtin, M. L. J., Winkel, C., Lugterburg, J., Mathies, A. R., J. Am. Chem. Soc. 109, 3108 (1987)

[10] El-Sayed, A. M., Logunov, S., Pure & Appl. Chem. 69, 749 (1997)

[11] Song, L., El-Sayed, A. M., Lanyi, J. K., Science 261, (5123), 891 (1993)

[12] Gai , F., Hasson, K. C., McDonald, J. C., Anfinrud, P. A., Science. 279, 1186 (1998)

[13] Heyes, D. C., El-Sayed A. M., J. Phys. Chem. B. 107, 12045 (2003)

[14] Garczarek, F., Wang, J., El-Sayed, A. M., Gerwert, K., Biophys. J. 87, 2676 (2004)

[15] Wang, J., El-Sayed, A. M., Biophys. J. 78, 2031 (2000)

[16] Rothschild, J. K., J. Bioenerg. Biomembr. 24, 147 (1992)

[17] Rothschild, K. J., J. Bioenerg. Biomembr. 24, 147 (1992)

[18] Earnest, T. N., Herzfeld, J., Rothschild, K. J., Biophys. J., 58, 1539 (1990)

[19] Bagley, K., Dollinger, G., Eisenstein, L., Singh, A., K., Zimanyi, L., Proc. Nat. Acad. Sci. USA. 79, 4972 (1982)

[20] Rothschild, K. J., Marrero, H., Proc. Nat. Acad. Sci. USA. 79, 4045 (1982)

[21] Heyes, D. C., El-Sayed, M. A., J. Biol. Chem. 277, 29437 (2002)

[22] Harada, I., Yamagishi, T., Uchida, K., Takeuchi, H., J. Am. Chem. Soc. 112, 2443 (1990)

[23] Ames, B. J., Ros, M., Raap, J., Lugtenburg, J., Mathies, A. R., Biochemistr. 31, 5328 (1992)

[24] Hashimoto, S., Sasaki, M., Takeuchi, H., Needleman, R., Lanyi, K. J., Biochemistry**.** 41, 6495 (2002)

[25] Koglin, E., Séquaris, J-M., Top. Curr. Chem. 134, 1 (1986)

[26] Grabbe, S. E., Buck, P. R., J. Am. Chem. Soc. 111, 8362 (1989)

[27] Cotton, M. T., Van Duyne, P. R., FEBS lett. 147, 81 (1982)

[28] Fleichmann, M., Hendra, P. J., McQuillan, A. J., Chem. Phys. Lett. 26,163 (1974)

[29] Cotton, M. T., Schultz, G. S., Van Duyne, P. R., J. Am. Chem. Soc.**,** 1980,27 (1980)

[30] Stewart, S., Fredericks M. P., Spectrochimica Acta Part A.**,** 55, 1641 (1999)

[31] Smulevich, G., Spiro, G. T., J. Phys. Chem.**,** 89, 5168 (1985)

[32] Nabiev, I., Morjani, H., Manfart, M., Eur. Biophys. J. 19, 311 (1991)

[33] Huang, X., El-Sayed, H. I. , Qian, W., El-Sayed, A. M., Nano Lett. 7,1591 (2007)

[34] Tripp, R. A., Dluhy, R.A., Zhao, Y., *Nanotoday.* 3, 31 (2008)

[35] Frens, G., Nat. Phy. Sci. 241, (1973)

[36] Lee, P. C., Meisel, D., J. Phys. Chem. 86, 3391 (1982)

[37] Mahmoud, M. A., El-Sayed, M. A., J. Phys. Chem. C. 112, 14618 (2008)

[38] Smith, O. S., Braiman, M.S., Myers, A. B., Pardoen, A. J., Courtin, J. M., Winkel, C., Lugtenburg, J., Mathies, R., J. Am. Chem. Soc.**,** 109, 3108 (1987)

[39] Moskovits, M., J. Raman Spectrosc. 36, 485 (2005)

[40] Hao, E., Schatz, C. G., J. Chem. Phys.**,** 120, 357 (2004)

[41] Jiang, J., Bosnick, K., Maillard, M., Brus, L., *J. Phys. Chem. B.* 107, 9964 (2003)

[42] Nie, S., Emory, S. R., *Science.* 275, 1102 (1997)

CHAPTER VI

DIFFERENTIAL CURRENT MEASUREMENTS OF bR FILMS IN PRESENCE OF Au AND Ag NANOPARTICLES.

Abstract:

In order to establish whether a plasmonic field can improve the photochemical efficiency of bR, current measurements of bR films deposited on indium-tin-oxide (ITO) are performed. Under CW white light excitation, the differential current of pure bR films is compared to that of bR films embedded with Au or Ag nanospheres. It was found that Au nanosphere does not increase bR photochemical efficiency while Ag nanoparticles seems to have an ideal concentration range where the area of the "OFF peak" current is increased of about 17%

Introduction

Bacteriorhodopsin (bR) is a protein-chromophore complex able to undergo a photochemical reaction where photons are converted to a proton gradient. The chromophore is a retinal Schiff base bounded to the protein through a lysine residue. The absorption of light triggers a photocycle where intermediates are generated to transport a proton from the cytoplasmic side of the membrane to the extracellular, before reestablishing its initial form[1]. Measurements of the light-induced transient current have been performed in various bR films[2-6] where the protein was deposited on an electrode made of tin-oxide glass, which is transparent in the visible range. In this chapter, we report current measurement done under CW excitation, but pulsed excitation could be

used as well. While CW excitation provides a measure of the overall current released by the protein, which is directly related to its ability of pumping protons, pulse excitation gives more information on the molecular mechanism underneath the generated current. Three components are observed (B1, B2 and B3). B1 is the fast component, in the nanosecond time scale[8, 9], found to be related to the retinal Schiff base isomerization, accompanying the formation of the intermediate K[9, 10]. The B2 component has been assigned to the proton transport though the membrane, a good correlation between B2 and the L to M transition in the photocyle has been found for a wide range of pHs[11], and a slow component, B3, in the millisecond time scale, whose origin is related to the differential current observed under CW excitation[6].

CW excitation instead gives rise to two current spikes, for randomly deposited bR films on ITO. The origin of such spikes was first interpreted as due to charge-displacement at the membrane level[12], but later, a different model was proposed assigning the differential current to pH change at the bR/ITO electrode interface, upon bR proton release and uptake. Metal oxide electrodes (like ITO), have in fact, an electrochemical potential equilibrium that is pH dependent[13]. The current produced still can be correlated to the proton pump efficiency of the bR, and consequently it can be used as a method to compare efficiencies. The CW excitation on randomly oriented bR dry films, being a surface phenomenon, has the advantage to be virtually independent from the film thickness[13]. The first layer of bR patches is the one affecting the current peak, while the other layers produce only small modification to the peak shape. This makes comparison of currents from different films easier, as long as the same film area is excited in all the samples. Samples of bR with different concentrations of Au and Ag nanaoparticles were exposed to CW white light excitation and their differential currents were measured as function of the nanoparticles concentrations and light intensities. The CW excitation conditions were chosen to evaluate the applicability of bR in solar cells related

applications. It was found that for Ag nanoparticles there seems to be an optimal concentration for which the OFF peak current is increased of about 17%.

6.1 Differential current measurements of bR film with dual excitation: CW white light and CW 808 nm

With the knowledge of what has been learnt on chapter 4, regarding the effect of Au NRs plasmonic field on the proton pump dynamics of the intermediate M_{412}, the first idea was to add NRs, having longitudinal plasmon band in the 800 nm range and measured the differential current when NRs were excited by an independent CW source, the same used in the M_{412} experiment (808 nm).

Two sources need to be overlapped on the film, one to provide excitation to the bR system (the CW white light) and a second to excite the NRs plasmon band. The differential current is then measured in presence of both. It is important to establish the effect on the generated differential current of having the extra CW source on while having the CW source at 808 nm. We had reason to believe that the extra source would not cause changes to the current, since no absorption takes place in the film in this wavelength region. Films of pure bR where tested and surprisingly we observed a large decrease (about 30% with 0.12 W/cm^2 power) in current intensity when the 808 nm light is on.

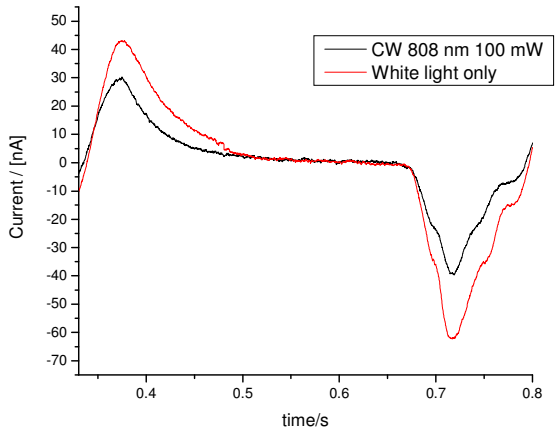

Fig. 6.1: Current decrease when CW 808 nm light is shone on the bR film.

The reason for such drastic decrease in current was addressed by further measurement, revealing bleaching of the film upon exposure to the 808 nm light.

Due to the unexpected outcome the current measurements with NRs will not be executed.

Materials and methods

Purple membrane was prepared from strain S9-P and purified according to the standard procedure reported on Chapter II. Bacterioopsin (bO) was obtained from bR by bleaching with hydroxylamine[14], the product, retinaloxime, was removed by washes with bovine serum[15] followed by deionized water.

Starting bR solutions are prepared by adding deionized water with concentration on the order of 50-100 μM.

Solutions of Au and Ag nanospheres citrate capped were prepared according to the procedure described previously. The Au nanoparticles have a diameter of 13-15 nm and a concentration about 15 nM (OD=0.36 in a 1 mm cuvette at 522 nm) while the Ag NPs

have about 70 nm in diameter with an OD of 0.28 units of absorbance at 438 nm in a 1 mm quartz cuvette.

Solutions of bR with various amounts of Ag or Au NPs were prepared and after vigorous stirring, and then poured on precleaned ITO glass slides (8mm x12mm).

The ITO slides are then let to evaporate the excess water and films are obtained.

Absorption spectra of the films are taken using an Ocean Optics HR4000CG-UV-NIR spectrometer. The films are light adapted for 1 hr before measurements are taken. The ITO with randomly oriented films on it represents the working electrode which is placed in a glass cuvette (10x10x45 mm) along with the reference electrode (a blank ITO glass slide) filled with an electrolyte solution at pH 7 containing NaCl 50 mM and KH_2PO_4 10 mM. The working electrode is connected to the negative input using a copper alligator clip, while the reference electrode is connected to the positive input of a Keithley current amplifier (model 428). The amplification was set to 10^8 V/A for all samples.

The light source is a Mercury-Xenon arc lamp (200W), the white light goes though two apertures, and afterward collected by a soft focusing lens. The beam diameter at the sample was 0.8 cm. A water filter (WF) is placed before the sample to reduce the NIR and UV wavelengths of the lamp spectrum; low pass filters will be placed on the beam path to block the wavelength range corresponding to the Ag NPs plasmon excitation, to be able to compare the differential current of bR film with Ag NPs in presence and absence of surface plasmon.

The modulation of the cw white light is obtained using a modified chopper, with a fixed repetition rate of 4 Hz. The output of the current amplifier was sent to an oscilloscope (Lecroy 420 500 MHz), triggered by the chopper control box. Typically current signals were averaged over 150 chopper modulations to improve the signal to noise ratio.

A schematic of the set-up used is reported in fig. 6.2.

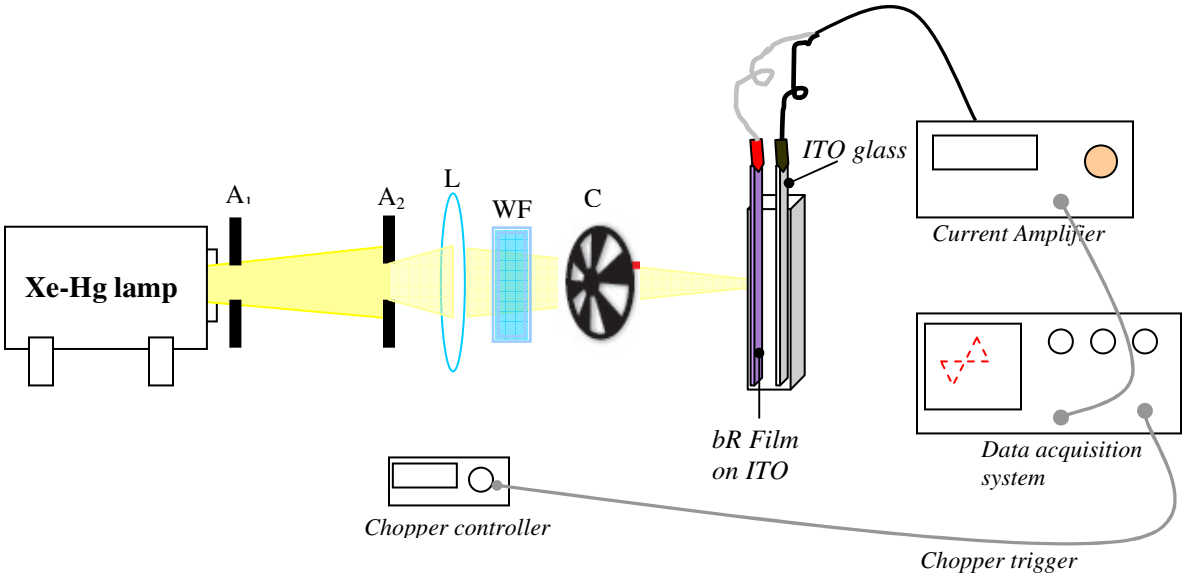

$A_{1,2}$=aperture L=lens WF=water filter C=Chopper

Fig: 6.2: Set-up used for differential current measurements using CW excitation.

Samples preparation:

Films of pure bR on ITO glass slides are obtained simply by pouring bR solution using a glass transfer pipet. For the samples containing nanoparticles the solutions are obtained simply by mixing bR in deionized water with previously synthesized nanoparticles solutions.

The samples are then let to dry overnight on a flat surface at room temperature. Absorption spectra of the films obtained are taken before and after exposure. No bleaching was observed.

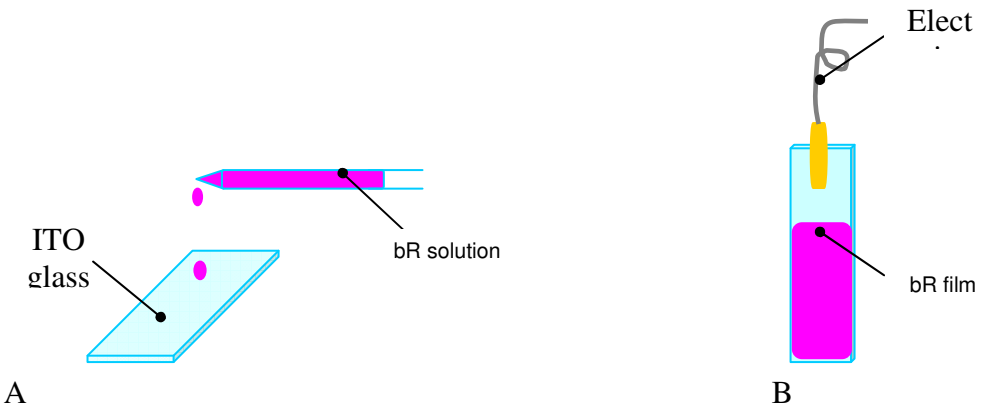

Fig. 6.3: A) Sample preparation for bR film on ITO substrate. B) The ITO glass is not completely covered to allow good electric contact to the ITO substrate.

6.2 Current measurements on pure bR films

Preparing two bR films having different thickness, and measuring their current under identical excitation conditions tests the independence of the current from film thickness, for randomly oriented bR films. Differential currents were measured for the two samples and fig. 6.4 reports the experimental data. Very little difference in current peaks and shape, for the two samples, proves it.

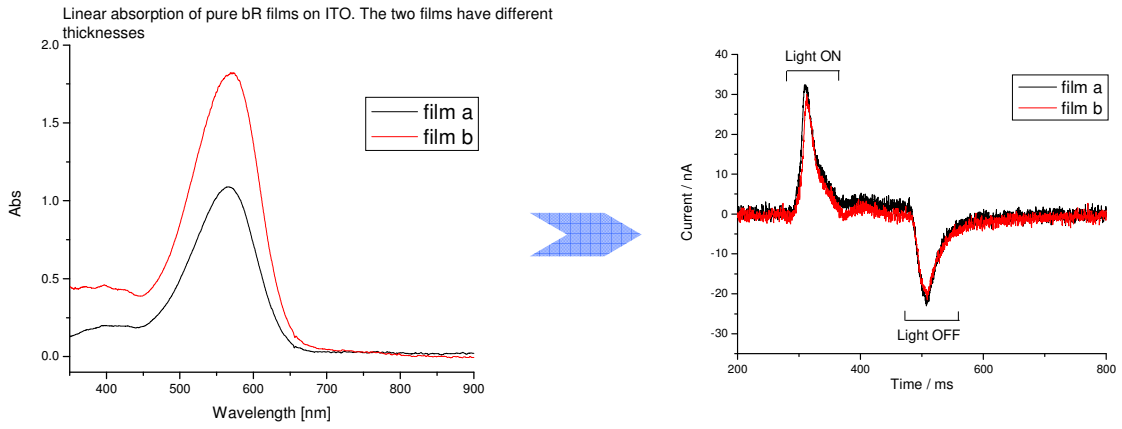

Fig. 6.4: Differential current curves for two bR films on ITO with different thickness. The differential current is indeed found thickness independent

Current measurement with different excitation conditions are purposely chosen: one where only a water filter (WF) is in place, and a second one where low pass filters are in place to block high energy wavelength up to 550 nm (see fig. 6.7). The different illumination conditions are aimed to provide current data from bR films in presence and absence of the surface plasmon when NPs are embedded in the film.

Current measurement for pure bR under the conditions described above are taken for different incident intensities and the data reported in fig. 6.5 and 6.6.

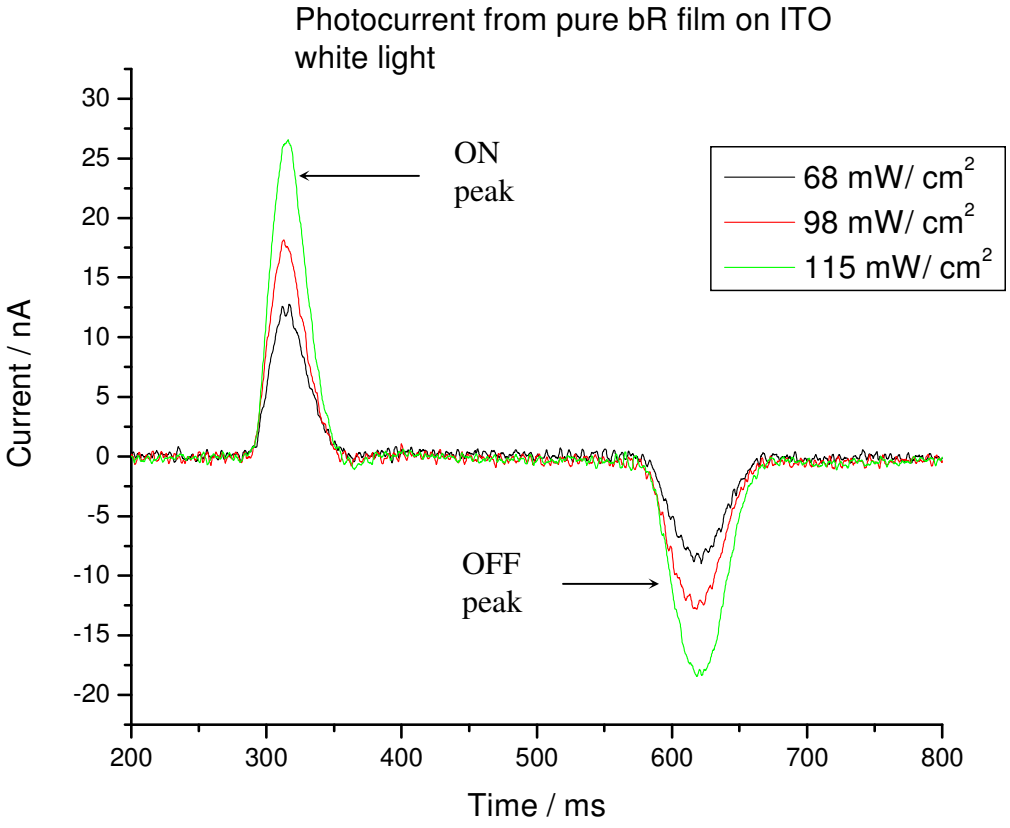

Fig. 6.5: Differential current for pure bR film on ITO glass substrate with pH 7 buffer for different illumination intensities, only WF was present. The peak indicated as "ON peak" is the differential current released when the light is on, while the "OFF peak" when the light is blocked.

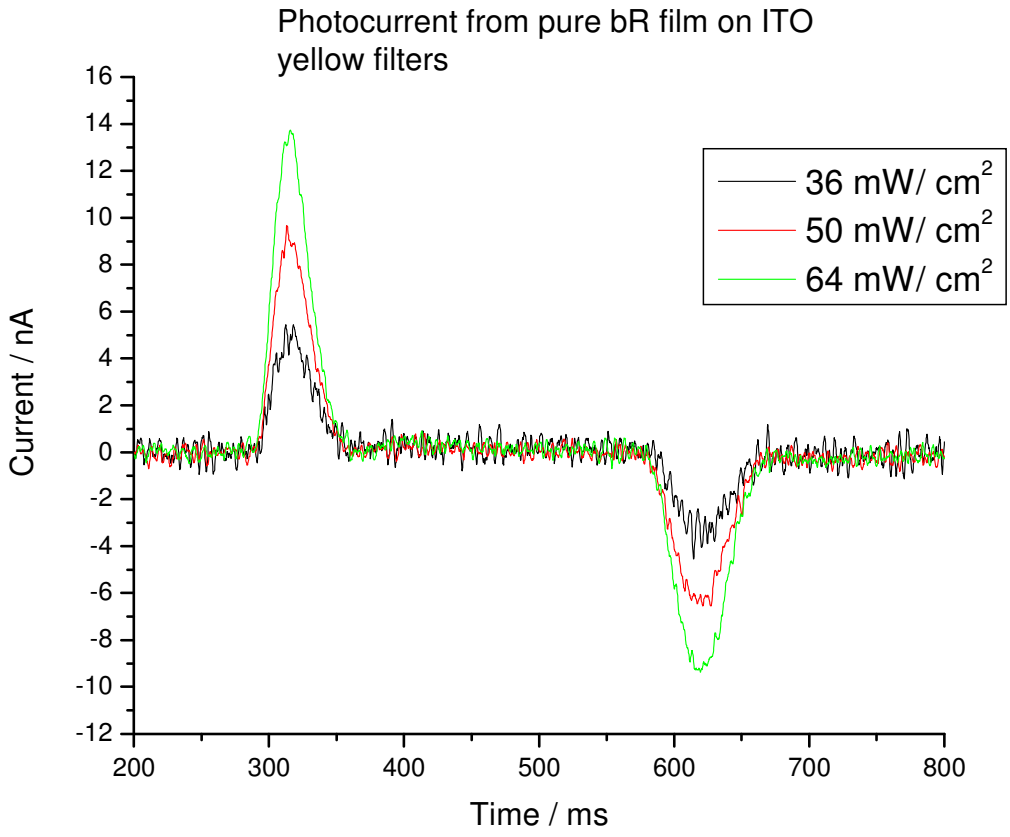

Fig. 6.6: Differential current for pure bR film on ITO glass substrate with pH 7 buffer for different illumination intensities, WF and low pass filters on.

After repeating the current measurements for various samples it turned out that the peak intensity is subject to relatively large changes: in particular the ON peak suffers changes up to ±10% in value (calculated as standard deviation) while the OFF peaks are more reproducible, with a ±6% dispersion. Instead what was found to be more reproducible, were the integrated peak area values; variations are again larger for the ON peak with about ±7%, while the off peak variations are contained to a ±4% in value.

6.3 bR film embedded Ag NPs: differential current measurements

Ag nanoparticles citrate capped were obtained according with the procedure reported in literature by Lee and coworkers[16].

Fig.6.7 shown the surface plasmon band for the Ag NPs synthesized and that of the filters used to block it.

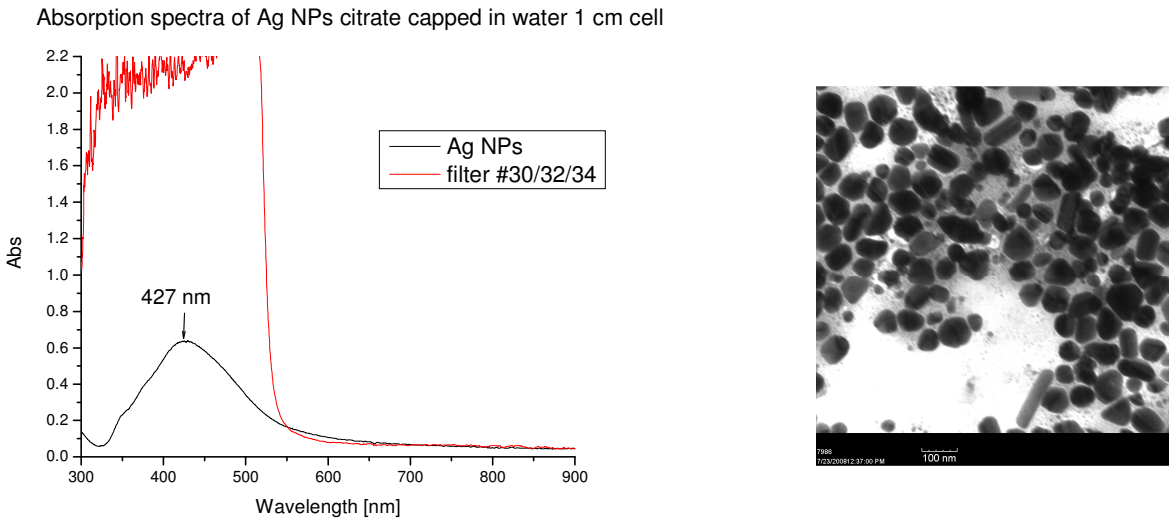

Fig 6.7: On the left is shown the absorption spectra of the Ag nanoparticles used in the samples preparation (red) along with the absorption spectra of the filters used to block the surface plasmon of the Ag NPs. On the right is a TEM image of the Ag NPs showing an average size of 80 nm for the particles synthesized.

Solutions of bR with different amounts of Ag NPs are prepared. Table 5.1 contains the different volumes used to prepared samples I, II and III with increasing concentration of Ag NPs freshly prepared.

Table 6.1: Dosage used on the Ag NPs embedded films preparation

Sample	bR solution/ μL	Ag NPs solution/ μL
I	150	60
II	150	90
III	150	110

Current measurements are performed on each film using the two different excitation conditions. The data obtained for sample II are reported below in fig 6.7

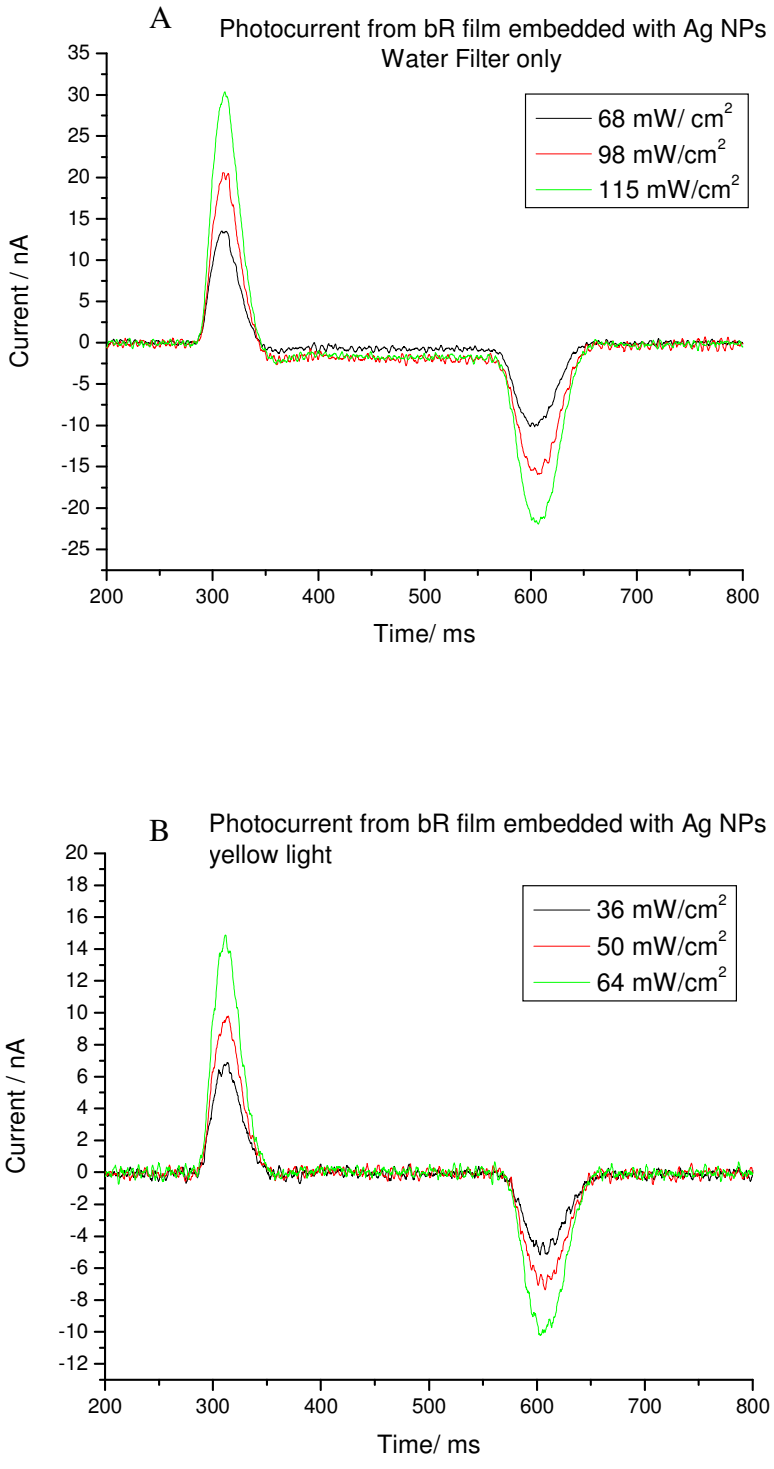

Fig. 6.8: A) Sample II differential current measured when a WF is n placed. B) Sample II differential current when low pass filter are in place to block the surface plasmon from the Ag NPs present

The integrated area for the ON and OFF peaks have been calculated using Origin 7.0

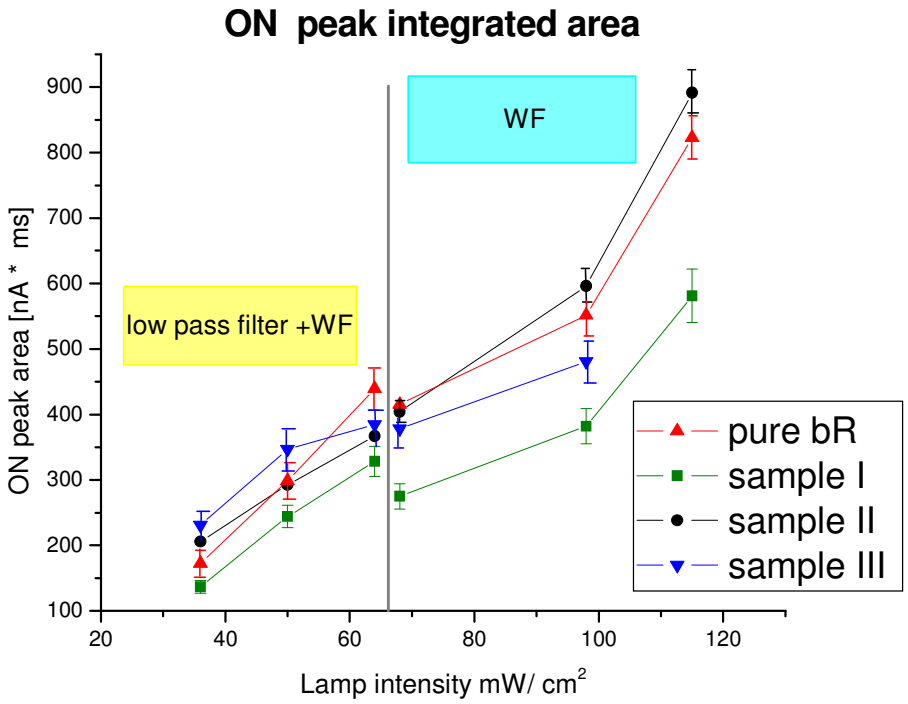

Fig 6.9: Integrated values for the ON peaks at various irradiation energies when only the water filter is placed before the sample (data point on the right) and when low pass filter are placed and no plasmon excitation takes place (data point on the left).

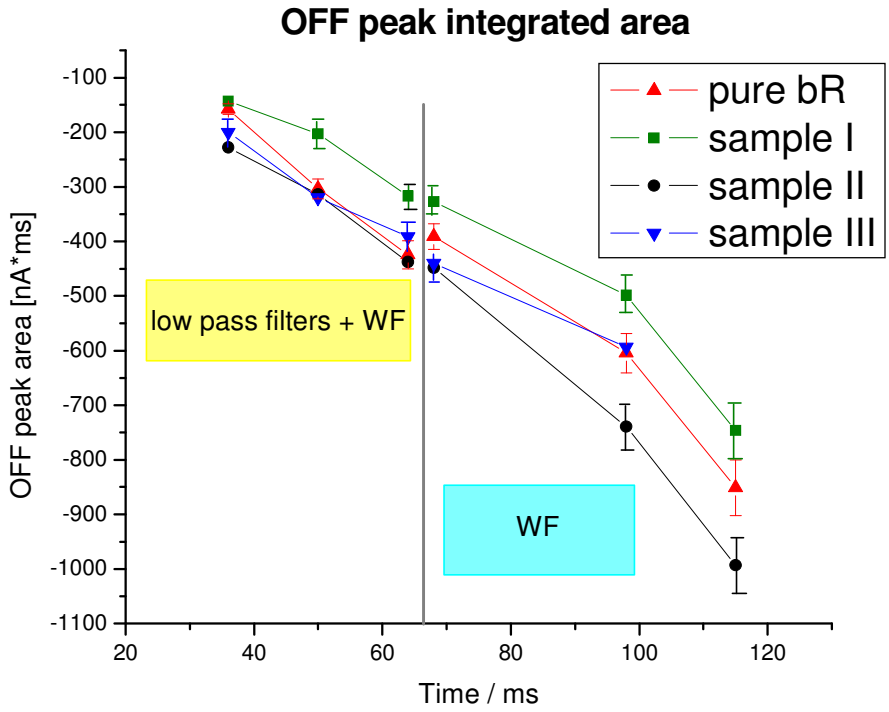

Fig. 6.10: Integrated values for the OFF peaks at various irradiation energies when only the water filter is placed before the sample (data point on the right) and when low pass filter are placed and no plasmon excitation takes place (data point on the left)..

A recurrent behavior for the samples containing nanoparticles is that the baseline after the ON peaks is offset when the water filter is in place. The offset is not present, for the same sample when the low pass filters are in place. A sample containing Ag NPs is then prepared in bacterioopsin (bO) rather than bR. bO does not contain the chromophore Retinal Base Schiff, but provides the same matrix. A film of Ag NPs embedded in bO is prepared and current measurement are performed as described. When the plasmon is excited (only WF on the beam path) a small current is measured as shown in fig. 5.9, the current is not present when the low pass filters are blocking the plasmon, suggesting that the surface plasmon induces a weak current flow. A pH change at the ITO substrate is the reason for observing a current, as discussed previously, and the source for the pH change reside on the capping material. Even though not proved yet, there are reasons to

believe that citrate can reduce, in presence of light, silver atoms and form CO_2[17]. The CO_2 released would be responsible for small change in pH at the ITO/bO interface causing the small current flow. When the plasmon is not excited instead the reaction does not take place as efficiently and no current is register as shown in fig 6.10.

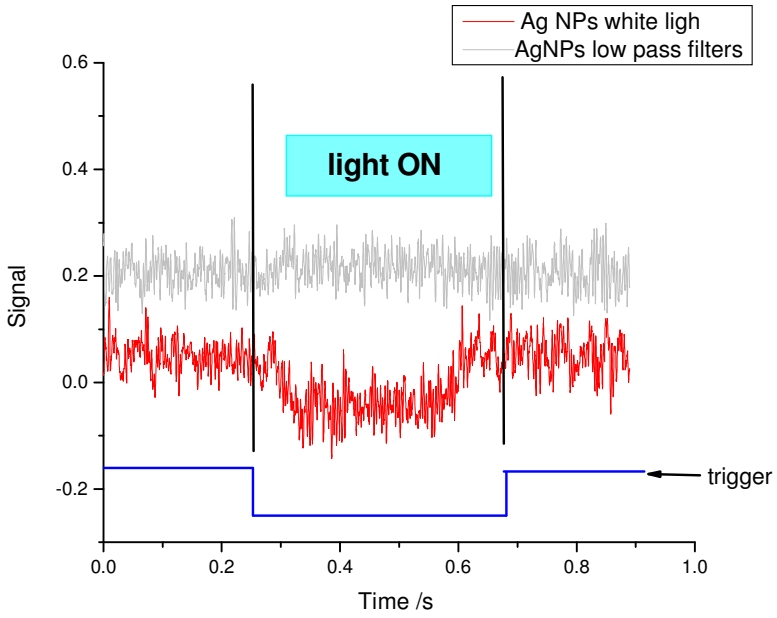

Fig 6.11: Current measurement for Ag NPs embedded in bO. Red data show a current generated upon excitation of the Ag NPs plasmon. The gray data instead is relative to excitation with low pass filters, no current is measured under these conditions.

Discussion:

As mentioned the integrated area of the OFF peak is more reliable from sample to sample and will be making our considerations based on this parameter to compare the efficiency of one film versus the other. From fig. 5.8 sample II emerges as that with the largest integrated area for the OFF peak (negative value) in the WF excitation (when the surface plasmon is excited). When the plasmon is off, because of the low pass filters the values obtained for the films are very close one to the other. The increase is about 17% when

compared to the pure bR film. For sample I and III the behavior is different, sample I differential current is overall less than the pure bR, while sample III values are comparable with that of the pure bR films. To make sure that the values obtained were not the result of equipment problem (for instance a bad electric contact between the ITO surface and the alligator clip could vary the current value quite a bit), the experiment is repeated using freshly prepared Ag nanoparticles and new films are cast. The results supported what was found previously, suggesting that Ag NPs increase the efficiency of the bR differential current when embedded in it, for a limited concentration range. The effect cannot be simply due to thermal processes from nanoparticles, as suggested by the current trend with the NPs concentration. The underlying reason for having larger current is not clear and the concentration dependence is not yet understood.

REFERENCES:

[1] Hauptus, U., Tittor, J., Oesterhelt, D., Ann. Rev. Biomol. Struct. 28, 367 (1999)

[2] Miyasaka, T., Koyama, K., Chem. Lett. 9, 1645 (1991)

[3] Miyasaka, T., Koyama, K., Itoh, I., *Science.* 255, 342 (1992)

[4] Keszthelyi, L. O., P., FEBS Lett. 109, 189 (1980)

[5] Keszthelyi, L. T.-B., R., Der, A., J. Mol. Struct. 297, 13 (1993)

[6] Wang, J.-P., Song, L., Yoo, S., El-Sayed, M. A., J. Phys. Chem. 101, 10599 (1997)

[7] Hong, T. F., Montal, M., Biophys. J. 25, 465 (1979)

[8] Trissl, H. W., Biochim. Biophys. Acta. 806, 124 (1985)

[9] Groma, G. I., Raksi, F., Szabo, G., Varo, G., Biophys. J. 54, 77 (1988)

[10] Keszthelyi, L. O., P., Biophys. Chem. 18, 397 (1983)

[11] Liu, Y. S., Biophys. J. 57, 943 (1990)

[12] Koyama, K., Yamaguchi, N., Miyasaka, T., Science. 265, 762 (1994)

[13] Robertson, B., Lukashev, P. E., Biophys. J. 68, 1507 (1995)

[14] Oesterhelt, D. Shuhmann, L., Gruber, H., FEBS letters. 44, 257 (1974)

[15] Grooth, J. M. H., Smith, O. S., Courtin, J., Berg, E., Winkel, C., Lugtenburg, J., Griffin, R. G., Herzfeld, J., Biochemistry 29, 6873 (1990)

[16] Lee, P. C., Meisel, D., J. Phys. Chem. 86, 3391 (1982)

[17] Maillard, M., Huang, P., Brus, L., Nano Lett. 3, 1611 (2003)

CHAPTER VII

INTRODUCTION: NONLINEAR OPTICS AND ITS APPLICATIONS

7.1 Nonlinear optics (NLO) fundamentals: microscopic and macroscopic Polarization description.

7.1.1 Macroscopic description of the Polarization

The interaction between an oscillating field *E* and charges present in a molecule cause changes in the dipole moment of the molecule μ, due to charge redistribution. The induced polarization can be described as a power series in the electric field:

$$\mu_i = \mu_i^0 + \alpha_{ij} E_j + \beta_{ijk} E_j E_k + \gamma_{ijkl} E_j E_k E_l + \ldots \quad (7.1)$$

Where μ_i^0 is the molecule permanent dipole, α_{ij} is the first order polarizability, β_{ijk} is the second-order polarizability (also called first hyperpolarizability), and γ_{ijkl} being the third-order microscopic polarizability, also called second hyperpolarizability. Equation 7.1 can be express as a Taylor series where factorials coefficient are introduced[1]. In 7.1 the linear term describes a regime where the molecule polarization is linearly proportional to the applied electric field, however, when a high electric field is applied the polarization

becomes a nonlinear function of the field strength. The terms beyond αE are referred to as *nonlinear terms.*

7.1.2 Macroscopic description of the Polarization

The phenomenological interaction of light in a dielectric medium can be described through a relation analogous to 7.1, where the field applied *E(t)* and the resulting polarization density *P* of the medium are related through 7.2:

$$P = P_0 + \chi^{(1)}E + \chi^{(2)}EE + \chi^{(3)}EEE + ... \tag{7.2}$$

The polarization density $P^{(0)}$ (*t*) represent the field-independent polarization, present in some materials. $\chi^{(1)}$ is the linear polarizability, responsible for linear optical effects, while $\chi^{(2)}$ and $\chi^{(3)}$ are the second and third-order susceptibility respectively. Terms that are higher than $\chi^{(1)}$ are called nonlinear terms

Such polarization *P* can be the result of a perturbation of the electron density in the medium or other interactions like dipoles alignment, separation of charges etc.

The optical properties of a particular dielectric medium are described by the field-dependent susceptibility, $\chi(E)$.

Normal ambient light conditions, where the interactive electric field is weak, allow for neglect of nonlinear terms in 7.2, living the linear term only $\chi^{(1)}$. Such quantity

describes “linear optical phenomena” like absorption, reflection and refraction. For instance the linear index of refraction for a given material is define as

$$n = \sqrt{1 + \mathrm{Re}\,\chi^{(1)}} \tag{7.3}$$

For strong optical fields, enough to cause distortion of bonded electrons clouds without causing dielectric breakdown, higher orders are no longer negligible, and the optical properties are now defined by the intensities of the applied fields. The consequence of having nonlinear terms provide a mechanism for an optical field to interact inside the dielectric medium, causing a new set of phenomena that are not observed in linear regime as change of phase, or propagation direction as well as different absorption mechanism though two-photon absorption etc.

This new ensample of phenomena are known collectively as nonlinear optical phenomena (NLO) and the material in which such processes take place is a nonlinear medium. Phenomena that depend on the square of the applied field are called “second-order effects”. Examples are second-harmonic generation (SHG)[1], sum and difference-frequency mixing and electro-optic effect (also known as Pockels effect).

The phenomena on which this thesis is focus are the so-called “third-order effects”. Third-order effects include four-wave mixing (FWM), third harmonic generation (THG), self-focusing-defocusing, intensity-dependence refractive index, two-photon absorption and others.

7.2 Relationship between $\chi^{(3)}$ and γ

In a molecular medium, the polarization of the individual molecule is affected by the surrounding molecules. The field experienced locally by the m*th* molecule E_m is different from the applied field E_0. The two fields, E_m and E_0 can be related through the Lorentz-Lorentz local field factors[2, 3] $f(\omega)$, which accounts for intermolecular interactions. In isotropic media the local field factor is given by:

$$f(\omega) = \frac{[n_0]^2 + 2}{3} \tag{7.4}$$

The second-order hyperpolarizability γ_{ijkl} for an isotropic medium is an average over all the possible orientations of the molecules with respect to the applied field[3, 4] $\langle\gamma\rangle$. For a linear molecule, the second-order polarizability $\langle\gamma\rangle$ can be expressed in terms of the molecular tensor elements as:

$$\langle\gamma\rangle = \frac{1}{5}\left(\gamma_{xxxx} + \gamma_{yyyy} + \gamma_{zzzz} + 2\gamma_{xxyy} + 2\gamma_{yyzz}\right) \tag{7.5}$$

The following relationship then exists between $\langle\gamma\rangle$ and $\chi^{(3)}$:

$$\chi^{(3)} = f(\omega) N \langle\gamma\rangle \tag{7.6}$$

Where N represents the number of molecules per unit volume.

7.3 Characteristics of $\chi^{(3)}$ and γ

$\chi^{(3)}$ and γ are both complex quantities. They both have a real and an imaginary part:

$$\chi^{(3)} = \mathrm{Re}\,\chi^{(3)} + i\,\mathrm{Im}\,\chi^{(3)} \tag{7.7}$$

$$\langle\gamma\rangle = \mathrm{Re}\langle\gamma\rangle + i\,\mathrm{Im}\langle\gamma\rangle \tag{7.7a}$$

$\chi^{(3)}$ and γ become real when the frequencies of applied electric fields are far from any electric-dipole allowed transitions (including electronic, vibrational, rotational, etc.). As the frequency or one of their combinations becomes resonant with a transition they acquire an imaginary part. As in other complex quantities, they can be specify in term of their modulus ($\left|\chi^{(3)}\right|, |\gamma|$) and phase angle φ:

$$\chi^{(3)} = \left|\chi^{(3)}\right| \exp(i\varphi) \tag{7.8}$$

$$\gamma = |\gamma| \exp(i\varphi) \tag{7.8a}$$

Where

$$\varphi = \arctan\left(\frac{\mathrm{Im}\,\chi^{(3)}}{\mathrm{Re}\,\chi^{(3)}}\right) \tag{7.9}$$

$$\varphi = \arctan\left(\frac{\mathrm{Im}\,\gamma}{\mathrm{Re}\,\gamma}\right) \tag{7.9a}$$

and

$$\left|\chi^{(3)}\right| = \sqrt{\left(\mathrm{Re}\,\chi^{(3)}\right)^2 + \left(\mathrm{Im}\,\chi^{(3)}\right)^2} \tag{7.10}$$

$$\langle\gamma\rangle = \sqrt{\left(\mathrm{Re}\,\gamma\right)^2 + \left(\mathrm{Im}\,\gamma\right)^2} \tag{7.10a}$$

7.4. Nonlinear refractive index and two-photon absorptions: fundamentals and applications

7.4.1. Nonlinear refraction index

This study focuses on the determination of third-order effects, in particular two-photon and nonlinear refractive index. Both phenomena are contained within the complex quantity described as $\chi^{(3)}$ and a more quantitative description is provided by their expression as field intensity dependent, *I*. The intensity dependent index of refraction is defined as:

$$n = n_0 + n_2^{(I)} I \tag{7.11}$$

The index of refraction defines the propagation of an electromagnetic wave in a medium. The possibility of changing the index of refraction of the medium through nonlinear processes would open the possibility of controlling the propagation of a second optical

field in the medium[5]. Such concept is used in a nonlinear Mach-Zehnder interferometer illustrated in fig.7.1.

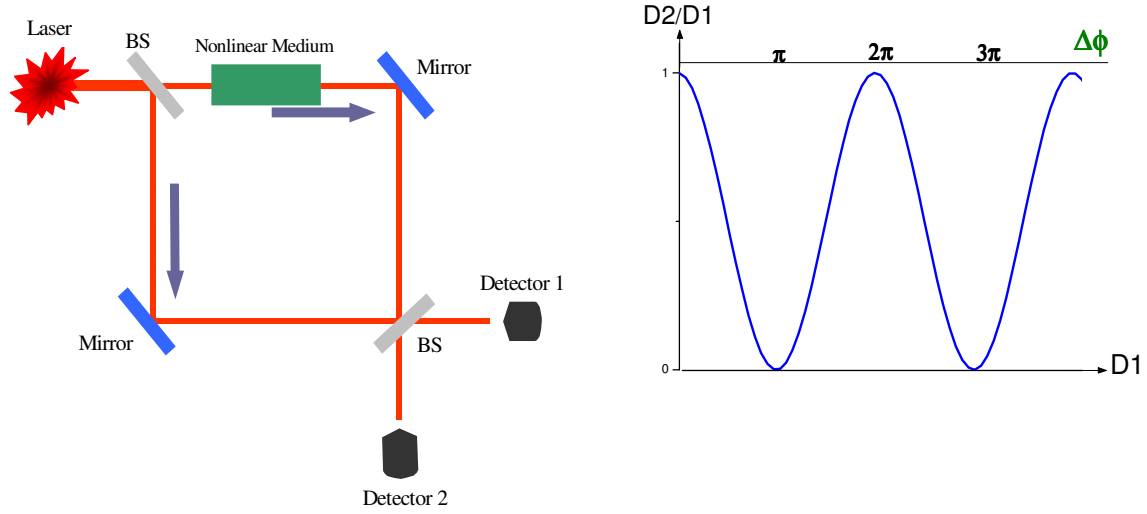

a b

Fig. 7.1. (a) Nonlinear Mach-Zehnder interferometer. The beam is split into 2 arms, and when the refractive index of the nonlinear medium changes, a phase shift is produced causing a change in the resulting intensity on Detector 2 (D2). D2/D1 oscillates between 1 and zero depending upon the phase shift generated by the nonlinear medium. (b) Intensity change at detector 2 as function of the input intensity.

The input beam is divided in 2 arms; in one arm a nonlinear material is placed. Each beam travels an effective distance, which is fixed for the reference arm (arm without nonlinear material) while it can change depending upon the incident intensity for that comprising the NLO material. The phase shift generated will affect the intensity measured by detector 2 (D2) of the recombined beams. When the phase difference, indicated as $\Delta\phi=0$, the two beams interfere constructively giving the same initial intensity (after taking into consideration losses due to scattering, absorption etc.). As the material

refractive index changes according to (7.11), the phase change will be intensity dependent and (7.12) gives its full expression:

$$\Delta\phi^{NL} = \frac{2\pi L n_2 I_{NLO}}{\lambda} \qquad (7.12)$$

Where I_{NLO} is the beam intensity in the NLO material and L is the distance traveled in the medium. Destructive interference takes place when $\Delta\varphi^{NL} = \pi, 3\pi, 5\pi, \ldots$ where the intensity out is zero (D2=0). The output intensity on D2 can be varied continuously between zero and the initial input intensity as shown on fig 8.1.

Variables to the set-up described in 1.1 can be implemented; in particular a third beam (or control beam) can be used to induce an index change in the nonlinear material. The input beam can be substituted with short pulses rather than a cw beam, representing information as "optical bits". The on and off intensity of the beam can be interpreted as 0 or 1 in an "optical logic" format. The Mach-Zehnder interferometer is one of many other applications based on refractive nonlinearities: Fabry-Perot etalon, prism coupler, and directional coupler are some example of devices used on a regular basis. The possibility of using optical signals to process information, and to transmit them over long-distances through optical fiber, presents a distinct advantage in respect to conventional electronics limited by the switching component usually represented by a capacitor. The inherent limitation is the rate of charging and discharging given by $\approx 1/RC$, where R is the resistance and C the condenser capacitance. With this technology the switching rates is not expected to operate above 10 GHz. In the optical case, switching rates could be as

high as 100 THz, with a 4 orders of magnitude increase, generating a large impact on conventional electronics.

7.4.2 Two-photon absorption

There is a finite probability for a medium to absorb two photons simultaneously to access a higher energy state, this concept was first introduced by Maria Göppert-Mayer[6] in 1931. Such process is observed when high photon densities sources, like lasers, are used. The process depends on the square of the laser intensity and it is contained in the third-order nonlinearity tensor.

In absence of linear absorption the intensity of a beam propagating along the z direction in a nonlinear absorbing material can be described by (7.13)

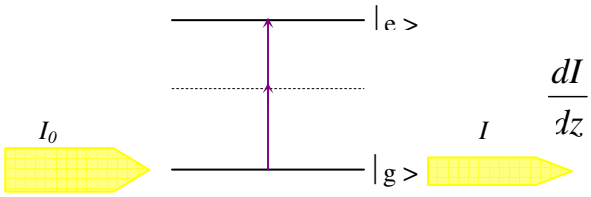

$$\frac{dI}{dz} = -\beta I_v^2 \tag{7.13}$$

Fig. 7.2: Illustration of the two-photon absorption process

Where β is defined as the macroscopic two-photon coefficient.

Two-photon absorption is well known in organic molecules and it has found applications in optical limiting, 3D optical data storage[7-10], photodynamic therapy[11-13] and microfabrication[14-16] , where greater spatial resolution and penetration depths have the advantageous properties such applications rely upon.

An optical power limiting material is capable of reducing the intensity of a beam through optical processes (nonlinear absorption, excited state absorption, scattering etc.) when its intensity reach a threshold value I_0. Materials with such properties are desirable for protection of sensors and human eyes from high intensity light beams like lasers; other applications include pulse shaping and optical data processing applications[17-19]. An ideal I_{out} versus I_{input} for such material is shown in fig. 7.3

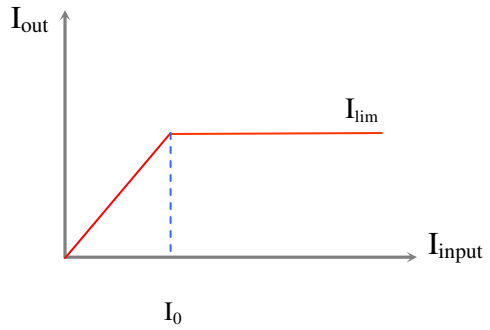

Fig. 7.3. Optical response out of an ideal optical power limiting material. When the input beam intensity, $I_{input}<I_0$ the output intensity is proportional to the input intensity, while when $I_{input}>I_0$ the output intensity stays constant to a value indicated as I_{lim}

Ideal optical limiting material are then transparent under "ordinary condition" while they can promptly absorb or block intense laser light; and two-photon absorption[20-22] (TPA) is one of the main processes, together with reverse saturable absorption (RSA), limiting materials rely upon. TPA is very attractive for its instantaneous response compare to RSA where the limiting properties are dictated by the population of triplet states generated through intersystem crossing from the one-photon accessible S_1 state[23-28]. The NIR region is where a large variety of sensors are utilized for industrial processes and quality control[29, 30], where optical limiting materials are desirable as sensor protectors.

The demand for two-photon absorber in the NIR, especially in the telecommunication region between 1300 to 1550 nm, is represented by applications in ultrafast optical clock recovery; directly related to the optical signal processing of ultrafast pulses, which require any kind of optical transceiver or regenerator in order to collect and read such optical signals. Two-photon absorbing materials have been successfully implemented in clock recovery systems used to synchronize the incoming data when photo-detectors and electrical circuit are limited by their speed. Many efforts are being made in designing more effective organic two-photon absorbers, but the criteria have not been fully developed yet[31]. A systematic approach to this problem is determining their structure-properties relationship[32-36]. Organic molecules have the advantage that their structure can be altered and engineered to enhance their properties. To date, TPA based optical limiters are represented mostly by inorganic semiconductors[37], especially in the NIR region where very few from the organic optical limiters have been reported so far; among which highly conjugated systems with strong TPA centered around 1000 nm have been exploited by Marder and coworkers [38, 39]. Fused azulene and oligomeric porphyrins have shown large TPA cross-section between 1200 and 1400 nm[40, 41] along with nickel bis(diothiolene) complexes[42]; and lately symmetric heptamethine dyes have shown promising TPA in the 1200-1400 nm range as well[43].

For the Vis-NIR region the linear quadrupolar structure D-A-D is commonly used[31, 44, 45]; where D represent a donor group, π is a conjugated bridge and A is an acceptor group. Theoretical calculations show in fact that there is still much potential for organic system to develop large two-photon cross-sections[46-48].

7.5 Aim of the section

This section is concerned with the study of squaraine type molecules via DFWM and Z-Scan in the 1.3 to 1.5μm range also known as the telecommunication range (or telecom range) to determine their third-order susceptibility. For our study it was important to determine both the real and the imaginary part of both γ and $\chi^{(3)}$, when possible, the later of particular interest for device type of applications. Intrinsic problem with determining such nonlinear properties will be discussed, as well as advantages and limitation of the two techniques used. The squaraine nonlinearity will be compared with that of other molecular systems (donor-π-acceptor) that are of interest for this wavelength range.

REFERENCES:

[1] Meyers, F., Marder, S. R., Perry, J. W., Chemistry of advanced material, ed. L.V. Interrante. 1998, New York: Wiley.

[2] Shen, Y.R., *The principle of nonlinear optics*. 1984, New York: Wiley.

[3] Butcher, P. N., Cotter, D., *The elements of nonlionear optics*. 1990, Cambridge: Cambridge Univ. Press.

[4] Bredas, J.L., Adant, C., Tackx, P., Persoons, A., Pierce, B. M., Chem. Rev. 94, 243 (1994)

[5] Prasad, P.N., William, D. J., *Introduction to nonlinear optical effects in molecules and polymers*. 1991, New York: Wiley.

[6] Goppert-Mayer, M., Ann. Phys. Lepz., 9, 273 (1931)

[7] Corredor, C. C., Huang, Z,-L., Belfield, K. D., Adv. Mater., 18, 2910 (2006)

[8] Pudavar, H. E., Joshi, M. P.; Prasad, P. N.; Reinhardt, B. A., Appl. Phys. B. **74**, 1338 (1999)

[9] Parthenopoulos, D. A., Rentzepis, P. M., Science. 245, 843 (1989)

[10] Strickler, J. H., Webb, W. W., Opt. Lett. 1991. **16**: p. 1780-1782.

[11] Bhawalkar, J. D., Kumar., N. D.; Zhao, C. F.; Prasad P. N., J. Clin. Laser Med. Surg. 15, 201 (1997)

[12] Fisher, A. M, Murphree, A. L., Gomer, C. J., Lasers Surg. Med. 17, 2 (1995)

[13] Fisher, W.G., Patridge, W. P., Dees, C., Wachter, E. A, Phtochem. Photobio. 66, 141 (1997)

[14] Cumpson, B. H., Sundaravel, A. P.; Barlow, S., Dyer, D., Ehrlich, J. E., Erskine, L. L., Heikal, A. A., Kuebler, S. M., Lee, I. -Y. S., Rumi, M., Wu, X. -Li, Marder, S. R.; Perry, J. W., *Two-photon polymerization initiators for three-dimensional optical data storage and microfabrication.* Nature. 398, 51 (1999)

[15] Maruo, S., Nakamura, O., Kawata, S. Optic. Lett. 22, 132 (1997)

[16] Zhou, W.H., Kuebler, S. M., Braun, K. L., Yu, T. Y., Cammack, J. K., Ober, C. K., Perry, J. W., Marder, S. R., Science. 296, 1106 (2002)

[17] Reddy, P.J.K., Curr. Sci. 61, 520 (1991)

[18] Penzkofer, A., Appl. Phys. B. 46, 43 (1988)

[19] Crane, L. R., Khoshevisan, M., Lewis, K., VanStryland, E. W., Mat. Res. Soc. 374**, (**1995) (Pittsburg PA)

[20] Ehrlich, J. E., Wu, X. L., Lee, I.-Y. S., Hu, Z.-Y., Rockel, H., Marder, R. S., Perry, W. J., Optic. Lett. 22, 1843 (1997)

[21] Bhawalkar, J., He, G., Prasad, P. Pep. Proc. Phys. 59, 1041 (1996)

[22] Baldeck, P. L., Morel, Y., Andraud, C., Nicoud, J.-F., Ibanez, A., Photon. Sci. News. 4, 5 (1998)

[23] Tutt, L., McCahon, S.W., Optic. Lett.15, 700 (1990)

[24] Su, W., Copper, T. M., Chem. Mater. 10, 1212 (1998)

[25] Mansour, K., Fuqua, P., Marder, R. S., Dunn, B., Perry, W.J., Proc. SPIE Int. Soc. Opt. Eng. 19**, (**1994)

[26] Perry, W. J., Mansour, K., Marder, R. S., Perry, K. J., Alvarez, D., Choong, I., Optic. Lett. 19, 625 (1994)

27. Perry, W. J., Mansour, K., Miles, P., Chen, T. C., Marder, R. S., Kwang, G., Kenney, M., Polym. Mater. Sci. Eng. 72, 222 (1995)

[28] Sun, Y.-P., Riggs, J. E., Liu, B., Chem. Mater. 9, 1268 (1997)

[29] Marquez, A. J., Diaz., A.M., Pascual Reguera, M.I*.,* Sens. Actua. B: Chemi., B107,. 64 (2005)

[30] Solberg, C., Develop. Food Sci. 38, 529 (1997)

[31] Moura, G. L. C., Simas, A. M., Chem. Mater. 20, 4142 (2008)

[32] Albota, M., Beljonne, D., Bredas, J.-L., Ehrlich, J. E., Fu, J.-Y., Heikal, A. A., Hess, S. E., Kogej, T., Levin, M. D., Marder, R. S., McCord-Maughon, D., Perry, W. J., Rockel, H., Rumi, M., Subramanian, G., Webb, W. W., Xu, C., Science. 281**,** 1653 (1998)

[33] He, G. S., Gen,.C. X., Prasad, P. N., Optic. Lett. 20, 435 (1995)

[34] Reinhardt, B. A., Brott, L. L., Clarson, S. J., Dillard, A. G., Bhatt, J. C., Kannan, R., Yuan, L., He, G. S., Prasad, N. P., Chem. Mater. 10, 1863 (1998)

[35] Birge, R. R., Acc. Chem. Res. 19, 138 (1986)

[36] Rumi, M., Ehrich, J. E., Heikal, A. A., Perry, J. W., Barlow, S., Hu, Z., McCord-Maughon, D., Parker, T. C.; Rockel, H., Thayumanavan, S., Marder, S. R., Beljonne, D., Bredas, J. L., J. Am. Chem. Soc. 122, 9500 (2000)

[37] Van Stryland, W. E., Woodal, A. M., Vanherzeele, H., Soileau, J. M., Optic. Lett. 10, 490 (1985)

[38] Beverina, L., Fu, J., Leclercq, A., Zojer, E., Pacher, P., Barlow, S., Van Stryland, W. E., Hagan, J. D., Bredas, J. -L., Marder, R. S., J. Am. Chem. Soc. 127, 7282 (2005)

[39] Zheng, S., Leclercq, A., Fu, J., Beverina, L., Padilha, L. A., Zojer, E., Schmidt, K., Barlow, S., Luo, J., Jian, S. -H., Jen, A. K.-Y., Yi, Y, Shuai, Z., Van Stryland, E. W., Hagan, D. J., Bredas, J. -L., Marder, S. R., Chem. Mater. 19, 432 (2007)

[40] Kurotobi, K., Kim, K. S., Noh, S. B., Kim, D., Osuka, A., Angew. Chem. Int. Ed. 45, 3944 (2006)

[41] Drobizhev, M., Stepanenko, K., Rebane, A., Wilson, C. J., Screen, T. E.O., Anderson, H. L., J. Am. Chem. Soc. 128, 12432 (2006)

[42] Cho, J.-Y., Barlow, S., Marder, S. R., Fu, J., Padilha, A. L., Van Stryland, W. E., Hagan, J. D., Bishop, M., Optic. Lett. 32, 671 (2007)

[43] Bouit, P.-A., Wetzel, G., Berginc, G., Loiseaux, B., Toupet, L., Feneyrou, P., Bretonniere, Y., Kamada, K., Maury, O., Andraud, C., Chem. Mater. 19, 5325 (2007)

[44] Spangler, C., J. Mater. Chem 9, 2013 (1999)

[45] Lemercier, G., Mulatier, J.-C., Martineau, C., Anemian, R., Andraud, C., Wang, I., Stephan, O., Mnari, N., Baldeck, P. C.R. Chimie. 8, 1308 (2005)

[46] Ventelon, L., Moreaux, L., Mertz, J., Blanchard-Desce, M., Synth. Met. 127, 17 (2002)

[47] Zojer, E., Beljonne, D., Kogej, T., Vogel, H., Marder, S. R., Perry, J. W., Bredas, J. L., J. Chem. Phys.116, 646 (2002)

[48] Zojer, E., Beljonne, D., Pacher, P., Bredas, J. L.,. Chemistry. 10, 2668 (2004)

CHAPTER VIII

ENGINEERING CONJUGATED SYSTEMS WITH LARGE NONLINEARITIES BY TUNING THE BOND LENGTH ALTERNATION IN DONOR/ACCEPTOR POLYENE SYSTEM.

Introduction

The development of organic materials for third order optical applications has been the focus of much effort in recent years[1-3]. Materials with sufficiently high nonlinearities that satisfy practical application requirements have yet to be discovered[4]. The materials that are employed continue to relay largely on inorganic[5-7] and semiconductor type of materials[8-10]. Organic molecules have several advantages over presently available nonlinear materials, given the fact that their properties can be tailored and modified for a particular application, along with their physical properties to improve processibility (drop-casting, spin-coating etc...). Still being investigated, are defined guidelines to make materials with large third order nonlinearities for optical applications. This chapter is dedicated to report theoretical studies based on an effort to rationalize the origin of microscopic third-order nonlinearity $\langle\gamma\rangle$ in unsaturated organic compounds.

8.1 The quantum chemical description

From a quantum-chemical point of view, one of the best ways to describe the interaction of light with a molecule is the sum-over-state technique (SOS), derived from the perturbation theory[11]. SOS is used to identify the excited states that play major role in determining nonlinearities[12, 13], while complete treatments would require the contribution from several states[14]. The SOS expression for the dominant component of the second hyperpolarizability tensor (Taylor series) γ_{xxxx} where *x* corresponds to the long axis of the molecule is expresses by equation 8.1.

$$\gamma_{xxxx} = 24\left(\sum_{m\neq g}\sum_{n\neq g}\sum_{p\neq g} \frac{\langle g|\mu_x|m\rangle\langle m|\overline{\mu}_x|n\rangle\langle n|\overline{\mu}_x p\rangle\langle p|\mu_x|g\rangle}{E_{gm}E_{gn}E_{gp}} - \sum_{m\neq g}\sum_{p\neq g} \frac{\langle g|\mu_x|m\rangle\langle m|\mu_x|g\rangle\langle g|\mu_x|p\rangle\langle p|\mu_x|g\rangle}{E_{gm}E_{gp}E_{gp}} \right) \tag{8.1}$$

Where $\langle g|\mu_x|m\rangle$ is the electronic transition moment along the *x*-axis between the ground state $\langle g|$ and an excited state $|m\rangle$. The $\langle m|\overline{\mu}_x|n\rangle$ operator represent the difference in dipole between the *m* and *n* states[15].

Equation 8.1 becomes slightly modify when NLO properties are evaluated. The expression for the denominator E_{gm} for instance becomes $(E_{gm} - h\nu - i\Gamma_{gm})$.

Where $h\nu$ is the incident photon energy and Γ_{gm} is a damping factor, dependent on the excited state under analysis, in this case *m.*

The denominator expression explains the resonance enhancement factor. The denominator is considerably reduced as the incident photons are approaching an electronic transition.

An accurate description of γ_{xxxx} would involve a large number of states, although a simplified version of equation 8.1 has been found reducing it to a three terms expression (equation 8.2)[16, 17]. For the simplified expression described in equation 8.2, the first excited state is strongly coupled with the ground state, along with a few higher excited states e', again, strongly coupled to the first excited state.

$$\gamma^{[\mathrm{mod}\,el]}_{xxxx} = 24\left(\frac{M^2_{ge}\Delta\mu^2}{E^3_{ge}} - \frac{M^4_{ge}}{E^3_{ge}} + \sum_{e'}\frac{M^2_{ge}M^2_{ge'}}{E^2_{ge}E_{ge'}}\right) \tag{8.2}$$

Where Δμ indicates the difference in dipole between the first charged transfer state and the ground state. M_{ge} and $M_{ge'}$ are the transition dipoles between the first and the higher excited state respectively.

When only three states are considered equation 8.2 becomes:

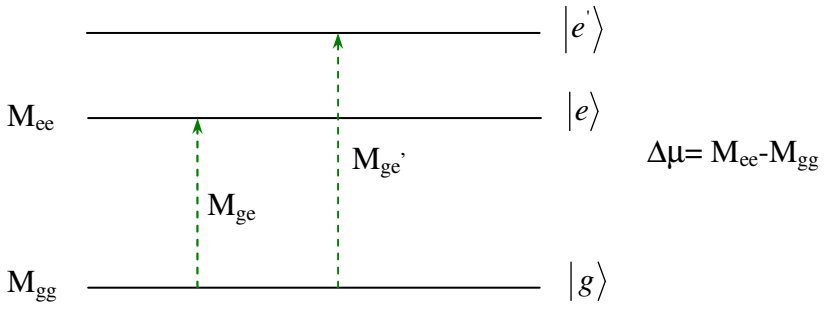

Fig. 8.1: Illustration of the three-state model.

$$\gamma^{[\mathrm{mod}\,el]}_{xxxx} = 24\left(\frac{M^2_{ge}\Delta\mu^2}{E^3_{ge}} - \frac{M^4_{ge}}{E^3_{ge}} + \frac{M^2_{ge}M^2_{ge'}}{E^2_{ge}E_{ge'}}\right) \tag{8.3}$$

Term notation: D N T

From a physical standpoint, the three terms can be described as follows:

D and N terms: D is the dipolar term, while N is the negative term. They both depend exclusively from the first excited state. As the BLA decreases, N increases, bringing a negative contribution that reaches a peak at the cyanine limit; D vanishes ($\Delta\mu=0$).

T term: also known as the two-photon term, takes into account the participation of higher energy state, beside the one photon allowed.

The model provides clues to key parameters that have direct impact on γ_{xxxx} and can be controlled by rational planning of the molecule structure.

8.2 Molecular structure and NLO properties relationship

The macroscopic nonlinearity of an organic material is defined by the microscopic nonlinearity of molecules that form the material. Conjugated molecules with their highly polarizable π-electronic cloud[6]. Substitution in the chain, with either donor or acceptor groups, induce different properties to the molecule, for instance favoring the two photon term rather than the N term. A model that provides structure –properties relationship for organic dyes is provided, aiming to optimize molecular structure to provide higher nonlinearities through the introduction of a parameter called Bond-Length Alternation (BLA).

8.2.1 Ground-state polarization and bond-length alternation BLA

The second order polarizability $\langle\gamma\rangle$ is, according to this model, directly correlated to the charge separation degree of the molecule ground state. The charge separation or polarization of the ground state, is a function not only of the donor and acceptor groups present, but it depends on the nature of the particular conjugated system and lastly, the environment surrounding the system [2] (i.e. polarity of the solvent).

Polyene systems have alternating double and single bonds, and for donor acceptor polyene, the ground state polarization can be directly related to a parameter called bond length alternation (BLA), defined as the difference in length between adjacent carbon-carbon single and double bond. For a neutral polyene system, the BLA is 0.11 Å (1.45 Å -1.35 Å=0.11 Å). BLA is then directly related to the mixing of resonance structures that contribute to the ground state, with BLA decreasing as the cyanine limit is approached[18-20]. The cyanine limit represents a situation where there are equal contribution between the two charge-transfer forms as shown in fig 8.2.

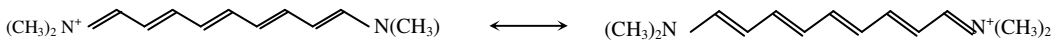

Fig. 8.2: Cyanine type system, where the two charge-transfer forms have the same energy and contribute in an equal way to the ground state structure, virtually producing a BLA equal to zero.

In order to correlate $\langle\gamma\rangle$ to the ground state polarization, a donor/acceptor polyene system BLA is modified by an external field, such that its BLA could be lowered to a cyanine limit, and its $\langle\gamma\rangle$ calculated[21] for various BLA values using different

calculation methods (valence-bond charge transfer theory[22], refined free-electron model[23] and even *ab initio*[24, 25]). The donor/acceptor system under analysis is shown in fig. 7.2

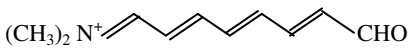

Fig. 8.3: Structure of the conjugated donor/acceptor polyene molecule whose $\langle\gamma\rangle$ was calculated as function of BLA

The SOS calculation for $\langle\gamma\rangle$ was obtained including 30 states. For incident wavelengths far away from any resonance (static $\langle\gamma\rangle$), the trend observed for the different methods remains the same[15, 26], and is the one reported in fig 8.4.

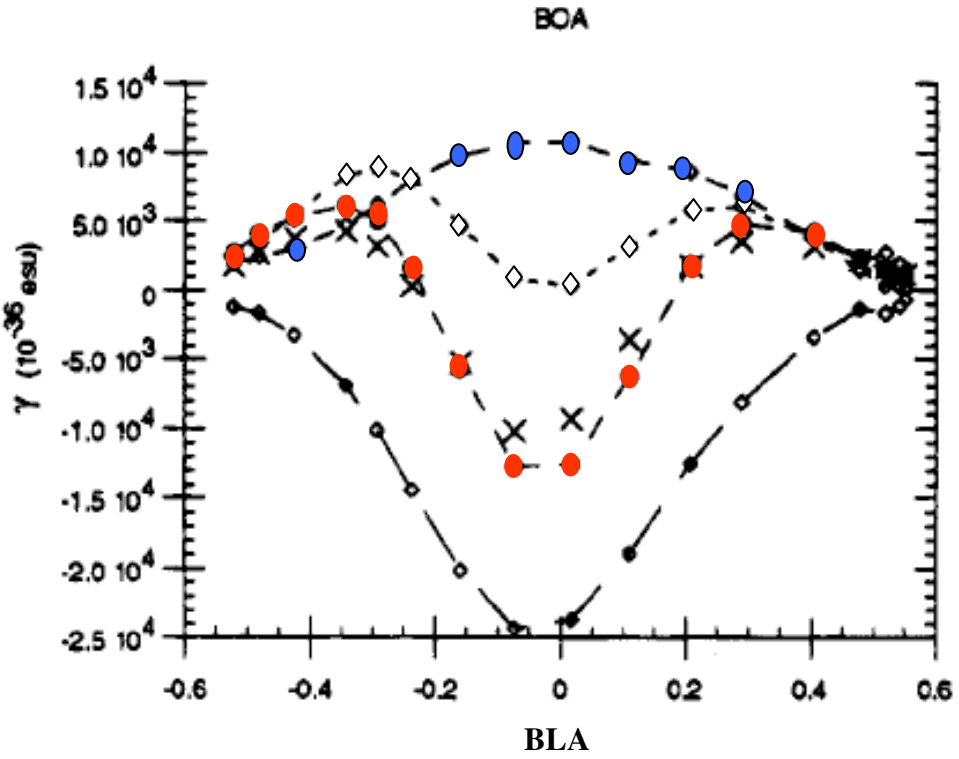

Fig. 8.4: Plot showing γ_{xxxx} according to the three-state model (red circle) in the SOS method (crosses). Each term's contribution is reported on the graph as well. The D term (diamonds), the N term (open circle) and T term (blue circle). [Ref. 15]

The $\langle\gamma\rangle$ function with BLA shows two positive maxima, and one negative. The positive maxima are located in between the neutral polyene and the cyanine limit (BLA=0). The large negative $\langle\gamma\rangle$ corresponds to a cyanine-like structure. Fig 8.4 reports the contribution of each term in equation 8.3.

The D term has a positive contribution to $\langle\gamma\rangle$, rationalizing the origin of larger $\langle\gamma\rangle$ value for polyene that are substituted with donor/acceptor groups versus neutral polyene[27].

The T term is always positive, with a maximum at the cyanine limit, contrasting the

negative term N, which has larger magnitude and a maximum at the cyanine limit, where $\langle\gamma\rangle$ reaches its largest magnitude value, with a negative sign.

The dependence of $\langle\gamma\rangle$ from the solvent polarity measured in donor/acceptor molecules, gave a confirmation of the trend as predicted by the three-state model [2].

8.2.2 Conjugated organic materials

The electron density of saturated organic molecules is strongly localized in the σ-bonds between atoms. As a result, the polarizability is given roughly by the sum of each individual σ-bond[6, 28-30]. For one-dimensional conjugated molecules, the largest contribution to the nonlinearity is caused by the π-system. The nonlinearity $\langle\gamma\rangle$ varies with a relation of the form:

$$\langle\gamma\rangle \propto n^{q} \tag{8.4}$$

Where n is the number of double bonds in the molecule. Equation 8.4 is often called power law dependence and it holds true at wavelength far from resonance. Superlinear dependence of $\langle\gamma\rangle$ with increasing length of the system reaches saturation for different n values, depending upon the model and the structure under consideration[27, 31-33]. The power law has been determined experimentally for various conjugated systems including polyene[30], cyanine[34], polyphenyl oligomers[35] and polythiophene oligomers[33, 36]

The superlinear dependence of $\langle\gamma\rangle$ with the extension of the conjugation is very well known structure-properties relationship. As the conjugation increases, the HOMO-LUMO gap decreases (up to a point), red-shifting the lowest transition, the $\pi \rightarrow \pi^*$ [37, 38]. The HOMO-LUMO gap has been identified as a parameter that quickly extrapolates a material third-order nonlinearity[39]

Among the conjugated systems, conjugated polymers are the most studied as third-order nonlinear materials. Polyacetylene[4, 40, 41] and polidiacetylene[42, 43] are among the most promising materials for optical switching type of applications[4, 44].

As nonlinear absorber polymer like MEH-PPV[45, 46], and PPV[47-49] have received a lot of attention, for application like optical data storage[50] and two-photon fluorescence imaging[51, 52].

The saturation point reached by equation 8.4 somehow implies that the effective π delocalization length, L_s, is finite[35, 38] and increasing the conjugated system length indefinitely does not enhance $\langle\gamma\rangle$ in a superlinear fashion after L_s has been reached. For polyene type of systems, L_s is estimated to be between 10 and 30 repeated units[4, 27, 53, 54]. The research focus has then moved towards small discrete molecules were the density number N ($\chi^{(3)} \propto \gamma N$) can be maximized. For Two-phoyon type of applications the structure-properties relationship have led the way to engineered system with large two-photon cross sections[55]. Table 8.1 reports some of the dipolar (donor-acceptor) and quadrupolar system (donor-acceptor-donor, and acceptor-donor-acceptor) with large two-photon absorption cross sections. For comparable conjugation length, quadrupolar systems have shown larger two-photon cross section than dipolar system as calculation and experimental data proved[56, 57].

Table 8.1: Two photon absorption peak cross section for dipolar and quadrupolar π conjugated molecules.

Molecular structure	Type	Peak two-photon cross section/ 10^{-50} cm^4 s
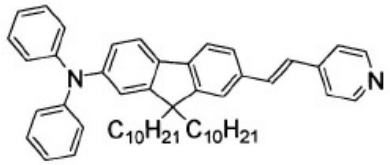 Ref [[58]]	D-A	1.94
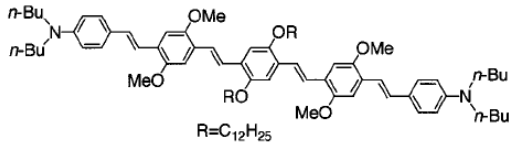 Ref [[59]]	D-A-D	1420
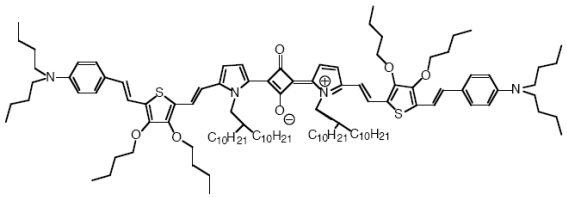 Ref [[60]]	D-A-D	18000

8.3 Squaraine dyes

One of the few molecules with negative $\langle\gamma\rangle$ aside from the already mentioned cyanine, are squaraine –type of molecules[61-65]. Squaraines (also called squarilium dyes), consist of two electron donating end groups and a central electron withdrawing 1,3-

disubstituted C_4O_2-unit forming a D-A-D alignment. Their electronic ground state structure is commonly described by multiple mesomeric forms as shown in fig. 8.5

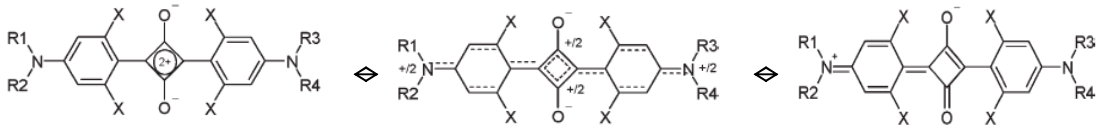

Fig. 8.5: Different resonance structures for squaraine derived dyes. Ref. [66]

X-ray crystallography studies [67, 68] have confirmed that their electronic structure and spectroscopic properties are closely related to that of symmetric cyanine molecules[69]. The potential for large nonlinearity in short squaraine dyes has been investigated; three-level model theoretical calculation aimed to maximize their nonlinearity have been published in the off resonance regime [70].

Other quantum-chemical calculations in centrosymmetric squaraine systems[71, 72]shows a large contribution to their nonlinearity by the two-photon absorption state lying just above the one photon allowed state[73]. The two-photon states play a major role in determining the magnitude and the sign of the second order hyperpolarizability $\langle\gamma\rangle$ [63, 65, 74], found to be positive in proximity of the two-photon resonance, since the T term in equation 8.3 becomes predominant over the N term. Behavior that is confirmed by the data in the experimental section of this thesis.

Disubstituted squaraine molecules, and even polysquaraines[75] with long conjugation chains, have recently been synthesized. Their absorption wavelength have shown to red-shift from the visible towards the edge of the NIR, while their nonlinear properties were

enhanced by addition of weak donor groups[76]. Quadrupolar squaraine molecules are expected to have large two-photon absorption cross-section, which justify the interest for these molecules.

In this thesis extended conjugated squaraine molecules will be analyzed, the microscopic and macroscopic third-order nonlinearity will be determined at 1300 and 1500 nm, a relatively unexplored area of the NIR spectrum as far as two-photon dyes are concerned.

8.4 Two-photon and higher order absorption processes

The nonlinear absorption properties at 1300 nm for the extended conjugated squaraine molecules do not fit a pure two-photon absorption model, especially when in high density states (spin-coated films). Striking proofs comes from the z-scan open aperture data, where a simple two-photon absorption type of nonlinearity cannot properly describe the nonlinear absorption in the samples. Open aperture Z-scan is sensitive to all absorption processes taking place at the sample, including higher order effects; such as excite state absorption (ESA), accessed via two-photon absorption[77]. A possible scheme for ESA in extended squaraine systems at 1300 nm is illustrate in fig. 8.6:

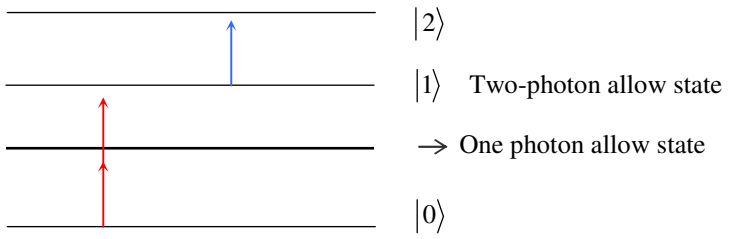

Fig. 8.6: Three level system illustrating the two-photon induced ESA. Level $|0\rangle$ represent the ground state, level $|1\rangle$ is a two-photon allow state while $|2\rangle$ is a higher energy state access through ESA from $|1\rangle$

The propagation equation (8.5) describes the beam intensity *I* as it goes through the sample along the z-axis, and two-photon induced ESA takes place:

$$\frac{dI}{dz} = -\beta I^2 - \sigma_E N_e I \tag{8.5}$$

Where β is the macroscopic two-photon cross section, σ_E represents the ESA cross section, and N_e the density of excited states created by two-photon absorption.
A three level model will be used to take ESA into account and complete the understanding of the origin of the nonlinearity in these novel compounds.

Two-photon induced ESA is a fifth-order nonlinear process and both open and closed aperture Z-scan traces are affected by higher order nonlinearity. By populating the excited state the nonlinear refraction component (closed aperture trace) is described by equation (8.6)[77]

$$\Delta n = n_2 I + k\sigma_r N \tag{8.6}$$

Where $k=2\pi/\lambda$ and σ_r is the excited state refractive index cross section, while N is the molecular density. The molecules that are in an excited state, contribute to the overall index change Δn, simply by having a different index of refraction σ_r, than the ground state. Such contribution is often difficult to isolate, since σ_r is unknown and difficult to obtain experimentally.

The closed aperture data obtained were not corrected for higher order nonlinearities like in equation 8.6.

REFERENCE

[1] Prasad, P. N., William, D. J., *Introduction to nonlinear optical effects in molecules and polymers*. 1991, New York: Wiley.

[2] Marder, S. R., Perry, J. W., Bourhill, G., Gorman, C. B., Tiemann, B. G., Mansour, K., Science. 261, 186 (1993)

[3] Eaton, D. F., Science. 253, 281 (1991)

[4] Boyd, G.T., J. Opt. Soc. Am. B. 6, 685 (1989)

[5] Fisher, R., *Optical phase conjugation*, ed. Academic. 1983, New York.

[6] Bredas, J.L., Adant, C., Tackx, P., Persoons, A., Pierce, B. M., Chem. Rev. 94, 243 (1994)

[7] Weis, R. S., Gaylord, T. K., Appl. Phys. A. 37, (1985)

[8] Klimov, V., Dneprovskii, V., Karavanskii, V., Proc. Soc. Photo-Opt. Instrum. Eng. 2145, 102 (1994)

[9] Jain, R. K., Opt. Eng. 21, 199 (1982)

[10] Henneberger, F., Puls, J., Spiegelberg, C., Schulzgen, A., Rossman, H., Jungnickel, V., Ekimov, A. I., Semicond. Sci. Technol. 6, A41 (1991)

[11] Orr, B.J., Ward, J. F., Mol. Phys. 20, 513 (1971)

[12] Kanis, D. R., Ratner, M. A., Marks, T. J., Chem. Rev. 94, 195 (1994)

[13] Pierce, B.M., J. Chem. Phys. 70, 165 (1989)

[14] Dirk, C.W., Kuzyk, M. G., Phys. Rev. A. 3, 1219 (1989)

[15] Meyers, F., Marder S. R., Perry, J. W., *Chemistry of advanced material*, ed. L.V. Interrante. 1998, New York: Wiley.

[16] Meyers, F., Marder S. R., Pierce, B. M., Bredas, J. -L., Chem. Phys. Lett. 228, 171 (1994)

[17] Dirk, C.W., Cheng, L. T., Kuzyk, M. G., Int. J. Quantum Chem., 43, 27 (1992)

[18] Groth, P., Acta Chem. Scand. B. 41, 547 (1987)

[19] Chentli-Bechikha, F., Declercq, J. P., Germain, G., Meerssche, M., Cryst. Struct. Commun. 6, 412 (1977)

[20] Marder, S.R., Perry, J. W., Tiemann, B. G., Gorman, C. B., Gilmour, S., Biddle, S. L., Bourhill, G., J. Am. Chem. Soc. **115**, 2524 (1993)

[21] Gorman, C. B., Marder, S. R., Proc. Nat. Acad. Sci. USA. 90, 11297 (1993)

[22] Lu, D.Q., Chen, G. H., Perry, J. W., Goddart, W. A., J. Am. Chem. Soc. 116, 10679 (1994)

[23] Kunh, C., Synth. Met. 41-43, 3681 (1991)

[24] Rivail, J.L., Rinaldi, D., Chem. Phys. 18, 233 (1976)

[25] Dehu, C., Meyers, F., Hendrickx, E., Clays, K., Persoon, A., Marder, S. R., Bredas, J. -L., J. Am. Chem. Soc. 117, 10127 (1995)

[26] Meyers, F., Marder S. R., Pierce, B. M., Perry, J. W., J. Am. Chem. Soc. 116, 10703 (1994)

[27] Garito, A.F., Heflin, J. R., Wong, K. Y., Zamani-Khamiri, O., *Organic material for nonlinear optics*, ed. R.A. Hann, Bloor, D. 1989: Roy. Soc. Chem.

[28] Cojan, C., Agrawal, G. P., Flytzanis, C., Phys. Rev. B. 15, 909 (1977)

[29] Pierce, B. M., J. Phys. Chem. 91, 791 (1989)

[30] Hermann, J. P., Ducuing, J., J. App. Phys. 45, 5100 (1974)

[31] Nalwa, H. S., Adv. Mater. 5, 341 (1993)

[32] De Melo, C. P., Silbey, R., Chem. Phys. Lett. 140, 537 (1987)

[33] Thienpont, H., Rikken, G. L. J. A., Meijer, E. W., ten Hoeve, W., Wynberg, H., Phy. Rev. Lett. 65, 2141 (1990)

[34] Hermann, J.P., Opt. Commun. 12, 102 (1974)

[35] Zhao, M.-T., Samoc, M., Singh, B. P., Prasad, P. N., J. Phys. Chem. 93, 7916 (1989)

[36] Zhao, M.-T., Samoc, M., Singh, B. P., Prasad, P. N., J. Phys. Chem. 89, 5535 (1988)

[37] Fabian, J., Hartmann, H., *Light absorption of organic colorants*, ed. Springer. 1980, Berlin.

[38] Bredas, J. L., Adant, C., Beljione, D., Meyers, F., Shuai, Z., Synth., Met. 55-57, 3933 (1993)

[39] Halvorson, C., Cao, Y., Moses, D, Heeger, A. J., Synth. Met. 55-57, 3941 (1993)

[40] Dorsinville, R., Yang, L., Alfano, R. R., Tubino, R., Destri, S., Sol. State. Comm., 68, 875 (1988)

[41] Gorman, C. B., Ginsburg, E. J., Sailor, M. J., Moore, J. S., Jozefiak, T. H., Lewis, R. H., Grubbs, R. H., Marder, S. R., Perry, J. W., Synth. Met. 41-43, 1033 (1991)

[42] Nunzi, J.M., Charra, F., Mol. Cryst. Liq. Cryst. Sci. Technol.- Sec. B: Nonlinear optics. 2, 131 (1992)

[43] Etemad, S., Baker, G. L., Synth. Met. 28, D159 (1989)

[44] Kuzyk, M.G., Garvey, D. W., Vigil, S. R., Welker, D. J., Chem. Phys. 245, 533 (1998)

[45] Martin, S. J., Bradley, D. D., Lane, P. A., Mellor, H., Burn, P. L. Phys. Rev. B. 59, 15133 (1999)

[46] De Boni, L., Andrare, A. A., Correa, D. S., Balogh, D. T., Zilio, S. C., Misoguti, L, Mendoca, C. R., J. Phys. Chem. B. 108, 5221 (2004)

[47] Zaopo, A., Dubistsky, Y., Hudyakov, D.,Nadtochenko, V., Synth. Met. 119, 639 (2001)

[48] Chung, S. J., Maciel, G. S., Pudavar, H. E., Lin, T. -C., He, G. S., Swiatkiewicz, J., Prasad, P. N., Lee, D. W., Lin, J.-I., J. Phys. Chem. A. 106, 7512 (2002)

[49] Meyer, R. K., Benner, R. E., Vardeny, Z. V., Liess, M., Ozaki, M., Yoshino, K., Ding, Y., Barton, T., Synth. Met. 84, 549 (1997)

[50] Wang, X., Krebbs, L. J., Al-Muri, M., Pudavar, H. E., Ghosal, S., Liebow, C., Nagy, A., Schally, A. A., Prasad, P. N., Proc. Nat. Acad. Sci. USA. **96**, 11081 (1999)

[51] Belfield, K. D., Shafer, K. J., Liu, Y., Ren, X., Van Stryland, E. W. J. Phys. Org. Chem. 13, 837 (2000)

[52] Kohler, R. H., Cao, J., Zipfel, W. R., Webb, W., W., Hansen, M., R., Science. 276, 2039 (1997)

[53] Beratan, D. N., Onuchic, J. N., Perry, J. W., J. Phys. Chem., 91, 2696 (1987)

[54] Kajzar, F., taliani, C., Zamboni, R., Rossini, S., Danielei, R., Synth. Met. 54, 21 (1993)

[55] Kogei, T., Beljionne, D., Meyers, F., Perry, J. W., Marder, S. R., Bredas, J. L., Chem. Phys. Lett. 298, 1 (1998)

[56] Albota, M.B., D.; Bredas, J.-L.; Ehrlich, J. E.; Fu, J.-Y.; Heikal, A. A.; Hess, S. E.; Kogej, T.; Levin, M. D.; Marder, R. S., McCord-Maughon, D., Perry, W. J.; Rockel, H.; Rumi, M.; Subramanian, G.; Webb, W. W.; Xu, C., Science. 281, 1653 (1998)

[57] Yang, M., Jiang, Y., Phys. Chem. Chem. Phys., 3, 167 (2001)

[58] He, G.S., Yuang, L., Cheng, N., Bhawalkar, J. D., Prasad, P. N., Brott, L., Clarson, S. J., Reinharrdt, B. A., J. Opt. Soc. Am. B. 14, 1079 (1997)

[59] Rumi, M.E., J. E.; Heikal, A. A.; Perry, J. W.; Barlow, S.; Hu, Z.; McCord-Maughon, D.; Parker, T. C.; Rockel, H.; Thayumanavan, S.; Marder, S. R.; Beljonne, D.; Bredas, J. L., J. Am. Chem. Soc. 122, 9500 (2000)

[60] Chung, S.J., Zheng, S., Odani, T., Beverina, L., Fu, J., Padhila, L. A., Biesso, A., Hales, J., Zhang, X., Schmidt, K., Ye, A., Zojer, E., Barlow, S., Hagan, D. J., Van Stryland, E. W., Yu, Y., Shuai, Z., Pagani, G. A., Bredas, J. L., Perry, J. W., Marder, S. R. J. Am. Chem. Soc. 128, 14444 (2006)

[61] Zhou, Q.L., Shi, R. F., Zamani-Khamari, O., Garito, A. F., Nonlinear Opt. 6, 145 (1993)

[62] Yu, Y.Z., Shi, R. F., Garito, A. F., Grossman, C. H., Opt. Lett. 19, 786 (1994)

[63] Poga, C., Brown, T. M., Kuzyk, M. G., Dirk, C. W.,. J. Opt. Soc. Am. B. 12, 531 (1995)

[64] Dirk, C.W., Herndon, W. C., Cervanteslee, F., Selnau, H., Martinez, S., Kalamegham, P., Tan, A., Campos, G., Velez, M., Zyss, J., Ledoux, I., Cheng, L. T., J. Am. Chem. Soc. 117, 2214 (1995)

[65] Tran, K., Scott, G. W., Funk, D. J., Moore, D. S., J. Phys. Chem. 100, 11863 (1996)

[66] Stokes, R., J., Ingram, A., Gallagher, J., Armstrong, D., R., Smith, W., E., Graham, D., Chem. Commun. 5, 567 (2008)

[67] Kobayashi, Y., Goto, M., Kurahashi, M., Bull. Chem. Soc. Jpn. 59, 311 (1986)

[68] Lawrentz, U., Grahn, W., Dix, I., Jones, P. G., Acta Cryst. C. 57, 126 (2001)

[69] Mamicchioli, F., Tatikolov, A. S., Vanossi, D., Ponterini, G., Photochem. Photobiol. Sci. 3, 369 (2004)

[70] Dirk, C. W., Herdon, W. C., Cervantes-Lee, F., Selnau, H., Martinez, S., Kalameghan, P., Tan, A., Campos, G., Velez, M., Zyss, J., Ledoux, I., Cheng, L. T., J. Am. Chem. Soc. 117, 2214 (1995)

[71] Heflin, J. R., Cai, Y. M., Garito, A. F., J. Opt. Soc. Am. B. 8, 2132 (1991)

[72] Yang, M., Jiang, Y. Phys. Chem. Chem. Phys. 3, 4213 (2001)

[73] Andrews, J. H., Khaydarov, J. D.V., Singer, K. S., hull, D. L., Chuang, K. C., J. Opt. Soc. Am. B. 12, 2360 (1995)

[74] Andrews, J. H., Khaydarov, J. D.V., Singer, K. S., Opt. Lett. 19, 984 (1994)

[75] Ajayaghosh, A., Chem. Soc. Rev. 32, 181 (2003)

[76] Peterman, R., Tian, M., Tatsuura, S., Furuki, M., Dyes Pigm. 57, 43 (2003)

[77] Said, A. A., Wamsley, C., Hagan, D. J., Van Stryland, E. W., Reinhardt, B. A., Roderer, P., Dillard, A. G., Chem. Phys. Lett. **228,** 646 (1994)

CHAPTER IX

THEORY OF DEGENERATE FOUR WAVE MIXING (DFWM) AND Z-SCAN

9.1 Theory of DFWM

Two theoretical approaches are commonly used to describe the DFWM theory: the Nonlinear Optic description (NLO) and the laser-induced grating (LIG). The former explains the phenomena as the interaction of intense optical fields in a medium where a third-order polarization is induced. The nonlinear polarization dipole radiates a fourth wave, consisting of the DFWM signal[1, 2]. LIG provides a more intuitive approach, describing the DFWM signal as the result of diffraction from a laser induced grating. The two approaches, though different, are interchangeable. For instance, while the LIG approach does not described instantaneous effects, the NLO approach does[3, 4].

The experimental configuration employed for all the experiments is a variable of the "forward scatter" (FS-DFWM) geometry commonly called "folded-box CARS" configuration[5-10] (fig. 9.1). Other geometries can be employed, like the "counter-propagating" (CP-DFWM)[11-13], "nearly counter-propagating" (NCP-DFWM) and a two beams "self-diffraction" (SD-DFWM)[14, 15].

In this chapter, an overview of the NLO model applied to the FS-DFWM configuration is presented, and the same model will be used to extract expression for the macroscopic third-order susceptibility $\left|\chi^{(3)}\right|$, and the orientationally averaged third-order polarisability $\langle\gamma\rangle$. Time-resolved DFWM will be described in terms of the LIG model.

9.1.1 DFWM from a NLO prospective

Different authors in the literature have analyzed the CP-DFWM configuration. This is one of the most used configurations, since it was recognized that the D-wave (the DFWM signal) is the complex-conjugated of the probe, this translate as D being the time-reversed replica of the probe[16, 17].

Phase conjugation as a phenomenon has been investigated, mostly using the CP-DFWM configuration, for potential application in aberration correction and adaptive optics[13, 18]. Other applications involve information storage[19] and improved laser resonator[20, 21]

A complete NLO treatment for the CP-DFWM configuration have been analyzed first by Yariv and Pepper[22] in 1977 for a non-absorbing sample, later Caro and Gower, have generalized their analysis including the effect of linear absorption. The analysis reported here is an overview of what they reported. They were able to relate through their steady-state theory[3], the parameters that relate the amplitude of the DFWM signal to the third order polarization of the material.

The equations reported here are very generic and can be applied to a FS configuration as well as others.

Widely used assumptions were made for the incident beams, one involving the angle between them to be small, so that the three can be regarded as collinear over the interaction length. Each of the incident beams is then approximated to a monochromatic planar wave front (steady-state approximation).

According to the condition above the incident fields induce in the medium a polarization $\vec{P}^{(3)}$ given by[23]

$$\vec{P}^{(3)}(\vec{r},t) = \varepsilon_0 \int_{-\infty}^{+\infty} d\tau_1 \int_{-\infty}^{+\infty} d\tau_2 \int_{-\infty}^{+\infty} d\tau_3 R^{(3)}(\tau_1,\tau_2,\tau_3)\vec{E}(\vec{r},t-\tau_1)\vec{E}(\vec{r},t-\tau_2)\vec{E}(\vec{r},t-\tau_3) \tag{9.1}$$

Where $R^{(3)}$ is the time-domain response function, a 4th rank tensor which relates the magnitude of the third-order polarization to the magnitude of the applied field at all times prior to *t*[23].

The Fourier component, at frequency ω of the D-wave can be written as[3, 24, 25]

$$\vec{P}^{(3)}(\vec{r},t) = \frac{1}{2}\left[\vec{P}_{\omega}^{(3)}(\vec{r})\exp(-i\omega t) + c.c\right] \tag{9.2}$$

where

$$\left(P_{\omega}^{(3)}(\vec{r})\right)_i = \varepsilon_0 \frac{3}{4}\sum_{jkl}\left\{\chi_{ijkl}^{(3)}(-\omega;\omega,\omega,-\omega)A_F(\vec{r})_j A_B(\vec{r})_k A_P^*(\vec{r})_l \times \exp\left[i\left(\vec{k}_F + \vec{k}_B - \vec{k}_P^*\right)\cdot\vec{r}\right]\right\} \tag{9.3}$$

The indices "*ijkl* " represent Cartesian coordinates. The label "F", "B", and "P" refer to the F-pump, B-pump, and the Probe. A_i is the scalar amplitude of the field along one of the axes. The approximation assumes that the nonlinear interaction is weak, and the incident fields amplitudes can be considered to be constant as they go through the medium. In the small angle limit the electric field polarization of the probe can be considered as polarized along one of the axes (x or y-polarized). Equation 9.3 can than be simplify to

$$\left(P_{\omega}^{(3)}(\vec{r})\right)_D = \varepsilon_0 \frac{3}{4} \chi_{DFBP}^{(3)}(-\omega;\omega,\omega,-\omega) A_F(\vec{r})_j A_B(\vec{r})_k A_P^*(\vec{r})_l \times \exp\left[i\left(\vec{k}_F + \vec{k}_B - \vec{k}_P^*\right)\cdot \vec{r}\right] \quad (9.4)$$

The interaction of the F-pump, B-pump and the Probe fields give rise to a polarization $\left(P_{\omega}^{(3)}(\vec{r})\right)_D$ that radiates the signal wave D whose amplitude and polarization is determined by $\chi_{DFBP}^{(3)}$ [26-29]. The effects induced by nonlinear absorption, self-focusing/defocusing on the incident beams is not considered in the analysis[30]. Such processes are usually avoided by reducing the beams intensities.

9.1.2 Forward scatter DFWM

The three collinear beams for the forward scattering geometry could take several forms. In fig. 9.1 the three beams, the B- and F-pump and the probe are arranged on the vertices of a square. The B- and F-pumps lie on the *xz*-plane forming an angle θ_1, while the probe lies on the plane perpendicular to it forming an angle θ_2. The propagation direction of the scattered wave can be deduced by the phase matching conditions. A schematic is shown in fig. 9.1 and 9.2 where the beams pattern after the sample indicate the resulting DFWM signal and the ancillary beams produced for the FS and NCP geometry.

From the beams pattern in fig. 9.2 the beam that is ultimately used for $\left|\chi^{(3)}\right|$ is beam 4.

Other beams involving the product of all three incident waves are present, they are indicated in fig. 9.2 as beams 5 and 6, whose expressions are not considered in this treatment. The remaining beams are produced by the interaction of 2 beams only; essentially they are the result of self-diffraction interactions.

The FS geometry compared to the CP and NCP configuration provides a longer interaction path length, and is used when the physical pulse length is shorter than the nonlinear medium length. Such geometry is often implemented with femtosecond pulses, as in our case, where the physical length of the pulse is about 30 μm.

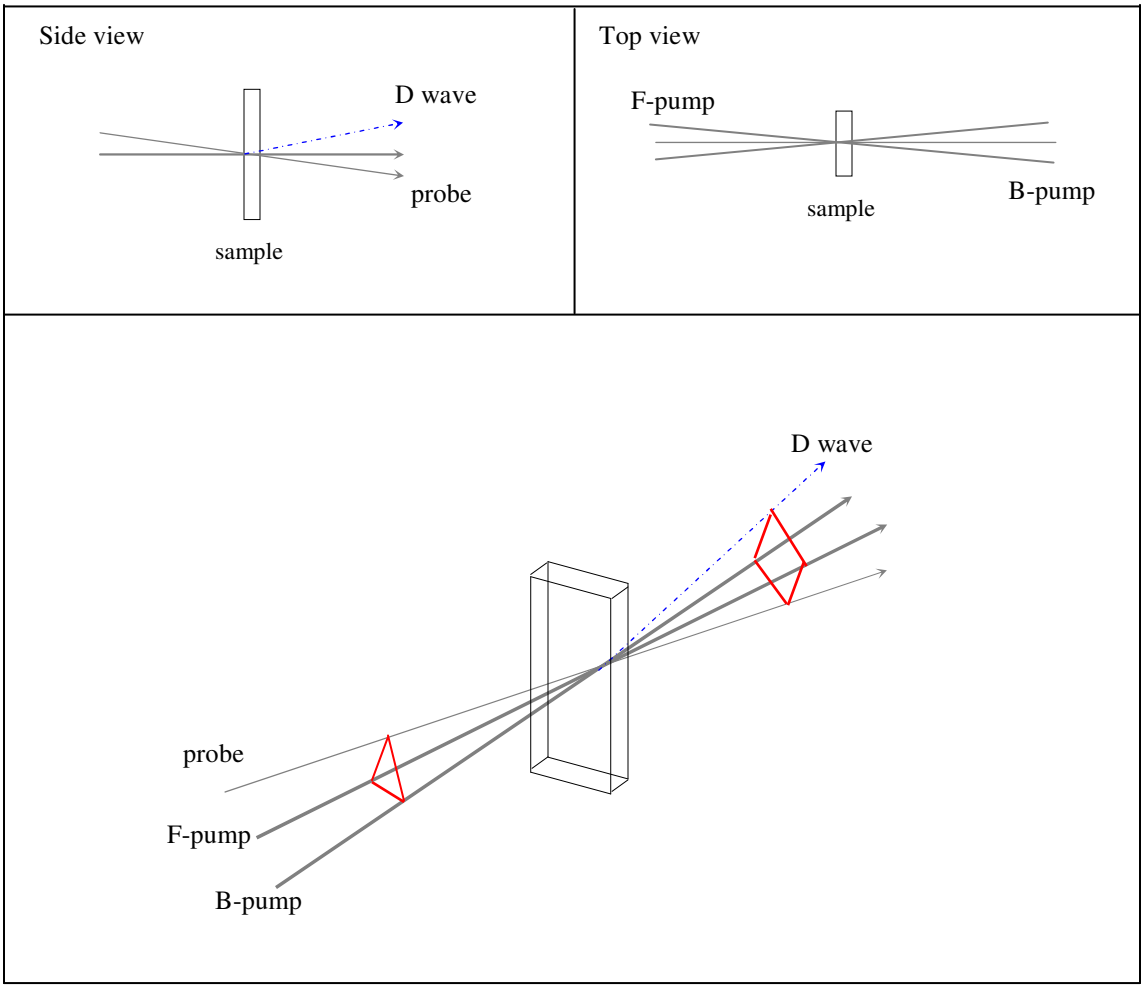

Fig. 9.1: Schematic of the "folded-box CARS" configuration used in our set-up. Two writing beams and the diffracting beam

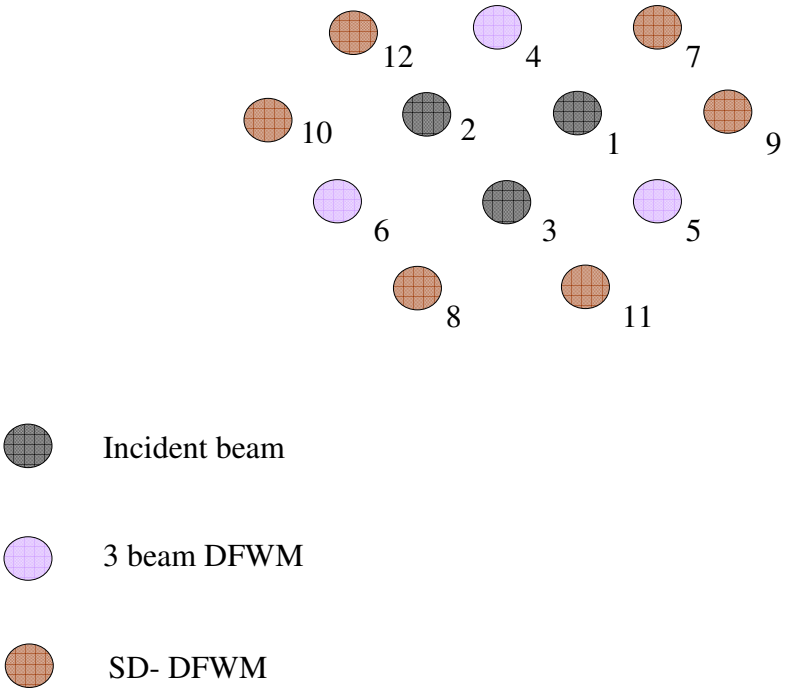

Fig. 9.2: Schematic of the FS-DFWM beams on the *xy*-plane after the nonlinear medium. Incident beams are indicated as 1, 2 and 3. The DFWM beams are labeled 4, 5 and 6. 4 being the one used for the $\left|\chi^{(3)}\right|$ measurements

9.1.3 Phase matching

Nonlinear optic interactions involve power transfer into the generated wave in an effective fashion only when the polarization and the field it generates oscillate at the same frequency, and remain in phase as the wave propagates. The condition can be expressed invoking the energy conservation[23, 31] (equation 9.5), through a phase matching equation, which can be considered as a conservation of the linear momentum (equation 9.6).

$$\omega_D = \omega_F + \omega_B - \omega_P \tag{9.5}$$

$$\Delta\vec{k} = (\vec{k}_F + \vec{k}_B - \vec{k}_P) - \vec{k}_D \tag{9.6}$$

Where $\left|\vec{k}\right| = \frac{2\pi n_0}{\lambda}$

The phase matching condition is satisfied when the phase mismatch, $\Delta\vec{k}$ is zero. The polarization that generates the DFWM wave will radiate in such direction to minimize $\Delta\vec{k}$.

For the FS-DFWM configuration a perfect phase matching is possible for any of the output waves. The mismatch can be minimized by keeping the incident angle, θ_1 and θ_2 small.

The mismatch for beam 4 is described by 9.7

$$\Delta\vec{k} = (\vec{k}_1 + \vec{k}_2 - \vec{k}_3) - \vec{k}_4 \tag{9.7}$$

that can be written as function of angles θ_1 and θ_2 as follow:

$$\left|\Delta\vec{k}\right| = \left|\vec{k}\right|\left\{\left[3 - 2\cos(\theta_1) - 2\cos(\theta_2) + 2\cos(\theta_1)\cos(\theta_2)\right]^{1/2} - 1\right\} \tag{9.8}$$

The intensity of the D wave generated depends on the phase mismatch, equation (9.9) describes the intensity of D as function of Δk

$$I_4 = I_1 I_2 I_3 \frac{9\omega^2 \left|\chi^{(3)}\right|^2 T(1-T)^2}{16c^4 n_0^4 \varepsilon_0^2 \alpha_0^2} \left[\frac{\sin(|\Delta k| L/2)}{|\Delta k| L/2}\right] \qquad (9.9)$$

Where T is the medium transmittance, n_0 , ε_0 and α_0 are the medium lineal index of refraction, dielectric constant and the intensity absorption coefficient respectively, while L is its path length. Calculation shows that when the incident angles are smaller than 5°, the phase mismatch can be neglected.

9.1.4 The DFWM signal intensity and its relationship to the material $\chi^{(3)}$

The intensity of the D wave can be derived by introducing equation (9.4) as a polarization source into Maxwell's equations[23, 30, 32]. The nonlinear interaction is assumed to be small, with a small energy transfer to the D wave. A differential equation describing the amplitude of D as it goes through the sample (along z-axis) can be written applying the slow varying envelope approximation, SVEA[1, 22, 23] as follow:

$$\frac{dA_D(z)}{dz} = \frac{3i\omega}{8cn_0} \chi^{(3)}_{DFBP}(-\omega;\omega,\omega,-\omega) A_F(0) A_B(0) A^*_P(0) \exp(-\frac{1}{2}\alpha_0 L) \exp(-\alpha_0 z) \qquad (9.10)$$

With the appropriate boundary conditions equation 9.10 can be integrated over the entire length of the nonlinear material, obtaining the intensity of the D wave as function of the three incident beams.

$$I_D = I_F I_B I_P \frac{9\omega^2 \left|\chi^{(3)}\right|^2 T(1-T)^2}{16c^4 n_0^4 \varepsilon_0^2 \alpha_0^2} \tag{9.11}$$

where T is the medium transmission. In the absence of absorption equation 9.11 becomes

$$I_D = I_F I_B I_P \frac{9\omega^2 \left|\chi^{(3)}\right|^2 L^2}{16c^4 n_0^4 \varepsilon_0^2} \tag{9.12}$$

Equation 9.12 ties the amplitude of the D wave to the sample properties; its length, L, and its third-order nonlinearity $\left|\chi^{(3)}\right|$, and to the other incident beams. A cubic dependence on the incident field is shown. What is important to realize is that the D wave gives access to the magnitude of $\left|\chi^{(3)}\right|$, while the phase information is lost.

9.1.5 Additional waves produced in the FS-configuration

Other difference-frequency mixing terms in $P^{(3)}(r,t)$, contributes besides the field product of $A_F A_B A_P^*$ which generates wave D[25, 33] as shown in fig 9.2.

Other two third-order polarizations which still describe the same difference mixing interaction involving three incident waves can be individuate; the $A_B A_P A_F^*$ and the $A_F A_P A_B^*$ terms, giving beam 5 and 6.

The phase mismatch is again small when the beams angles are small.

Self-diffraction terms are produced by the third-order polarization when products of only two distinguishable incident fields are involved. The terms produced contain field products of the form $A_P A_P A_F^*$ and $A_F A_F A_P^*$.

Formally, SD-DFWM waves are never phase matched, and again, the mismatch can be negligible when the beam angles are small. SD-DFWM beams are used both for alignment purposes and for third-order susceptibility measurements[34-36].

9.1.6 DFWM in the laser-induced gratings (LIG) formalism

In the LIG formalism, the generation of a DFWM signal is described as a two step processes[37]. The first being the formation of a laser-induced grating (LIG) by the interference of two beams in the nonlinear medium (the writing beams), and the second being the diffraction of an incident beam from the formed LIG. The intensity of the diffracted beam provides information on the grating amplitude and therefore the magnitude of the medium nonlinearity. As the diffraction occurs, more than one order can be generated, depending upon the nature of the grating[38-41].

The interference of the writing beams (also called excitation beams) is described with the approximation of having two monochromatic plane waves, crossing with an angle θ_w (see fig. 9.3). The fields are polarized along the *y*-axis overlapping inside the nonlinear medium as shown. An interference pattern is created[37, 42] as the two waves interact. In the figure below (9.3) the intensity of the two interacting waves is considered equal ($I_1=I_2$).

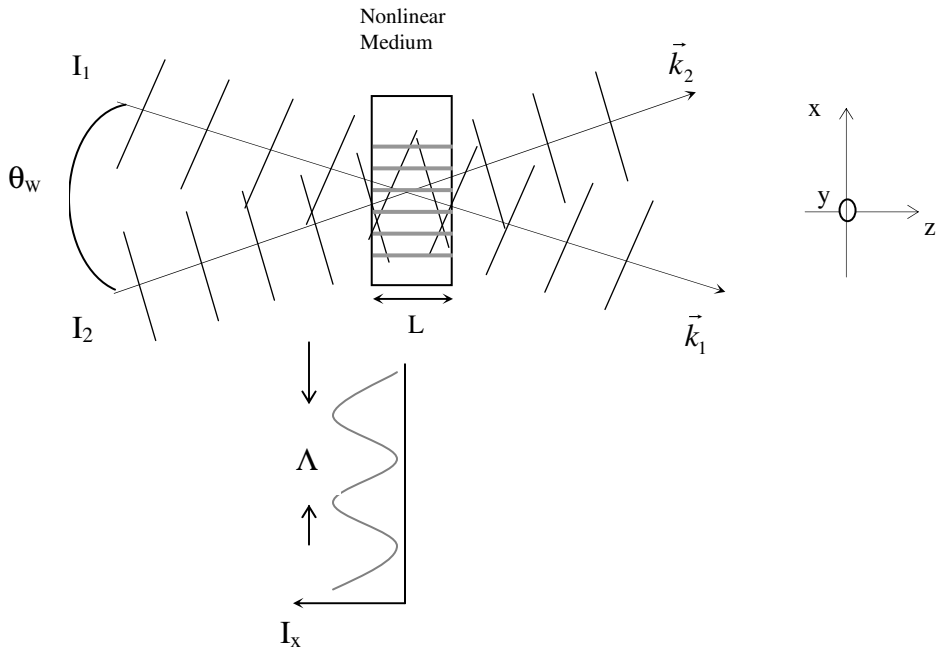

Fig. 9.3: Formation of a LIG by interference of two polarized fields, I_1 and I_2

The field from the two wave constructively interfere when the relative phase ϕ_{12} is equal to 0, 2π,4π…, and so on, while the interaction is destructive when ϕ_{12} is equal to π,3π,5π… As a result, the intensity of the interference is modulated along the *x*-axis as shown in fig. 9.3 an is described by equation 9.13

$$I(x) = I_1 + I_2 + 2\Delta I \cos(|\vec{q}_{21}|x) \tag{9.13}$$

where $\Delta I = \sqrt{I_1 I_2}$ and $\vec{q}_{21}$ is the grating vector, determined by the wave vectors of the interfering waves:

$$\vec{q}_{21} = \vec{k}_2 - \vec{k}_1 \tag{9.14}$$

The grating period Λ is determined by the beam angle θ_w by

$$\Lambda = \frac{\lambda}{2n_0 \sin(\theta_w / 2)} \tag{9.15}$$

The material optical properties define the nature of the grating at the wavelength, λ, of the writing beams. The intensity modulation causes modulation in the complex refractive index *n* (see equation 7.3) of the nonlinear medium. When the modulations are due to change in the real part of *n,* a *phase grating* is created, while changes in the imaginary part of *n* results in an *amplitude grating*. A mixed grating is obtained when both the real an imaginary part of *n* are modulated[37].

Gratings occur even when the interfering waves have orthogonal polarization[42-44]. In the case of intensity gratings, what gets spatially modulated is the intensity, while the polarization is uniform. For polarization gratings, instead the intensity is constant, while the polarization is spatially modulated[27, 28, 41].

9.2 General conditions for phase and amplitude gratings.

As mentioned, the grating can be different in nature, depending upon the material optical properties at the wavelength of the interfering beams.

When completely off-resonance, a grating can arise through $\chi^{(3)}$, which can in fact be express as an intensity-dependent refractive index for its real part. As already mentioned, as the intensity is modulated, changes in the refractive index, cause $\chi^{(3)}$ to ultimately change, creating a phase grating. When the interference beams wavelength is resonant with the nonlinear material optical transition, the ground state population is perturbed, as

the molecules are excited. The intensity modulation causes a spatial modulation in the ground state population. Usually, the ground and excited states have different polarisability, which causes the susceptibility to be spatially modulated. Upon absorption, (due to linear or nonlinear processes) *thermal gratings* can be induced[45-48]. In experimental measurements, the issues related to thermal gratings will be invocated to explain some of the problems related with the DFWM measurements.

When thermal gratings are created the sample temperature becomes modulated, as nonradiative relaxation take place in the medium. Such temperature modulation causes changes in the refraction index, followed by a change in the medium density directly related to temperature increase.

9.2.1 Thermal nonlinearities

Thermal nonlinearities in absorbing media are due to change in the refractive index with respect to temperature[49-51]. The increase in temperature has two contributions[24, 52, 53]:

$$\Delta n = \left(\frac{\partial n}{\partial T}\right)_{\rho} \delta T + \left(\frac{\partial n}{\partial \rho}\right)_{T} \delta \rho \tag{9.16}$$

One contribution is due to the change of index with temperature, and a second due to the change in density of the medium. In fluids, the second term $(\partial n/\partial \rho)_{\mathrm{T}}$ is predominant[24, 47, 52]. For short pulses, the initial phase is a temperature increase $(\partial n/\partial T)_{\rho}$, where a pure phase grating is formed. After the heat is deposited, the spatial modulation in temperature, forces thermal expansion of the area where the grating peaks

are towards the area of grating minimum. This results in a density-pressure wave that generates an acoustic standing wave. Such acoustic grating is a major component of thermal grating[24, 52, 54, 55]

The nonlinearity of the medium, in this case, becomes a function of time, and of the thermal properties of the heated regions in the sample. Thermal diffusion is a slow process compared to other nonlinear mechanism. It can vary between 10^{-9} and 1 second[49, 56, 57]. This creates tangible problems when measurements are done with a laser repetition rate shorter than the thermal grating relaxation, in this case the medium does not have sufficient time to complete the thermal diffusion process, causing thermal effects to accumulate. Thermal nonlinearity will have a large impact, especially in high density samples (films) as describe in the experimental section.

9.3 Measuring $\chi^{(3)}$ and $\langle\gamma\rangle$

9.3.1 Macroscopic nonlinearity $\chi^{(3)}$

Absolute measurements of $\chi^{(3)}$ require the knowledge of numerous factors (see equation 9.11 and 9.12), like the interaction length of the beams, their absolute energy, the pulse shape, dimension etc. Even though the effort involved with absolute $\left|\chi^{(3)}\right|$ measurements, absolute $\left|\chi^{(3)}\right|$ values are reported in literature[34, 58-60].

To avoid the higher degree of complication imposed by absolute measurements, a reference whose $\left|\chi^{(3)}\right|$ is known will be used in all the measurements reported in this

thesis. This simplifies the measurement, recognizing that the values obtained are as accurate as the standard.

All DFWM measurements conducted at 1300 and 1500 nm are referenced to fused silica[61, 62], a $\left|\chi^{(3)}\right|$ = 1.5 10^{-14} esu will be used for both wavelengths.

The following approach to determine $\left|\chi^{(3)}\right|$, based on the power dependence, is appropriate only when the nonlinearity is due to fast effects[63, 64]. The DFWM signal, indicated as S_D and the beams irradiance I_B are related by the equation 9.17 (see equation 9.12)

$$\log(S_D) = m \cdot \log(I_B) + k \tag{9.17}$$

Where the coefficient *m* will have a slope of 3 when a "fast" third-order nonlinearity is the source. The material nonlinearity is instead contained in *k.*

A non-cubic behavior could be due to several factors, when the laser intensity is close to saturation in a saturable absorber, or when damage is induced by the laser. Another possible cause is thermal effects due to multiphoton absorption, like in some of the samples under investigation.

If a cubic behavior is respected for the sample, then the $\left|\chi^{(3)}\right|_{\text{sample}}$ can be measured relative to a reference $\left|\chi^{(3)}\right|_{\text{refer}}$. The DFWM signal is then collected under the same conditions for the sample and the reference, as a function of the incident beams irradiance I_D (same conditions do not include the energy range of the incident beams). Both signals are plotted using the cubic function that follows:

$$S_D = \nu \cdot S_L^3 \tag{9.18}$$

The $\left|\chi^{(3)}\right|_{\text{sample}}$ can be calculated as follows for a non absorbing medium:

$$\left|\chi^{(3)}\right|_{\text{sample}}=\left|\chi^{(3)}\right|_{\text{refer}}\left(\frac{n_{sample}}{n_{refer}}\right)^{2}\left(\frac{\nu_{sample}}{\nu_{refer}}\right)^{\frac{1}{2}}\frac{L_{\text{Re}f}}{L_{sample}} \tag{9.19}$$

When the sample absorbs at the laser wavelength the appropriate expression is instead

$$\left|\chi^{(3)}\right|_{\text{sample}}=\left|\chi^{(3)}\right|_{\text{refer}}\left(\frac{n_{sample}}{n_{refer}}\right)^{2}\left(\frac{\nu_{sample}}{\nu_{refer}}\right)^{\frac{1}{2}}\frac{L_{\text{Re}f}\cdot\alpha_{0}}{\sqrt{T}(1-T)} \tag{9.20}$$

Where T and α_0 are the transmission and linear absorption coefficients respectively. L_{Ref} and L_{sample} is the optical path length, while n_{sample} while n_{ref} are their linear refractive indices.

Equation 9.19 will be largely used to obtain the $\left|\chi^{(3)}\right|$ magnitude of various samples.

9.3.2 Microscopic third-order nonlinearity $\langle\gamma\rangle$ and the internal reference method

The molecular polarizability $\langle\gamma\rangle$ can be determined as orientational average from $\left|\chi^{(3)}\right|$ measurements, when the macroscopic polarizability can be described as a sum of the independent microscopic polarizability for a known volume impling that there cannot be strong interactions between the individual molecules, and therefore the individual molecule should stay, on average, apart from each other. Dissolving the molecule of

interest in a solvent would achieve the conditions just described. When solutions are considered as formed by a solvent (solv) and a solute (solu), for which $\langle\gamma\rangle$ is to determine. The solution nonlinearity can be written as follows

$$\left|\chi^{(3)}_{ijkl}\right|_{solution} = \left\{\left[\mathrm{Re}\,\chi^{(3)}_{ijkl}(solv) + \mathrm{Re}\,\chi^{(3)}_{ijkl}(solu)\right]^2 + \left[\mathrm{Im}\,\chi^{(3)}_{ijkl}(solu)\right]^2\right\}^{1/2} \tag{9.21}$$

In equation 9.21 any electronic resonance of solvent is remover, supposing that the laser wavelength is completely detuned from it, this implies that $\mathrm{Im}\,\chi^{(3)}_{ijkl}(solv)=0$.

The contribution of the solute and the solvent can be written in terms of their microscopic nonlinearities as follow:

$$\mathrm{Re}\,\chi^{(3)}_{ijkl}(solu) = N\left[f(\omega)\right]^4 \mathrm{Re}\langle\gamma\rangle_{ijkl} \tag{9.22}$$

$$\mathrm{Im}\,\chi^{(3)}_{ijkl}(solu) = N\left[f(\omega)\right]^4 \mathrm{Im}\langle\gamma\rangle_{ijkl} \tag{9.23}$$

Where N is the number density expressed as mol/ cm^3, while $f(\omega)$ is the Lorentz local field factor, defined as

$$f(\omega) = \frac{n(\omega)^2 + 2}{3}$$

When the solute concentration is small, the number density for the solvent can be assumed to be close to that of the pure solvent and treated as a constant. As equations 9.22 and 9.23 are introduced in equation 9.21 the solution nonlinearity can be expressed as

$$\left|\chi^{(3)}_{ijkl}(N)\right|_{solution} = \left\{\left[\mathrm{Re}\,\chi^{(3)}_{ijkl}(solv) + N\left[f(\omega)\right]^4\,\mathrm{Re}\left\langle\gamma\right\rangle_{ijkl}\right]^2 + \left[N\left[f(\omega)\right]^4\,\mathrm{Im}\left\langle\gamma\right\rangle_{ijkl}\right]^2\right\}^{1/2} \tag{9.24}$$

In the limit N=0 the

$$\left|\chi^{(3)}_{ijkl}(N)\right|_{solution} = \left|\mathrm{Re}\,\chi^{(3)}_{ijkl}(solv)\right| = \left|\chi_{solv}{}^{(3)}\right|$$

$\left|\chi_{solv}{}^{(3)}\right|$ is determined in a separate experiment (using a material with known nonlinearity as described in equation 9.19).

The solvent is used as an internal reference from which the solute $\langle\gamma\rangle$ can be determined in a concentration dependent study[65]. Equation 8.13 can be recast in terms of the solute concentration

$$\frac{\left|\chi^{(3)}(c)\right|_{solution}}{\left|\chi^{(3)}\right|_{solv}} = \left\{\left[1 + c\cdot g\cdot\cos(\varphi)\right]^2 + \left[c\cdot g\cdot\sin(\varphi)\right]^2\right\}^{1/2} \tag{9.25}$$

where

$$g = \frac{m\cdot N_a\left[f(\omega)\right]^4\left\langle\gamma\right\rangle}{\left|\chi^{(3)}\right|_{solv}}$$

The factor m is needed when the number density is express in molecules /m^3, while the concentration is expressed in mol/ dm^3, in this instance m=1000.

By fitting the ratio between the solution $\left|\chi^{(3)}\right|$ and the solvent $\left|\chi^{(3)}\right|$ as function of the solute concentration *c*, according to equation 9.25 both the magnitude and the phase of $\langle\gamma\rangle$ can be determined.

Assuming a positive real part for the solvent, toluene[66], in the near infrared wavelengths range, the ratio in 9.25 is determined by the magnitude of $\langle\gamma\rangle$ and its sign. It turns out that the phase in solution is still very challenging to determine. For instance, high quality data is necessary to distinguish between a phase of 30 and 150 degrees, even as the number of data points are increased the fitting quality is not improved. This method is indeed useful in providing a way to estimate $\langle\gamma\rangle$ [67].

9.3.3 Time resolved DFWM

Time-resolved DFWM can be explained in a more intuitive fashion using the LIG approach. Fig. 9.4 illustrates the general idea. The writing beams (B-pump and F-pump) excite the nonlinear medium establishing a grating amplitude, that relaxes over time. The change in the grating amplitude is sampled by the probe beam pulse, which is delayed by τ_d relative to the writing beams. The material excitation and relaxation dynamics are given by the evolution of the DFWM signal. The decay kinetics help indicate which nonlinear mechanism is responsible for the grating. The mechanism is considered instantaneous when in the femtosecond time scale

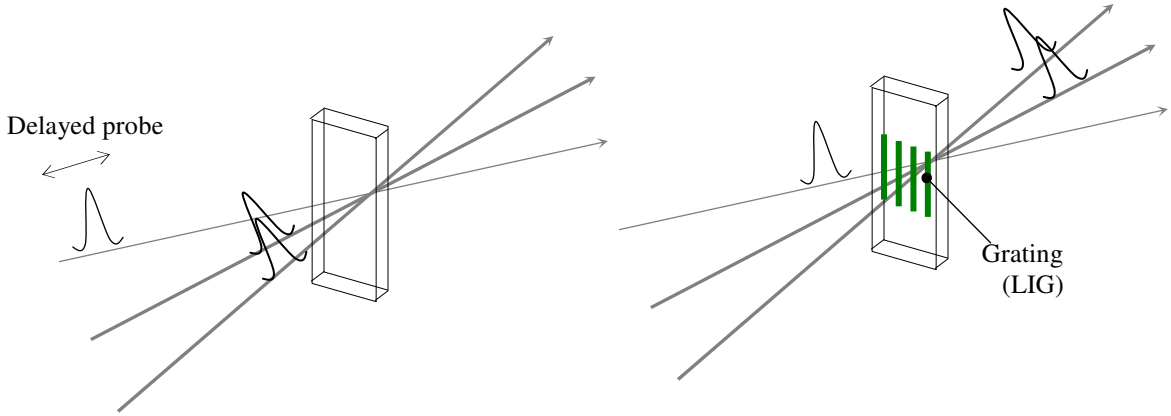

Fig.9.4: Illustrations showing the general idea for time resolved DFWM. On the left the probe is delayed compared to the two writing beams. On the right, after the writing beams have passed through the sample, creating the grating, its amplitude is sampled by the delayed probe.

Fast responses

Authors have described time-resolved FWM signals for fast responses[39, 68] as follows:

$$I_D(t) \propto I_B(t-\tau_d) I_F(t) I_P(t) \tag{9.26}$$

Where I_D is the DFWM signal intensity, I_F, I_B and I_P, are the intensities of the writing beams (F and B pump), and that of the delayed probe P respectively. The signal then becomes the tripled correlation of the laser pulse[68, 69]. For a Gaussian type of description, the third-order correlation function τ_D is related to the fundamental pulse FWHM τ through the following relationship[70]:

$$\frac{\tau_D}{\tau} = 1.22 \tag{9.27}$$

Slow responses

The response function in this case is more complex. For a complete treatment, the literature can be consulted on the topic[39, 71, 72]. After the grating amplitude is created by the excitation pulsed (B and F –pumps), the gratings attains its peak value and it decays as function of time. Being $f(t)$ the function describing the signal decay, the detected signal S_D varies with the probe delay τ_d as follow:

$$S_D \propto \exp(-2\tau_d / \tau_r) \tag{9.28}$$

Where τ_r is the grating lifetime[40, 73].

9.4 Theory of Z-scan

The Z-scan technique provides magnitude and sign of the Real part of $\chi^{(3)}_{xxxx}(-\omega,\omega,\omega,-\omega)$ and magnitude of the imaginary part of $\chi^{(3)}_{xxxx}(-\omega,\omega,\omega,-\omega)$ by using a single beam. The real part is obtained through the nonlinear refractive index n_2^I and the immaginary part through the nonlinear absorption coefficient β[74]. The experiment set-up is illustrate in fig. 9.5.

A pulsed laser having a gaussian profile propagating along the *z-axis* is focused, the sample is then translated through its focus as shown in figure 9.5. The light transmitted by the sample falls onto an aperture in the far-field, behind which a detector is placed (D1). The sample can be a solution or a thin film, but in either case, its length has to be small compared to the diffraction length of the focused beam z_0, which is defined as

$$z_0 = \frac{k w_0}{2} \tag{9.29}$$

Where w_0 is the beam radius at the focal plane.

This insures that the beam size is almost constant throughout the entire sample length.

The sample transmission is measured as function of its position along the z-axis as D1/D3; D3 being the reference detector.

Part of the transmitted beam is reflected to a third detector (D2) with no aperture in front. The data collection mode where the ratio of D2/D3 is obtained as function of the sample position is called 'open aperture', where D1/D3 is called instead 'closed aperture'. The open aperture provides the nonlinear absorption coefficient β. As the sample moves toward the focal plane, the beam intensity increases, and as a direct consequence of nonlinear absorption, the transmitted beam at D2 would be attenuated (see fig.9.5). When no linear absorption processes are taking place at the sample, the transmitted intensity at D2 would instead be a constant throughout the entire scan.

The closed aperture Z-scan provides instead n_2^I. From the prospective of a propagating beam, a nonlinear medium can be described as a thin lens with a variable focal length. For materials having $n_2^I < 0$ and zero nonlinear absorption (β=0), the z-scan will appear as in fig 9.5. Initially the transmittance remains relatively constant. As the sample approaces the focal plane, and the intensity increases, the sample acts as a negative lens, defocusing the beam and contrasting the focusing effect of lens L in fig. 9.5. The overall effect is a reduced divergence at the detector D1. At the aperture, the beam waist is

smaller, allowing more light through, and an increase in transmittance is registred. As the sample goes through the focal plane at $z > 0$, the opposite occurs, and the sample defocuses the already defocusing beam, reducing the amount of light through the aperture.

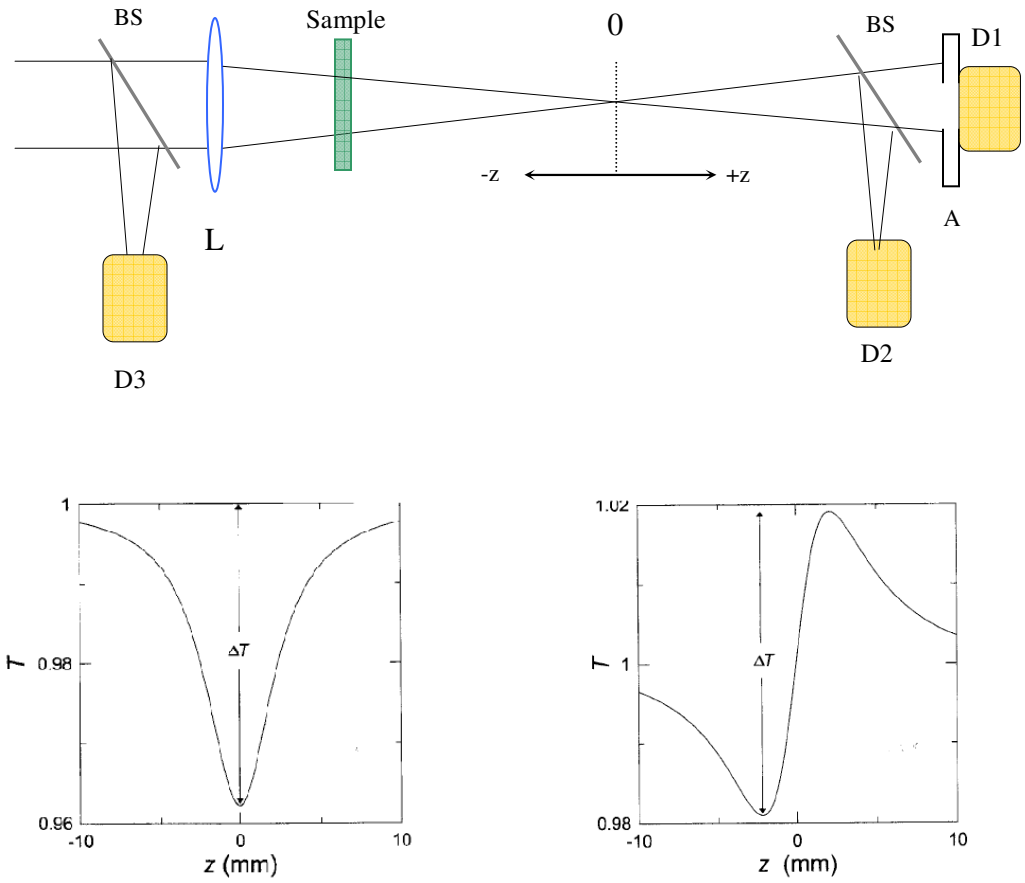

Fig. 9.5: Z-scan set-up for acquiring both open and closed aperture simultaneously. The Z-scan traces for the open (left) and closed aperture (right) for a material with $n_2>0$ are shown. From Ref [

In the case of n_2^I >0 and β=0, the situation is reversed, causing the transmittance to decreased for negative z values and increased for positive z values. The closed aperture z-scan immediately reveals the sign of n_2^I and its magnitude as related to the difference in transmittance between the peak and valley. This can be determined from an analysis of the z-scan curve[74].

When both n_2^I and β are non zero, the closed aperture peak is decreased and the valley incresed. In this case, β can still be determined independently from the open aperture analysis[74] and the ratio of closed aperture z-scan divided by the open aperture z-scan provides the closed aperture without nonlinear contribution[74].

The primary limitation of the z-scan technique is that the origin of mechanism for the nonlinearity is unknown[75]. No information is provided by the simple one beam version. More information is provided by the two beams version of the z-scan, where time resolved experiments are possible[76].

Nonetheless, z-scan has been largely used to analyze nonlinear properties of a wide variety of compounds; semiconductors[77-79], glass embedded with metal nanoclusters[75], carbon nanotubes[80], along with organic dyes[81] and polymers[82, 83].

9.5 Measuring nonlinearities via Z-scan technique

The Z-scan trace for a self-focusing medium ($n_2^I > 0$) is shown in fig. 9.5. The transmittance minimum is reached before the focus and a peak transmittance is resisted beyond the waist. The opposite is true for a self-defocusing medium ($n_2^I < 0$). The

nonlinear index n_2^I can be determined, for a thin Kerr medium, from the difference ΔT between the peak and the valley (maximum and minimum) as:

$$\Delta T = 0.406\,\kappa \left| n_2^I \right| I_0 L_{eff} \tag{9.30}$$

Where $L_{eff} = (1 - e^{-\alpha_0 L})/\alpha_0$ and α_0 is the linear absorption coefficient. K=2π/λ and I_0 is the irradiance at the beam waist w_0.

For measuring the nonlinear absorption of β, the open aperture Z-scan trace is used instead. A minimum in transmittance occurs when the sample is at the waist and the irradiance is the largest. A simple equation apply again:

$$\Delta T = \frac{1}{2}\beta I_0 L_{eff} \tag{9.31}$$

The complete treatment for deriving the transmittance T, as a function of the sample position can be found in the paper from Sheik-Bahae et al[74]. The equation used is simply reported below:

Open Aperture $$T(z) = 1 - \frac{\beta I_0 L_{eff}}{(2)^{3/2}(1 + z^2/z_0^2)} \tag{9.32}$$

Closed aperture $$T(z) = 1 - \frac{4k\Delta n}{\left[(z/z_0)^2 + 9\right]\left[(z/z_0)^2 + 1\right]}\left(\frac{1 - e^{-2\alpha L}}{2\alpha}\right) \quad (9.33)$$

Most treatments assume that the input laser beam is Gaussian. Laboratory lasers are not perfectly Gaussian, an issue that has been considered by a number of authors who examined the effect of beam shapes (other than Gaussian) in the Z-scan data[84, 85]. A parameter M^2 is introduced by some authors to describe their closeness to a Gaussian[85, 86]. Once the value of M^2 has been established (M^2=1 for a perfect Gaussian beam, M^2>1 for all the others) the nominal values for the other beam parameters as the beam waist w_0, the waist position z_0 and the irradiance I_0 will be determined accordingly[86].

9.5.3 Thermo-optical effects in Z-scan

Both linear and multiphoton absorption in a z-scan set up could induce density variations in the sample under analysis, as already mentioned for the DFWM technique (see section 9.2.1). Changes in the sample density will affect the closed aperture signals, where refractive index changes, due to temperature and density gradient will add to the variation induced by the nonlinearity[74, 87, 88]. When the laser pulse duration and spacing τ_p (where τ_p=1/laser repetition rate) is close to the acoustic transit time[89] τ_a defined as:

$$\tau_a = \frac{w}{v_s}$$

Where w is the beam radius at the sample and v_s the sound speed in the sample, acoustic effect will be detected during measurements.

Irrespective of the laser pulse, thermal effects come into play in the long-time exposure of the sample. This occurs when τ_p is shorter than the characteristic time necessary for the material to diffuse the heat,τ_d [89]. τ_d values can vary from the μs[89] to ms time-scale, and are usually much larger than τ_a. Cumulative effects such as thermal lensing have been investigated in literature[89-91]. A way of managing it consists of reducing the laser repetition rate, since larger τ_p can help reduce thermal lensing in the sample. Other solution proposed by Falconieri[89] and Gnoli[92] use data time correlation to extrapolate instantaneous nonlinear responses without thermo-optical contributions.

REFERENCES:

[1] Shen, Y. R., *The principle of nonlinear optics*. 1984, New York: Wiley.

[2] Butcher, P. N., Cotter, D. *The elements of nonlionear optics*. 1990, Cambridge: Cambridge Univ. Press.

[3] Caro, R. G., Gower, M. C., EEE J. Quantum Electron. 18, 1376 (1982)

[4] Laubereau, A., Top, App. Phys. **35**, 421 (1993)

[5] Laubereau, A., Von der Linde, D., Kaiser, W, Opt. Commun. 7, 173 (1973)

[6] Bogdan, A. R., Prior, Y., Bloembergen, N., Opt. Lett. 6, 82 (1981)

[7] Kobayashi, T., Terasaki, A., Hattori, T., Kurokawa, K., Appl. Phys. B. 47,107 (1988)

[8] Schmid, W., Vogtmann, T., Schwoerer, M, Opt. Commun. 121, 55 (1995)

[9] Williams, S., Rahn, L. A., Zare, R. N., J. Chem. Phys. 104, 3947 (1996)

[10] Hauer, J., Buckup, T., Motzkus, M., Phys. Chem. A. 111,10517 (2007)

[11] Caro, R. G., Gower, M. C, IEEE J. Quant. Electron. 18, 1376 (1982)

[12] Yariv, A., IEEE J. Quant. Electron. 14, 650 (1978)

[13] Pepper, D. M., Opt. Eng. 21**,** 156 (1982)

[14] Fujiwara, M., Kuroda, R., Nakatsuka, H., J. Opt. Soc. Am. B. 2, 1634 (1985)

[15] Acioli, L. H., Gomes, A. S. L., Leite, J. R. R., De Araujo, C. B, IEEE J. Quant. Electron. 26, 1277 (1990)

[16] Bloom, D. M., Bjorklund, G. E., Appl. Phys. Lett. 31, 592 (1977)

[17] Jensen, S. L., Hellwarth, R. W., Appl. Phys. Lett. 32, 166 (1978)

[18] Marin, G., Lam, L. K., Hellwarth, R. W., Opt. Lett. 5, 185 (1980)

[19] Psaltis, D., Mok, F., Sci. Am. 11, 52 (1995)

[20] Pepper, D. M., Rockwell, D. A., Dunning, G. J., IEEE Circuits Devices Mag. 9, 21 (1991)

[21] Damzen, M. J., Green, R. P. M., Crofts, G. J., Opt. Lett. 17, 1331 (1992)

[22] Yariv, A., Pepper, D., M., Opt. Lett. 1,16 (1977)

[23] Butcher, P. N., Cotter, D., *The elements of nonlionear optics*. 1990, Cambridge: Cambridge Univ. Press.

[24] Shen, Y.R., IEEE J. Quant. Electron. 22, 1196 (1986)

[25] MacKenzie, H. A., Hagan, D. J., Al-Attar, H. A., IEEE J. Quant. Electron. 22, 1328 (1986)

[26] Kühlke, D., Appl. Phys. B. 34, 129 (1984)

[27] Eyring, G., Fayer, M. D., J. Chem. Phys. 81**,** 4314 (1984)

[28] Fourkas, J. T., Trebino, R., Fayer, M. D., J. Chem. Phys. 97, 78 (1992)

[29] Fourkas, J. T., Trebino, R., Fayer, M. D., J. Phys. Chem., 97, 69 (1992)

[30] Yariv, A., *Quantum electronics*. 1989, New York: Wiley

[31] Bloembergen, N., J. Opt. Soc. Am. 70,1429 (1980)

[32] Fisher, R. A., *Optical phase conjugation*. 1983, New York: Academic

[33] Heilweil, E. J., Hochstrasser, R. M., Souma, H.,Opt. Commun. 35, 227 (1980)

[34] Byrne, H. J., Blau, W, Jen, K. -Y, Synth. Met. 32, 229 (1989)

[35] Horan, P., Blau, H., Berglund, P., Appl. Opt. 29, 31 (1990)

[36] Puech, K., Henari, F. Z., Blau, W. J., Duff, D., Schmid, G., Chem. Phys. Lett. 247, 13 (1995)

[37] Eichler, H. J., Gunter, P., Pohl, D. W., *Laser-induced Dynamic grating*. 1986, Berlin: Springer.

[38] Eichler, H. J., Opt. Acta. 24, 631 (1977).

[39] Wherrett, B. S., Smirl, A. L., Boggess, T. F., IEEE J. Quant. Electron. 19, 680 (1983)

[40] Trebino, R., Gustafson, E. K., Siegman, A. E., J. Opt. Soc. Am. B. 3,1295 (1986)

[41] Fourkas, J. T., Trebino, R., Fayer, M. D., J. Phys. Chem. 97, 69 (1992)

[42] Smirl, A. L., Boggess, T. F., Wherrett, B. S., Perryman, G. P., Miller, A., IEEE J. Quant. Electron. 19, 690 (1983)

[43] McEwan, K.J., Harrison, K. J., Madden, P. A., Molec. Phys. **69**, 1025 (1990)

[44] Nunzi, J. M., Charra, F., Mol. Cryst. Liq. Cryst. Sci. Technol.-- Sec. B: Nonlinear optics. 2, 131 (1992)

[45] Nelson, K. A., Lutz, D. R., Fayer, M. D., Madison, L., Phys. rev. B. 24, 3261 (1981)

[46] Miller, R. J. D., Casalegno, R., Nelson, K. A., Fayer, M. D., Chem. Phys. 72, 371 (1982)

[47] Desai, R. C., Leverson, M. D., Barker, J. A., Phys. Rev. A. **27**,1968 (1983)

[48] Genberg, L., Bao, Q., Gracewski, S., Miller, R. J. D., Chem. Phys. 131, 81 (1989)

[49] Chang, T. Y., Opt. Eng. 20, 220 (1981)

[50] Prasad, P. N., William, D. J., *Introduction to nonlinear optical effects in molecules and polymers*. 1991, New York: Wiley.

[51] Bredas, J. L., Adant, C., Tackx, P., Persoons, A., Pierce, B. M., Chem. Rev. 94, 243 (1994)

[52] Gower, M. C., Prog. Quant. Electron. 9, 101 (1984)

[53] Terazima, M., Chem. Phys. 189, 793 (1994)

[54] Punchenkov, O. V., Malkin, S., Chem. Phys. Lett. 251, 242 (1996)

[55] Fayer, M. D., IEEE J. Quant. Electron. QE-22,1437 (1986)

[56] Stegeman, G. I., Wright, E. M., Finlayson, N., Zanoni, R., Seaton, C. T., J. Lightwave Technol. **6**, 953 (1988)

[57] Stegeman, G. I., Miller, A., *Photonic in Switching*. 1993, Boston: J. E. Midwinter

[58] Carter, G. M., Thakur, M. K., Chen, Y. J., Hryniewcz, J. V., Appl. Phys. Lett. 47, 457 (1985)

[59] Maloney, C., Byrne, H., Dennis, W. M., Blau, W., Chem. Phys. 121, 21 (1988)

[60] Fukumi, K., Chayahara, A., Kadoro, K.,Sakaguchi, T., Horino, Y., Miya, M., Hayakawa, J., Satou, M., Jap. J. Appl. Phys. 30, L742 (1991)

[61] Santran, S., Canioni, L., Sarger, L., Cardinal, T., Fargin, E., J. Opt. Soc. Am. B. 21, 2180 (2004)

[62] Zakery, A., Ruan, Y., Rode, A. V., Samoc, M., Luther-Davies, B., J. Opt. Soc. Am. B. 20, 1844 (2002)

[63] Smith, P. W., Tomlinson, D. J., Maloney, P. J. 6, 581 (1981)

[64] Shinojima, H., Yumoto, J., Uesugi, N., Appl. Phys. Lett. 60, 298 (1991)

[65] Kamada, K., Ueda, M., Sakaguchi, T., Ohta, K.,Fukumi, Chem. Phys. Lett. 249, 329 (1996)

[66] Xuan, N. P., Ferrier, J. L., Gazengel, J., Rivoire, G., Opt. Commun. 51, 433 (1984)

[67] Sahraoui, B., Sylla, M., Bourdin, J. P., Rivoire, G., Zaremba, J., J. Modn. Opt. 42, 1095 (1995)

[68] Carter, G. M., J. Opt. Soc. Am. B. 4, 1018 (1987)

[69] Maloney, C., Blau, W., Drexhage, K. H., Opt. Lett. 11, 434 (1986)

[70] Luan, S., Hutchinson, M. H. R., Smith, R. A., Zhou, F., Meas. Svi. Technol. 4, 1426 (1993)

[71] Eichler, H. J., Langhans, D., Massmann, F., Opt. Commun. 50, 117 (1984)

[72] Levine, A. M., Ozizimir, E., Trebino, R., Hayden, C. C., Johnson, A. M., Tokuda, K. L., J. Opt. Soc. Am. B. 11, 1609 (1994)

[73] Goldberg, S. Y., Pines, D., Meltsin, A., Fainberg, B., Huppert, D., Mol. Cryst. Liq. Cryst. Sci. Technol.-- Sec. B: Nonlinear optics. 5, 307 (1993)

[74] Sheik-Bahae, M., Said, A. A., Wei, T.-H., Hagan, D., Van Stryland, E. W., IEEE J. Quant. Electron. 26, 760 (1990)

[75] Haglund, R. F., Yand, R. H., Magruder, R. H., Wittig, J. E., Becker, K., Zuhr, R. A., Opt. Lett. 18, 373 (1993)

[76] Tseng, K. Y., Wong, K. S., Wong, G. K. L., Opt. Lett. 21, 180 (1996)

[77] Lee, K., Cho, W., Park, J., Kim, J., Park, S., Kim, U., Opt. Lett. 19, 1116 (1994)

[78] Brinda, K. S., Singh, C. P., Oak, S. M., Opt. Commun. 271, 248 (2007)

[79] Zhang, X., Fang, H., Tang, S., Ji, W., Appl. Phys. B. 65, 549 (1997)

[80] Maeda, A., Matsumoto, S., Kishida, H., Takenobu, T., Iwasa, Y., Shiraishi, M., Okamoto, H., Phy. Rev. Lett. 94, 047404/1 (2005)

[81] Swiatkiewicz, J., Prasad, P. N., Reinhardt, B. A., Opt. Commun. 157, 135 (1998)

[82] Yang, L., Dorsinville, R., Alfano R. R., Zou, W. K., Yang, N.L., Opt. Lett. 16, 758 (1991)

[83] Samoc, M., Samoc, A., Luther-Davies, Bao, Z., Yu, L., Hsieh, B., Scherf, U., J. Opt. Soc. Am. 15, 817 (1998)

[84] Hermann, J. A., Wilson, P. J., Int. J. Nonlin. Opt. Phys. 2, 613 (1993)

[85] Siegman, A. E., Proc. SPIE Int. Soc. Opt. Eng. 1224, 2 (1990)

[86] Chapple, P. B., Wilson, P. J., J. Nonlin. Opt. Phys. Mat. 5, 419 (1996)

[87] Heyes, J. N., Appl. Opt. 11**,** 455 (1972)

[88] Mian, S. M., McGee, S. B., Melikechi, N., Opt. Commun. 207, 339 (2002)

[89] Falconieri, M., J. Opt. A. 1, 662 (1999)

[90] Wei, T. H., Huang, T. H., Lin, M. S.. Appl. Phys. Lett. 72, 2505 (1998)

[91] Misoguti, L., Mendonca, C. R., Zilio, S. C., Appl. Phys. Lett. 74, 1531 (1999)

[92] Gnoli, A., Razzari, L., Righini, M., Opt.Express. 13, 7976 (2005)

CHAPTER X

DFWM AND Z-SCAN SET-UPS AND MEASUREMENTS

Abstract

The second order hyperpolarizability $\langle\gamma\rangle$ at 1300 and 1500 nm was measured for extended squaraine dyes via DFWM and Z-scan. All the measurements were performed using using 100 fs laser pulses. The squaraine systems under analysis revealed large magnitude for $\langle\gamma\rangle$, on the order of 10^{-32} esu, with large contribution for the imaginary part, especially at 1300nm. The macroscopic nonlinearity $\left|\chi^{(3)}\right|$ was measured for some of the dye at 1300 nm in thin film, where two-photon absorption cross sections on the order of 10-9 m W^{-1} were found. The data from the z-scan (open aperture) revealed a contribution from excited state absorption along to two-photon absorption. The values are reported and the results discussed.

10.1 The laser system

The femtosecond laser source used for determining $\left|\chi^{(3)}\right|$ and $\langle\gamma\rangle$ is a Spectra-Physics Ti:sapphire regenerative amplifier (Spitfire) which generates ~100 fs pulses at 800 nm with a repetition rate of 1 KHz and 1mJ of peak energy per pulse. This in turn pumps a Spectra-Physics optical parametric amplifier (OPA-800CF) that provides output pulses of <100 fs at 1300 and 1500 nm with an average energy of 60 μJ per pulse at 1 KHz.

10.2 DFWM Set-up description:

The signal generated at 1300 nm (or 1500 nm) from the OPA 800C propagates through a low pass filter that removes the residual 800 nm of the pumping beam. The filter has a high transmittance in the range 1200-1500 nm. The system includes a waveplate and polarizer that allows the power to be varied in a linear and continuous fashion, the half waveplate is mouthed on a rotating stage connected to a computer controlled stepper motor.

The beam gets focused down to a pinhole of about 100 μm in diameter where the beam is spatially filtered. The energy transmitted through the spatial filter is about 80% of the incident one.

The beam goes trough the first beam splitter where about 40% of the energy gets reflected and send to the first arm (beam1). The transmitted beam then goes trough a second beam splitter with a T/R ratio of about 50%. The reflected beam is beam 3and the last arm (beam 2) is the one furthest away from the laser source.

Beam1 is directed to a computer controlled corner cube mounted on a delay stage (Newport.PM500C.) that can be moved along the beam axis (see fig. 11.2) with a precision of 0.1 μm. A stage with relatively high precision is require for dynamic studies involving fs pulses, considering that a pulse of 100 fs in duration is about 30 μm long. On each arm, a system of polarizers and half waveplates (arm 2 is different) are utilized to control the polarization of each one of the beams independently. Polarizing optics are voluntarily placed on the last section of the beams optical path to maintain polarization as pure as possible.

Various apertures are placed along the beam path to facilitate the alignment.

In order to achieve the "folded BOXCARS" geometry (see chapter IX), beam 1 and 3 are at the same height, while beam 2 is 0.7 cm higher. The arrangement of beams appear as depicted in fig. 10.1 on a plane perpendicular to the direction of propagation after lens L_1.

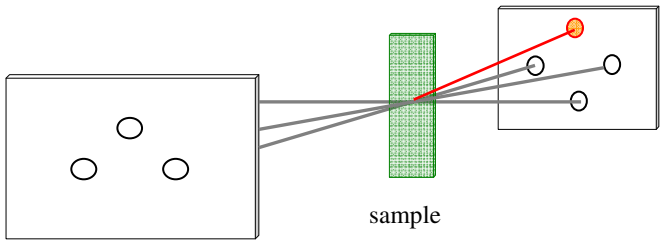

Fig.10.1: Beams configuration after the focusing lens L1 and as they go through the sample and the DFWM signal id generated (red beam)

The angle that beam 1 and 2 form with each other and with beam 3 is about 3°.

The three beams are focused using an achromatic plano-convex lens (focal length =350 mm). The three beams need to be spatially and temporally overlapped in order to generate the signal; the spatial overlap at the focus is obtained by using a CCD camera (BeamStar 2000 Vidicon). The temporal overlap is achieved instead by mean of a doubling crystal (BBO 1 mm thick). A more complete explanation is reported in section 10.2.3.

The direction of the propagating signal is defined by the phase matching requirements, as described in chapter 9. A collimating lens is positioned after the sample, with a focal length of 500 mm, establishing a magnification factor of about 1.4. An aperture is placed just after the collimating lens to block beams 1, 2 and 3 as well as self-diffracted beams and scatter coming from the sample, allowing the DFWM signal to pass. The position of the signal again is defined precisely so that the aperture can be placed accordingly. The signal travels to the detector trough a series of aperture and mirrors, such that as it propagates part of the incoherent scatter light gets removed. The signal gets finally focused and collected by photoreceiver D2.

Reference photoreceiver D1 monitors the laser stability over the course of measurements. The energy is measured at the sample level and it refers to beam 1 (the energy ratio between the three beams is known and constant)

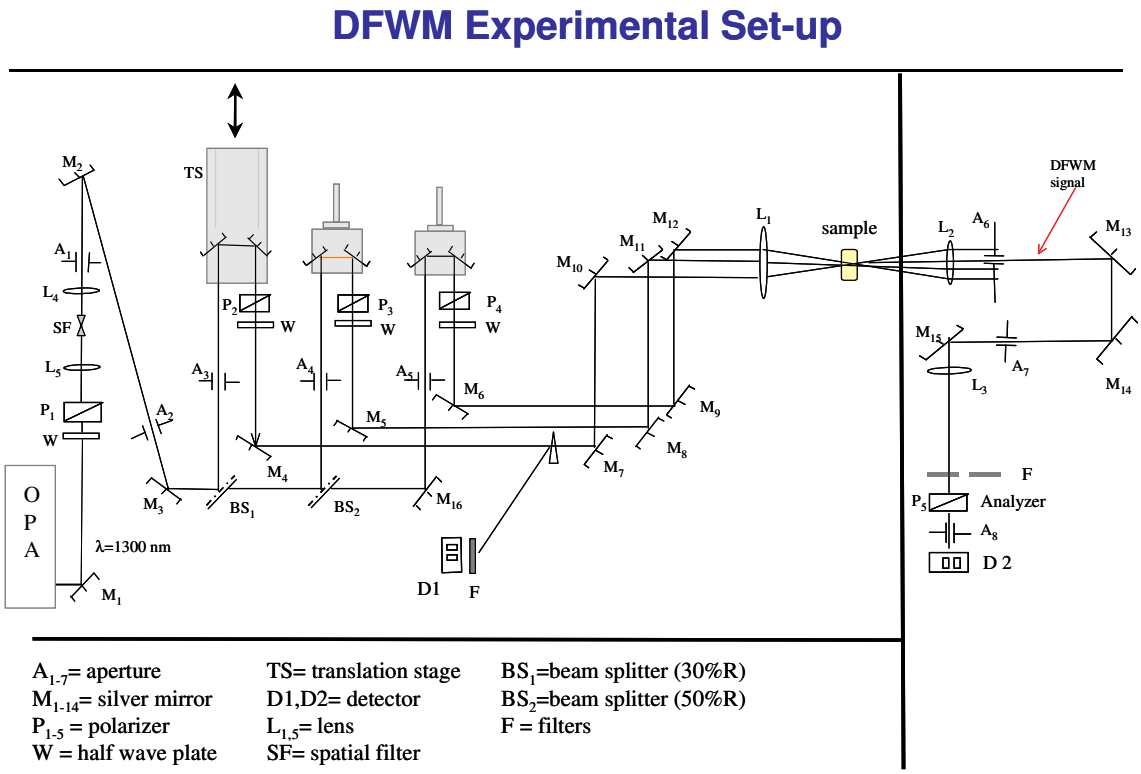

Fig.10.2: Schematic of the DFWM set-up

10.2.1 CCD camera and beam profile

The CCD camera utilized to record the beams spatial profile was a BeamStar 2000 Vidicon with relative software. The camera allows measuring wavelengths from 400 to over 2000 nm, with a max in sensibility around 800 nm. The horizontal and the vertical resolution were 13.0 μm/pixel and 13.8 μm/pixel respectively. The camera provides a profile of the beam as slices along two axes perpendicular to the beam propagation direction (named x and y), with power dependence that is not linear, in fact (output) $\propto$ $(\text{input})^{0.7}$ as reported from the factory.

After correction of the intensity data along the x and y axis, the beam waist is taken as the distance from the rotation axis at which the amplitude falls a factor 1/e of its maximum value or equivalently, the distance at which the intensity drops a factor $1/e^2$ of its peak value I_0.

An example of the profiles as they appear on the camera is reported below.

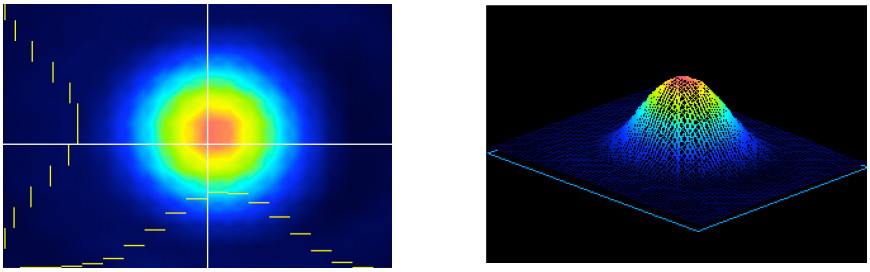

Fig.10.3: Spatial intensity distribution of the 1300 nm beam at 1 KHz as shown by the CCD camera.

10.2.2 Interaction length

The OPA output at 1300 nm, after going through a spatial filter is cylindrically Gaussian (as expected for a TEM_{00} type mode). The spatial intensity distribution profile was determined by the use of a CCD camera. Snapshots of the beam taken at about 3 meters down the optical table are shown in fig.10..3.

A soft focusing is applied to the beams with a double purpose; having a relatively large beam waist (beam radius) at the focus (w_0) together with a long Rayleigh range, defined as the region along the propagation direction where the beam waist (w_z) is $\sqrt{2}\, w_0$.

According to the Gaussian beam propagation the Rayleigh range can be calculate as:

$$x_R = \frac{\pi w_o^2}{\lambda} \tag{11.1}$$

Where λ is the wavelength of light. The beam waist at the focus w_0 can be determined in terms of the input beam parameters:

$$w_0 = \left(\frac{2\lambda}{\pi}\right)\left(\frac{F}{D}\right) \tag{11.2}$$

Where F represents the focal length of the lens, and D the diameter of the incident beam. The (F/D) ration is also known as the photographic f-number of the lens. The beams parameters for the set-up are reported on table 10.1.

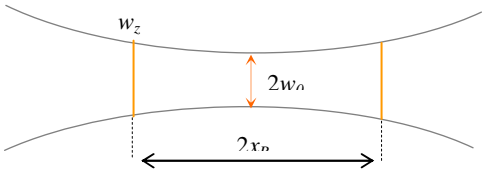

Fig.10.4: Reileigh range for a focusing Gaussian beam.

Table 10.1: Beam waist, w_0, and Reyleigh range value for the DFWM set-up

Beam #	**w_0/[μm]**	**Rayleigh range /[cm]**
1	135	2
2	130	2
3	115	1.7

The three beams are propagating toward the sample with on angle θ of about 3.2°, the region over which they are spatially overlapped can be easily determined using simple trigonometry. Assuming that the beams are spatially overlapped at the focus, the rate at which the two pump beams (1 and 2) are moving apart from each other is

$$d = 2 z_f \sin\frac{\theta}{2} \tag{11.3}$$

Fig. 10.5: Illustration of the beam divergence d as they move away from the focus Where d represents the displacement between the two beams and z_f the distance from the focus.

For a displacement equal to 10% of the beam waist at the focus (a long Raylegth range assures the waist to stay constant) solving for z_f would give a value of about ±0.3 mm around the focus. What is the threshold that determines the beam not to be overlapped is at this point arbitrary.

An experiment was conducted to test the physical length of the spatial overlap for the 3 beams around the focus. The CCD camera was bolted on a linear translation stage and starting at the focus; the stage was moved first in one direction and then in the opposite one.

The distance over which the beam waist of the 3 overlapped beams would not change was considered overlapping area. As soon as the beam waist increased the stage was stopped and brought back to the original position. By performing such test, the overlap region was estimated to be around 1 mm.

10.2.3 Temporal overlap

All three beams need to be overlapped both is space and time in the sample to be able to produce the maximum DFWM signal. Temporal alignment consists on allowing the same pulse to travel the exact same length on all three arms and merge at the sample. The strategy implemented involves using a nonlinear crystal to produce second-harmonic radiation. The phase matching[1] in the crystal from two overlapping beams (in space) is used to produce a beam at the second harmonic frequency in which one photon has been taken from one beam and one from the other. In order to have second harmonic generation in the crystal the two beams must be overlapped in time as well as in space. The second harmonic signal generated upon temporal overlap can be detected by eye on a white screen placed after the nonlinear crystal (the second harmonic signal is in the visible when 1300 nm are. To achieve the temporal overlap the delay line of beam 2 and 3 are moved, one at the time, until the respective second harmonic signals are detected on the screen. Eventually all 3 beams will be overlapped. The nonlinear medium used was a BBO crystal 1 mm thick.

10.2.4 Spatial Filter

The laser output should be as close to a TEM_{00} type as possible, mainly because of the large use of such spatial distribution to describe all kinds of phenomena[2, 3]. Unfortunately, aberrations in the beam are common, due to imperfect or damaged optics or even variation in the laser gain medium. Spatial filters are often used to improve beam quality by removing possible aberrations.

The two-dimensional beam intensity pattern at the focus represents the two-dimensional Fourier transform of the beam's initial intensity distribution. A perfect plane wave will focus down to a single spot, while a beam with higher spatial frequency will have a light pattern with other components around the central spot that still represents the plane wave[4]. By imposing a plane wave distribution at the transform plane (focal plane) by removing the higher frequency components, it is possible to obtain a more Gaussian like beam. Spatial filter acts like a low pass filter for spatial noise[5]

In order to do this a lens is used to focus the beam, a pinhole is placed at the focal plane to block unwanted structures that represents high frequency components, then a second lens is placed afterwards to collimate the beam. In the set-up described in this thesis, the power was reduce by 20%, producing a relatively good beam profile.

It is important to remember that a TEM_{00} type of mode, even though not an essential requirement for DFWM type of experiments, mainly because these are referential type of measurements, becomes very important for Z-scan type of measurements, where the beam spatial profile plays an important role.

10.2.5 Measurement procedure

Since the DFWM signal is collected directly, it is important to be as free of scattering as possible. When solution measurements are performed, the scattering is minimized by using clean cell and solutions that are particles free. When films are measured, scatter can be generated from multiple sources: the film itself (pinholes, rough surfaces, particles, crystal domain etc.) as well as the substrate.

It is important then that the film has a very good quality and this starts by using solutions and substrates that are free of particles. Cleaning the substrate and filtration of the solution increase the optical quality, as well as choosing the appropriate method to prepare the film. What has been observed is that spin-coated films usually have better optical quality than drop-casted ones.

The measurement routine starts by selecting the appropriate repetition rate for the sample and measuring the reference (slab of fused silica). The signal from the reference is collect by the data acquisition system (DAS) and sent to an oscilloscope, this makes it easy to check for scattering in the sample. By blocking one beam at a time the signal should disappear leaving the background noise from the detector.

By blocking the beams we are eliminating potential scatter coming from the beam itself and so an alternative method to insure the absence or presence of scatter is by delaying one of the beam using the delay stage. This allows us to have all three beams interacting at the sample, without temporal overlap and no DFWM signal is detected. Any signal left on the oscilloscope at this stage is then purely due to scatter. Each sample was scanned over different region to minimize the scattering and beam aberrations. This is

essential in films type of samples, where the scattering is highly dependent on the quality of the surface.

After bringing the delay stage back to zero delay, the signal from the sample gets optimized, and it is now ready for the data collection.

The data collection starts with a signal able to generate about 0.2 Volts on the detector D2 (signal) and filters are selected so that the reference has about 1 Volt.

The DAS interface was engineered so that the following parameter had to be defined: the number of data point to average at each energy; the increase in energy after the previous routine is completed (which is translated into degree of rotation for the waveplate) and the total number of energies.

Detector D2 has a filter wheel that allows exploring DFWM signals over a wide energy range.

10.3 Z-scan set-up description

The Z-scan technique, being a single-beam method requires a relatively simple apparatus. Fig. VV illustrates the experimental set-up. The Gaussian beam after the spatial filter is focused using a 15 cm focal length lens. The sample is moved along the beam propagation direction on a translation stage (Newport ILS100PP) with a resolution of 0.5 μm. The sample transmittance is measured as function of the sample position, z, for the closed aperture (detector D3) and the open aperture (detector D2) at the same time.

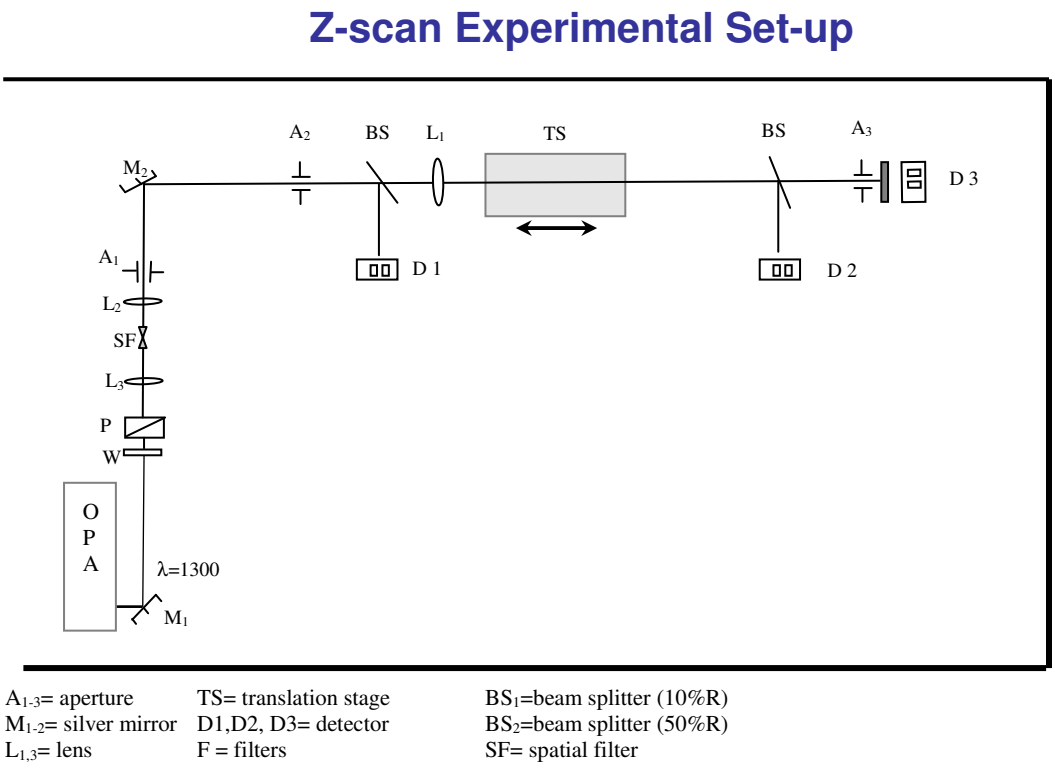

Fig 10.6: Experimental set-up for Z-scan measurements

The sample transmittance for the open and closed aperture is measured as the ratio between D3/D1 and D2/ D1 respectively. For each position the transmittance is averaged over a number of laser shots, preset through the DAS.

10.4 Structures and linear absorption properties of extended squaraine systems.

Squaraines contain a central electron-withdrawing ring with two or more electro-donating group have been identify as a candidates for large nonlinearities since the observation of Dirk et al in 1992.

The structure of the dyes under analysis are reported in fig. 10.7. Compound I to III have in common the same squarylium core, as we go from I to III each system is conjugated to an increasing number of weak donor groups increasing of the overall chain length. Donor group like thiophene and pyrrole are utilized to help keeping the structure more rigid. Compound IV clearly differs from the rest, having a double squarylium core and only one donor group on each side. Figure 10.7 reports the number of double bonds on the main chain for each compound, useful in the analysis that follows.

Linear absorption spectra of the dyes in solution are shown in fig. 10.8. Table 10.2 collects the value for the absorption maximum, molar extinction coefficient, ε_{01}, and the transition dipole moment μ_{01} obtained from the integrated strength of the one photon allow transition as[6, 7]:

$$\mu_{01} = \left[\frac{\left(\int \varepsilon_\nu d\nu \right)}{\nu_{01}} \cdot \frac{3\ln(10) hc\varepsilon_0}{2\pi^2 N_A} \right] \tag{10.4}$$

N_D*

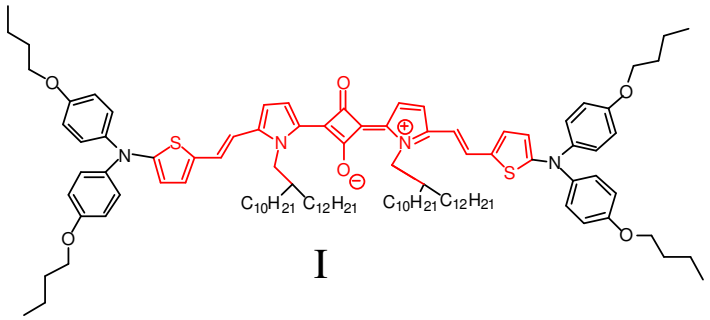

I

11

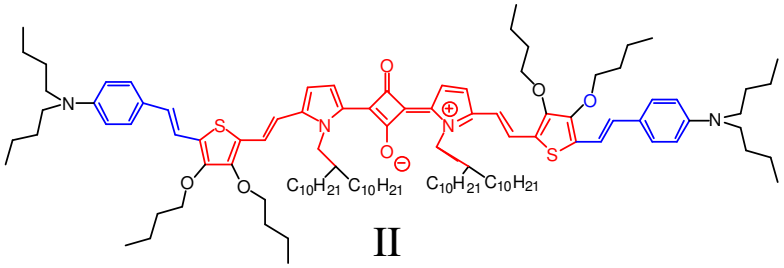

II

17

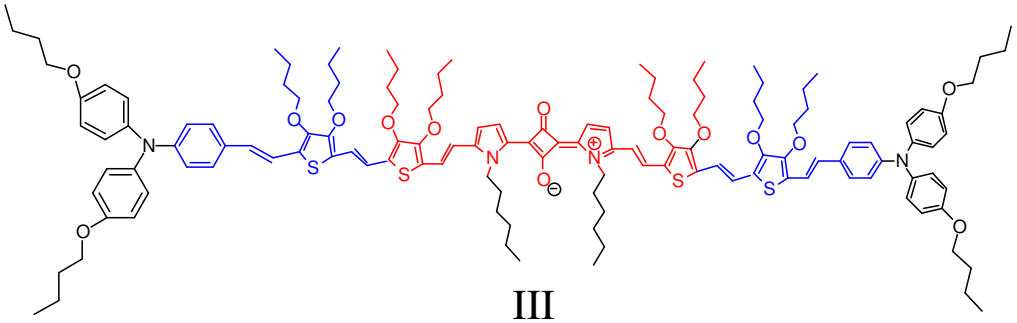

III

23

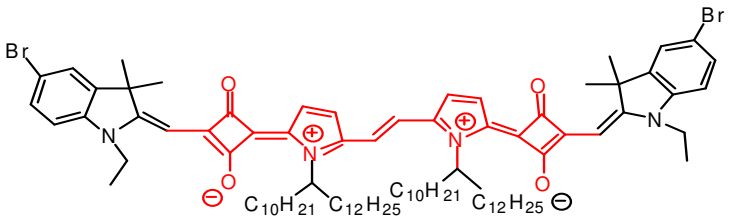

IV

9

* N_D= number of double bonds in the main chain

Fig. 10.7: Structures of the D-A-D squaraine systems under investigation. The number of double bond on the main chain is indicated to the right.

Where ε_ν is the dye extinction coefficient, ν_{01} is the peak transition frequency, h, c and ε_0 are Planck's constant, speed of light and dielectric constant in vacuum respectively, while N_A is the Avogadro's number and the integral in equation 10.4 is performed over the absorption band

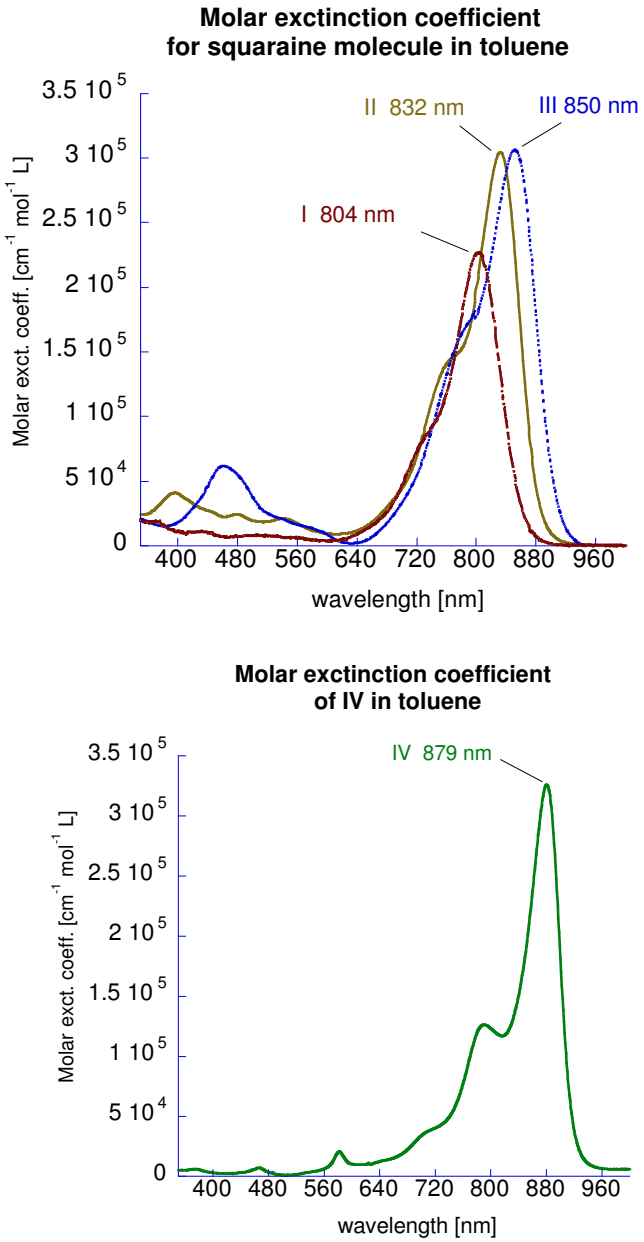

Fig. 10.8. Extinction coefficient of squaraine dyes in toluene.

Table 10.2: Linear properties of extended squaraine systems in solution

Compound #	λ_{max} in toluene /nm	ε / Mol^{-1} cm^{-1}	μ_{01}/ Debye
I	805	2.5 10^5	16
II	832	3.0 10^5	20
III	850	3.0 10^5	20
IV	879	4.0 10^5	21

10.5 DFWM measurements in solutions: extracting γ

The second-order hyperpolarizability $\langle\gamma\rangle$ is measured in toluene solutions via DFWM and Z-scan technique at 1500 and 1300nm.

10.5.1 Hyperpolarizability <γ> of squaraine type molecules via internal reference method at 1300 and 1500 nm.

A complete characterization of the nonlinear properties of the systems under analysis requires knowledge of their nonlinearity at the microscopic level before moving to the bulk (or high density) nonlinearity. The internal reference methods, described in chapter 9, will be use to extract $\langle\gamma\rangle$ at 1300 nm and 1500 nm for both D-A-D squaraines via DFWM measurements. The normalized $\langle\gamma\rangle$, calculated as $\langle\gamma\rangle$ divided by the number of double bonds, N_D, is then plotted as function of N_D. The results are reported and discussed.

Materials and methods

A solution of the dye in toluene is prepared with a known concentration, for squaraine dyes is on the order of 10^{-3} Mol. At least 10 others solutions with different concentrations are obtained by dilution of the original sample. After obtaining the DFWM signal and optimizing it for each solution, its power dependence is measured, at least twice, in a 1mm quartz cuvette. The reference material is a fused silica slab, 1 mm in thickness. Power dependence for the pure toluene is repeated regularly throughout the duration of the measurements to assure reproducibility. Z-scan measurements are performed on the same solutions for each dye as well. The measurements are performed both at 1KHz and at 50 Hz laser repetition rate for some of the dye, to exclude thermal contributions to the nonlinearity (see Chapter 9)

Results

The equation reported in Chapter 9, where the internal reference method was described in section 9.3, required the determination of $\left|\chi^{(3)}\right|_{solution}$ at different dye concentration, *c,* as reported in equation 10.5 shown below.

$$\frac{\left|\chi^{(3)}(c)\right|_{solution}}{\left|\chi^{(3)}\right|_{solv}} = \left\{\left[1 + c \cdot g \cdot \cos(\varphi)\right]^2 + \left[c \cdot g \cdot \sin(\varphi)\right]^2\right\}^{1/2} \qquad (10.5)$$

$\left|\chi^{(3)}\right|_{solution}$ is obtained by using equation 9.19. The coefficient ν from equation 9.18 is obtained by running the power dependence on each solution. The typical data set for power dependence is shown below.

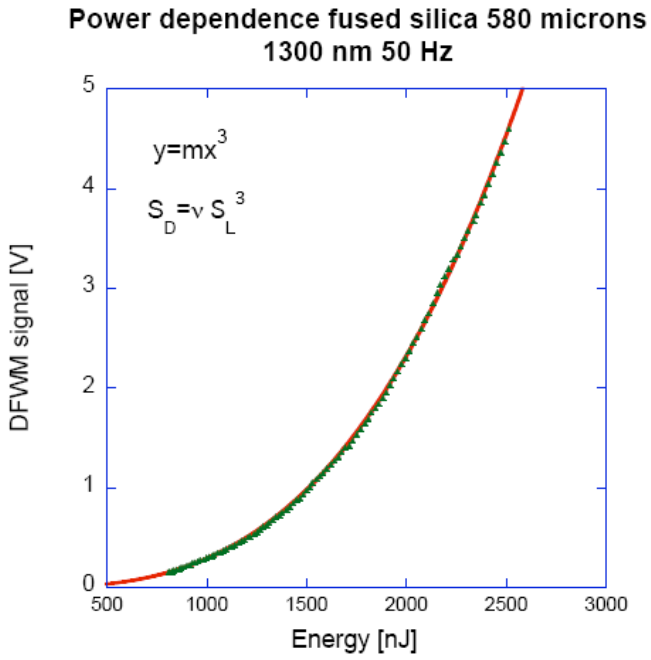

Fig. 10.9: Power dependence data for fused silica. Data points are in green and the cubic function used to fit the data is represented by the red line.

High repetition rate (1KHz) λ=1300 nm

For pure toluene, an average value of $\left\|\chi^{(3)}\right\|$= 8.9×10^{-14} esu is obtained when fused silica is the reference material; the index of refraction for toluene was 1.49. As a remainder $\left\|\chi^{(3)}\right\|$=$1.5\times10^{-14}$ esu is the value used for the fused silica, the index of refraction used was 1.45.

In fig. 10.11 experimental values and relative fitting are reported for compounds I, II III and IV at 1300nm. The phase values are obtained from z-scan measurements described in this chapter. As mentioned, the internal reference method is not very sensitive to the phase, making it very difficult to extract it from the DFWM data obtained. As proof in fig. 10.10 are reported the data for compound III fitted with different phase values: very little difference is found for the R parameter (also known as *goodness of fit*) when the phase values are imposed to be 60 and 20 degrees.

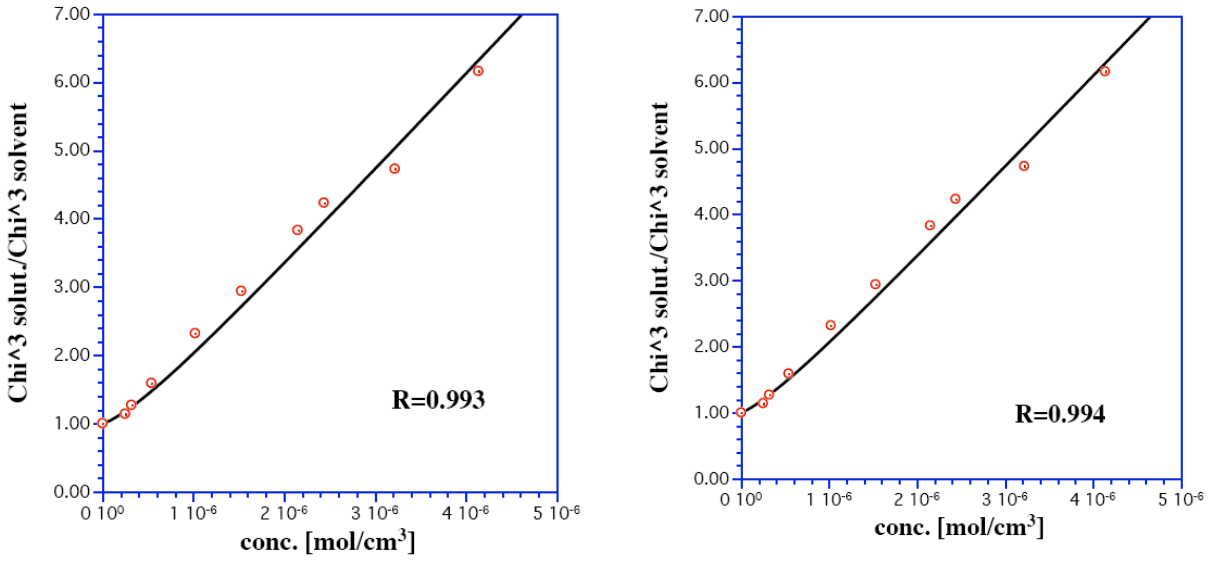

Fig 10.10: Data fitting using the internal reference method for compound III imposing different values for the phase: 20 degrees on the right and 60 on the left

Solution measurements at 1KHz provide positive values of γ for all compounds under analysis.

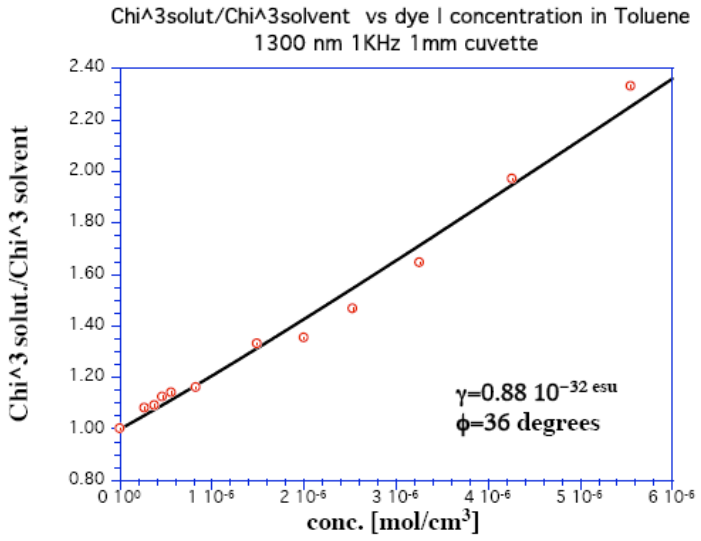

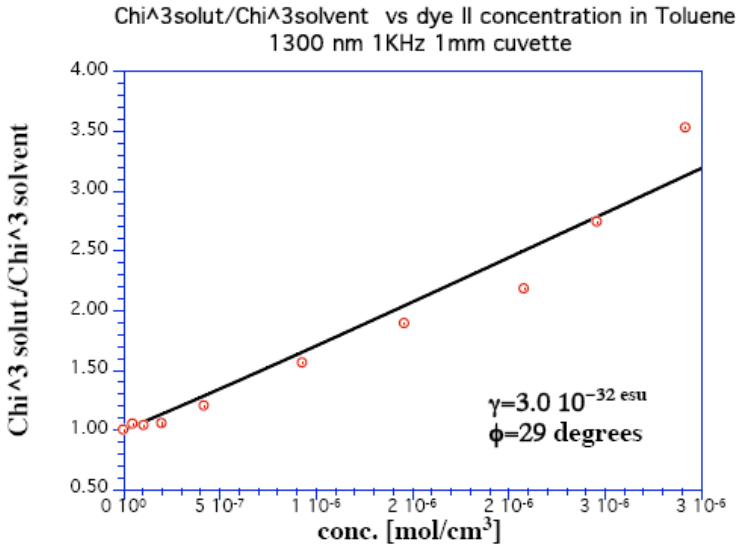

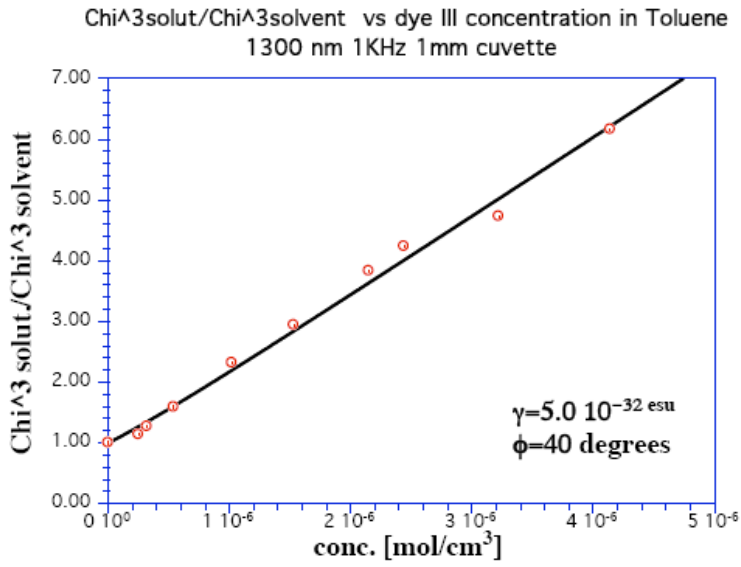

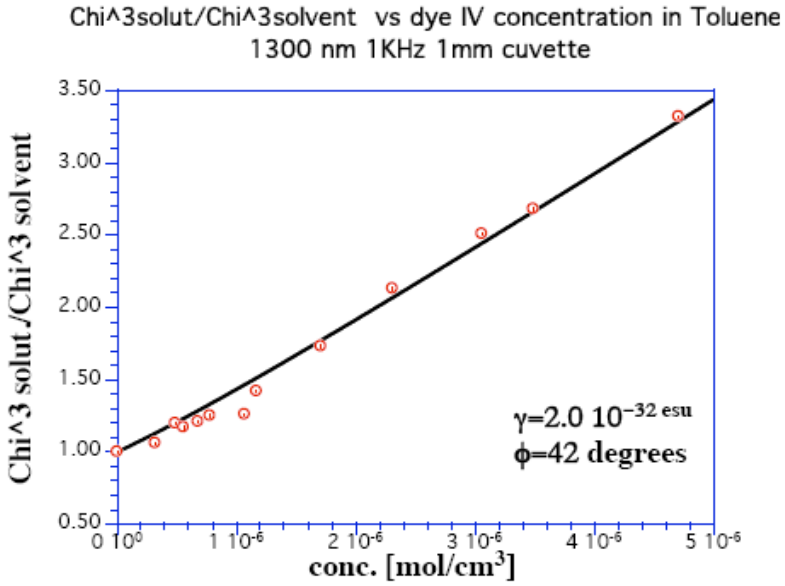

Fig. 10.11: Solution measurements at 1300 nm for determining the microscopic third order nonlinearity $\langle\gamma\rangle$ according to the internal reference method. The phase values were obtained from Z-scan measurements.

Low repetition rate (50 Hz) λ=1300 nm

The squaraine dyes under analysis have relatively large nonlinear absorption cross sections at 1300 nm and induced thermal gratings could overestimate the magnitude of $\langle\gamma\rangle$. The data at 50 Hz confirmed the values for the magnitude of $\langle\gamma\rangle$ obtained at 1 KHz removing the possibility of contribution from thermal processes[8-10].

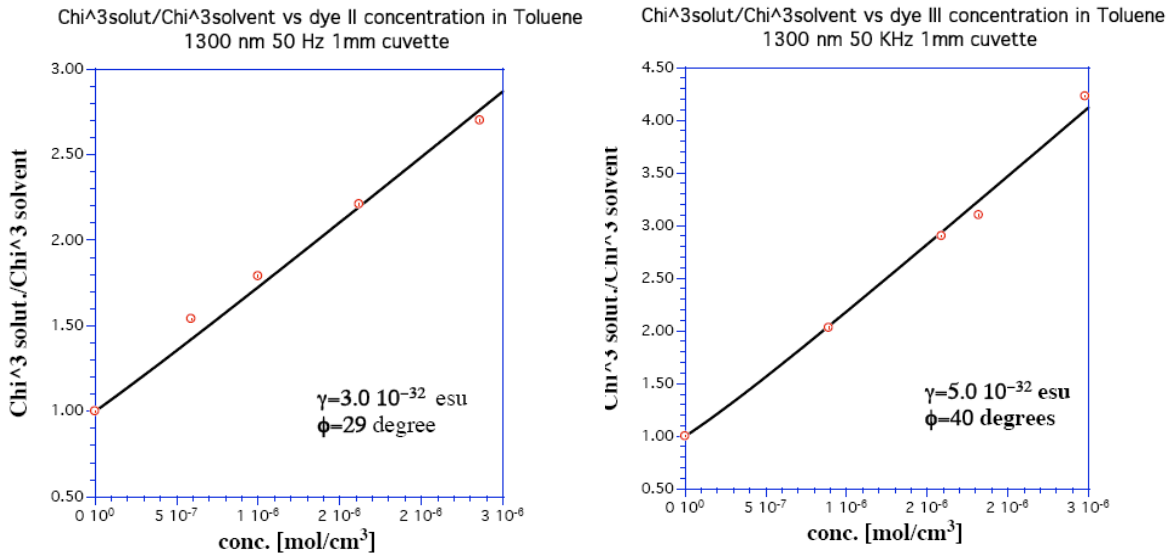

Fig. 10.12: Internal reference method for dye II and III repeated at low repetition rate (50 Hz) to investigate any contribution from thermal nonlinearity

When $\langle\gamma\rangle$ is determined using a reduced repetition rate, similar values were obtained for dye II and III at 1300 nm (within the experimental error). Dyes II and III have large imaginary parts compare to dye I and IV and it is safe to assume that no thermal effects would be observed from them either.

The $\langle\gamma\rangle$ values are then measured at 1500 nm at 1KHz only, since this wavelength is further detuned by the two-photon peak, and a smaller phase value is expected for the dyes.

<u>High repetition rate (1 KHz) λ=1500 nm</u>

For pure toluene an average value of $\left\|\chi^{(3)}\right\| = 9.06\times10^{-14}$ esu is obtained when fused silica is the reference material, the index of refraction for toluene was 1.49. For fused silica a $\left\|\chi^{(3)}\right\| = 1.5\times10^{-14}$ esu is used at 1500 nm, the refractive index remains at 1.45 as well.

The data obtained for the compounds are shown in fig. 10.13.

Again, the phase values used were obtained from Z-scan measurements at 1500 nm.

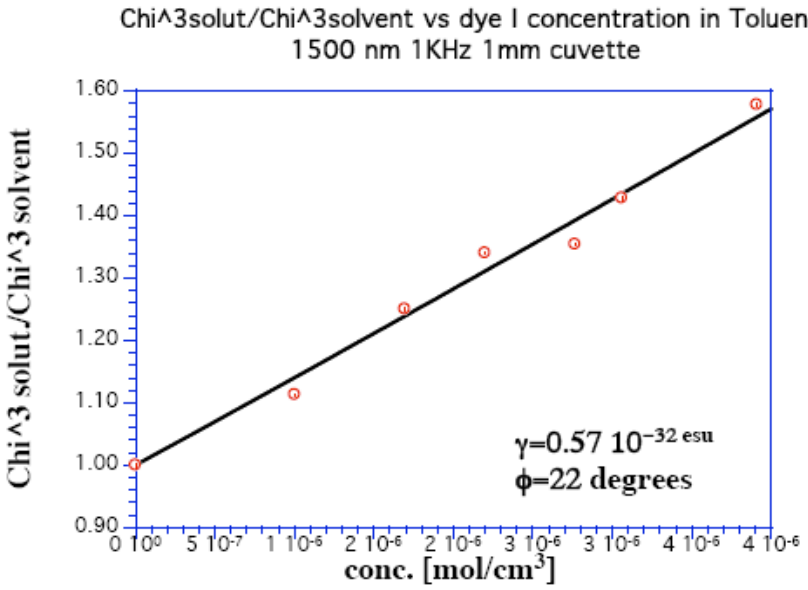

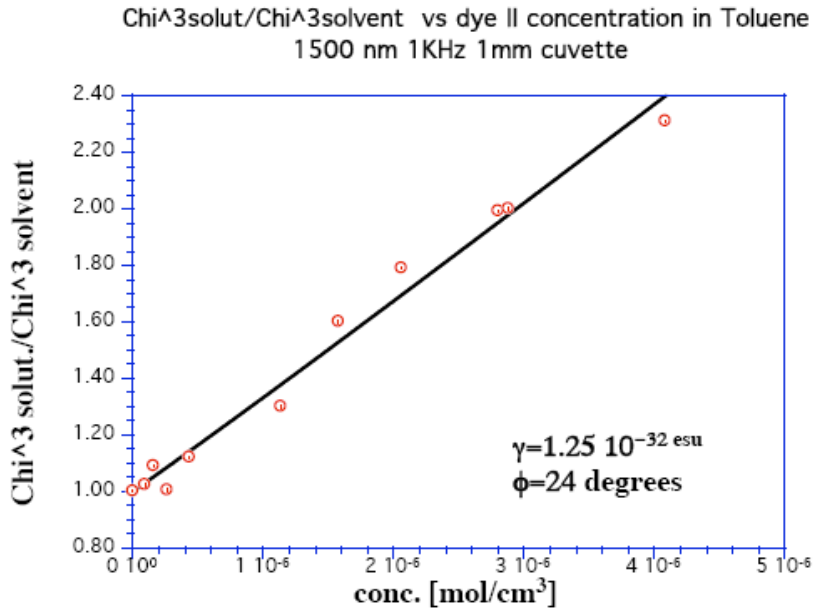
Chi^3solut/Chi^3solvent vs dye II concentration in Toluene
1500 nm 1KHz 1mm cuvette
Chi^3 solut./Chi^3 solvent
2.40
2.20
2.00
1.80
1.60
1.40
1.20
1.00
0.80
0 10^0
1 10^-6
2 10^-6
3 10^-6
4 10^-6
5 10^-6
conc. [mol/cm^3]
γ=1.25 10^-32 esu
ϕ=24 degrees

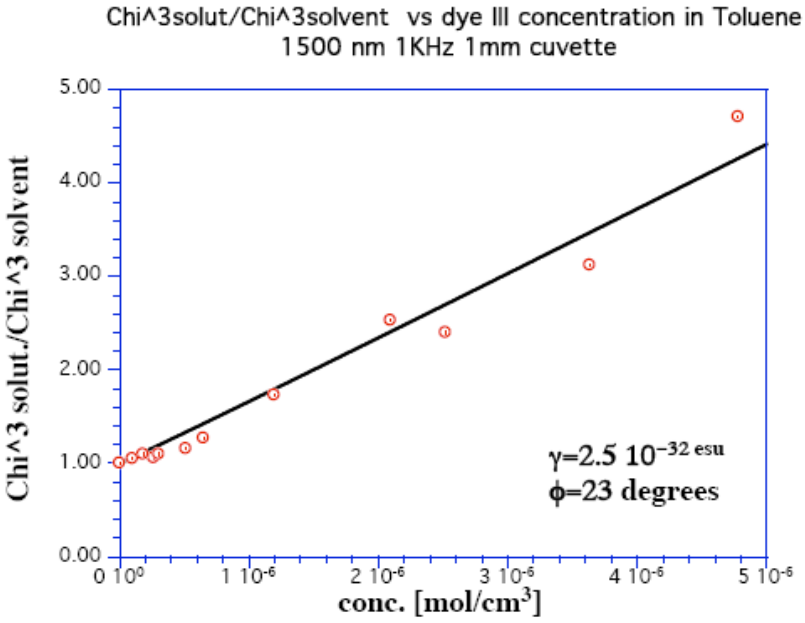
Chi^3solut/Chi^3solvent vs dye III concentration in Toluene
1500 nm 1KHz 1mm cuvette
Chi^3 solut./Chi^3 solvent
5.00
4.00
3.00
2.00
1.00
0.00
0 10^0
1 10^-6
2 10^-6
3 10^-6
4 10^-6
5 10^-6
conc. [mol/cm^3]
γ=2.5 10^-32 esu
ϕ=23 degrees

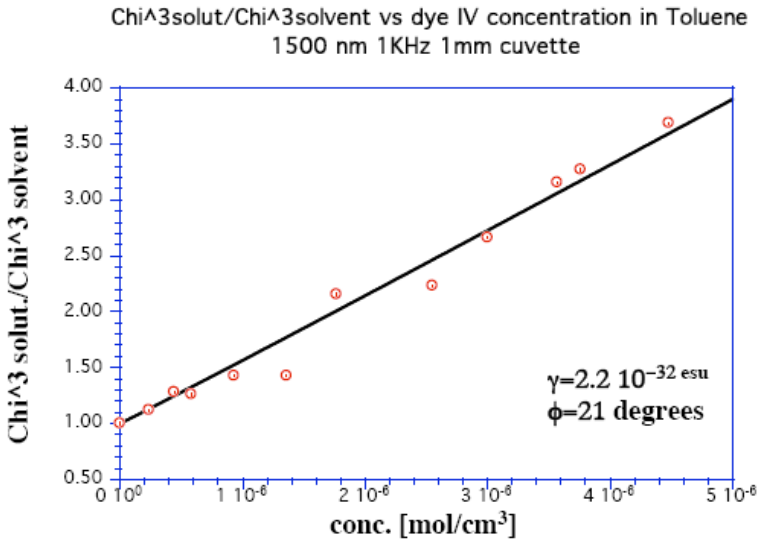

Fig. 10.13: Solution measurements at 1500 nm for determining the microscopic third order nonlinearity according to the internal reference method. The phase values were obtained from Z-scan measurements at 1500 nm.

Tables 10.3 and 10.4 summarize the values for the nonlinearity at 1300 nm and 1500 nm respectively. An overall error of ±15% was estimated for all the measurements

Table 10.3: Values obtained for the second order polarizability $\langle\gamma\rangle$ at 1300nm for the extended squaraine dyes using the internal reference method

Dye	$\langle\gamma\rangle$/ 10^{-32} esu	**Phase/**degrees	**Re**$\lvert\gamma\rvert$/10^{-32} esu	**Im**$\lvert\gamma\rvert$/10^{-32} esu
I	0.88±0.13	36±6	0.71	0.5
II	2.9±0.4	28±4	1.8	1.3
III	5±0.7	40±6	3.8	3.2
IV	2.0 ±0.3	42±6	1.5	1.3

Table 10.4: Values obtained for the second order polarizability $\langle\gamma\rangle$ at 1500nm for the extended squaraine dyes using the internal reference method

Dye	$\langle\gamma\rangle$ **/ 10^{-32} esu**	**Phase**	**Re$\lvert\gamma\rvert$/10^{-32} esu**	**Im$\lvert\gamma\rvert$/10^{-32} esu**
I	0.57±0.08	22±3	0.53	0.21
II	1.25±0.18	24±3	1.1	0.51
III	2.5±0.4	23±3	2.3	0.97
IV	2.2±0.3	21±3	2.0	0.79

10.5.2 Time-resolved DFWM at 1300 and 1500 nm.

Time-resolved DFWM was obtained by setting the energy to a value where the DFWM signal from the solution could be detected. The delay position for which the DFWM signal is maximum is set as zero. The delay line corresponding to the probe beam is moved to negative values so that the probed pulsed arrives before the two writing beams at the sample.

The DFWM signal is registered, as the delay is reduced to the initial position where the signal reaches the peak, and then delayed further to positive delay values, where the probe pulse arrives after the two writing beams and the grating dynamics are probed. For ultrafast type of nonlinear responses, the time resolved DFWM is a simple third order correlation of the ultrafast pulse (see chapte 9 section 9.3.1). Time resolved data are run for pure toluene and dye solutions at 1300 and 1500 nm. Here we reported the time-resolve DFWM data for dye II. Toluene is known to have an nonlinear time-response that is pulse-width limited, because at these wavelengths, the response is due to the electronic and nuclear polarization only[11]. All the squaraine dyes were found to have ultrafast nonlinearities at 1300 and 1500 nm as shown in fig. 10.14

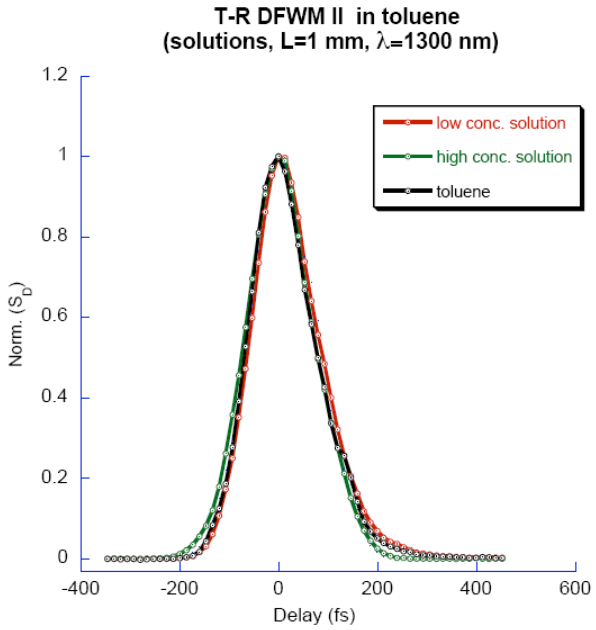

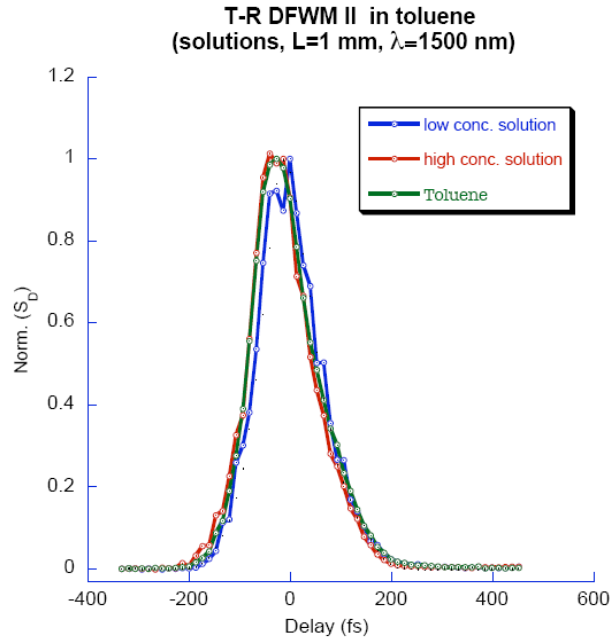

Fig. 10.14: Time-resolved DFWM for dye II at 1300 and 1500 nm.

10.5.3 Hyperpolarizability <γ> of squaraine type molecules via Z-scan at 1300 and 1500 nm.

Z-scan is a one beam technique for measurements of optical nonlinearities, including nonlinear refraction and nonlinear absorption. This technique complements DFWM, providing a way to measure the phase of $\langle\gamma\rangle$.

The second order hyperpolarizability $\langle\gamma\rangle$ is obtained from the $\left|\chi^{(3)}\right|_{solution}$ using equation 9.32 and 9.33. For the real part of $\left|\chi^{(3)}\right|_{solution}$, the solvent contribution has to be subtracted by the overall solution as shown in equation 10.6.

$$\mathrm{Re}\left|\chi^{(3)}\right|_{dye} = \mathrm{Re}\left|\chi^{(3)}\right|_{solution} - \mathrm{Re}\left|\chi^{(3)}\right|_{solvent} \tag{10.6}$$

Materials and methods

Solutions of each dye in toluene is prepared, in concentrations similar to that utilized on the DFWM set-up. Each solution is poured into a 1 mm quartz cuvette and Z-scan measurements will be taken for three different concentrations of each dye. The final value is then obtained as an averaged over the three values.

For Z-scan measurements, the spatial profile of the beam is very important as described in chapter 9. A beam scan is performed at the beginning to assess the value of M, before running the two standards, fused silica for the closed aperture (at this wavelengths fused silica does not have nonlinear absorption) and GaAs for the open aperture.

The value of M that will then be used for the samples is the one that fits both standards appropriately. Next, the contribution from the solvent, toluene in this case, has to be determined. Solvents at this wavelength do not have any contribution to the open aperture since their electronic transitions are too far away, but they contribute to the closed aperture. The z-scan of the pure solvent is measured and its contribution subtracted to that of each sample closed aperture (equation 10.6). In order to minimize the thermo-optic effects on the sample, data were taken both wavelengths at 50 Hz. Z-scan traces are reported in fig. 10.15-18 showing the fitting of both open and closed aperture described in chapter 9 section 9.5

Closed aperture signals are strongly asymmetric even at low laser repletion rate, both at 1300 and 1500 nm. The same solutions were first measured using 1 KHz repetition rate where the real part showed even more severe asymmetry. This suggests that the origin is largely thermo-optical. The dyes under analysis have nonlinearities especially at 1300 nm where the $Im\left|\chi^{(3)}\right|$ is as large as the $Re\left|\chi^{(3)}\right|$, increasing the uncertainty of the numerical evaluation imposed by the condition[2] $\beta/k\, n_2^I \leq 1$, a common situation in semiconductors type of materials where the condition above is not met[2]. At 1500 nm the, real part becomes larger than the imaginary, but the closed aperture trace remains quite asymmetric. The asymmetry is even more accentuated at higher irradiances as shown in fig 10.16 for dye II. The source of asymmetry in Z-scan closed aperture traces have been investigated in the literature; one of the causes has been shown to be beam ellipticity [12], however this is not the case since the closed aperture for the fused silica reference does not show such severe asymmetry (see fig. 10.19). The

large nonlinear absorption of the samples, accompanied by thermo-optical effects, is likely to be the source of the asymmetry.

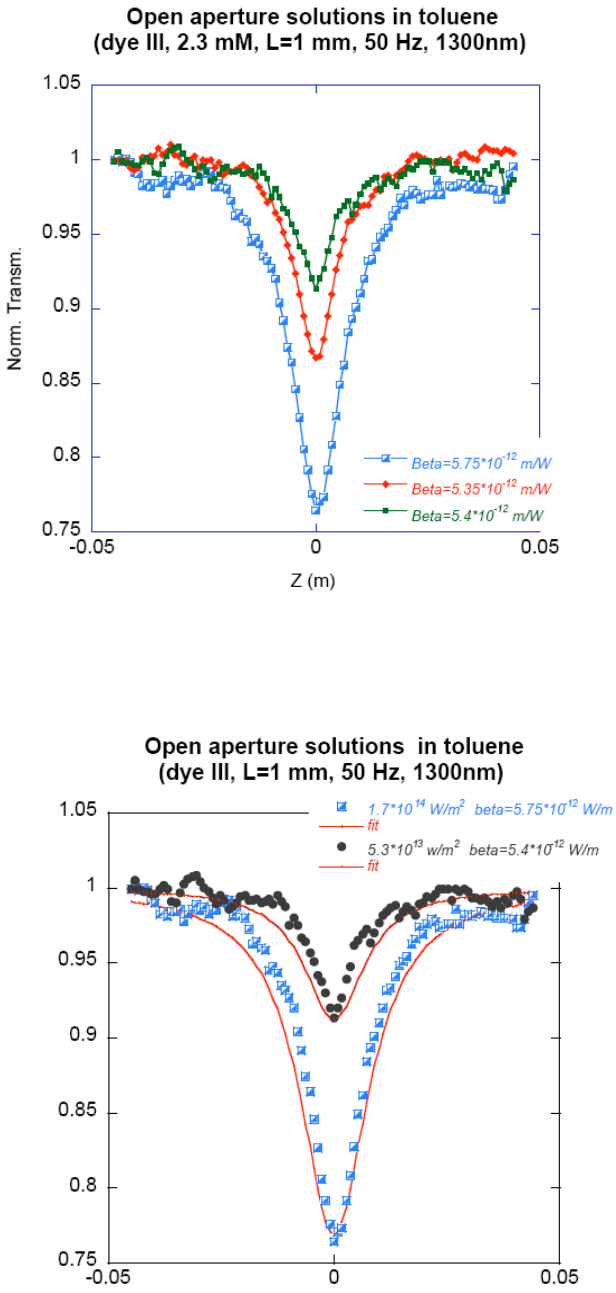

Fig. 10.15: Open aperture data (above) and fitting curve (below) for dye III in toluene solution at 1300 nm and 50 Hz

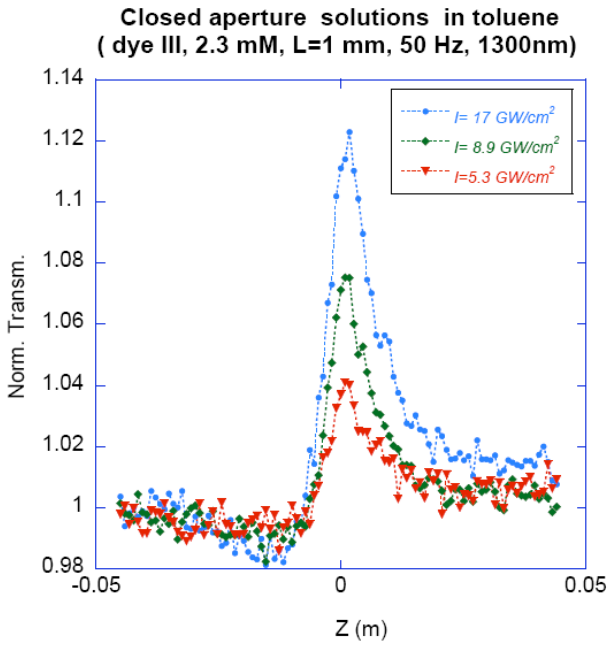

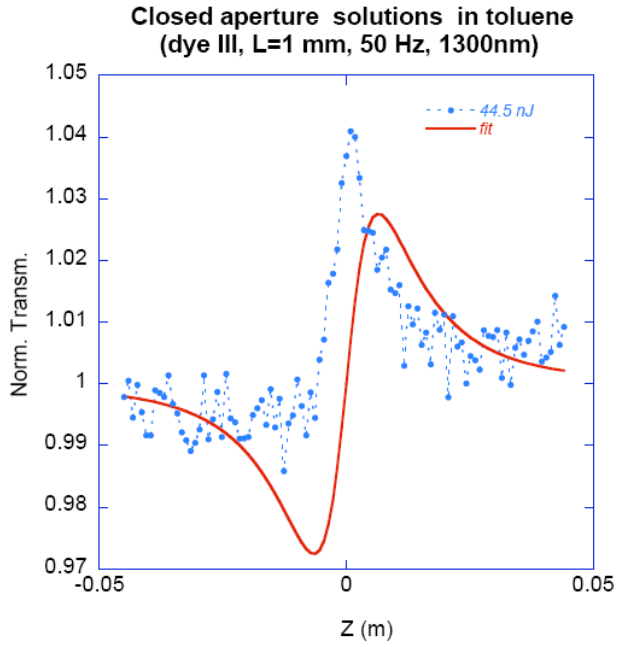

Fig. 10.16: (Above) Closed aperture Z-scan data at different energies for dye III in toluene at 1300 nm. (Below) Data fitted with the nonlinear refraction equation for Z-scan

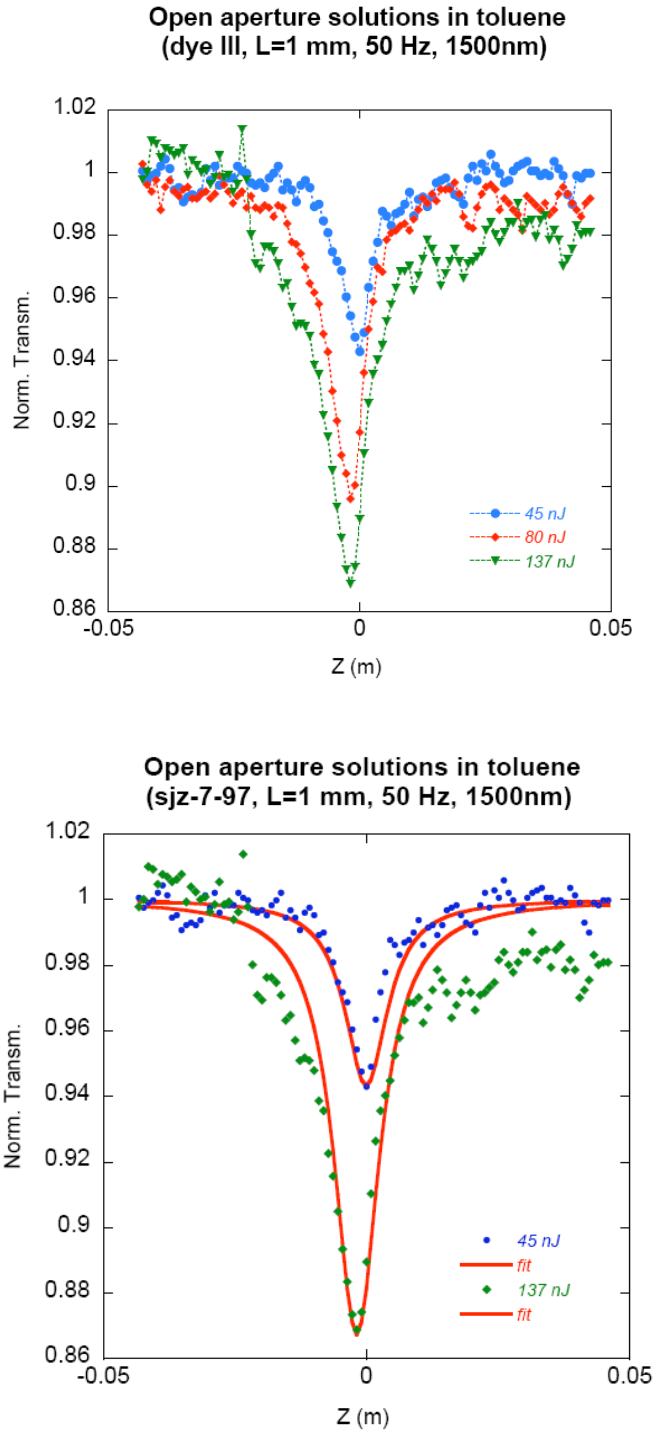

Fig. 10.17: Open aperture data (above) and fitting curve (below) for dye III in toluene solution at 1500 nm and 50 Hz

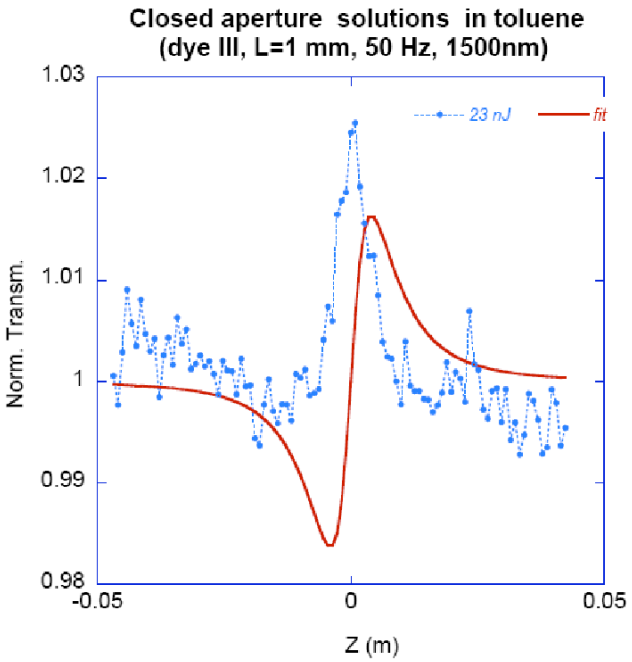

Fig. 10.18: Closed aperture Z-scan data for dye III in toluene at 1500 nm. The data were fitted with the nonlinear refraction equation for Z-scan

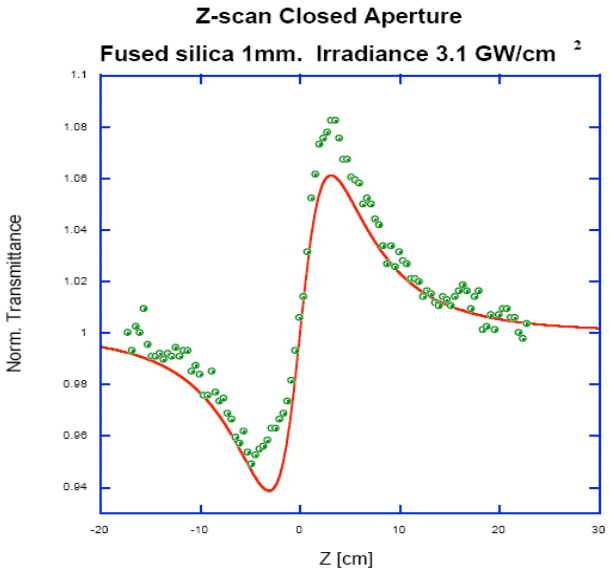

Fig.10.19: Closed aperture Z-scan at 1300 nm

Further reduction of the laser repetition rate were attempted at the expense of pulse to pulse energy stability (energy fluctuation over 30 % were observed at 10 Hz).

Tables 10.5 and 10.6, collect the values of $\langle\gamma\rangle$ for squaraine dyes under investigation at 1300 and 1500 nm.

Table 10.5: Second-order hyperpolarizability values at 1300 nm via Z-scan technique

Dye	$\langle\gamma\rangle$ **/ 10^{-32} esu**	**Phase**	**Re$\lvert\gamma\rvert$/10^{-32} esu**	**Im$\lvert\gamma\rvert$/10^{-32} esu**
I	0.83±0.13	36±6	0.66	0.48
II	3.3±0.5	28±4	2.9	1.6
III	9.3±1.3	40±6	7.1	5.9
IV	4.7 ±0.7	42±6	3.4	3.1

Table 10.6: Second-order hyperpolarizability values at 1500 nm via Z-scan technique

Dye	$\langle\gamma\rangle$ **/ 10^{-32} esu**	**Phase**	**Re$\lvert\gamma\rvert$/10^{-32} esu**	**Im$\lvert\gamma\rvert$/10^{-32} esu**
I	0.83±0.08	22±3	0.77	0.31
II	2.6±0.18	24±3	2.4	1.1
III	6.3±0.4	23±3	5.8	2.4
IV	3.8±0.3	21±3	3.5	1.3

Z-scan closed aperture traces at 1300 and 1500 nm revealed a positive sign for $\langle\gamma\rangle$. This is translated, according to the three-state model (equation 8.3), in the T term being larger than N. The two-photon term is enhanced at this wavelength range as suggested from the two-photon spectra of the dyes.

In equation 8.3, the only unknown term, is $M_{ge'}$, the transition dipole between the ground and the two-photon allowed state $\left|e'\right\rangle$ (the D term is zero for centrosymmetric molecule[13]). $M_{ge'}$ can be calculated from the two-photon absorption peak β_p according to the following equation[14]:

$$M_{ge'} = \frac{5\beta_p \varepsilon_0^2 n^2 c^2 \left(E_{ge} - \hbar\omega\right)^2 \Gamma}{\hbar\omega^2 L^4 M_{eg}^2} \tag{10.7}$$

Where L is the local field factor, Γ is the damping width, the two photon bandwidth will be used (the full width half maximum from fig. 10.20).

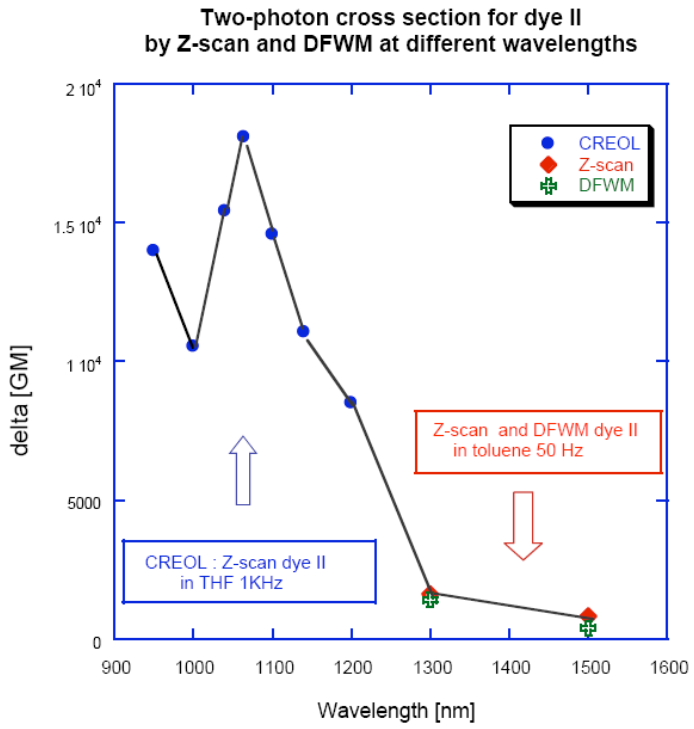

Fig. 10.20: Two-photon spectra for dye II in solution measured via Z-scan and DFWM at different wavelength. Part of the data are being provided by CREOL (University of Central Florida)

The two-photon spectrum for dye II was obtained via Z-scan in THF by Van Stryland's group at University of Florida CREOL. Their data, reported in fig.10.19 gave the two-photon peak maximum around 1064 nm.

The value obtained from equation 10.7 for the $M_{ge'}$ is 12.7 Debye.

This allows to calculate $\gamma^{[\mathrm{mod}\,el]}{}_{xxxx}$ from (8.3) as function of wavelength. The T term and the modulus of the N term were calculated to determine where the γ changes its sign. It was found that the N term takes over for the wavelength longer than 1690 nm as shown in fig. 10.21.

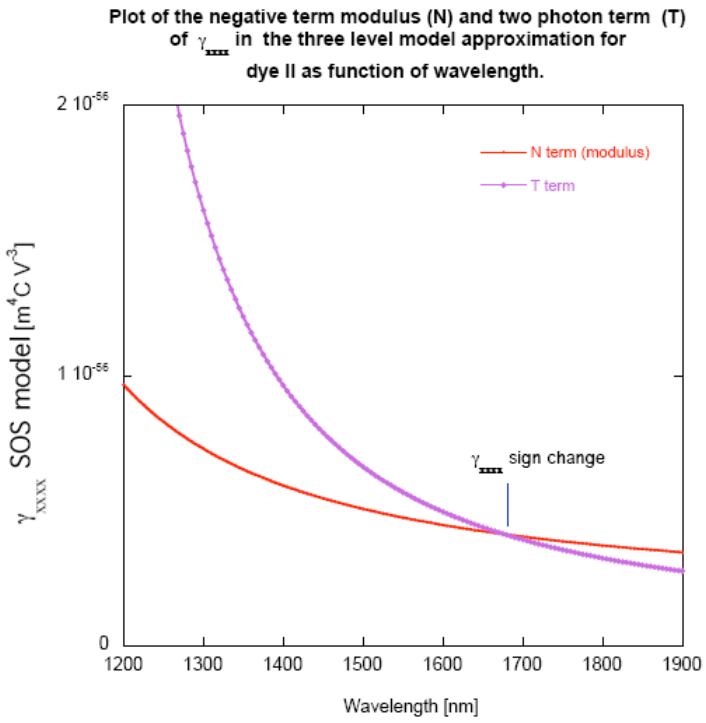

Fig. 10.21: Plot of the negative term (N) modulus, and two-photon term T for dye II in the three-state model approximation as function of wavelengths.

An way to compare the nonlinearity besides looking at the absolute values for each dye , is to normalize it for the number of double bonds contained in the main chain, N_D. This will provide a rough estimate of the nonlinearity per double bond. In fig 10.22 the normalized nonlinearity calculate from the DFWM data as $\langle\gamma\rangle / N_D$ at 1300 and 1500 nm give an interesting overview for the two different class of extended squaraine analized.

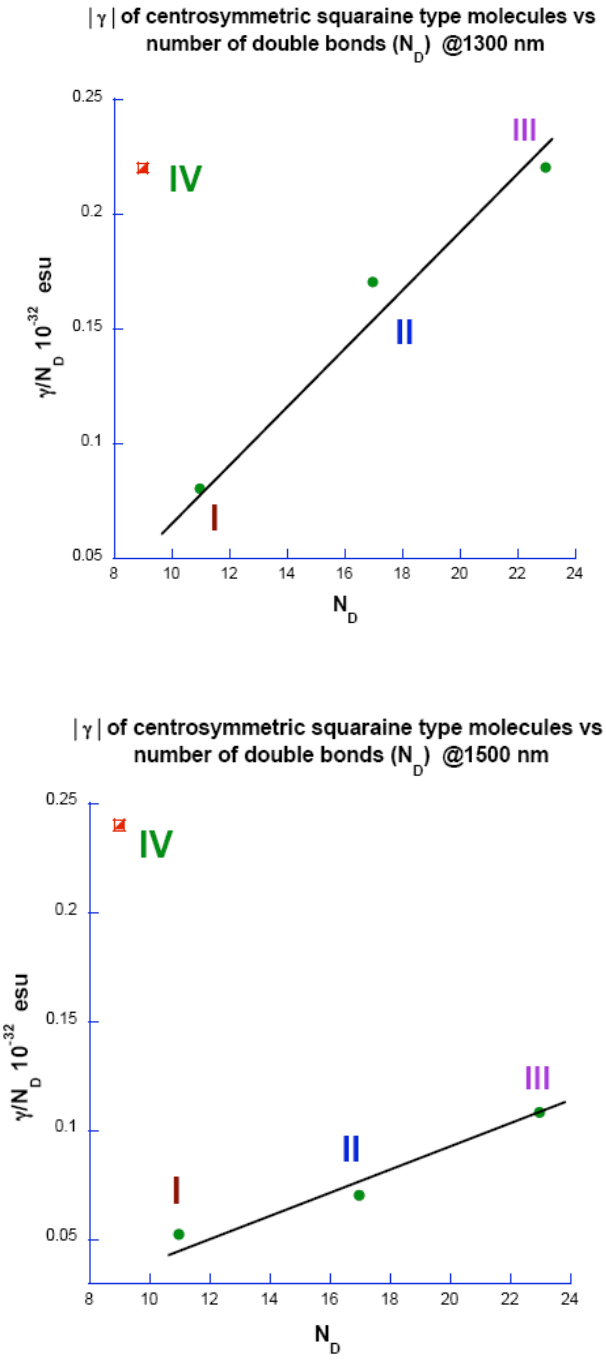

Fig. 10.22: Normalized $\langle\gamma\rangle$ values at 1300 and 1500 nm for extended squaraine dyes in solution.

10.6 Squaraine dyes $|\chi^{(3)}|$ nonlinearities in high-density states at 1300 nm.

High density states measurement are particularly important in assessing the properties of nonlinear organic molecules for photonic type of applications. Their macroscopic nonlineaity, in fact, cannot not be fully predicted by the low density state (microscopic $\langle\gamma\rangle$) measurement, considering that the overall interactions when the molecular density is high are different, and other effects like aggregation can play a big role in determining the nonlinearity.

$|\chi^{(3)}|$ was measured in the standard way using equation (9.12), where account was taken for the different path lengths of the reference and the neat film of each dye.
To ensure that the geometrical and temporal overlap was collinear over the full length of the sample, a slab of silica 500 μm was used instead of the regular 1 mm. The DFWM signal was proven not to remain proportional to the square of the path length as described in equation (9.12). $|\chi^{(3)}|$ magnitude decreases as the sample path length is increased. For instance films made using dye II having different thickness were made on silica substrate, measurement for $|\chi^{(3)}|$ showed always larger values for thin spin-coated film compare to thick sample (see fig. 10.23).
The possibility of molecular alignment from the substrate was explored, but proven not to be the source of the decrease in nonlinearity in thicker samples. Other possible explanation for such phenomenon could be related to self-focusing of the laser beams in

the thick samples versus the thin ones. Further analysis is required to determine the origin for such anomaly in the $\left|\chi^{(3)}\right|$ length dependence

10.6.1 Films preparation

All films were prepared from solution of the dyes, except dye II that is already a very viscous liquid at room temperature, due to the presence of long alkyl side-chain, added specifically to improve processability.

The dyes are soluble in several organic solvents like toluene, chlorobenzene and THF. The solution is filtrate using 0.2 μm filter. The pre-cleaned microscope slide substrate is flooded with the solution and the spin-coater is set to 800 rpm for 5 seconds, followed by an increase rpm cycle of 1400 rpm for 15 seconds to help remove the excess solvent. The films are left in vacuum oven overnight to completely evaporate the solvent (usually toluene).

The thickness of the films is necessary to determine their nonlinearity and after measurement are taken the films thickness are determined by profilometer.

The absorption spectra of the spin-coated films are shown in fig. 10.23. The spectra are taken using a double beam UV-Vis-NIR Cary spectrophotometer.

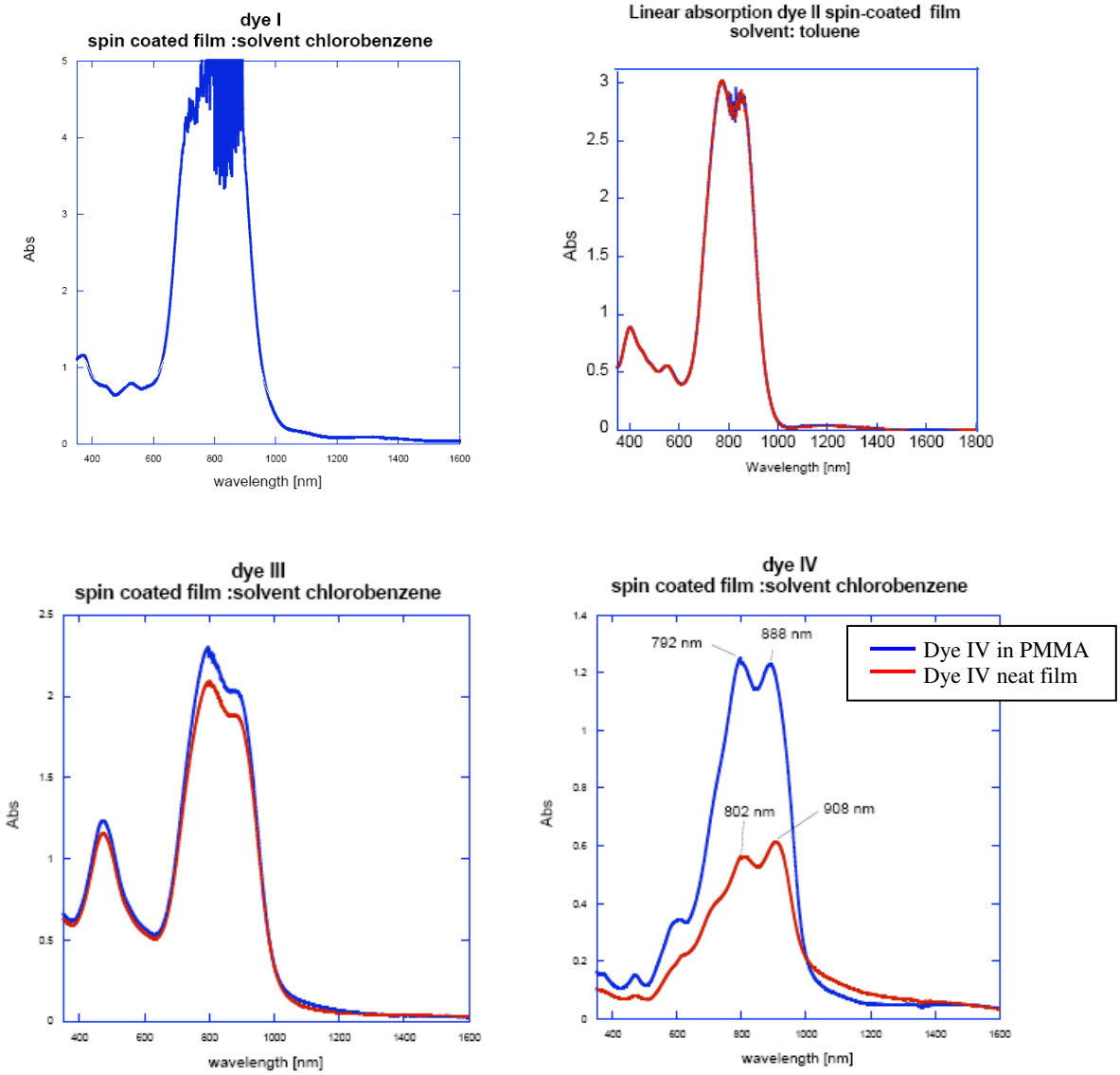

Fig 10.23: Linear absorption spectra of neat and blends of spin-coated films of squaraine dyes

Table 10.7 summarizes the peak values for both the spin-coated films and for the dyes in toluene solution. The recurrent presence of double peaks in films is evidence for excitonic splitting, squaraine are known to form both H and J-type aggregates[15-17].

Table 10.7: Absorption peaks for the spin-coated neat film of squaraine dyes on silica substrate.

Dye	Thin film peaks/nm	Peak in solution/nm
I	n.a.	805
II	772 853	830
III	797 880	850
IV	802 908	879

Dye II being a viscous oil type of material can be casted in different shape and thickness. In fig. 10.24 are shown thick films of neat dye simply sandwiched between two glass microscope slides with a metal spacer of known thickness placed in the middle.

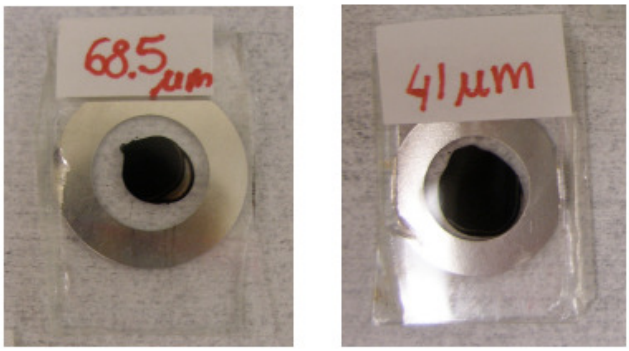

Fig. 10.24: Thick samples obtained without processing using dye II

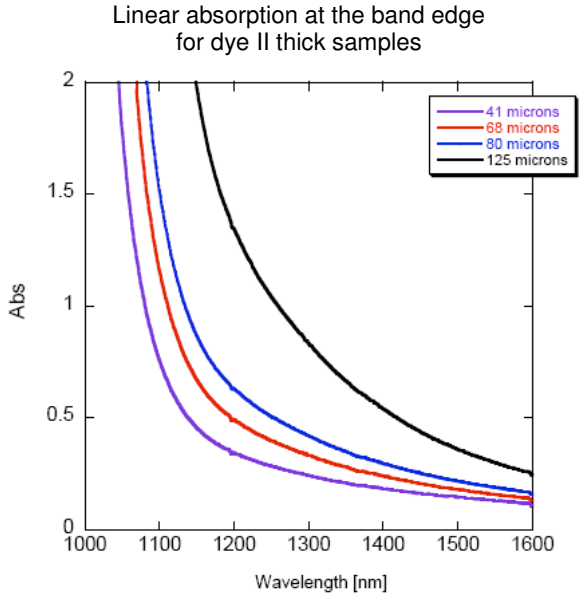

Fig:10.25: Absorption specta for dye II thick samples. The band edge for different thicknesses show linear losses at 1300nm.

10.6.2 DFWM measurements in films

The magnitude of $\left|\chi^{(3)}\right|$ was obtained via DFWM for some of the spin coated samples. In many cases, power dependence for the films were hypercubic, both at 1 KHz and 50 Hz laser repetition rate. The reported values of $\left|\chi^{(3)}\right|$ were exctratcted from the power dependence data, showing strictly cubic behavior. For dye IV, no value could be exctracted, the power dependece was always hypercubic, while for dye I there were insufficient material to repeat the masurements.

Dye II nonlinearity drops as thicker films were measured, as seen in table MM. Two thick samples were measured via DFWM at 1300 nm, although their nonlinearities were in agreement, the spin-coated films provided a considerably larger value (three times higher). Larger $\left|\chi^{(3)}\right|$ values could be due to partial aligment of the dye in the

sample. For instance molecules that are, even partially, alligned parallel to the beam incident field propagation direction would contribute more than molecule with a completely random orientation.

Table 10.8: Magnitude of $\left|\chi^{(3)}\right|$ for spin-coated and thick films at 1300 nm via DFWM at 1 KHz

Dye	$\left\|\chi^{(3)}\right\|$ / 10^{-10} esu	**Film thickness**
II	1.5±0.2	250 nm
II	0.4±0.06	14 μm
II	0.4±0.06	25 μm
III	3±0.5	226 nm

10.6.3 Time resolved DFWM in films

Time resolved DFWM is performed as described already in chapter 9. The time resolved response of each material is compared with that of the fused silica, known to the be instantaneous at this wavelength[18]. The time response after delaying the probe is shown in fig. 10.26 for dyes I, II and III. Al the dyes were found to have an ultrafast $\left|\chi^{(3)}\right|$ at 1300 nm.

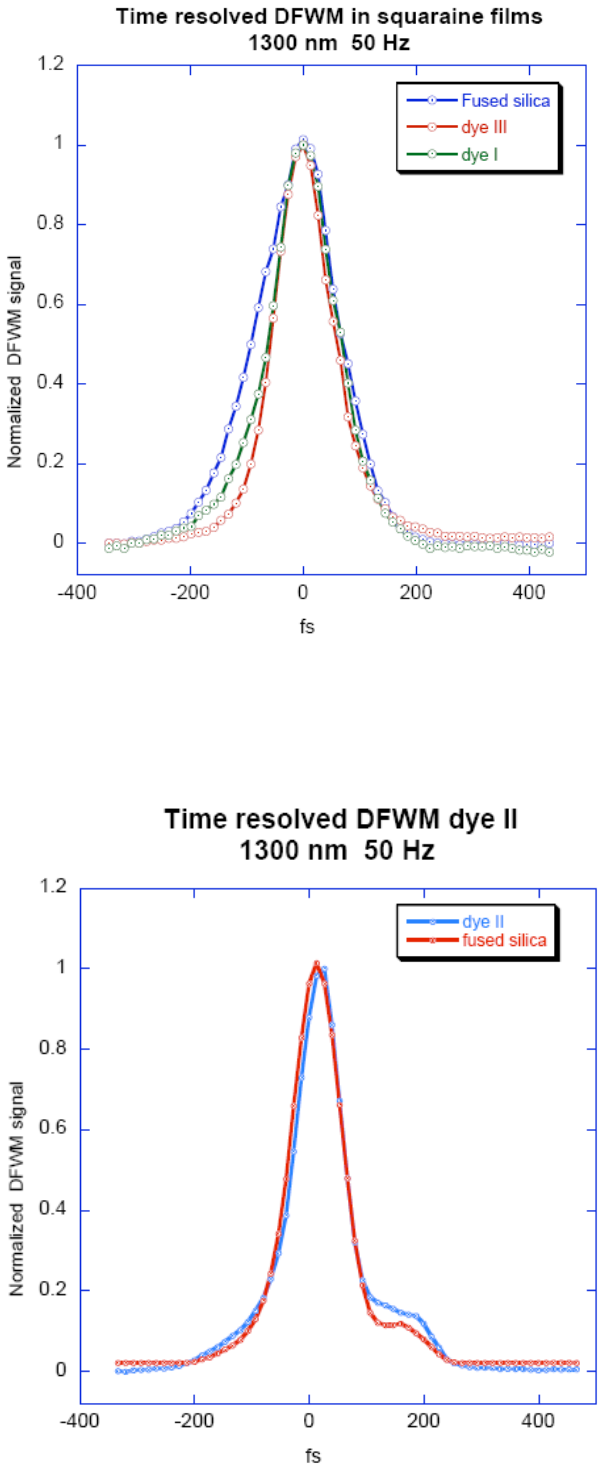

Fig. 10.26: Time-resolved DFWM in spin-coated dyes at 1300 nm

10.6.4 Z-scan nonlinear measurements in films at 1300 nm

For the Z-scan measurements, the laser repletion rate was found to have a large impact in the outcome of the closed aperture trace. At 1 KHz, the films show a negative $\mathrm{Re}\left|\chi^{(3)}\right|$, proven to be a thermo-optical distortion. Z-scan at 50 Hz provided positive $\mathrm{Re}\left|\chi^{(3)}\right|$, as it would be expected for these systems (positive $\langle\gamma\rangle$ values were obtained at 1300 nm)

The open aperture was first fitted with a purely two-photon absorption nonlinearity mechanism. A purely two-photon type of nonlinearity does not properly describe the data from an open aperture trace as can be seen from fig. 10.27. The open aperture data for dye III are not correctly described by a two-photon process solely.

Two-photon absorption processes may be accompanied by excited state absorption (ESA), as it has been demonstrated in many materials including charge transfer salts[19], nanocomposites[20] and organic molecules[21].

The standard Z-scan theory is inadequate to deal with these effects, but lately in the literature, new theories have produced analytical expressions that allow extracting two-photon and ESA cross-section from Z-scan data[22, 23].

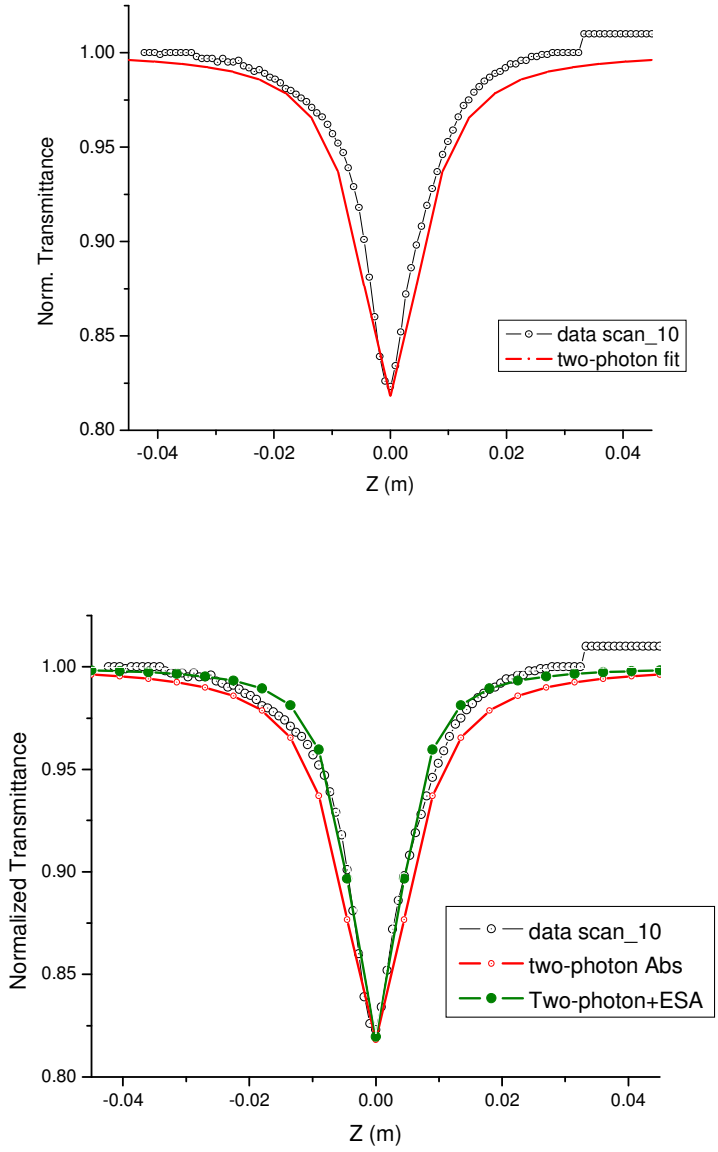

Fig. 10.27: (Above) fitting of open aperture Z-scan of dye III spin-coated film with two-photon absorption only. (Below) fitting using two-photon absorption induced ESA.

The three-level model introduced by Sutherland at al. in 2005[22] will be implemented to isolate the two-photon absorption from the ESA cross-section. Such model estimates an effective ESA cross section, σ_{eff}, without the complications involved in using the more

complete five-level system[24] involving multiple excited states, one of which being a triplet state.

In fig. 10.28 is an illustration of the three-photon absorption model. The condition for employing such model is being in a regime where $\tau_T > \tau_s \sim \tau_p$ where τ_T , τ_s are the singlet and triplet lifetimes respectively, while τ_p is the pulse width. Preliminary femtosecond pump-probe experiments have established the lifetime for singlet S_1 at 1300 nm to be about 25 ps, ensuring the applicability of the three-level model to the system under analysis.

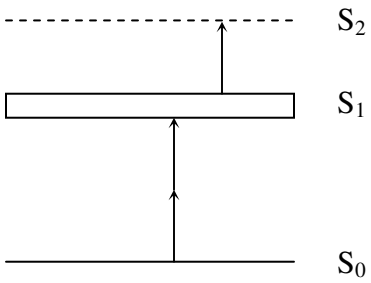

Fig. 10.28: Effective three-photon absorption model.

Table 10.9: Two-photon absorption values for spin-coated films implementing the three-state model on open aperture Z-scan at 1300 nm and 50 Hz.

Dye	**β/ 10^{-9} m W^{-1}**	**σ_{eff}/ 10^{-20} m^2**	**Film thickness / nm**	**Rep. Rate/ Hz**
II	1.35	7.0	950	50
III	1.5	7.0	226	50
IV	2.4	2.8	1900	50

Table 10.10: Two-photon absorption values for dye II thick films implementing the three-state model on open aperture Z-scan at 1300 nm and 50 Hz.

Dye II film thick./ μm	**β/ 10^{-9} m W^{-1}**	**σ/ 10^{-20} m**	**Transmittance %**
41	0.36	23.5	72
68.5	0.42	23.5	51
80	0.36	23.5	40

REFERENCES:

[1] Shen, Y.R., *The principle of nonlinear optics*. 1984, New York: Wiley

[2] Sheik-Bahae, M., Said, A. A., Wei, T.-H., Hagan, D., Van Stryland, E. W., IEEE J. Quant. Electron. 26, 760 (1990)

[3] Freitas, D. S., De Oliveira, J. R., De Moura, M. A., J. Phys. A. 31, 1761 (1998)

[4] Murray, J., Milam, D., Boley, C. D., Estabrook, K. G., Caird, J. A., Appl. Opt. 39, 1405 (2000)

[5] Celliers, P. M., Estabrook, K. G., Wallace, J., Murray, J. E., Da Silva, L. B., MacGowan, B., J., Van Wonterghem, B., M., Manes, K. R., Appl. Opt. 37, 2371 (1998)

[6] Mulliken, R. S., J. Chem. Phys. **7**, 14 (1939)

[7] Herzberg, G., *Molecular spectra and molecular structure. I. Spectra of diatomic molecules*. 1950, New York: Van Nostrand Reinhold Company

[8] Danehy, P. M., Paul, P. H., Farrow, R. I., J. Opt. Soc. Am. 12, 1564 (1995)

[9] Nelson, K. A., Lutz, D. R., Fayer, M. D., Madison, L., Phys. rev. B. 24, 3261 (1981)

[10] Desai, R. C., Leverson, M. D., Barker, J. A., Phys. Rev. A. 27, 1968 (1983)

[11] Eyring, G., Fayer, M. D., J. Chem. Phys. 81, 4314 (1984)

[12] Mian, S. M., Taheri, B., Wicksted, J. P., J. OPt. Soc. Am. B. 13, 856 (1996)

[13] Meyers, F., Marder S. R., Pierce, B. M., Perry, J. W., J. Am. Chem. Soc. 116, 10703 (1994)

[14] Rumi, M., Ehrlich, J. E., Heikal, A. A., Perry, J. W., Barlow, S., Hu, Z., McCord-Maughon, D., Parker, T., Rochel, H., Thayumanav, S., Beljonne, D., Bredas, J.-L., J. Am. Chem. Soc. 122, 9500 (2000)

[15] Saji, A., Basheer, C., Arum, K. T., Ramaiah, D., Das, S., J. Phys. Chem. A. 111, 3226 (2007)

[16] Sato, Y., Furuki, M., Tian, M., Isawa, I., Sun Pu, L., Appl. Phys. Lett. 80, 2254 (2002)

[17] Stenescu, M., Samha, H., Perlstein, J., Whitten, D. G., Langmuir. 16, 275 (2000)

[18] Santran, S., Canioni, L., Sarger, L., Cardinal, T., Fargin, E., J. Opt. Soc. Am. B. 21, 2180 (2004)

[19] Sutherland, R. L., Brant, M. C., Rogers, J. E., Slagle, J. E., McLean, D. G., Fleitz, P. A., J. Opt. Soc. Am. B. 22, 1939 (2005)

[20] Kurian, P. A., Vijayan, C., Sandeep, C. S. S., Philip, R., Sathiyamoothy, K., Nanotechnology. 18, 075708 (2007)

[21] Fakis, M., Tsigaridas, G., Polyzos, I., Giannetas, V., Persephonis, P., Spiliopoulos, I., Mikroyannidis, J., Chem. Phys. Lett., 2001. **342**: p. 155.

[22] Sutherland, R.L., Brant, M. C., J. OpT. Soc. Am. B. 22, 1939 (2005)

[23] Gu, B., Ji, W, Patil, P. S., Dharmaprakash, S. M., Wang, H. -T., Appl. Phys. Lett. 92, 091118 (2008)

[24] Khoo, I. C., Diaz, A., Ding, J., J. OPt. Soc. Am. B. 21, 1234 (2004)

CHAPTER XI

CONCLUSIONS AND FUTURE WORK

Conclusions

First part.

The presence of plasmonic field induced by colloidal gold nanoparticles in the vicinity of bR proteins was proven to affect the photocycle dynamics of its intermediates. The plasmonic field generated upon excitation of the surface electrons in gold nanoparticles changed the dynamics of both intermediates I_{460} and M_{412}, the former being directly correlated to the Retinal Schiff Base (RSB) isomerization and the latter to the reprotonation of the Schiff Base to complete the proton transport across the protein. Although the two intermediate dynamics occur over very different time-scales; I_{460} has a lifetime of about 500 fs while M_{412} few ms, both processes have a common denominator, large charge rearrangement are experienced by the protein at these particular stages of the photocycle. In the case of intermediate I_{460} a large dipole change characterized the electronic transition which is the precursor to the formation of the intermediate itself. The dipole change is localized at the RSB site where a large charge displacement takes place along the polyene chain of the RSB. The decay lifetime of the intermediate in presence of the external plasmonic field induced by Au nanospheres present in the vicinity of the protein, increases the lifetime of the I_{460} intermediate as shown in chapter III. The decay dynamic was shown to be a function of either the concentration of nanosphere or their sizes, enforcing the theory of the plasmonic field as the source of the

"perturbation". Other intermediates dynamics taking place on comparable time-scales, without involving dipole change or charge displacement, like the vibronic relaxation of intermediate J_{625} to K_{610}, are instead not affected by the presence of Au nanospheres. The phonon-phonon relaxation time in gold nanospheres is one hundred picoseconds eliminating the possibility that the observed change in the dynamic is a result of thermal effects resulting from such relaxation of the gold nanoparticles. This suggests that the field generated upon the plasmon excitation is the only cause of the observed changes in excited state I_{460} intermediate lifetime.

The actual vectorial transport of the proton from the cytoplasmic half channel to the extracellular half channel takes place during formation and decay of the intermediate M_{410}, this process involves the RSB deprotonation to Asp-85 (M_{410} rise) in the extracellular half channel, followed by its reprotonation by Asp-96 (M_{410} decay), located in the cytoplasmic half channel. Both the processes of M_{412} formation and decay notoriously involve proton movement along with large structural rearrangements of the protein secondary structure. In chapter IV it is shown that while the decay lifetime of M_{412} in presence of Au nanorods decreases, its rise time is not affected. The decay lifetime was shown to decrease both as function of the nanorods concentration and the exciting laser power. One of the concerned was to determine whether such increase in the kinetic could be due to thermal effects, considering the ability of nanorods to efficiently convert absorbed photon into heat. An estimate of the local temperature increase can be done using theoretical equations, where specific experimental parameters like the laser fluence, and the nanorods concentrations are plugged into the equation. A local temperature increase of about 0.3 °C was estimated, a value that would not explain

the large effect in decay dynamic observed (up to 35% decrease in lifetime). The bulk temperature was monitored as well, as function of the nanorods concentration, producing a trend that is not in agreement with the monotone decrease observed experimentally. These two observations led to believe that the change in dynamic observed for the decay of M_{412} cannot be simply due to thermal effects but are in fact associated with the nanoparticles plasmonic field. The same experiment was conducted in presence of Au nanospheres, present with even larger OD than nanorods, and no effect in the dynamic was observed. Nanospheres, like nanorods have similar heat conversion efficiency, but Nanorods are known to have larger peak enhancement factors (at least one order of magnitude larger) and are consequently able to produce larger plasmonic field intensity. Another consideration involves the average distance of the nanorods in the sample. As described in chapter II, nanosphere and nanorods when added to the bR sample in presence of a neutral pH buffer, go preferentially on the PM surface where they get adsorbed. Under a dark field microscope, the purple membrane patches appeared covered in nanoparticles leaving a small fraction of them floating freely in solution. It is hard to estimate what is the average distance of the nanorods on the patches; considering the 2-dimentional self assembly arrangement of the bR protein in a planar hexagonal lattice with a 63 Å unit cell [1], we estimate an average distance between nanorods of about 100 nm. Such distance insures that even the surrounding bR proteins, which are not covered by the nanorods are still being affected by the plasmonic field generated. A question that still needs to be raised is why the rise dynamic of M_{412} not affected by the plasmonic field? Possible reasons could lie on the different nature of the process, the proton is displaced over a much shorter distance (3.5 nm versus the 12 nm in the decay),

the environment in which the proton is travelling is again is rich in highly polar and rich charges, which could potentially screen the plasmonic field.

Secon part.

The D-A-D dyes under investigation show sharp linear absorption peaks in the NIR, with very large transition dipole moment (see table 10.2). As the conjugation length is increased, from I to III, the peak wavelength red shifts. The shift observed, per double bond added to the structure, is consistent with that of a polyene type system[2] rather than a cyanine[3, 4]. This implies that the cyanine character remains localized at the squarylium core and it does not propagate throughout the length of the molecule. At the same time the sharp absorption spectra resemble transition with no structural changes, typical of a cyanine system. Dye IV, differs from the other dyes for two main reasons: it has a considerably shorter chain length, with only two donor groups, and it contains two squarylium groups, coupled through a double bond. Dye IV even if considerably shorter than III, but with roughly double the delocalization length, has an absorption maximum that is 30 nm red shifted compare to it.

The second-order hyperpolarizability of the dyes was measured at 1300 and 1500 nm using femtosecond pulses both via DFWM and Z-scan. The Z-scan traces, even if affected by severe asymmetry, provided proof that the real part is positive at both wavelengths. The z-scan $\langle\gamma\rangle$ values are larger than those obtained by DFWM by a factor of 3 (for some of the dyes), but an agreement is found on the overall trend; the magnitude of γ increases from I to III, while the magnitude of IV is in between II and III (depending

upon the technique). When the magnitude of $\langle\gamma\rangle$ is normalized for the number of double bonds on the main chain of each dye, dyes I II and III lie along straight line as shown in fig. 10.22. This proves that increasing the conjugation length for these systems produces larger third-order nonlinearity. What is interesting is the relative position of IV, standing above the line defined by dyes I, II and III. This proves that a better strategy is maintaining the delocalization along shorter chain length than greatly increasing the conjugation length by adding more polyene character to the molecule.

At 1300 nm, all the dyes have large phase values; such large nonlinear absorptions are mainly due to two-photon absorption. The two-photon peak, was found according to both experimental[4] and theoretical study[6] to lay right above the one photon allow state (about 1 eV above). The large transition dipole moment between one photon and two photon allowed state combined with a small energy detune, enhances the two photon absorption cross section for these extended squaraine dyes, compared to other class of chromophores where low detuning energies are often precluded by broad one photon absorption band.

At 1500 nm, the phase decreases for all system, along with their magnitude. A decrease in magnitude of 25 to 35% (up to 50% for DFWM data) is observed for all dye. For wavelength further away from the two-photon peak, a decrease in the phase is observed for all the dyes bringing larger contribution from the real part versus the imaginary. Again, dye IV shows the largest nonlinearity per double bond. The two-photon cross section values obtained for such extended squarylimum dye in the tail region are comparable to two-photon peak values for D-A-D polyene type systems[7].

The nonlinear response is instantaneous when in solution and it is maintained for high-density states.

Large imaginary values for $\langle\gamma\rangle$ at 1300 nm translate to large imaginary $\left|\chi^{(3)}\right|$ in thin films, (and correspondently large β values). Of considerable interests are the large two-photon absorption cross section β in this region of the spectrum. In thin film dye II, III and IV have two-photon absorption cross-section comparable to that of semiconductors like GaAs (β=1.9 10^{-9} m/ W), which is largely used in photonic type of applications like signal reshaping[8] and optical clock recovery[9]. The nonlinearity was found not only due to two-photon processes, as suggested from the Z-scan aperture data, where in fact a fifth-order nonlinearity, with a two-photon induced excited state absorption describes the mechanism more accurately. The thin films are highly transparent in the spectral region of interest and dye II, with its viscous liquid state at room temperature can be cast into shapes compatible for efficient two-photon limiting applications.

Future work

The possibility of modifying protein dynamics using nanoparticles is a novelty and it could have significant implications, especially for medical applications. For instance being able to control the intake of drugs or other chemicals via transmembrane protein in cells would be of considerable interest. The effect has the advantage of having no restriction on the time scale of the dynamics involved, both ultrafast and millisecond time scale dynamic can be affected as proved for bR, with the requirement of having large

charge displacement or dipole changes involved. In this thesis the protein of choice was bR, a well known system that has been studied for more than thirty years, which has become the model system for ion transport in membrane, a very important function for biological system. We suggest that the next step would be the application of the same principle to a variety of protein, to generalize our findings.

The possibility of controlling protein functionality through light, in a completely reversible way and without damaging the protein could be of large interest.

A more complete approach to the study should involve a way to covalently attach the nanoparticles to specific sites on the protein rather than relaying on non-specific interactions, to help improve the sample to sample reproducibility.

REFERENCES:

[1] Henderson, R., Ann. Rev. Biophys. Bioeng. 6, 87 (1977)

[2] Bredas, J.-L., Adant, C., Tackx, P., Persoons, A., Pierce, B. M., Chem. Rev. 94, 243 (1994)

[3] Johr, T., Werncke, W., Pfeiffer, M., Lau, A., Dahne, L., Chem. Phys. Lett. 246, 521 (1995)

[4] Werncke, W., Pfeiffer, M., Lau, A., Grahn, W., Johannes, H. -H., Chem. Phys. Lett. 266, 99 (1997)

[5] Chung, S. J., Zheng, S., Odani, T., Beverina, L., Fu, J., Padhila, L. A., Biesso, A., Hales, J., Zhang, X., Schmidt, K., Ye, A., Zojer, E., Barlow, S., Hagan, D. J., Van Stryland, E. W., Yu, Y., Shuai, Z., Pagani, G. A., Bredas, J. L., Perry, J. W., Marder, S. R., J. Am. Chem. Soc. **128**, 14444 (2006)

[6] Schere, D., Dorfler, R., Feldner, A., Vogtmann, T., Schwoerer, M., Lawrentz, U., Grahn, W., Lambert, C., Chem. Phys. 279, 179 (2002)

[7] Rumi, M., Ehrich, J. E., Heikal, A. A., Perry, J. W., Barlow, S., Hu, Z., McCord-Maughon, D., Parker, T. C., Rockel, H., Thayumanavan, S., Marder, S. R.; Beljonne, D., Bredas, J. L., J. Am. Chem. Soc. 122, 9500 (2000)

[8] Mikroulis, S. S., Bogris, A., Roditi, E., Syvidis, D., SPIE proceedings, 5451, 259 (2004)

[9] Salem, R., Murphy, T. E., IEEE Photon. Technol. Lett. 16, 2141 (2004)